INVESTIGATION INTO THE INTERACTIONS OF NANO AND MICROPARTICLE DRUG CARRIERS WITH SIMULATED INTESTINAL MICROENVIRONMENT

Dhanya C. S.

PhD THESIS

2023

SREE CHITRA TIRUNAL INSTITUTE FOR MEDICAL SCIENCES AND

TECHNOLOGY, TRIVANDRUM

An Institution of National Importance established by an Act of the Indian Parliament
(Act No.52 of 1980)

Dept. of Science and Technology, Govt. of India
www.sctimst.ac.in

INVESTIGATION INTO THE INTERACTIONS OF NANO AND MICROPARTICLE DRUG CARRIERS WITH SIMULATED INTESTINAL MICROENVIRONMENT

A THESIS SUBMITTED BY

Dhanya C. S.

TO

SREE CHITRA TIRUNAL INSTITUTE FOR MEDICAL SCIENCES AND TECHNOLOGY, TRIVANDRUM.

IN PARTIAL FULFILMENT OF THE REQUIREMENTS

FOR THE AWARD OF

DOCTOR OF PHILOSOPHY

2023

DECLARATION BY THE STUDENT

CERTIFICATE

I, **Dhanya C. S.** hereby certify that I had personally carried out the work depicted in the thesis titled, **"Investigation into the Interactions of Nano and Microparticle Drug Carriers with Simulated Intestinal Microenvironment".**

No part of this thesis has been submitted for the award of any other degree or diploma prior to this date.

Dhanya C. S.

Date: 27-10-2023

श्री चित्रा तिरुनाल आयुर्विज्ञान और प्रौद्योगिकी संस्थान, त्रिवेंद्रम केरल– 695 011, भारत
SREE CHITRA TIRUNAL INSTITUTE FOR MEDICAL SCIENCES AND TECHNOLOGY, TRIVANDRUM
KERALA – 695 011, INDIA
((एक राष्ट्रीय महत्व का संस्थान, विज्ञान एवं प्रौद्योगिकी विभाग, भारत सरकार)
(An Institution of National Importance, Department of Science and Technology, Govt. of India)
टेलीफॉन नं/.Telephone No. 0471-2443152 फाक्स/Fax: 0471-2446433,2550728
ई-मेल/E-mail :sct@sctimst.ac.in वेबसाइट/ Website : www.sctimst.ac.in

CERTIFICATE BY THE RESEARCH GUIDE

Dr. Roy Joseph
Scientist G (Sr. Gr.)
Division of Polymeric Medical devices
BMT wing, SCTIMST

This is to certify that **Ms. Dhanya C. S.** from the **Division of Polymeric Medical Devices** of this institute has fulfilled the requirements prescribed for the Ph.D. degree of the Sree Chitra Tirunal Institute for Medical Sciences and Technology, Trivandrum.

The thesis entitled, **"Investigation into the Interactions of Nano and Microparticle Drug Carriers with Simulated Intestinal Microenvironment"** was carried out under my direct supervision. No part of the thesis was submitted for the award of any degree or diploma prior to this date.

Dr. Roy Joseph

Date: 27-10-2023

APPROVAL OF THE THESIS

The thesis entitled

INVESTIGATION INTO THE INTERACTIONS OF NANO AND MICROPARTICLE DRUG CARRIERS WITH SIMULATED INTESTINAL MICROENVIRONMENT

Submitted by

Dhanya C. S.

for the degree of

Doctor of Philosophy

of

SREE CHITRA TIRUNAL INSTITUTE FOR MEDICAL SCIENCES AND TECHNOLOGY, TRIVANDRUM

is evaluated and approved by

……

(Name & Signature of the Guide)

Dr. Roy Joseph

(P.Gopinath)

……

(Name & Signature of thesis examiner)

ACKNOWLEDGEMENTS

I would like to take this opportunity to thank those who have helped and supported me in completing my PhD work.

First and foremost, I would like to thank God, almighty for strengthening and sustaining me throughout this journey of PhD. I wish to express my sincere gratitude to my guide Dr. Roy Joseph for his continuous support, advice, encouragement, and motivation during the entire course of the work.

I am grateful to the Director of SCTIMST and the Head, BMT wing for providing all the facilities for carrying out my work. I am thankful to the Dean, Associate Dean, Registrar, and Deputy Registrar for their academic support and assistance.

I would like to thank my DAC members, Dr. Rekha M. R., Scientist F, Division of Biosurface Technology, BMT wing, SCTIMST; Dr. Ruby John Anto, Scientist G, Division of Cancer Research, Rajiv Gandhi Centre for Biotechnology; Dr. Anilkumar P. R., Scientist G, Division of Tissue culture, BMT wing, SCTIMST for their timely suggestions, ideas, and comments which helped in improving the quality of my work. I would like to acknowledge the Department of Biotechnology for the DBT-JRF fellowship.

I express my gratitude to all members of the Central Analytical Facility, Dr. Renjith S., Mr. Willi Paul, Dr. C. Radhakumary, Ms. Nimi, and Dr. Sasikala for extending me all the required analytical support. I would like to specifically thank Mr. Willi Paul for his support in developing a stable solid lipid nanoparticle suspension and

also for helping me with Raman Mapping, Texture analyzer, HPLC, and image analyzer.

I sincerely thank all members of the former Polymer Division, Dr. Sunita Prem Victor, Dr. Vineeth Vijayan, and Ms. Anjana, for extending me with Fluorescence spectroscopy and FTIR facilities.

I thank all members of Biosurface Technology, Dr. Rekha M.R., Dr. Priya, Dr. Caroline, Ms. Rajalekshmy, Ms. Sunitha, Dr. Dharavath Ravi, Ms. Linju, Ms. Aswathy, Ms. Nayana, Ms. Annie, and Mr. Dipin for helping me with UV-Visible spectroscopy and Dynamic Light scattering. I am grateful to Dr. Rekha M.R. for her support and advice in the development of the chitosan microparticle systems.

I am thankful to all members of the Division of Biophotonics and Imaging, Dr. Jayasree, Dr. Parvathy, Dr. Hema, Marina Victor, Dhanya G. R., Dr. Jibin, Mr. Jayaram, Ms. Rinta Paul, and Dr. Resmi for helping me with fluorescence microscopy analysis.

I would like to thank all members of the Division of Bioceramics, Dr. Manoj Komath, Mr. Vijayan, Dr. Suresh Babu, Mr. Nishad, Dr. Adarsh, Dr. Francis Boniface Fernandez, and Mr. Jijo for extending ICP-OES, SEM, XRD, and TEM facilities.

I express my sincere gratitude to all members of the Division of Tissue Engineering and Regeneration Technologies, Dr. Prabha D. Nair, Dr. Lynda V. Thomas, Dr. Amrita Natarajan, and Ms. Jijo Wilson for extending me with the fluorescence microscopy facility.

I am extremely thankful to all members of the Division of Dental Products, Dr. Lizymol, Dr. Kala, and Dr. Vibha for helping me with Dynamic light scattering.

I would like to thank all members of the Division of Molecular Medicine, Dr. Anoop Kumar, Ms. Aswathy, and Dr. Selva Sarma for extending me with a fluorescence plate reader. I thank Dr. T. V. Anilkumar, Dr. Reshmi, and Mr. Pratheesh of the Division of Experimental Pathology for their help and support.

I am greatly indebted to Dr. Harikrishnan, Dr. Sachin Shenoy, Mr. Manoj Kumar, and Mr. Sunil Kumar of the Division of Laboratory Animal Science/Division of *In vivo* Models and Testing for helping me with intestine collection from the carcass.

I am extremely thankful to Mr. Jithin Krishnan, Mr. Biju Benjamin, Mr. Arun, and Mr. Jithin from the Division of Medical Instrumentation for their help and friendly support. I also thank all members of the Network cell facility, Mr. Sajithlal, Dr. Arun Anirudhan, and Mr. Binu for their support. I sincerely thank all members of Precision Fabrication Facility, Dr. Ramesh Babu, Mr. Reji, and Mr. Prathyush for their help and support.

I thank all former and present members of Polymeric Medical Devices: Dr. Ramesh, Dr. Mayuri, Dr. Remya, Dr. Sudhin, Ms. Jincy Antony, Dr. Thirumalai Kumaran, Dr. Praveen, Mr. Vishak, Mr. Riju Chandran, Ms. Swathy Krishna, Ms. Lakshmi, Ms. Jasmin, Dr. Chandrasekhar, Dr. Reshma, Dr. Raj Kumar, Ms. Gopika Ramesh, Ms. Gopika Gopan, Dr. Resmi, Mr. Saravana Perumal, Ms. Eliza, Ms. Prima, Ms. Medha, Ms. Sarah, Ms. Theertha, Ms. Prathyusha and Mr. Rahul for their support and friendship.

I also extend my heartfelt gratitude to Ms. Jiji V., Mr. Gopikrishnan K., Ms. Soumya S. P., and Ms. Ciji Varghese of Rajiv Gandhi Centre for Biotechnology for their help in Confocal Laser Scanning Microscopy and ROI analysis.

I thank all members of the Accounts, Stores, and Purchase Division for their support.

I express my sincere gratitude to all my family members for their prayers, support, and encouragement which helped me in the completion of this program.

Dhanya C. S.

Date: 27-10-2023

TABLE OF CONTENTS

LIST OF FIGURES

LIST OF TABLES

LIST OF ABBREVIATIONS

Sl. No.	Abbreviation	Full Name
1.	5-FU	5-fluorouracil
2.	AgNP	Silver nanoparticle
3.	BSA	Bovine serum albumin
4.	CLSM	Confocal laser scanning microscopy
5.	CUR	Biocurcumin®/BCM-95®
6.	CUR-AgNP	Curcumin silver nanoparticle conjugate
7.	DA	Degree of acetylation
8.	DAPI	4,6-diamidino-2-phenylindole
9.	DD	Degree of deacetylation
10.	DLS	Dynamic light scattering
11.	DPX	Dibutylphthalate Polystyrene Xylene
12.	DSC	Differential Scanning calorimetry
13.	EDC	1-Ethyl-3-(3-dimethylaminopropyl)carbodiimide
14.	Eqn.	Equation
15.	FDA	Food and Drug Administration
16.	FTIR	Fourier transform infrared spectroscopy
17.	GI	Gastrointestinal
18.	GRAS	Generally recognized as safe
19.	HBSS	Hank's Balanced Salt Solution
20.	HPLC	High-performance liquid chromatography
21.	ICP-OES	Inductively coupled plasma optical emission spectroscopy
22.	JAM	Junctional Adhesion Molecules
23.	LA	Lauric acid
24.	LA-SLN	Lauric acid solid lipid nanoparticles
25.	LCS	Lysine chitosan
26.	MCS	N-maleoyl chitosan
27.	MLC	Myosin Light chain

28.	MTT	3-(4,5-dimethylthiazol-2-yl)-2,5-diphenyltetrazolium bromide
29.	NA	Numerical Aperture
30.	NMR	Nuclear Magnetic Resonance spectroscopy
31.	PBS	Phosphate buffer saline
32.	PEG	Polyethylene glycol
33.	PLA	Poly(lactic acid)
34.	PLGA	Poly(lactic-co-glycolic acid)
35.	RhB	Rhodamine B
36.	R-LA-SLN	Rhodamine B-loaded lauric acid solid lipid nanoparticles
37.	ROCK	Rho-associated kinase
38.	SDS-PAGE	Sodium dodecyl sulphate-polyacrylamide gel electrophoresis
39.	SEM	Scanning electron microscopy
40.	SLN	Solid lipid nanoparticles
41.	TEER	Transepithelial electrical resistance
42.	TEM	Transmission electron microscope
43.	TFu	N_3-O-toluyl-fluorouracil
44.	TGA	Thermogravimetric analysis
45.	TNBS	2,4,6-Trinitrobenzenesulfonic acid
46.	TPP	Tripolyphosphate
47.	XPS	X-ray photoelectron spectroscopy
48.	XRD	X-ray powder diffraction
49.	ZO-1	Zonula occludens

SYNOPSIS

Oral drug delivery is the most preferred route of drug delivery because of its patient compliance, ease of use, noninvasiveness, and cost-effectiveness. However, oral drug delivery poses significant barriers to achieving effective therapeutic outcomes. This is primarily due to the numerous biological barriers that exist throughout the gastrointestinal (GI) tract that a drug carrier must navigate through. The barriers to the GI tract include the harsh acidic pH environment in the stomach; the presence of degrading enzymes that render the drug ineffective; the mucus layer that impedes the movement of the drug and inefficient drug penetration across the intestinal tight junction barrier.

The major barriers to oral drug delivery can be addressed by designing the micro and nanocarriers appropriately. The physicochemical properties (size, shape, surface charge, hydrophilicity) of the particles constitute the synthetic identity. Upon interaction with the GI microenvironment, the particles may achieve a new biological identity that determines their biological effects. The functionalized particles can exploit the different characteristics of the digestive tract such as different pH, intestinal mucus layer, and intestinal absorption capacity. To develop an appropriate design of nano or microparticles for medical applications, fundamental factors of particles and their microenvironment must be taken into account. These include interactions between particles and their biological environment, the mechanisms of interaction, and the physicochemical properties of particles. The surface chemistry of the particles (size, surface charge, hydrophilicity/hydrophobicity) plays a key role in mucoadhesion, cellular uptake as well as intestinal tight junction opening.

The study mainly focused on the interactions of nano and micro drug delivery carriers with the simulated intestinal microenvironment. The particles that interact with the intestine are divided into different categories based on the material used to generate them: lipid-based nanocarriers, metallic nanoparticles (Au and Ag), and polymeric particles of chitosan. Based on this, the present study aimed to develop different drug carriers using materials of different surface chemistry and size (metallic, hydrophobic, and hydrophilic) to study their cellular interactions and drug-delivering efficacy. For achieving this objective, three different particle systems were developed and studied. Chitosan and functionalized chitosan particles were the microparticle-based drug delivery systems selected for the study. Curcumin-silver nanoparticle conjugate (CUR-AgNP) and solid lipid nanoparticles of lauric acid (LA-SLN) were the nano-drug delivery systems used for the study.

The thesis is divided into five chapters. The first chapter covers the introduction and background of the study and the second chapter deals with the literature review. The third chapter of the thesis describes the various materials and methods used to achieve the above-discussed objectives. This chapter is divided into three sections. The first section describes the synthesis and characterization of CUR-AgNP. A simple green synthesis approach was utilized for the synthesis of CUR-AgNP without the involvement of any harsh chemical reducing agent where curcumin acts as the reducing agent as well as the drug. The formation of the CUR-AgNP was confirmed by UV-Visible absorption and fluorescence spectroscopy. The particle size and morphology were determined by dynamic light scattering (DLS) and transmission electron microscopy (TEM). Physicochemical characterization of the

CUR-AgNP was carried out by zeta potential measurement, Fourier transform infrared spectroscopy (FTIR), X-ray powder diffraction (XRD), inductively coupled plasma optical emission spectroscopy (ICP-OES) and X-ray photoelectron spectroscopy (XPS). The degradation of curcumin and curcumin bound to the CUR-AgNP in intestinal pH 7.4 was studied using UV-Visible absorption spectroscopy and high-performance liquid chromatography (HPLC). The cytotoxicity exhibited by CUR-AgNPs towards colorectal cancer cells (HCT-116 and Caco-2) was evaluated by MTT (3-(4,5-dimethylthiazol-2-yl)-2,5-diphenyltetrazolium bromide) assay. The cellular uptake of the CUR-AgNPs in HCT-116 and Caco-2 cells was studied by confocal laser scanning microscopy (CLSM). The cellular uptake studies of CUR-AgNP in HCT-116 cells were also evaluated by Confocal Raman Mapping.

The second section describes the preparation of LA-SLN and rhodamine B (RhB) loaded solid lipid nanoparticles of lauric acid (R-LA-SLN) where RhB is taken as the model drug. The hot homogenization method was used to prepare LA-SLN and R-LA-SLN. The particle size and morphology were determined by DLS and TEM. Physicochemical characterization was done by FTIR, zeta potential measurement, Raman spectroscopy, and Differential Scanning Calorimetry (DSC). The entrapment efficiency and drug loading of the R-LA-SLN were calculated. The *in vitro* release of RhB from the R-LA-SLN was carried out at pH 7.4. The cell viability of LA-SLN against HCT-116 and Caco-2 cells was evaluated by MTT assay. The cellular uptake of R-LA-SLN and RhB dye by HCT-116 and Caco-2 cells was studied by CLSM. The cellular uptake studies of R-LA-SLN in HCT-116 cells were also evaluated by Confocal Raman Mapping. Caco-2 cells were used as an *in vitro* model of the

intestinal epithelial barrier. Transepithelial electrical resistance (TEER) studies were done on the Caco-2 cell monolayer after LA-SLN treatment, to study its ability in tight junction openings. The transport studies of RhB and RhB loaded in LA-SLN across the Caco-2 cell monolayer were also studied. The actin filament staining and zonula occludens (ZO-1) tight junction protein immunofluorescence staining were carried out to study the effect of LA-SLN in the tight junction opening of the Caco-2 cell monolayer. The mucoadhesion studies of LA-SLN were carried out on rat intestinal colon mucosa using a texture analyzer. To evaluate the interactions of LA-SLN with proteins in the GI tract, particles were incubated with pancreatin (composed of amylase, lipase, trypsin, protease, and ribonuclease), and hard corona formed on the surface of the particles were separated by Sodium dodecyl sulphate-polyacrylamide gel electrophoresis (SDS-PAGE).

The third section details the chitosan and functionalized chitosan microparticles. To incorporate amino groups, the chitosan polymer was modified with lysine to form a lysine chitosan (LCS) conjugate. To incorporate carboxyl groups, chitosan polymer was modified with maleic anhydride to form N-maleoyl chitosan (MCS) conjugate. LCS conjugate was synthesized by a 1-Ethyl-3-(3-dimethylamino propyl)carbodiimide (EDC) coupling reaction between the amino groups of chitosan and the carboxylic group of lysine. MCS conjugate formation takes place through the acylation process between the amino group of chitosan and the electrophilic carbonyl group from maleic anhydride, forming the amide bond. The LCS conjugate and MCS conjugate were further characterized by NMR (Nuclear Magnetic Resonance) spectroscopy, FTIR, zeta potential measurement, TGA (Thermogravimetric

Analysis), and XRD analyses to confirm the successful conjugation of lysine and maleic anhydride with chitosan. The variation of amino group content of chitosan and chitosan conjugates was determined by the degree of deacetylation. The extent of derivatization was also evaluated by 2,4,6-Trinitrobenzene Sulfonic Acid (TNBS) assay. The different charge-based chitosan microparticles were prepared from native chitosan and chitosan conjugates (LCS and MCS) by the ionic gelation method using tripolyphosphate (TPP) as the crosslinker. The physicochemical characterization of the prepared particles was done by FTIR, zeta potential measurement, and scanning electron microscopy (SEM). The water absorption studies of the microparticles were carried out separately in three different pH buffers to mimic the pH conditions of the GI tract. The microparticles were loaded with the anticancer drug 5-fluorouracil (5-FU) by remote loading and the entrapment efficiency and loading capacity were calculated. The drug release studies of the 5-FU from the microparticles were carried out at pH 1.2, 6.8, and 7.4 by the dialysis method. The drug release from the microparticles after coating it with Eudragit S100 was also carried out at different pH conditions (1.2, 6.8, and 7.4). The cytocompatibility of chitosan and its conjugates (LCS and MCS), as well as crosslinked chitosan, LCS, and MCS microparticles against HCT-116 and Caco-2 cells, were evaluated by MTT assay. The cytotoxicity of the drug and drug-loaded microparticles against HCT-116 and Caco-2 cells was determined by MTT assay after exposure for different periods (24, 48, and 72 hours). The effect of chitosan and modified chitosan particles on Caco-2 cell TEER and drug transport across the Caco-2 cell monolayer was studied. The actin filament staining and zonula occludens (ZO-1) immunofluorescence staining were carried out to study the effect of differently charged microparticles in the tight junction opening of the

Caco-2 cell monolayer. Mucin-binding studies were carried out to study the interactions of microparticles with mucin. Mucoadhesion studies of native chitosan and functionalized chitosan microparticles were carried out in rat intestines by texture analyzer and *in vitro* mucoadhesion studies. The microparticles were incubated with pancreatin and hard corona formed on the surface of the microparticle were separated by SDS-PAGE.

The fourth chapter details the results and discussion. This chapter is also divided into three sections. In the first section, the successful formation of the CUR-AgNP was discussed. The FTIR spectra of the CUR-AgNP showed a new peak at 1382 cm^{-1}, which may be due to the capping of CUR over the silver nanoparticles via the C=O group. From XPS analysis, it was further confirmed that the carbonyl group of curcumin was involved in the binding interaction between curcumin and AgNPs. The *in vitro* degradation studies revealed that curcumin exhibits around 59.8 % degradation and curcumin bound to CUR-AgNP exhibited only 28 % degradation at 24 hours in pH 7.4. The diketo moiety of curcumin is involved in the degradation process at pH 7.4, as the diketo moiety binds to metal ions the degradation of curcumin under physiological conditions could be prevented. Therefore, curcumin bound to CUR-AgNP exhibited substantial stability in pH 7.4 compared to free curcumin. The cellular uptake studies of CUR-AgNP in colorectal cancer cells revealed that the uptake occurs within an initial 0.5 hours of incubation and the particles were found to be localized in the cytoplasm of the cells. In Confocal Raman Mapping studies, the presence and distribution of the CUR-AgNP over the examined cell were mapped utilizing the fluorescence of the CUR-AgNP. The IC_{50} values of

curcumin towards HCT-116 and Caco-2 cells were found to be 13 μg/mL and 15 μg/mL, respectively. Whereas the IC_{50} values of the CUR-AgNP towards HCT-116 and Caco-2 cells were found to be 73 μg/mL and 204 μg/mL, respectively. Compared to curcumin the CUR-AgNP was found to be less effective in achieving cytotoxicity against colorectal cancer cells. So, a higher concentration of CUR-AgNP is required to achieve cytotoxicity against colorectal cancer cells.

The second section details the physicochemical characterization of LA-SLN and R-LA-SLN. R-LA-SLN had an entrapment efficiency of 80.31 ± 0.18 % with a drug loading of 10.2 ± 0.02 μg/mg lipid. The *in vitro* release studies of R-LA-SLN revealed a biphasic release pattern and released about 71.9 % dye in 10 hours. LA-SLN was found to be cytocompatible even at higher concentrations revealing that LA-SLN can be used as an oral drug delivery carrier. In the CLSM cellular uptake studies, R-LA-SLN was observed as distinct red dots in the cytoplasm whereas in the case of free RhB dye the red fluorescence was found to be distributed throughout the intracellular space. Cellular uptake of R-LA-SLN was observed to be higher compared to free RhB dye. In Confocal Raman Mapping after R-LA-SLN incubation with HCT-116 cells, the presence and distribution of RhB in the cytoplasm were mapped using the RhB characteristic peak at 1516 cm^{-1}. TEER is a very sensitive and reliable method to confirm the integrity and permeability of cellular monolayer by measuring the electrical resistance across it. LA-SLN exhibited about an 80 % reduction in TEER which indicates a loss of tight junction integrity and loss of barrier properties. The permeability of RhB loaded in R-LA-SLN across the Caco-2 cell monolayer was found to be 6 times greater than that of free RhB dye alone. The

disruption of actin filament and weaker fluorescence of ZO-1 tight protein compared to control cells confirms the LA-SLN-induced tight junction opening and increased paracellular permeability. Mucoadhesion is another important factor to consider when developing oral drug delivery carriers. Strong mucoadhesion indicates improved contact with the absorption site, resulting in effective absorption. The LA-SLN exhibited 1.7 times greater mucoadhesive force compared to chitosan particles, a material well-known for its mucoadhesive behavior. The major protein bound to the surface of the LA-SLN after incubating in pancreatin was found to be ribonuclease.

The third section details the physicochemical characterization of chitosan and chitosan conjugates (LCS and MCS) which confirms the successful conjugation of chitosan with lysine and maleic anhydride. The different surface-charged microparticles were prepared from native chitosan and chitosan conjugates by ionic gelation method. The zeta potential of the chitosan, LCS, and MCS microparticles was found to be +13.3 ± 0.17, +23.7 ± 0.58, and -9.54 ± 0.79 mV, respectively. The Chitosan, LCS, and MCS microparticles exhibited a higher percentage of water uptake and drug release at pH 1.2. To prevent the loss of the drug in the acidic conditions of the stomach the microparticles were coated with Eudragit®S-100. The coating also helped in controlling the release profile of 5-FU at pH 6.8 and 7.4, the initial burst release was nullified. Chitosan, LCS, and MCS microparticles were found to be cytocompatible even at higher concentrations therefore they can be used as oral drug delivery carriers. Drug-loaded microparticles exhibit significant cytotoxicity towards colorectal cancer cells in a dose-dependent and time-dependent

manner revealing their potential for colorectal cancer treatment. After treatment with cationic chitosan and LCS microparticles, the TEER values of Caco-2 cells were found to be decreased by around 75% and 80% whilst in the case of anionic MCS microparticles the TEER was reduced by about 40 %. The apparent permeability of 5-FU loaded in cationic chitosan and LCS microparticles was found to be 7.6 ± 0.63 and 9.2 ± 0.80 cms^{-1}, respectively. While anionic MCS microparticles exhibited only 3.2 ± 0.21 cms^{-1} apparent permeability. The disruption of actin filament and weaker fluorescence of ZO-1 tight protein compared to control cells confirms tight junction opening and increased paracellular permeability. Actin filaments were observed to be more discontinuous and disrupted in the case of LCS microparticle-treated cells compared to chitosan and MCS microparticles. The ZO-1 staining intensity was found to be less in the LCS microparticle-treated cells compared to chitosan and MCS. Mucin is the primary functional component of the mucus layer. The tenacious and sticky network of mucin fibers prevents the diffusion of foreign particles by trapping and these entrapped particles are eliminated through constant secretion and shedding of mucus. Chitosan, LCS, and MCS microparticles were found to exhibit less interaction with mucin. So, the microparticles can efficiently overcome the mucus barrier and reach the intestinal epithelium. The mucoadhesion was found to be significantly higher for functionalized LCS and MCS microparticles compared to chitosan microparticles. The major protein bound to the surface of the microparticles after incubating in pancreatin was found to be ribonuclease.

Chapter 5 gives the summary and conclusion of the study. In the case of CUR-AgNP, the curcumin bound to the conjugate was able to exhibit substantial stability in

intestinal pH (7.4) compared to free curcumin. However, a higher concentration of CUR-AgNP is required to elicit cytotoxicity in colorectal cancer cells. This limits the application of CUR-AgNP for colorectal cancer treatment. Due to this reason, we haven't further proceeded with this system and have not carried out the interactions of CUR-AgNP with the simulated intestinal microenvironment. In the second system, LA-SLN exhibited higher cellular uptake compared to free RhB dye. Lauric acid solid lipid nanoparticle induces tight junction opening and increases the paracellular transport of the drug. Lauric acid solid lipid nanoparticles also showed a substantially higher mucoadhesive property and can be used as a potential carrier for oral drug delivery. However, the drug loading capacity of the LA-SLN was found to be poor. In the case of the third system, drug-loaded microparticles exhibit significant cytotoxicity toward colon cancer cells. Mucin binding was found to be less for chitosan, LCS, and MCS particles which is advantageous for oral drug delivery systems. The modified LCS and MCS particles showed significantly higher mucoadhesion compared to native chitosan microparticles. The cationic LCS and chitosan microparticles exhibited better tight junction opening and 5-FU drug transport across the Caco-2 cell monolayer compared to anionic MCS particles. Among the chitosan systems, lysine chitosan microparticles were found to be the most suitable carrier for colon drug delivery.

1 INTRODUCTION

Drug delivery is the process of administering a pharmaceutical compound to achieve a therapeutic effect in patients (Tiwari et al., 2012). Drug delivery systems act as an interface between the patient and the drug. It facilitates the introduction of a therapeutic substance into the body and improves its efficacy and safety by controlling the rate, time, and place of release of drugs in the body (Sung and Kim, 2020). The major routes of drug delivery include intravenous, intramuscular, intradermal/transdermal, intranasal, and oral routes (Homayun et al., 2019). Oral drug delivery is the most preferred route of drug delivery due to its non-invasiveness, improved patient compliance, and great convenience of self-medication (Pinto, 2010).

Some of the challenges of oral drug delivery are associated with the properties of the drugs such as poor water solubility, instability, low permeability, and rapid metabolism (Prabhu et al., 2005). The physiology of the gastrointestinal (GI) tract also contributes to the poor absorption and bioavailability of the drugs (Sant et al., 2012). The biological barriers to drug delivery include the harsh acidic environment in the stomach and digestive enzymes that render drugs ineffective (Ahadian et al., 2020). The mucus layer is a selective barrier that prevents the drug from reaching the intestinal epithelium (Leal et al., 2017). The intestinal epithelial tight junction is one of the major barriers to drug absorption in the GI tract (Alqahtani et al., 2021).

Micro and nanotechnologies have extensive applications in oral drug delivery intending to increase the efficacy of the drug delivery system (Ahadian et al., 2020). The major barriers to oral drug delivery can be addressed by designing the micro and

nanoparticles with precise control over their architecture and size (Ahadian et al., 2020). Micro and nanoparticles can be modified in different ways to develop particles with different sizes, shapes, charges, functional groups, and targeting agents for achieving the final aim (Mandracchia and Tripodo, 2020). Recent research has focused on the development of nano or microparticles for oral administration rather than the intravenous route of administration, emphasizing the interactions between particles and the intestine as the prime focus (Vitulo et al., 2022). This enables the nano or microparticle functionalization to take advantage of different characteristics of digestive tracts such as pH, intestinal mucus layer, and intestinal absorption capacity (Vitulo et al., 2022).

To develop an appropriate design of nano or microparticles for medical applications, fundamental aspects of particles and their microenvironment must be taken into account. These include interactions between particles and their biological environment, the mechanisms of interaction, and the physicochemical properties of particles (Auría-Soro et al., 2019). The surface chemistry of the particles (size, surface charge, hydrophilicity/hydrophobicity) is considered to play an important role in mucoadhesion, cellular uptake as well as intestinal tight junction opening.

The present investigation focuses on the interactions of nano and micro drug delivery carriers with the simulated intestinal microenvironment. The particles that interact with the intestine are divided into different categories based on the material used to generate them: lipid-based nanocarriers, metallic nanoparticles, and polymeric nano or microparticles (Vitulo et al., 2022). Based on this, the current study aimed to develop drug carriers with different surface chemistry and size (metallic,

hydrophobic, and hydrophilic) to investigate their interactions with simulated intestinal microenvironments and to evaluate their drug-delivering efficacy. To achieve this objective, chitosan, and functionalized chitosan microparticles were selected as the polymeric drug delivery systems. Curcumin-silver nanoparticle conjugate (metallic) and solid lipid nanoparticles of lauric acid (lipid nanocarrier) were the nano-drug delivery systems used for the study. The surface properties of the drug delivery carriers are critical in determining their safety and biological effects.

The thesis is divided into five chapters. The first chapter covers the introduction and background of the study. The second chapter deals with the review of the literature and it provides a detailed description of oral drug delivery, barriers to oral drug delivery, nano and microparticles, physicochemical properties of particles, and their interaction with the intestine (proteins, mucoadhesion, mucin, and intestinal tight junction). The third chapter deals with the materials, methods, and protocols used in the work. This chapter is divided into three sections.

The first section describes the synthesis and characterization of the metallic curcumin-silver nanoparticle conjugate (CUR-AgNP). The hydrophobic nature of curcumin results in poor aqueous solubility, its rapid degradation and elimination from the body subsequently leads to poor bioavailability constitutes major barriers to its application (Stanić, 2017). Binding to a metallic ion like silver is a simpler and more convenient way to increase curcumin stability without compromising its therapeutic efficacy. Although several research groups have concentrated on the synthesis, stability, and applications of the curcumin-silver nanoparticles, there is

inadequate information on the stability of the conjugates formed by individual curcuminoids with silver at physiological pH.

A simple green synthesis approach was utilized to develop a stable CUR-AgNP without the involvement of any harsh chemical reducing agent where curcumin acts as the reducing agent as well as the drug. The formation of the CUR-AgNP was monitored and confirmed by UV-Visible absorption and fluorescence spectroscopy. The CUR-AgNP was characterized for its physicochemical properties by various techniques. The physiological stability of curcumin and curcumin bound to the CUR-AgNP in intestinal pH 7.4 was studied using UV-Visible absorption spectroscopy and high-performance liquid chromatography (HPLC). The cytotoxicity exhibited by curcumin and CUR-AgNPs towards colorectal cancer cells (HCT-116 and Caco-2) was evaluated by MTT (3-(4,5-dimethylthiazol-2-yl)-2,5-diphenyltetrazolium bromide) assay. The cellular uptake of the CUR-AgNPs in HCT-116 and Caco-2 cells was studied by confocal laser scanning microscopy (CLSM). The cellular uptake studies of CUR-AgNP in HCT-116 cells were also evaluated by Confocal Raman Mapping. We envision that these relatively stable CUR-AgNPs could serve as effective and potential therapeutic agents at physiological pH.

The second section describes the preparation and characterization of lipid nanocarrier. Lauric acid (LA) is the lipid selected for the synthesis of solid lipid nanoparticles as it is reported to have high intestinal absorption (Prasadani et al., 2017). However, only a few studies on LA have been reported, and in these studies, it was used in combination with other lipid mixtures (Rehman et al., 2017, 2015). The preparation of solid lipid nanoparticles of LA alone, as well as its

characterization, cytotoxicity, and cell uptake studies, have not been reported in the literature. We considered these facts and investigated the potential of lauric acid solid lipid nanoparticles (LA-SLN) as an oral drug delivery carrier. Based on this, LA-SLN was prepared by incorporating rhodamine B (a fluorescent lipophilic dye) as the model drug. Rhodamine B (RhB) is a fluorescent dye that can be easily identified and measured by analytical techniques. Rhodamine B has a molecular weight of 479.02 daltons and has an octanol/water partition coefficient (log Kow = 1.95) that is similar to that of several drugs (Iyer and Eddington, 2019).

In this work, LA-SLN and RhB-loaded solid lipid nanoparticles of lauric acid (R-LA-SLN) were prepared by the hot homogenization method. The particles were investigated for their physicochemical properties, entrapment efficiency, drug loading, and drug release profile at pH 7.4. The cytocompatibility of LA-SLN was evaluated by MTT assay. The cellular uptake of R-LA-SLN and RhB dye by HCT-116 and Caco-2 cells was studied by CLSM. The cellular uptake studies of R-LA-SLN in HCT-116 cells were also evaluated by Confocal Raman Mapping. Transepithelial electrical resistance (TEER), actin filament staining, and tight junction protein (Zonula occludens, ZO-1) immunofluorescence staining were carried out in Caco-2 cell monolayer after LA-SLN treatment, to study its ability in tight junction openings. The transport studies of RhB and RhB loaded in LA-SLN across the Caco-2 cell monolayer were also studied. The mucoadhesion studies of LA-SLN were carried out on rat intestinal colon mucosa using a texture analyzer. To evaluate the interactions of LA-SLN with proteins in the GI tract, particles were incubated with pancreatin (composed of amylase, lipase, trypsin, protease, and

ribonuclease), and hard corona formed on the surface of the particles were separated by Sodium dodecyl sulphate-polyacrylamide gel electrophoresis (SDS-PAGE).

The third section focuses on chitosan biopolymer and functionalized chitosan microparticles. In oral drug delivery, the surface charge of the particles plays an important role in their interactions with the intestine (different pH conditions of the gastrointestinal tract, mucin, mucoadhesion, and intestinal tight junction opening). 5-Fluorouracil (5-FU) is the drug of choice for colorectal cancer treatment (Dos Santos et al., 2021). 5-fluorouracil is a hydrophilic drug that is administered intravenously. The limitations of intravenous administration of 5-FU include a short half-life, lack of specificity at high doses, off-target toxicity, and side effects on the GI tract, particularly diarrhoea, mucositis, and microbiota disorders (Dos Santos et al., 2021). The hydrophilic nature of 5-FU limited its oral bioavailability due to poor intestinal permeability and GI absorption (Ahmad et al., 2022). The intestinal tight junctions act as a barrier to the permeability of hydrophilic drugs. Considering the preference for oral drug delivery currently, research is more focused on improving the oral bioavailability of 5-FU. The tight junction opening is associated with the surface charge of the drug delivery carriers incorporated with 5-FU. To evaluate this, cationic chitosan and anionic N-maleoyl chitosan (MCS) particles were prepared, and studied their efficacy on tight junction opening and successive drug transport as well as interactions with intestine (proteins, mucin, pH, and mucoadhesion).

The chitosan polymers were modified to incorporate positively charged amino groups and negatively charged carboxyl groups into the backbone of chitosan. To incorporate amino groups, the chitosan polymer was modified with lysine to form a

lysine chitosan (LCS) conjugate. To incorporate carboxyl groups, chitosan polymer was modified with maleic anhydride to form N-maleoyl chitosan (MCS) conjugate. LCS conjugate was synthesized by a 1-Ethyl-3-(3-dimethylamino propyl) carbodiimide (EDC) coupling reaction between the amino groups of chitosan and the carboxyl group of lysine. MCS conjugate formation takes place through the acylation process between the amino group of chitosan and the electrophilic carbonyl group from maleic anhydride, forming the amide bond. The LCS conjugate and MCS conjugate were further characterized to confirm the successful conjugation of lysine and maleic anhydride with chitosan. The different charge-based chitosan microparticles were prepared from native chitosan and chitosan conjugates (LCS and MCS) by the ionic gelation method using tripolyphosphate (TPP) as the crosslinker and characterized. The water absorption studies of the microparticles were carried out separately in three different pH buffers to mimic the pH conditions of the GI tract. The microparticles were loaded with the anticancer drug 5-FU by remote loading and the entrapment efficiency and loading capacity were calculated. The drug release studies of the 5-FU from the microparticles were carried out at pH 1.2, 6.8, and 7.4 by the dialysis method. The drug release from the microparticles after coating it with Eudragit® S100 was also carried out at different pH conditions (1.2, 6.8, and 7.4). The cytocompatibility of chitosan and its conjugates (LCS and MCS), as well as crosslinked chitosan, LCS, and MCS microparticles against HCT-116 and Caco-2 cells, were evaluated by MTT assay. The cytotoxicity of the drug and drug-loaded microparticles against HCT-116 and Caco-2 cells was determined by MTT assay after exposure for different periods (24, 48, and 72 hours).

The effect of chitosan and modified chitosan particles on Caco-2 cell TEER and drug transport across the Caco-2 cell monolayer was studied. The actin filament staining and ZO-1 immunofluorescence staining were carried out to study the effect of differently charged microparticles in the tight junction opening of the Caco-2 cell monolayer. Mucin-binding studies were carried out to study the interactions of microparticles with mucin. Mucoadhesion studies of native chitosan and functionalized chitosan microparticles were carried out in rat intestines by texture analyzer and *in vitro* mucoadhesion studies. The microparticles were incubated with pancreatin to study the interactions of proteins in the GI tract and hard corona formed on the surface of the microparticle were separated by SDS-PAGE.

Chapter 4 details the results obtained from the experiments and discusses them with the help of already published scientific data. This chapter is also divided into three sections: curcumin-silver nanoparticle conjugate, Lauric acid solid lipid nanoparticles, and chitosan and functionalized chitosan particles.

Chapter 5 summarizes the significant findings of this work and concludes the thesis with a note on future work.

2 REVIEW OF LITERATURE

2.1. Oral drug delivery

Oral drug delivery is the most common route of drug delivery because of the advantages such as patient preference, cost-effectiveness, the convenience of drug administration, and ease of developing large-scale oral dosage forms (Alqahtani et al., 2021). Compared to the parenteral routes of drug delivery such as intravenous, subcutaneous, and intramuscular routes, the patient's preference for oral formulations is very high (Ingersoll and Cohen, 2008). According to the current estimates, oral formulations account for about 90% of the global market share of all pharmaceutical formulations intended for human use (Alqahtani et al., 2021). Orally administered pharmaceuticals represent 84% of the best-selling medications, which are currently valued at $35 billion with a 10% annual growth rate (Prasad et al., 2017). Orally administered drugs can be targeted to specific locations within the gastrointestinal (GI) tract to treat stomach and colorectal cancers, inflammations, infections, gastro-duodenal ulcers, bowel diseases, and gastroesophageal reflux disorders (Alqahtani et al., 2021).

Despite the advantages of oral drug delivery, there are several challenges which include the physicochemical properties of the drug comprising poor water solubility, low permeability, instability, and rapid metabolism (Prabhu et al., 2005). The physiology of the GI tract can also lead to poor absorption and availability of drugs due to low mucosa permeability and degradation of the drug before absorption (Sant et al., 2012).

2.2. Gastrointestinal tract

The GI tract is composed of the oral cavity, esophagus, stomach, small intestine, and colon (figure 2.1). The GI tract has a large surface area (300-400 m^2) for drug absorption by absorptive epithelial cells (enterocytes) (Ensign et al., 2012). The smaller surface area and thicker mucous layer (1.5 mm) of the stomach reduce its drug absorption ability compared to the intestine (Mudie et al., 2010). The small intestine is the longest and most convoluted part of the GI tract (≈ 6 m in length), where digestion is completed with the help of enzymes from the liver and pancreas (Reinus and Simon, 2014).

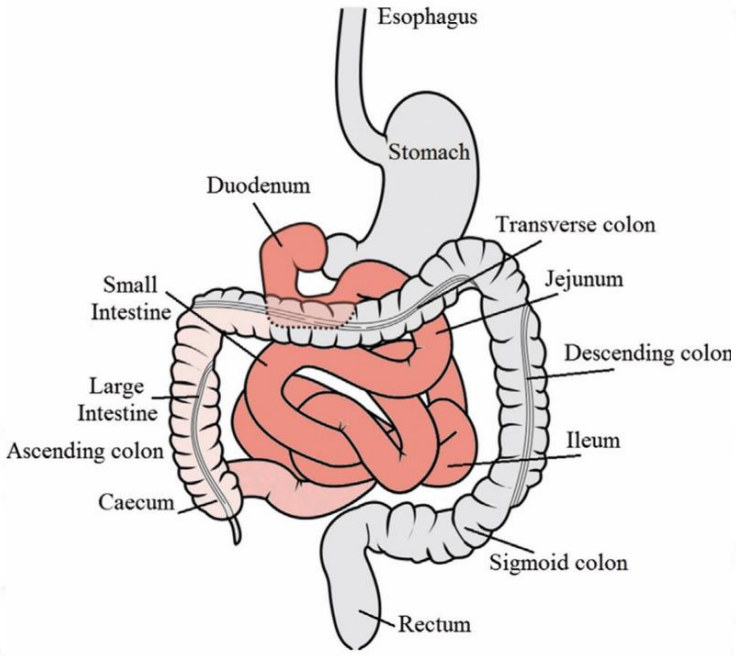

Figure 2.1. Schematic diagram of the GI tract. The major regions of drug absorption are shown in red color (Alqahtani et al., 2021).

The small intestine is divided into three distinct sections: duodenum, jejunum, and ileum, each has distinctive characteristics that influence nutritional absorption (Masaoka et al., 2006). Most of the orally administered drugs are mainly absorbed by

the duodenum and jejunum regions of the GI tract (Alqahtani et al., 2021). The final major part of the GI tract is the large intestine. It can be divided anatomically into four parts: ascending, transverse, descending, and sigmoid colon. The primary function of the large intestine is to absorb water from the indigestible contents (Kahai et al., 2022). Drug absorption in the GI tract is often constrained by intricate physiological barriers in the different GI tract regions (Ahadian et al., 2020).

2.3. Physiological barriers to oral drug delivery

The biochemical, mucus diffusional, and cellular permeability barriers of the GI tract are the main obstacles to oral drug delivery (figure 2.2).

2.3.1. Biochemical barriers

The major biochemical barriers to the bioavailability of orally administered drugs are enzymatic and pH degradation. The large pH gradient, which ranges from pH 1-2.5 in the stomach to pH 7-8 in the colon represents a great challenge for oral drug delivery (Vitulo et al., 2022). The harsh acidic conditions of the stomach (pH 1-2.5) are the first biological barrier to any orally administered drug, denaturing most of the administered molecules and significantly reducing their efficacy (Homayun et al., 2019). Additionally, the lumen enzymes in the stomach (such as pepsin) and duodenum (such as biliary and pancreatic secretions that include lipases, peptidases, and amylases) also pose challenges for oral drug delivery (Amara et al., 2019). About 94 - 98% of ingested pharmaceuticals are lost as a result of deamidation, oxidation, or hydrolysis in the presence of drug-degrading enzymes and acidic pH of the stomach (Raja et al., 2019).

2.3.2. Mucosal diffusion barrier

Mucus is a viscoelastic hydrogel secreted by the goblet cells (Brown et al., 2019). The mucus lines the GI tract and acts as a strong physical barrier to the penetration of therapeutics from the lumen to the underlying intestinal epithelium (Ahadian et al., 2020). Mucins are glycosylated glycoproteins that constitute the major structural component of mucus (Dhanisha et al., 2018). Most mucin glycoproteins have high sialic acid and sulfate content, which results in a strong net-negative surface charge (Shogren et al., 2002).

The mucus protects the underlying epithelium from foreign pathogens and particles (Atuma et al., 2001). Mucus is constantly secreted, shed, discarded or digested, and recycled (Lai et al., 2009). The lifetime of mucus is short and often measured in minutes to hours, intestinal mucus is turned over every 50-270 minutes (Lehr et al., 1991). The small intestine has a single unattached and loose mucus layer (Atuma et al., 2001; Johansson et al., 2013). While the stomach and colon have two layers of mucus, a firmly adherent inner layer lies immediately adjacent to the epithelial lining and a less dense unattached loosely adherent outer layer (Atuma et al., 2001; Johansson et al., 2013). Constant turnover of the loosely adherent mucus layer aids in the removal of potentially harmful substances (Brown et al., 2019).

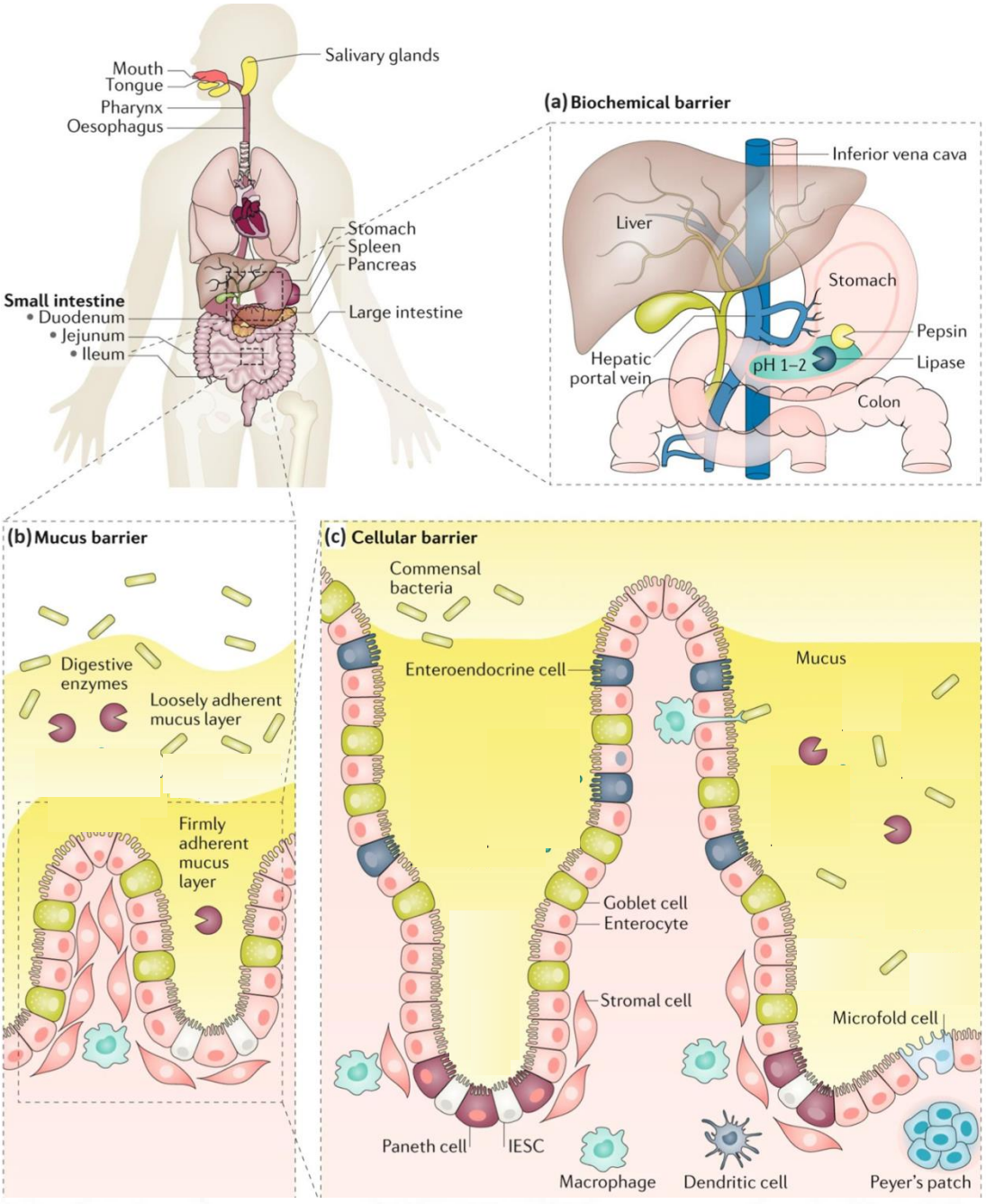

Figure 2.2. Schematics of physiological barriers in oral drug delivery (Adapted from Brown et al., 2019).

2.3.3. Cellular permeability barrier

One of the major barriers to drug absorption in the GI tract is the epithelial lining of the intestine below the mucus barrier. The GI epithelium serves as a barrier between

the body and the external environment (Suzuki, 2013). The intestinal epithelium provides a selectively permeable barrier that restricts the permeation of toxins, antigens, and pathogens while enabling the appropriate absorption of nutrients and water (Suzuki, 2013). The intestinal epithelium is composed of tight junctions and three different types of cells, namely, enterocytes, goblet cells, and microfold cells (Han et al., 2019). Goblet cells, which secrete mucus, constitute 10–20% of epithelial cells, while M-cells, which cover Peyer's patches represent <1% (Brown et al., 2019). The most abundant cells in the epithelium layer are the enterocytes.

Drug absorption through the enterocytes occurs by either transcellular or paracellular pathways (Figure 2.3) (Vitulo et al., 2022). The transcellular route involves the diffusion of lipophilic drugs across the cell membrane phospholipid of the intestinal enterocytes (Alqahtani et al., 2021). The drugs absorbed through the transcellular pathway are unionized and have a molecular weight greater than 300 g/mol (El-Kattan et al., 2012). In the paracellular route, hydrophilic drugs pass through the tight junctions between cells. The drugs absorbed through this route are small hydrophilic molecules with molecular weights lesser than 200 g/mol (Alqahtani et al., 2021). The absorption through the paracellular pathway is mostly low as the pore diameter of the tight junctions between cells is 4-8 A°. This limits the free transepithelial passage of most drug molecules across the intestinal membrane. Additionally, the paracellular transport accounts for 0.1-0.01 percent of the total surface area of the intestinal membrane and this provides only a limited window for drug absorption (Sugano et al., 2002).

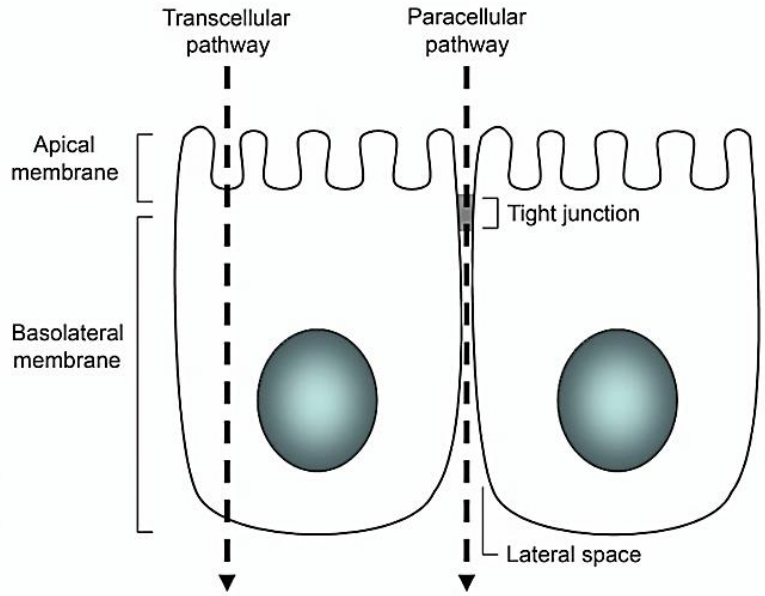

Figure 2.3. Schematics of transcellular and paracellular pathways (Sandek et al., 2009).

2.3.3.1. Tight junction

The intercellular tight junction structures regulate the paracellular permeability and act as a selectively permeable barrier (figure 2.4). They control the paracellular movement of ions, solutes, and water, and are also known to function as a fence to maintain cell polarity by impeding the free diffusion of proteins and lipids between the apical and basolateral domains of the plasma membrane (Farhadi et al., 2003; Turner, 2009). Tight junctions are multi-protein complexes made up of a variety of cytosolic proteins like zonula occludens (ZO) and transmembrane proteins like claudins and occludins, junctional adhesion molecule (JAM) and tricellulin (Suzuki, 2013). The intracellular domains of the transmembrane protein interact with the ZO cytosolic proteins, which in turn bind the transmembrane protein to the perijunctional actomyosin ring (Suzuki, 2013). The interaction of tight junction proteins with the actin cytoskeleton is important to maintain the structure and function of the tight junction. Myosin light chain (MLC) activity (phosphorylation) controls the

circumferential contraction and tension in the perijunctional actomyosin ring (Madara et al., 1987). The actomyosin ring contracts when MLC phosphorylation is induced by kinases such as myosin light chain kinase and Rho-associated kinase (ROCK), which results in the opening of the paracellular pathways (Suzuki, 2013).

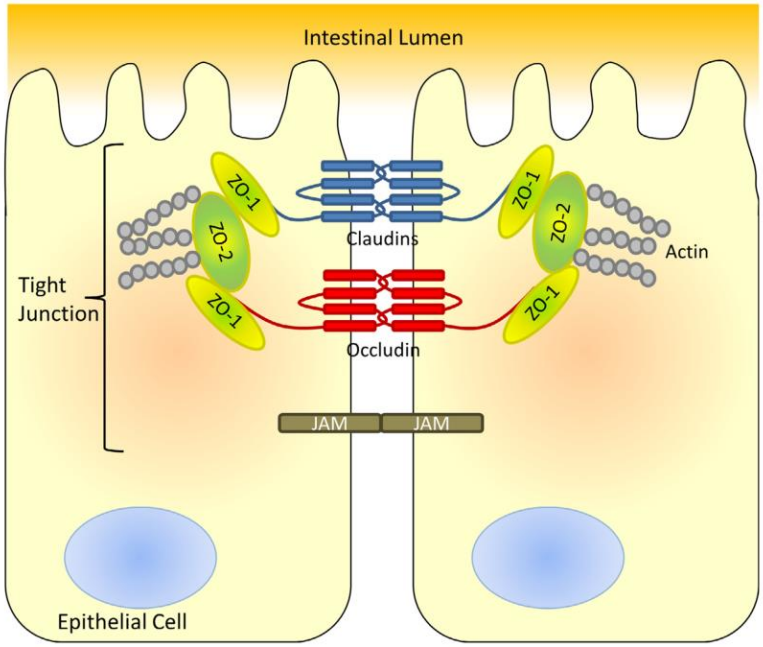

Figure 2.4. Schematic representation of intestinal epithelial cell tight junction proteins (Collins et al., 2017).

2.4. Nano and microparticles

Nanoparticles are defined as particles with sizes between about 1 and 100 nm, in at least one dimension, and exhibit properties that differ from the bulk samples of the same material (Auffan et al., 2009). The distinctive physiochemical properties and high surface area to volume ratio of nanoparticles enable high drug loading (Mandracchia and Tripodo, 2020). The stability of nanoparticles in aqueous physiological environments can be exploited for the successful loading and delivery of poorly water-soluble drugs (Nasrollahi et al., 2016). Furthermore, nanoparticles

can be modified with different targeting or imaging agents so they can be utilized for imaging and targeted drug delivery applications (Nasrollahi et al., 2020). To overcome the challenges involved in oral drug administration, biocompatible nanocarriers have been introduced for the delivery of drugs with low oral stability, bioavailability, and solubility (Ahadian et al., 2020).

In addition to nanoparticles, microparticles are often used in oral drug delivery as they provide a way to increase the bioavailability of pharmaceuticals by controlling the shape, size, geometry, and functional properties of the particles (Augustine et al., 2018; Moreno et al., 2018; Park et al., 2017; Swider et al., 2018). Microparticles are particles in the size range of 1 to 1000 μm (Lengyel et al., 2019). Since nanoparticles are considerably smaller than the human cell (≈100 μm) they can be used for intracellular drug delivery application while microparticles can be used as a reservoir for the controlled release of drugs (Mandracchia and Tripodo, 2020). Nano and microparticles can protect the drugs from the acidic environment of the stomach as well as the mucus layer and enhance the membrane permeability which promotes drug absorption and bioavailability (Ahadian et al., 2020). Mucoadhesive properties of the nano and microparticles enhance drug permeation by increasing the residence time in the GI tract (Zhang et al., 2013). Nano and microparticles can be designed appropriately to overcome oral drug delivery barriers and also facilitate the site-specific delivery of drugs.

The nano or microparticles that can interact with the intestine can be divided into different categories based on the material used to generate them. They can be

classified into metallic nanoparticles, lipid-based nanocarriers, and polymeric microparticles (Ahadian et al., 2020; Vitulo et al., 2022).

2.4.1. Metallic nanoparticles

Metallic nanoparticles interact with the intestine when they are used as therapeutic agents or when they are ingested with food, as they can be used as food preservatives or coloring agents such as TiO_2 (EFSA Panel on Food Additives and Flavourings (FAF) et al., 2021; Medina-Reyes et al., 2020). The most extensively utilized metallic nanoparticles from the medical point of view are silver (Ag) and gold (Au), but data have also been obtained on titanium, palladium, zinc, and copper. Because of their chemical properties, the surface of metallic nanoparticles can be easily functionalized to conjugate targeting agents and active biomolecules, multiple drugs can be also loaded on the same nanoparticle (Ahadian et al., 2020). Metallic nanoparticles have been used as anticancer agents or to counteract bacterial or viral infections (Mubeen et al., 2021; Zhao et al., 2022). Silver nanoparticles are extremely reactive and can interact with various cellular components through the induction of reactive oxygen species which leads to mitochondrial damage and eventually apoptosis.

2.4.1.1. Curcumin-silver nanoparticle conjugate

2.4.1.1.1. Curcumin

Turmeric the powdered rhizome of Curcuma longa, is a common spice that has long been known for its medicinal properties (Aggarwal et al., 2007). Turmeric has traditionally been used in Ayurveda and is believed to be effective against disorders of the skin, bone, and digestive systems (Prasad and Aggarwal, 2011). In turmeric,

the active ingredients are yellow-colored pigments called curcuminoids which constitute around 1-6 % of the dry weight of turmeric (Anderson et al., 2000; Nelson et al., 2017). The crude extract of curcuminoids constitutes 60-70 % of curcumin, 20-27 % of demethoxycurcumin, and 10-15 % of bisdemethoxycurcumin (Nelson et al., 2017). In commercial extracts, curcumin (1,7-bis(4-hydroxy-3-methoxyphenyl)-1,6-heptadiene-3,5-dione) exists along with demethoxycurcumin and bisdemethoxycurcumin in the ratio 77:17:3 (Anderson et al., 2000; Kurien et al., 2017). Curcumin is the major constituent of curcuminoids (Anderson et al., 2000). Currently, curcumin is being widely promoted as a therapeutic due to its antioxidant (Sugiyama et al., 1996), anticancer (Lee et al., 2009), antimicrobial (De et al., 2009), and anti-inflammatory properties (Aggarwal and Harikumar, 2009). However, curcumin's potential for therapeutic translation and clinical applicability has been significantly hindered by low oral bioavailability due to its poor aqueous solubility and rapid degradation in physiological pH (Flora et al., 2013). The stability of curcumin is very important to retain its bioactivity (Lee et al., 2013). The degradation products are biologically active, however, their biological activities were substantially less when compared with curcumin (Zhu et al., 2017). So, keeping curcumin stable in the intestinal pH is essential to keep its bioactivity.

2.4.1.1.2. Structure of curcumin

The structure of curcumin comprised of three chemical entities: two aromatic ring systems containing o-methoxy phenolic groups, connected by a seven-carbon linker consisting of an α,β-unsaturated β-diketone moiety (Priyadarsini, 2014). The chemical structure of curcumin is shown in figure 2.5.

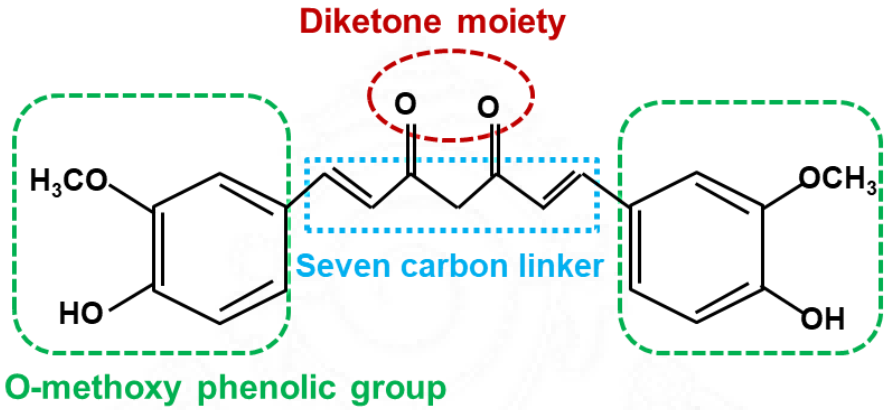

Figure 2.5. Chemical structure of curcumin.

2.4.1.1.3. Degradation of curcumin

Curcumin undergoes degradation when exposed to sunlight and with an increased pH in aqueous-organic solutions, which is a major issue as far as its physiological applications are concerned (Priyadarsini, 2014). Degradation of curcumin at physiological pH results in the rapid disappearance of its orange-yellow color (Gordon et al., 2015). Wang et al. reported that curcumin degraded rapidly in an aqueous solution (phosphate, citrate phosphate, carbonate buffers, and serum-free cell culture medium) in a pH-dependent manner (Wang et al., 1997). In an acidic environment (pH = 3.0 - 6.5), the half-life of curcumin in an aqueous buffer was around 100 - 200 minutes, whereas in a neutral and alkaline environment (pH >7), the half-life of curcumin was around 10 minutes (Wang et al., 1997).

The degradation of curcumin in an aqueous buffer occurs through two major mechanisms: the hydroxyl ion-dependent mechanism and the phenolic radical mechanism (figure 2.6). The degradation products produced from the alkaline hydrolysis of the diketone group of curcumin are ferulic acid, feruloyl methane (Heger et al., 2014). The feruloyl methane could be further hydrolyzed to generate

vanillin (Tønnesen and Karlsen, 1985). In the phenolic radical mechanism, curcumin is first converted to a phenolic radical which then moves to the heptadienedione chain and begins a chain reaction of curcumin degradation (Gordon et al., 2015; Griesser et al., 2011). The autoxidation product formed through the radical-mediated process is bicyclopentadione (Zhu et al., 2017).

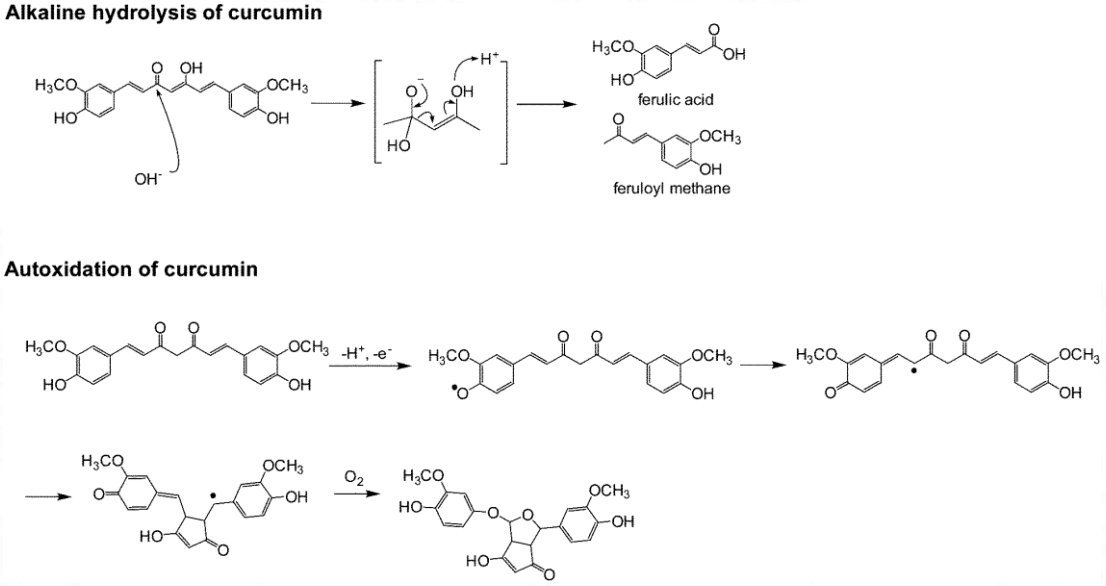

Figure 2.6. Degradation pathways of curcumin (Zhu et al., 2017).

There is a plethora of literature on various methods to improve curcumin stability. Curcumin stability was found to be improved by nanoencapsulation in polymers and cyclodextrin (Esatbeyoglu et al., 2012), redox-active antioxidants (Nimiya et al., 2016), nanoliposomes (Chen et al., 2015), conjugation with hyaluronic acid (Manju and Sreenivasan, 2011), chitosan-chlorogenic acid (Fan et al., 2017), and binding to metallic cations such as zinc, copper, and palladium (Pucci et al., 2013; Sareen et al., 2016; Valentini et al., 2009; Zebib et al., 2010).

2.4.1.1.4. Chemistry of metal-curcumin interactions

The α,β-unsaturated β-diketone moiety of curcumin acts as a strong chelating agent which forms strong complexes with most of the known metal ions (Prasad et al., 2021). The β-diketo moiety of curcumin is involved in binding to metal. Curcumin metal coordination occurs via the enolic group, where the enolic proton is replaced by the metal ion while the o-methoxy phenolic moiety stays intact in complexes (Priyadarsini, 2014). Metal-curcumin complexes not only alter the physicochemical properties of curcumin but also affect the biological reactivity of metals (Priyadarsini, 2014).

A more facile and convenient way to enhance curcumin stability without compromising its therapeutic efficacy is by binding to a metallic ion. Furthermore, there have been reports on the application of curcumin silver nanoparticles for a variety of therapeutic purposes. Prasad et al. reported that curcumin metal complexes exhibit antioxidant activity, inhibit inflammation, enhances antimicrobial, antiviral, and anticancer activities (Prasad et al., 2021). Curcumin metal complexes were reported to have improved solubility, stability, bioavailability, and biochemical activities compared to curcumin alone (Khorasani et al., 2019; Wanninger et al., 2015). Another work by Orteca et al. revealed that curcumin complexed with gallium improves its stability, cellular uptake, and bioavailability in both *in vitro* and *in vivo* cancer models (Orteca et al., 2019). Jaiswal and Mishra revealed that curcumin silver nanoparticles were effective against both Gram-positive and Gram-negative bacteria (Jaiswal and Mishra, 2018) and also reported enhanced antibiofilm activity (Loo et al., 2016). Curcumin silver nanoparticles also inhibit respiratory syncytial virus

infection with no host cell toxicity (Yang et al., 2016) and have the potential to be used for nucleic acid sensing (El Khoury et al., 2015) and collagen stabilization (Srivatsan et al., 2015). Prasad and Lall reported that zinc-curcumin conjugates exhibited improved antioxidant, anti-inflammatory, anticancer, antimicrobial and antidiabetic properties (Prasad and Lall, 2022).

2.4.2. Lipid-based nanocarriers

Lipid-based nanocarriers have been widely used in drug delivery due to their versatility, low toxicity, and biocompatibility and their use by intravenous administration has been already approved by the Food and Drug Administration (FDA) and European Medicines Agency (Halwani, 2022). Nowadays research is more focused on developing lipid-based carriers for oral drug delivery, since they are derived from dietary lipids they facilitate oral permeability and biodegradability (Vitulo et al., 2022).

Currently, lipid nanoparticles have become one of the most attractive carriers for delivering mRNA (Pardi et al., 2018). Recently, the US FDA granted emergency use authorization (EUA) to two mRNA-based vaccines, namely, BNT162b2 (Pfizer-BioNTech) and mRNA-1273 (Moderna), produced using lipid nanoparticles, for clinical therapies against COVID-19, for the first time (Meo et al., 2021). The unique nanocarrier, ‘lipid nanoparticles’, is responsible for the extraordinary success of these two mRNA-based vaccines, which achieved 95% effectiveness in phase III clinical trials (Khurana et al., 2021).

The first nanocarriers approved by the FDA for clinical use are liposomes (Noble et al., 2014). Liposomes are spherical vesicles constituted by lipid bilayers and

composed of an aqueous inner core that encapsulates hydrophilic drugs and an amphiphilic lipid bilayer, which encapsulates hydrophobic drugs (Çağdaş et al., 2014). The basic composition of liposomes is phospholipids and sterols (cholesterol), where the phospholipids stabilize the liposomal membrane. However, different components such as surfactants, bile acids, or specific ligands can be added to this simple structure, to aid the targeting of the liposomes to intestinal cells (Vitulo et al., 2022). Furthermore, they can be used as the carrier of biomolecules like peptides, antigens, or antibodies that are covalently attached to the polyethylene glycol (PEG)-coated surface of liposomes (Ahadian et al., 2020). Liposome functionalized with PEG reduces their recognition by phagocytic cell, resulting in increased circulation time and improved biodistribution (Immordino et al., 2006).

Nanoemulsions are dispersions of an oily and an aqueous phase with the addition of an adequate surfactant, although they are thermodynamically unstable due to the surfactant proportion (3-10%). On the other hand, surfactants added at higher concentrations (20%), stabilize microemulsions, making them thermodynamically stable (Makadia and Siegel, 2011). Schwarz et al. introduced solid lipid nanoparticles in the early 1990s (Schwarz et al., 1994). It has attained much interest recently as an alternative carrier to conventional colloids such as nanoemulsions, micelles, and liposomes (Lin et al., 2017)

2.4.2.1. Solid lipid nanoparticles

Solid lipid nanoparticles (SLN) have a solid lipid core matrix that can solubilize lipophilic drugs and the lipid core is stabilized by a layer of surfactant (Mehnert and Mäder, 2001). Solid lipid nanoparticles have been widely used as carriers for oral

drug delivery, and they can be prepared with either physiological lipids or lipids that are "generally recognized as safe" (GRAS) (Attama et al., 2012). Monoglycerides, diglycerides, triglycerides, fatty acids, steroids, and waxes that do not melt at room temperature are the most common lipids used in the preparation of SLN (Naseri et al., 2015). In comparison to other lipid nanoparticles, SLN exhibited high stability in the harsh conditions of the GI tract (Ahadian et al., 2020). Sanjula et al. reported that SLN can be functionalized and non-covalently coated with carboxymethyl chitosan to improve their stability and drug bioavailability (Sanjula et al., 2009). Several studies reported that hydrophobic drugs, such as nitrendipine and nimodipine, had higher oral bioavailability when loaded in SLN (Kumar et al., 2007; Luo et al., 2011). However, due to the hydrophobic nature of the SLN, the encapsulation of hydrophilic drugs is limited. The incorporation of an SLN core with hydrophilic viscosity-enhancing polymers, such as PEG, via a water-oil-water double emulsion method, is proposed for increased hydrophilic drug loading efficiency in the core of SLN. The core of orally administered SLN in this strategy is composed of a solid lipid core and a hydrogen-bonded rich aqueous phase encapsulating insulin, which is either dispersed in the lipid phase or forms a central core in the lipid matrix (Boushra et al., 2016). Although surface functionalization of SLN with PEG increases their hydrophilicity, it also reduces the mucoadhesion of SLN.

2.4.2.1.1. Lauric acid

Lauric acid (LA) is a saturated medium-chain fatty acid with a backbone of 12 carbon atoms (figure 2.7) (Khan et al., 2021). Lauric acid is the major fatty acid in coconut oil, accounting for 45-53% of the total (Dayrit, 2015).

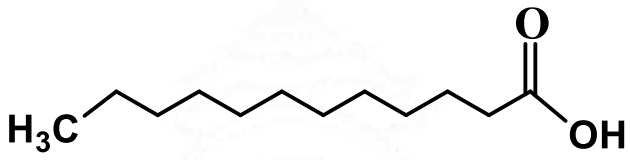

Lauric acid

Figure 2.7. Structure of lauric acid.

The metabolic and physiological properties of LA contribute to the properties of coconut oil. Prasadani et al. stated that maximum caffeic acid absorption was found in the presence of coconut oil, because of the fatty acid composition of coconut oil (Prasadani et al., 2017). Medium-chain fatty acids enter the bloodstream more easily from the GI tract than other lipid molecules that require a complex digestive process (Shah and Limketkai, 2017). Even though 95% of medium-chain triglycerides were absorbed through the portal vein, only 25 - 30% of LA was absorbed through the portal vein, indicating a decreased first-pass effect (Eyres et al., 2016). LA has a greater tendency for lymphatic absorption (Mu and Høy, 2000), which is important when targeting malignancies spread through lymphatics (Sleeman, 2000). LA was also found to have potent antibacterial properties against a variety of fungi, viruses, and gram-positive bacteria (Dayrit, 2015; Silva et al., 2015). Considering all of these properties, LA was projected to be a good candidate material for carrying the drug in nanoparticle-mediated oral drug delivery systems.

2.4.3. Polymeric microparticles

To prepare nano or microstructural oral drug delivery materials, natural polymers, synthetic polymers or their combinations, cellulose derivatives, polysaccharides or

proteins, and plant or animal waxes can be used (Ahadian et al., 2020). Polymeric nano and microparticles made of PLGA [poly(lactic-co-glycolic acid)], PLA [poly(lactic acid)], PLA-PLGA copolymer, Carbopol [poly(acrylic acid)] and poly (N-isopropylacrylamide) have been extensively used in the pharmaceutical field as carriers for oral drug delivery because of its biocompatibility, enzymatic degradation, and bioadhesion (Woodley, 2001). The biodegradability and biocompatibility of these polymers have been approved by the FDA and the European Medicines Agency for a variety of medical and pharmaceutical applications, including drug delivery (Woodley, 2001).

The most commonly researched polymer for oral drug delivery is PLGA, due to its biocompatibility, biodegradability, and FDA approval (Ahadian et al., 2020). Due to the hydrophobic nature of PLGA, it is suitable for the oral delivery of water-insoluble anti-cancer drugs such as paclitaxel and curcumin resulting in enhanced bioavailability of drugs and sustained drug release by degradation of the PLGA nanoparticles (Khalil et al., 2013).

Natural polymers used in oral drug delivery include modified polysaccharides such as chitosan, alginate, pectin, gelatin, and dextran due to their biocompatibility, bioadhesion, and enzymatic degradation (Ahadian et al., 2020). Chemical modification of chitosan enhances mucoadhesion, intestinal permeability, physiological stability, and bioavailability and can be used for oral delivery of anti-cancer and peptide drugs (Iqbal et al., 2012).

2.4.3.1. Chitosan

Chitin is the second most abundant polysaccharide in nature after cellulose and is found in the exoskeletons of crustaceans, crabs, shrimps, and cell walls of fungi (Elieh-Ali-Komi and Hamblin, 2016). Chitosan is obtained from the partial deacetylation of chitin (Rekha and Sharma, 2011). Chitosan is a cationic copolymer of D-glucosamine and N-acetyl D-glucosamine units linked by β-(1 → 4)-glycosidic bonds (Li et al., 2018). Chitosan is an attractive candidate for biomedical applications due to its biological properties such as nontoxicity, biocompatibility, and biodegradability (Zhao et al., 2018). Under mild reaction conditions, the hydroxyl groups and their reactive amino group can be easily modified to produce modified chitosan with desired properties (Rekha and Sharma, 2011).

2.4.3.2. Modification of chitosan

Chitosan is modified through acylation, carboxylation, alkylation, and quaternization to improve water solubility, pH sensitivity, and the targeting of chitosan derivatives (Wang et al., 2020). Chitosan dissolves only under acidic conditions and has poor solubility in natural humoral or intracellular environments at pH 6.8 to 7.4, restricting its applications to drug delivery (Zhao et al., 2018). Chemical modification introduces a hydrophilic group to the amino or hydroxyl group of chitosan at the same time this method destroys the original hydrogen bond and crystallinity of chitosan (figure 2.8.) (Wang et al., 2020).

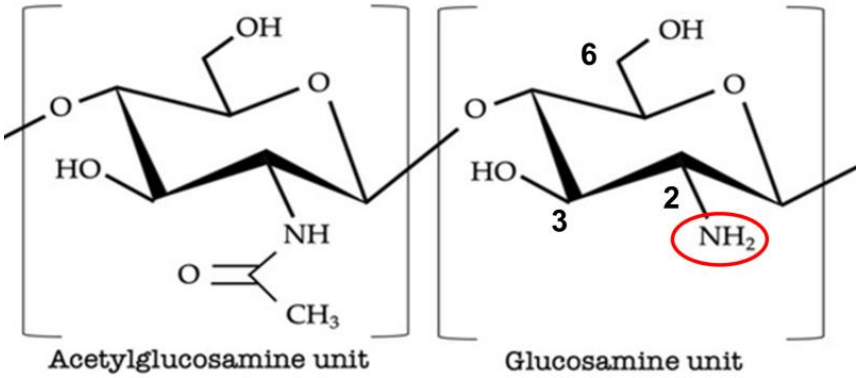

Figure 2.8. Structure of chitosan

2.4.3.2.1. Destruction of hydrogen bonding

Acylated modified chitosan: The most common modification of chitosan is acylation. Chitosan acylation is the reaction of chitosan with a variety of organic acids and organic acid derivatives (mainly anhydride and acyl chloride), introducing aliphatic or aromatic acyl groups to the molecular chain (Cui et al., 2020). The acylation reaction weakens the crystallinity and enhances the water solubility of chitosan by the destruction of intramolecular and intermolecular hydrogen bonding. The molecular chain of chitosan consists of two hydroxyl groups, a primary C6-OH hydroxyl group, and a secondary C3-OH hydroxyl group (figure 2.8). The activity of C2-NH_2 of chitosan is greater than the primary hydroxyl group so the order of activity of the acylation reaction follows the order C2-NH_2 > C6-OH > C3-OH. Acylation reaction occurs with C2-NH_2, resulting in an amide bond formation called N-acylation (Al-Remawi, 2015). N-acylated chitosan can be used as a carrier or as a sustained-release agent in pharmaceutical applications (Medeiros Borsagli et al., 2018).

Alkylation-modified chitosan: A hydrophobic alkyl group can be introduced to chitosan leading to weakened intermolecular hydrogen bonds and improvement in solubility.

2.4.3.2.2. Introduction of the hydrophilic group

Hydrophilic groups like the carboxylic acid group, quaternary ammonium group, sulfonic acid group, phosphoric acid group, amino group, hydroxyl group, ether bonds composed of an oxygen group, the hydroxyl group, the carboxylate group, and the block polyether group can be introduced to chitosan (Wang et al., 2020).

Carboxylated chitosan: The carboxylation reaction utilizes glyoxylic acid or chloroalkanoic acid, which reacts with C2-NH_2 or C6-OH groups of chitosan to form –the COOH group.

Quaternary ammonium chitosan: The positively charged hydrophilic quaternary ammonium group is introduced to chitosan to improve water solubility. The quaternization occurs with C2-NH_2 groups of chitosan (Wang et al., 2020). N, N, N-trimethyl chitosan (TMC) is a quaternary ammonium chitosan.

2.4.3.2.3. Formation of the hydrophilic group

Chitosan esterification reaction where the chitosan reacts with carboxylic acid or oxy-containing mineral acid. In chitosan etherification chitosan molecule reacts with an alkylating reagent agent (e.g., dimethyl sulfate, chloroacetic acid, and ethylene oxide) to form a chitosan-etherified derivative (Wang et al., 2020).

2.5. Colorectal cancer

Colorectal cancer is cancer that occurs in the large intestine (colon) and rectum regions of the GI tract. Colorectal cancer is the third most common cancer and the second most deadly cancer (Xi and Xu, 2021).

2.5.1. Designing of nano and microparticles for colon-targeted drug delivery

The GI tract represents a harsh environment for oral drug delivery. The active drug component has to survive the acidic pH of the stomach and also cross the intestinal barrier including the mucus layer and the enterocytes. For this reason, the nano and micro drug carriers can be functionalized to prevent the attack of pH and enzymes and to favor their passage through the intestine.

To protect the drug delivery carriers from low pH, different formulations of Eudragit® polymers have been already used in the pharmaceutical industry. pH-responsive Eudragits® are methacrylic acid copolymers that can dissolve above specific pHs, allowing the site-specific delivery of drugs to the various regions of the GI tract including the small intestine or colon (Patra et al., 2017). Eudragit E100, a cationic polymer having dimethyl aminoethyl methacrylate as a functional group dissolves in the acidic pH conditions of the stomach and swells at a pH less than 5.0 (Farooq et al., 2017). Eudragit L100-55 dissolves at a pH greater than 5.5 used for duodenum targeting; Eudragit L100 dissolves at a pH 6-7 used for targeting jejunum; and Eudragit S100 dissolves at a pH greater than 7 used for ileum and colon targeting (Arruebo and Sebastian, 2020). Subudhi et al. reported that Eudragit S100-coated citrus pectin nanoparticles exhibited site-specific delivery of 5-fluorouracil for the effective treatment of colorectal cancer (Subudhi et al., 2015). Another study by El-

Maghawry et al. revealed that Eudragit S100-coated PLGA nanoparticles help in the colonic-specific delivery of etoricoxib drug for the treatment of inflammatory bowel diseases (El-Maghawry et al., 2020).

5-fluorouracil (5-FU) is a hydrophilic drug widely used for colorectal cancer treatment. Water soluble amphoteric derivative of chitosan (CTAA) formed by using trimellitic acid chloride, was crosslinked with alginate to prepare a (CTAA/alginate) film that can protect the 5-FU from being absorbed and degraded by the upper GI tract before reaching the colon (Kavianinia et al., 2015). Another work by Huang et al. reported that O-carboxymethyl chitosan (OCMC), a carboxymethylated derivative, possesses improved water solubility and pH sensitivity and can be used for intestine-targeted drug delivery. Spherical microcapsules (GA-OCMC LbL) with a core-shell structure were prepared by a layer-by-layer assembly (LbL) with the use of gum arabic (GA) and OCMC improved the bioavailability of omeprazole as well as enhanced stability in simulated gastric fluid (Huang et al., 2019).

2.6. Physicochemical properties of particles

The physicochemical properties of the nano or microparticles (size, surface charge, shape, hydrophilicity/hydrophobicity play an important role in their interaction with the GI tract (figure 2.9). It also has an influence on cellular uptake and subsequent cellular interactions.

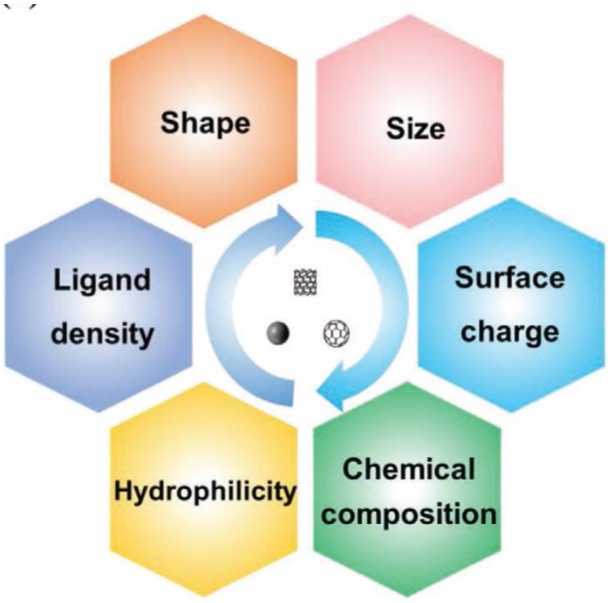

Figure 2.9. Physicochemical properties of particles

2.6.1. Zeta potential

Zeta potential is an analytical technique used to determine the surface charge of nano or microparticles in a colloidal solution (figure 2.10). The surface of a charged particle attracts and firmly binds to a thin liquid layer of opposite charge known as the stern layer; when the particle diffuses in solution, it is involved by an outer diffuse layer composed of loosely associated ions, resulting in the formation of an electrical double layer (Clogston and Patri, 2011). Zeta potential is the electrical potential of the double layer, which is determined by measuring the velocity of charged particles moving toward the electrode across the sample solution in the presence of an external electric field (Sapsford et al., 2011). The magnitude of zeta potential is used to predict colloidal stability. Zeta potential with values greater than +25 mV or less than -25 mV has a high degree of stability. Lower zeta potential values in dispersions will cause aggregation, coagulation, or flocculation due to van der Waals interparticle attraction (Sapsford et al., 2011).

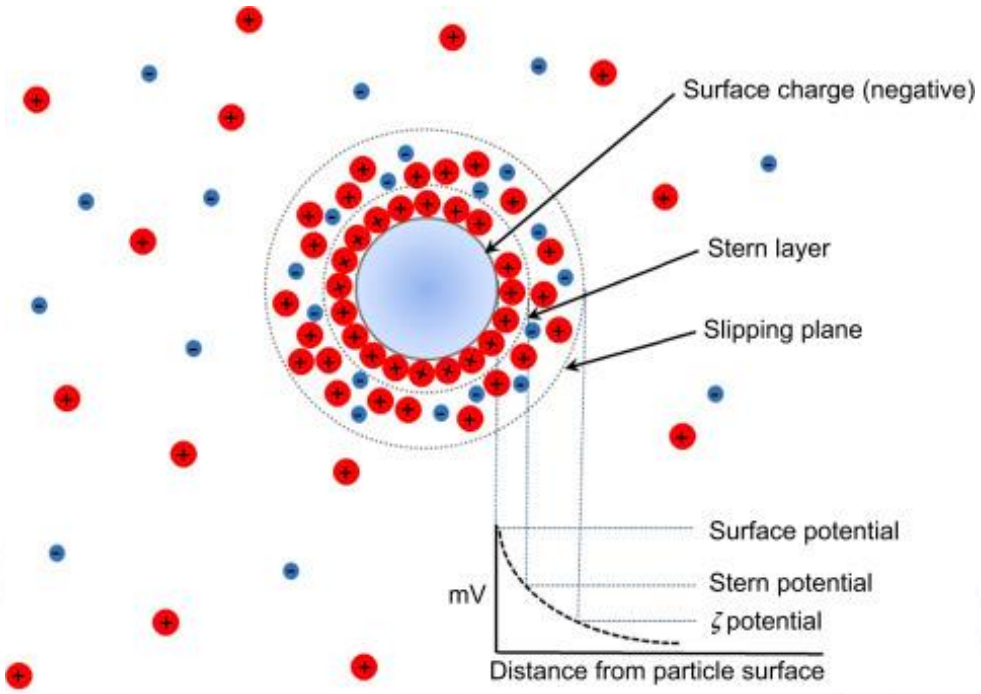

Figure 2.10. Illustration of zeta potential (Pate and Safier, 2016).

2.7. Interactions with proteins

When nano or microparticles interact with proteins in biological environments, they are surrounded by a layer of proteins adsorbing to the surfaces called protein corona (Kopac, 2021). The physicochemical properties of the particles such as the size, surface chemistry, and charge are key factors influencing the behavior of protein corona (Kopac, 2021). The interaction of nano or microparticles with proteins in their surroundings is a critical factor in determining their biological fate (Cao et al., 2019). Various types of nanoparticles have been studied for their interactions with proteins in the blood and lungs (Konduru et al., 2017; Lacerda et al., 2010). In contrast, much less is known about the interactions of ingested particles with proteins from foods or the human GI tract (Martirosyan and Schneider, 2014). However, these interactions, are likely to have a significant impact on the GI fate and potential

toxicity of any ingested particles (Cao et al., 2019). When TiO_2 nanoparticles were incubated in casein solution there was a pronounced decrease in the rate and extent of gastric digestion of the casein (Cao et al., 2019).

2.8. Interactions of particles with mucus

2.8.1. Mucin interactions

Mucin is the most abundant protein in mucus. The negative charge of mucins leads to the adhesion of positively charged drug delivery carriers through electrostatic interactions (Vitulo et al., 2022). The intestinal mucus is composed of two layers, a loosely adhered layer nearer to the intestinal lumen and a firmly adherent layer in contact with the intestinal epithelium. The firm binding of the nano or microparticles to the upper layer led to the quick clearance of the particles and also reduced their opportunity to reach the epithelium. So the ability of nano or microparticles to bind to the mucus layer could be regarded only partially as positive (Ensign et al., 2012). Lieleg et al. studied the effect of surface charge as a selection criterion for particle translocation in mucin hydrogels. They found that the mobility of carboxyl-terminated (strongly negatively charged) and amine-terminated (strongly positively charged) particles was suppressed compared to PEG-coated polystyrene particles (Lieleg et al., 2010) which indicates that the higher the surface potential, the stronger the suppression of particle mobility.

2.8.2. Mucoadhesion

For effective oral drug delivery, mucus is a barrier that needs to be overcome or a lining that can be used to improve the oral bioavailability of the drug by increasing mucoadhesion of the drug delivery system (Boegh and Nielsen, 2015).

Mucoadhesion refers to the ability of pharmaceutical dosage form to adhere to mucosal membranes in the human body and provide temporary retention (Khutoryanskiy, 2011). Mucoadhesive drug delivery systems interact with the mucus layer covering the mucosal epithelial surface and increase the residence time of the dosage form at the site of absorption and thereby increasing the local concentration and the fraction absorbed from the mucosal surface (Boddupalli et al., 2010).

2.8.2.1. Mechanism of mucoadhesion

The mechanism of mucoadhesion is divided into the contact (wetting) stage and the consolidation stage (Boddupalli et al., 2010). The first stage is denoted by the contact between the mucoadhesive and the mucus membrane where the formulation spreads out and swells to make deep contact with the mucus layer (Hagerstrom et al., 2003).

The mucoadhesive materials are activated by the presence of moisture in the consolidation step. The moisture will effectively plasticize the system, enabling mucoadhesive molecules to become free, conform to the shape of the surface, and bond mainly by weaker van der Waals and hydrogen bonds (Smart, 2005). Two theories that explain the consolidation step are the diffusion theory and the dehydration theory. In diffusion theory, the mucoadhesive molecules and the mucus glycoproteins interact with each other by interpenetrating their chains and forming secondary bonds (Boddupalli et al., 2010). To happen this, the mucoadhesive device has characteristics favoring both chemical and mechanical interactions. Molecules with hydrogen bond forming groups -OH or –COOH, an anionic surface charge, a high molecular weight, flexible chains, and surface active properties can exhibit mucoadhesive properties (Hägerström et al., 2003).

2.8.2.2. Theories of mucoadhesion

The phenomenon of mucoadhesion has been explained based on several general theories:

2.8.2.2.1. Electronic theory

The electronic theory is applied, when the mucoadhesive polymer and the mucus have distinct electronic properties, and electron transfer occurs resulting in the formation of an electrical double layer and electrostatic attraction between oppositely charged surfaces (Derjaguin et al., 1977).

2.8.2.2.2. Adsorption theory

According to the adsorption theory, specific interactions like hydrogen bonds and van der Waals forces are responsible for the attraction between the mucus and the mucoadhesive polymers (Kinloch, 1980). When the mucoadhesive polymers are amphiphilic, hydrophobic effects play an important role in mucoadhesion (Khutoryanskiy, 2011). The adsorption theory also takes into account the possibility of chemisorption, which occurs when strong covalent bonds are created between the mucoadhesive polymer and mucins (Khutoryanskiy, 2011).

2.8.2.2.3. Wetting theory

The wetting theory relates the surface tension of the mucus and the mucoadhesive polymer with its ability to spread on the mucus layer (Peppas and Buri, 1985). This theory is primarily applicable to liquid mucoadhesive forms. Excellent mucoadhesive performance is associated with the better ability of the polymers to spread on the surface of the mucosal tissue (Khutoryanskiy, 2011).

2.8.2.2.4. Diffusion theory

The diffusion theory takes into account the penetration of mucoadhesive macromolecules into the mucus gel and the diffusion of soluble mucins into the dosage form resulting in the formation of an interpenetration layer (Kinloch, 1980). Effective adhesion is typically attained when the interpenetration layer thickness reaches 0.2-0.5 mm (Khutoryanskiy, 2011).

2.8.2.2.5. Fracture theory

According to the fracture theory, the strength of the adhesive bond is correlated with how difficult it is to separate two surfaces after adhesion (Ponchel et al., 1987). This theory is applicable to determine the fracture strength of adhesive bonds involving solid and rigid mucoadhesive materials.

2.8.2.2.6. Mechanical theory

According to mechanical theory, surface roughness favors adhesion due to an increased contact area. This theory applies to rough and porous materials (Garti, 2008).

2.8.2.3. Influence of surface chemistry of the particles on mucoadhesion

Mucoadhesion is achieved in general by strong attractive interactions with the mucosa, which include physical entanglement between polymer chains and the mucus, electrostatic interactions between the mucus's negative charge and positively charged mucoadhesive assemblies, weak noncovalent interactions (e.g., hydrogen bonds) between the mucus and anionic polymers, and the formation of disulfide bridges between the cysteine units of mucin and thiolated polymers (Schattling et al., 2017).

The surface properties of the nano or microparticles influence mucoadhesion. Polymeric particles can interact with the mucus through electrostatic, van der Waals, hydrophobic, or hydrogen-bonding interactions, which may lead to the long residence time of drugs in the absorption region (Woodley, 2001). Anionic polymers like alginate, poly(acrylic acid), and carboxymethyl cellulose form a hydrogen bond with the mucus and enhance mucoadhesion (Schattling et al., 2017). Positively charged particles can enhance mucoadhesion through the formation of electrostatic interactions with negatively charged mucus (Ensign et al., 2012). Liu et al. reported that cationic solid lipid nanoparticles loaded with N_3-O-toluyl-fluorouracil (TFu) increased the oral absorption of TFu 2-fold compared to TFu suspension (Liu et al., 2010). The enhanced controlled drug release is due to the increased bioadhesion of the carrier by the electrostatic interaction between negatively charged mucosal surface and positively charged colloidal particles (Liu et al., 2010). The positive charge of chitosan enhances drug absorption and coating nanoparticles with chitosan is an effective method to enhance mucoadhesion (Kawashima et al., 2000). Trimethyl chitosan (TMC) is a positively charged derivative of chitosan, because of its persistent cationic nature, it is one of the most powerful mucoadhesive polymers (Ways et al., 2018). High molecular weight variants of chitosan exhibit better mucoadhesion (Takeuchi et al., 2005). Thiolated chitosan exhibited enhanced mucoadhesion due to the covalent disulfide bond formation between the thiol groups and cysteine on mucus glycoprotein (Bravo-Osuna et al., 2007).

2.9. Interactions of particles with intestinal tight junctions

The physicochemical properties of the nano and microparticles play an important role in tight junction opening and increasing the intestinal permeability of drugs. The paracellular pathway is related to the charge and size-selective transport of materials through the tight junctions between intestinal epithelial cells (Slifer and Blikslager, 2020). The cationic nature of chitosan is involved in the transient opening of the intestinal tight junction (Sonaje et al., 2012). Ranaldi et al. observed that chitosan and other polycations (polyethylenimine, poly-L-lysines) can induce a reversible increase in tight junction permeability (Ranaldi et al., 2002). Another study by Sadeghi et al. reported that quaternized derivatives of chitosan, i.e., trimethyl chitosan (TMC), dimethylethyl chitosan (DMEC), diethylmethyl chitosan (DEMC), and triethyl chitosan (TEC) are able to decrease the Transepithelial Electrical Resistance (TEER) value in the following order TMC > DMEC > DEMC = TEC > chitosan, indicating their abilities to open the tight junctions. These findings indicate that the higher the cationic charge higher the TEER reduction (Sadeghi et al., 2008).

Some reports revealed that not only cationic charge but also anionic charge, mediates tight junction opening. Lamson et al. reported that the anionic silica nanoparticles with a size ≤ 200 nm induce tight junction relaxation, increasing intestinal permeability and enabling the oral delivery of proteins (Lamson et al., 2019). Chang et al. studied the effect of gold nanoparticles with three different negative surface charges (-4.5, -17.52, and -27.5 mV) on intestinal tight junction opening and paracellular permeability (Chang et al., 2020). It has been found that gold nanoparticles with higher negative zeta potential (-27.5 mV) triggered the high-

frequency transient opening of tight junctions of the enterocyte layer and accompanied stronger paracellular permeability. Another work by wang et al., revealed that negatively charged carboxymethyl chitosan/chitosan nanoparticles showed enhanced epithelial permeation and increased bioavailability compared to positively charged nanoparticles (Wang et al., 2017).

2.10. Caco-2 cells - *In vitro* model for intestinal absorption

Caco-2, the human epithelial cell line has been widely used as an intestinal epithelial barrier model (Lea, 2015). Caco-2 cells were derived from human colorectal adenocarcinoma cells. Caco-2 cells differentiate to form tight junctions between cells when cultured as a monolayer to serve as a model of the paracellular movement of compounds across the monolayer (figure 2.11) (van Breemen and Li, 2005). TEER was measured using a voltmeter with a chopstick electrode (Millicell ERS system) to ensure the integrity of the monolayers formed. Caco-2 cells were grown on the surface of a transwell plate made from polycarbonate, polyester, or polyethylene terephthalate (Lea, 2015).

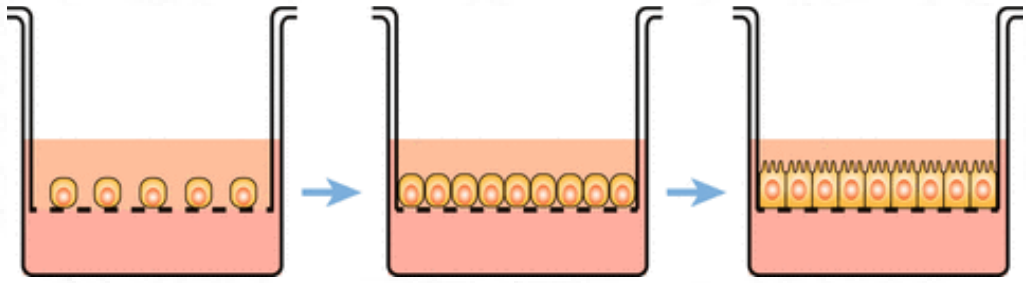

Figure 2.11. Illustration of Caco-2 cell differentiation on a tissue culture insert. After the Caco-2 cells reach confluence (middle) they start to differentiate spontaneously, and after a total culture period of around 21 days they will appear with dense microvilli on the apical side characteristic of small intestinal enterocytes

2.11. Importance of the current work

Currently, research is more focused on the development of oral drug delivery carriers. To overcome the barriers of drug delivery, nano or microparticles were developed. The physicochemical properties of the particles (size, shape, surface charge) play an important role in the interaction of these particles with the GI tract. These interactions determine the fate of the particles in the biological system. Considering the importance, the study focused on the interactions of nano or micro-delivery carriers with the simulated intestinal microenvironment and evaluated their drug-delivering efficacy.

3 MATERIALS AND METHODS

The main focus of the work was to study the interactions of nano and micro drug delivery carriers with the simulated intestinal microenvironment. For achieving this objective, drug carriers of different surface chemistry and size were developed, and studied their simulated intestinal microenvironment interactions and drug-delivering efficacy. Three systems were studied and they were: (a) metal-drug conjugate (system I), (b) hydrophobic solid-lipid nanoparticles (system II), and (c) hydrophilic microparticle systems with different surface charges (system III). Curcumin-silver nanoparticle conjugate (CUR-AgNP) was the first system used for the study and lauric acid solid lipid nanoparticle (LA-SLN) was the hydrophobic system used. Chitosan was selected as the hydrophilic system and it was further functionalized with lysine amino acid and maleic anhydride to prepare different charge-based chitosan particles. Microparticles of chitosan and functionalized chitosan particles were used as the drug carriers. CUR-AgNP and LA-SLN were the nanoparticle drug delivery systems used for the study.

3.1. Materials

The materials used for the work, their make, sources, purity, etc. are given in table 3.1.

Table 3.1. Materials used for the work

Sl. No.	Name of the chemical/reagent/test kit	Grade	Source
1.	1-(3-Dimethylamino-propyl)-3-Ethyl Carbodiimide Hydrochloride (EDC.HCl)	Extra pure, 99%	Sisco Research Laboratories (SRL) Pvt. Ltd., Mumbai, India.
2.	4,6-diamidino-2-phenylindole (DAPI)	Blue fluorescent dye, Excitation wavelength range: 358⁄461nm.	Invitrogen, Thermo Fisher Scientific, Mumbai, India.
3.	5-Fluorouracil	≥99% (HPLC), powder	Sigma-Aldrich (Bangalore, India)
4.	Acetic acid glacial	99-100% for synthesis	Merck, Bangalore, India.
5.	Acrylamide 3x Cryst.	For molecular biology, 99.9%	SRL Pvt. Ltd., Mumbai, India.
6.	Ammonium persulphate (APS)	For electrophoresis, 99 %	SRL Pvt. Ltd., Mumbai, India.
7.	Antibiotic-Antimycotic (100X)	10,000 units/mL of penicillin, 10,000 µg/mL of streptomycin, and 25 µg/mL of Gibco Amphotericin B	Gibco, Thermo Fisher Scientific, Mumbai, India.
8.	Antirabbit IgG-Texas Red® antibody Produced in the donkey.	Texas red - bright red fluorescent dye. Excitation wavelength: 594 nm Emission wavelength: 623 nm	Sigma-Aldrich, Bangalore, India.
9.	Anti-ZO-1 antibody	Recommended for detection of ZO-1 of the mouse, rat and human origin by WB, IP, IF and IHC(P)	Santa Cruz Biotechnology, USA.
10.	Anti-ZO-1 antibody FITC	FITC- green fluorescent dye. Excitation/Emission: 494/525 nm	Santa Cruz Biotechnology, USA.
11.	Biocurcumin®/BCM-95®	Total curcuminoid content-87.5%, and out of this, the curcumin content: 66.9%.	Arjuna Natural Extracts Ltd., Kerala, India.
12.	Bovine serum albumin (BSA)	Cell culture tested	Sigma-Aldrich, Bangalore, India.
13.	Chitosan	Medical grade	SRL Pvt. Ltd., Mumbai, India.
14.	Citric acid	Anhydrous, A. R.	Himedia, Mumbai, India.
15.	Coomassie® Brilliant blue G 250	For electrophoresis	Sigma-Aldrich, Bangalore, India.
16.	Copper(II) sulfate pentahydrate ($CuSO_4$ * 5 H_2O)	For analysis EMSURE® ACS, ISO, Reag. Ph Eur	Merck, Bangalore, India.

17.	Dialysis tubing cellulose membrane	Molecular weight cut-off = 14,000, avg. flat width 25mm (1.0 in.), avg. diameter 16 mm, when full.	Sigma-Aldrich, Bangalore, India.
18.	Double stain apoptosis detection kit	Acridine orange/Ethidium bromide	Originlab, India.
19.	DPX mountant	For histology	Sigma-Aldrich, Bangalore, India.
20.	Dulbecco's Modified Eagle Medium (DMEM), high glucose	With L-glutamine, 4.5 gms Glucose per liter, and Sodium pyruvate	Himedia, Mumbai, India.
21.	Eudragit® S100	Methacrylic Acid - Methyl Methacrylate Copolymer (1:2) Ph Eur	Evonik industries, Germany.
22.	Fetal bovine serum (FBS)	Heat inactivated	Gibco, Thermo Fisher Scientific, Mumbai, India.
23.	Folin-Ciocalteu's phenol reagent	Reagent for analysis	Merck, Bangalore, India.
24.	Glucosamine Hydrochloride	Extra pure, 99% for biochemistry	SRL Pvt. Ltd., Mumbai, India.
25.	Glycerol	99% (GC)	Sigma-Aldrich
26.	Glycine	For molecular biology	Spectrochem Pvt. Ltd., Mumbai, India.
27.	Hydrochloric acid, fuming 37% (HCl)	For analysis EMSURE® ACS, ISO, Reag. Ph Eur	Merck, Bangalore, India.
28.	Lauric acid pure	(n-Dodecanoic acid) $C_{12}H_{24}O_2$ Melting point (44-46 ºC).	SD Fine-Chem Ltd., Mumbai, India.
29.	L-Lysine monohydrochloride	For biochemistry	Merck, Bangalore, India.
30.	Maleic anhydride	For synthesis	Merck, Bangalore, India.
31.	Mark12™ unstained standard	Protein ladder, 12 polypeptides in the range of 2.5–200 kDa.	Invitrogen, Thermo Fisher Scientific, Mumbai, India.
32.	Methanol	For analysis EMPARTA® ACS	Merck, Bangalore, India.
33.	Millipore trans-membrane inserts (0.4µm PCF, 12mm diameter)	Polycarbonate cell culture inserts with pore size of 0.4 µm used in a 24-well plate for cell attachment, cell culture, cell differentiation, drug transport & permeability.	Merck, Bangalore, India.
34.	MTT (Thiazolyl Blue Tetrazolium Bromide)	Cell culture tested	Himedia, Mumbai, India.
35.	Mucin from porcine stomach	Type III, bound sialic acid 0.5-1.5%, partially purified powder	Sigma-Aldrich, Bangalore, India.
36.	N, N, N', N'-Tetramethyl Ethylenediamine	For electrophoresis and molecular biology	SRL Pvt. Ltd. Mumbai, India.

	(TEMED)		
37.	N, N-Methylene Bisacrylamide 3x Cryst.	For molecular biology, 99.5%	SRL Pvt. Ltd., Mumbai, India.
38.	N-Acetyl-D-Glucosamine	Extra pure AR, 99% for biochemistry	SRL Pvt. Ltd., Mumbai, India.
39.	OmniPur® Bromophenol Blue, Sodium Salt	Molecular Biology Grade	Sigma-Aldrich, Bangalore, India.
40.	Pancreatin from porcine pancreas	A mixture of several digestive enzymes produced by the exocrine cells of the porcine pancreas	Sigma-Aldrich, Bangalore, India.
41.	Picrylsulfonic acid solution (TNBS)	5% (w/v) in H_2O, BioReagent, suitable for the determination of primary amines	Sigma-Aldrich, Bangalore, India.
42.	Pluronic® F-127 (Poloxamer 407)	Powder, BioReagent, suitable for cell culture.	Sigma-Aldrich, Bangalore, India.
43.	Potassium chloride (KCl)	For analysis EMSURE®	Merck, Bangalore, India.
44.	Potassium dihydrogen phosphate (KH_2PO_4)	For analysis EMSURE® ISO	Merck, Bangalore, India.
45.	Potassium sodium tartrate tetrahydrate ($C_4H_4KNaO_6$ * 4 H_2O)	for analysis EMSURE® ACS, ISO, Reag. Ph Eur	Merck, Bangalore, India.
46.	Rhodamine B	Purity > 95% (HPLC).	TCI Chemicals Pvt. Ltd., Chennai, India.
47.	Rhodamine phalloidin	Excitation/Emission: 540/565 nm. Red-orange fluorescent dye, tetramethylrhodamine (TRITC).	Invitrogen, Thermo Fisher Scientific, Mumbai, India.
48.	Silver nitrate	99.9% purity	Spectrochem Pvt. Ltd., Mumbai, India.
49.	Sodium carbonate (Na_2CO_3)	Anhydrous extra pure AR	SRL Pvt. Ltd., Mumbai, India.
50.	Sodium chloride (NaCl)	For analysis EMSURE® ACS, ISO, Reag. Ph Eur	Merck, Bangalore, India.
51.	Sodium dodecyl sulphate (SDS)	BioReagent, suitable for electrophoresis, for molecular biology, ≥98.5% (GC)	Sigma-Aldrich, Bangalore, India.
52.	Sodium hydrogen carbonate ($NaHCO_3$)	Extra pure	Himedia, Mumbai, India.
53.	Sodium hydroxide (NaOH)	Pellets for analysis EMSURE®	Merck, Bangalore, India.
54.	Sodium tripolyphosphate ($Na_5P_3O_{10}$)	Technical grade, 85%	Merck, Bangalore, India.
55.	Span® 80	For synthesis.	Sigma-Aldrich, Bangalore, India.
56.	Tetrahydrofuran (THF)	For HPLC	Spectrochem Pvt. Ltd., Mumbai, India.
57.	TRIS	Tris(hydroxymethyl)-aminomethane, EMPROVE®	Merck, Bangalore, India.

		EXPERT	
58.	Trypsin-EDTA (1X)	0.25%, phenol red	Gibco, Thermo Fisher Scientific, Mumbai, India.
59.	Ultrafiltration discs, 100 kDa NMW	100 kDa NMWL, Biomax® polyethersulfone, 44.5 mm diameter	Merck, Bangalore, India.

3.2. Methods

3.2.1. System I: Curcumin-silver nanoparticle conjugate

To develop a metallic system, curcumin, a potent therapeutic agent, was conjugated with silver nanoparticles. Curcumin is hydrolytically unstable at intestinal pH (Dulbecco and Savarino, 2013) leading to poor bioavailability in the biological milieu. The stability of curcumin is very important to retain its biological activity. To improve physiological stability, curcumin was conjugated with silver nanoparticles using the following procedure:

3.2.1.1. Synthesis of curcumin-silver nanoparticle conjugate

The CUR-AgNP was prepared using previously reported procedures with slight modifications (Khan et al., 2019; Sindhu et al., 2014). The CUR-AgNP was prepared by treating silver nitrate with curcumin (i.e., Biocurcumin®/BCM-95®) at pH 7, where curcumin (CUR) acts as a reducing agent of Ag^+ ions (figure 3.1.). In brief, 1 mM silver nitrate was prepared in 50 mL of deionized water and its pH was adjusted to 7 with 1M NaOH. CUR stock (4 mg/mL) was prepared in ethanol and 280 μL was added dropwise to the former silver nitrate solution under constant stirring. This solution was incubated in the dark at room temperature. After 5 days of incubation, a small amount of precipitated CUR was observed. The stable CUR-Ag nanoparticle suspension was collected and the precipitate was discarded. Amicon stirred cell

apparatus, equipped with a 100 kDa biomax polyethersulfone membrane filter was used to concentrate and separate the stable nanoparticle suspension. An aliquot of this concentrated solution was used for further studies in cell lines. Another aliquot of CUR-AgNP was lyophilized (Labconco, USA) and these lyophilized particles were used for physicochemical characterization and degradation studies.

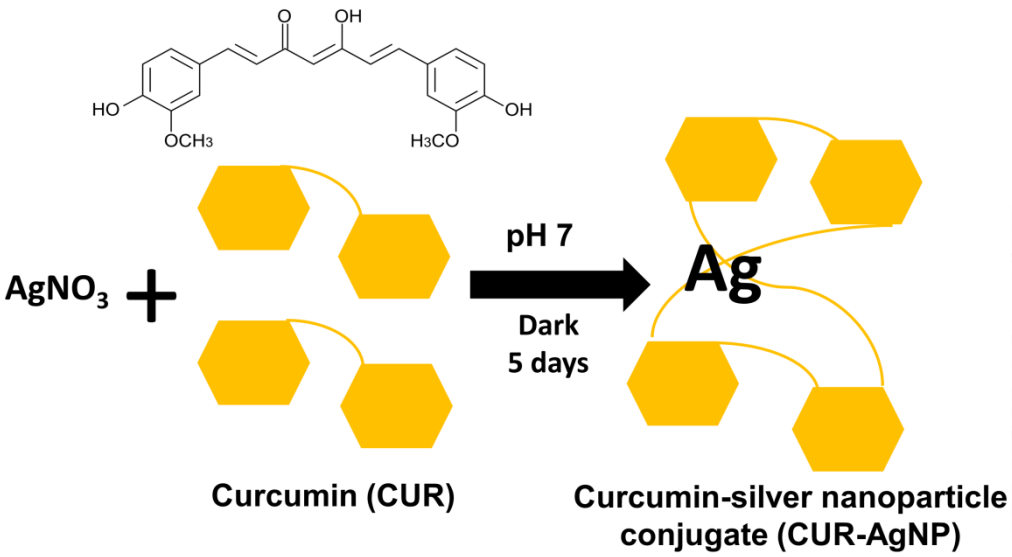

Figure 3.1. Schematic of CUR-AgNP synthesis.

3.2.1.2. Physicochemical characterization

3.2.1.2.1. UV-Visible absorption and fluorescence spectroscopy

Using the stable particle suspension, the successful formation of the CUR-AgNP was monitored by UV-Visible absorption spectroscopy (UV-1800 Shimadzu Spectrophotometer, Japan) and fluorescence spectroscopy (JASCO FP-8200 spectrophotometer).

3.2.1.2.2. Determination of particle size and zeta potential

The technique of dynamic light scattering (NanoZS, Malvern Instruments, UK) was used to determine the hydrodynamic size of the CUR-AgNP. The laser used for the

measurement had a wavelength of 633 nm and a scattering angle of 90°. The measurement was carried out at 25 °C, the dispersant viscosity was 0.89 cP and the refractive index of the CUR-AgNP was 1.33. The zeta potential of the CUR-AgNP in phosphate buffer (PBS, pH 7.4) was determined by zetasizer (NanoZS, Malvern Instruments, UK).

3.2.1.2.3. X-ray diffraction (XRD) analysis

The X-ray powder diffraction (XRD) technique (Bruker D8 Advance, Japan) was used to determine the phase purity of the CUR-AgNP.

3.2.1.2.4. Transmission electron microscopy (TEM) analysis

Transmission electron microscopy (TEM, Hitachi H-7650) was used to determine the size and morphology of the CUR-AgNP. Here, a drop of the CUR-AgNP suspension was cast onto copper grids covered with carbon films, dried, and visualized using TEM.

3.2.1.2.5. FTIR analysis

Fourier transform infrared (FTIR) spectrophotometer (Nicolet 5700, Thermo Fischer Scientific, USA) was used to identify the functional groups present in the CUR-AgNP. The FTIR spectra of CUR and CUR-AgNP were recorded over a scan range of 500-3800 cm^{-1} using the KBr pellet method.

3.2.1.2.6. Inductively coupled plasma optical emission spectroscopy (ICP-OES) analysis

The silver ion release from the CUR-AgNP was analyzed by inductively coupled plasma optical emission spectroscopy (ICP-OES) [Perkin Elmer optima 5300 DV, Singapore). CUR-AgNP was incubated in 10 mL of deionized water for 24 hours for

ICP-OES analysis. The supernatant from centrifuged samples was collected for analysis. The samples were acidified with nitric acid and the concentration of the analyte element was calculated using a calibration plot obtained by analyzing standard solutions. Win Lab 32 software was used to record and process the results.

3.2.1.2.7. X-ray photoelectron spectroscopy (XPS) analysis

X-ray photoelectron spectroscopy (XPS) analysis of CUR-AgNP was performed using PHI5000 VersaProbe II (ULVAC-PHI Inc., USA) instrument with a micro-focused (200 μm,15 KV) monochromatic Al-Kα X-Ray source (hν=1486.6 eV).

3.2.1.3. Estimation of the curcumin content in CUR-AgNP

The individual curcuminoid components of the biocurcumin®/BCM-95® were identified and quantified by high-performance liquid chromatography (HPLC). For HPLC analysis LC-2010A, HT (Shimadzu, Japan) model machine was used. The analysis was done using 40% tetrahydrofuran (THF), 60% water, and 1% citric acid (pH 3) as mobile phase at a flow rate of 0.7 mL/min with an isocratic pump at 30 °C using a C18 column. The curcuminoids were analyzed at a single wavelength of 420 nm with a 20 μL injection volume. LC-solution software was used to acquire and process the data. The calibration curve of individual curcuminoids was drawn by plotting the peak area against different concentrations of BCM-95® in ethanol (66.9, 33.45, 16.72, 8.36, 4.18, and 2.09 μg/mL) with R^2=0.999. The bound curcuminoids in the CUR-AgNP were estimated from their peak area.

3.2.1.4. In vitro degradation studies of curcumin

The *in vitro* degradation studies of curcumin and the curcumin bound on the CUR-AgNP in phosphate buffer (pH 7.4) were analyzed at different time intervals by UV-Vis absorption spectroscopy. The ratio of peak heights corresponding to the absorption maxima at 420 nm and 260 nm (A_{420}/A_{260}) was calculated for this purpose. Comparing the peak height ratio A_{420}/A_{260} of different time intervals with that of the 0^{th} time was calculated as the extent of degradation (%) by using equation (Eqn.) 1.

$$Degradation\ (\%) = 100 - (R_t/R_0 \times 100) \qquad Eqn.\ 1$$

Where R_t is the ratio A_{420}/A_{260} at the time, 't', and R_0 is the ratio A_{420}/A_{260} at the time, 'zero'. HPLC analysis was further done to confirm the stability of the CUR-AgNP in phosphate buffer. By comparing the peak area at a particular time with that of the peak area at the time 'zero' the degradation (%) was calculated using Eqn. 2.

$$Extend\ of\ degradation\ (\%) = 100 - (A_t/A_0 \times 100) \qquad Eqn.\ 2$$

Where A_t is the peak area at the time 't' and A_0 is the peak area of a particular curcuminoid at the time 'zero'.

3.2.1.5. Cellular interaction of CURAgNP with colorectal cancer cells

3.2.1.5.1. Cellular uptake of CUR-AgNP by HCT-116 and Caco-2 cells

The cellular uptake of the CUR-AgNP was studied by a confocal laser scanning microscope (CLSM) [Olympus FV3000]. HCT-116 and Caco-2 cells were grown on coverslips in a 6-well plate at a density of $3x10^5$ cells/well and incubated at 37 °C for 24 hours. The cells were then exposed to 50 μg/mL of CUR-AgNP for different time

intervals (0.5, 1, 2, and 4 hours). After incubation, the cells were rinsed three times with PBS. The cell nucleus was stained with 4,6-diamidino-2-phenylindole (DAPI, 1:10,000) for 5 minutes. The cells were washed with PBS and the coverslips were removed from the PBS and the excess buffer was blotted and air-dried. The coverslips (cell side down) were mounted on clean microscope slides using DPX (Dibutylphthalate Polystyrene Xylene) mountant and the fluorescent images were acquired using a 60X oil objective. The cellular uptake of the CUR-AgNP was evaluated quantitatively by drawing the region of interest (ROI) around the cells. To get the fluorescence intensity, cellSens software was used to draw 3 ROI (one ROI/cell) from a 60X image with a 3.0X zoom.

3.2.1.5.2. Cellular uptake studies of CUR-AgNP by Confocal Raman Mapping

The cellular uptake of the CUR-AgNP in HCT-116 cells was also investigated by Confocal Raman Mapping. For this, the cells were seeded on Calcium Fluoride slides. The CUR-AgNP treated cells at two different time points (2 and 4 h) were monitored using a 50x Nikon (Numerical Aperture (NA) = 1.0) objective under the microscope. A white light image was recorded when the cells were illuminated from the bottom and focused. Stokes shifted Raman spectra in the range of 400-4000 cm^{-1} with 1 cm^{-1} resolution were collected after the samples were excited with the 532 nm excitation wavelength laser. Before each measurement, a silicon standard (Raman peak centered at 520 cm^{-1}) was used for calibration. The distribution of the CUR-AgNP on the HCT-116 cells was obtained from Hyper Spectral mapping. In the spectral imaging mode, a complete 2D array of Raman spectra of the cells and buffer was recorded (Integration time of 0.5s) at each imaging point (depth scan, 80 x 80

points for 40 x 40 μm^2). After the background subtraction and cosmic ray removal, spectral de-mixing was carried out using the Witec Project Plus software. Two distinct spectral groups for cells (cluster 1) and buffer (cluster 2) were extracted using the cluster analysis function. The third cluster group corresponding to the fluorescence pixels from the CUR-AgNP was also extracted. The distribution of the two Raman spectral groups and the fluorescence group over the examined cell was color-coded which distinctly showed the uptake of the CUR-AgNP by the cells.

3.2.1.5.3. Cytotoxicity of curcumin and CUR-AgNP toward colon cancer cells

The cytotoxicity of the curcumin and CUR-AgNP against HCT-116 and Caco-2 cells was determined by MTT assay. In a 96-well plate, HCT-116 and Caco-2 cells were seeded at a density of 1.0 x 10^4 cells/well. The cells were grown in Dulbecco's Modified Eagle medium (DMEM) supplemented with 10% fetal bovine serum (FBS) for HCT-116 cells and 20% FBS for Caco-2 cells and incubated at 37 °C in 5% CO_2 and 95% humidity. After two days of culture, the cells were exposed to a series of concentrations of CUR-AgNP suspension (10, 25, 50, 100, 200, 300, and 400 μg/mL) and curcumin dissolved in DMSO (10, 15, 20, 40 and 50 μg/mL) and then incubated at 37 °C for 24 hours. The test material was removed after incubation and the cells were treated with 10 μL of MTT solution (5 mg/mL) in each well and incubated for 4 hours at 37 °C. After incubation, the culture media in each well was replaced with 200 μL DMSO to dissolve the formed insoluble formazan crystals. At 570 nm, the absorbance (Abs) of each well was measured using an automated plate reader (Tecan, Infinite F50). The cell cytotoxicity exhibited by the CUR-AgNP was calculated using Eqn. 3:

$$Cell\ cytotoxicity\ (\%) = 100 - ([Abs]sample/[Abs]\ control) \times 100 \quad Eqn.\ 3$$

3.2.2. System II: Lauric acid solid lipid nanoparticles

Solid lipid nanoparticles (SLN) have gained more interest owing to their non-toxicity, biocompatibility, and biodegradability. Lauric acid (LA), a medium-chain saturated fatty acid that tends to get absorbed easily in the intestine was selected for the synthesis of solid lipid nanoparticles (LA-SLN). A fluorescent lipophilic dye rhodamine B (RhB) was incorporated into LA-SLN as a model drug. The interaction of RhB-loaded LA-SLN and free RhB dye with cells was studied to evaluate the capability of LA-SLN for intracellular drug delivery.

3.2.2.1. Preparation of lauric acid solid lipid nanoparticles

The hot homogenization method was adopted for the synthesis of solid lipid nanoparticles of lauric acid (LA-SLN) and rhodamine B dye-loaded LA-SLN, abbreviated as R-LA-SLN (Adib et al., 2016). This was done at temperatures that were higher than the lipid's melting point. Lauric acid (1 g) was melted at 70 $^{\circ}$C and an oil phase surfactant span® 80 (300 μL) was added to the molten lipid (figure 3.2). This was taken as the oil phase. Poloxamer 407 (1.5 g) was added to 50 mL of deionized water and kept at 70 °C for the preparation of the aqueous phase. Rhodamine B (RhB) dye stock solution (2 mg/mL) was prepared in water and 500 μL of it was added dropwise into the oil phase under stirring at 30,000 rpm using an IKA® T10 basic ULTRA-TURRAX® homogenizer. To prepare the oil in water nanoemulsion, the aqueous phase was added to the oil phase under homogenization for 10 minutes at 70 °C. Rapid cooling of the hot nanoemulsion to room temperature using an ice bath leads to the formation of R-LA-SLN suspension. The same

procedure was adopted for the preparation of LA-SLN suspension without the addition of RhB dye. Using an Amicon stirred cell apparatus with a 100 KDa Biomax polyethersulfone membrane separated both R-LA-SLN and LA-SLN. The separated particles were frozen at -20 °C and then lyophilized (Labconco, USA) without the addition of any cryoprotectants. These lyophilized particles were used for further studies.

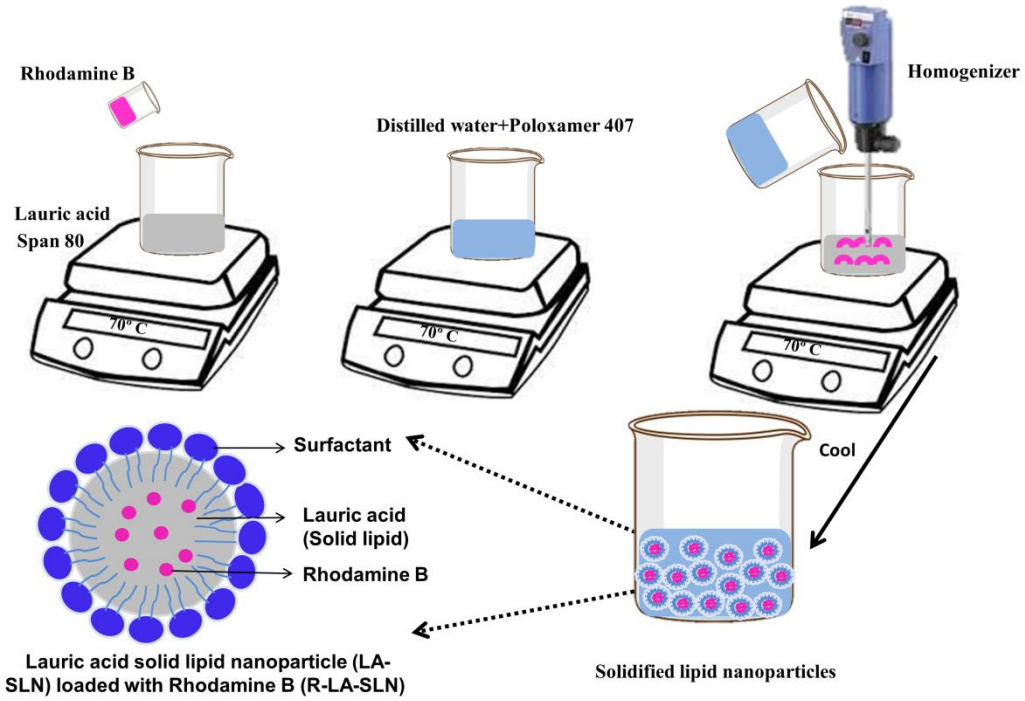

Figure 3.2. Schematic of the preparation of lauric acid solid lipid nanoparticles.

3.2.2.2. Physicochemical characterization

3.2.2.2.1. Determination of particle size and zeta potential

The hydrodynamic diameter (volume distribution) of the R-LA-SLN suspension, LA-SLN suspension, and redispersed lyophilized R-LA-SLN were measured by the dynamic light scattering technique (Nano ZS, Malvern Instruments, UK). The mean values of three measurements were reported. The measurement laser had a

wavelength of 633 nm and a scattering angle of 90°. The viscosity of the dispersant (water) and the refractive index of lauric acid were taken as 0.89 cP and 1.423, respectively (Petrochenko et al., 2018; Sandhya et al., 2016). The zeta potential of the R-LA-SLN and LA-SLN suspensions was measured by a zetasizer (NanoZS, Malvern Instruments, UK). The surface charge of the LA-SLN and R-LA SLN after suspending in phosphate buffer (pH 7.4) was also measured.

3.2.2.2.2. Transmission electron microscopy (TEM) analysis

The size and morphology of the R-LA-SLN were determined by TEM, Hitachi H-7650. The R-LA-SLN was dropped onto the carbon-coated copper grids, air-dried, and observed using TEM.

3.2.2.2.3. FTIR analysis

The absorption spectra of lauric acid, Poloxamer-407, LA-SLN, R-LA-SLN, and RhB were taken using a Fourier transform infrared spectrophotometer (Nicolet 5700, Thermofischer Scientific, USA). The FTIR spectra were recorded over a scan range of 500-3500 cm^{-1} using the KBr pellet method.

3.2.2.2.4. Confocal Raman Microscope analysis

The Raman spectra of LA-SLN, R-LA-SLN, and RhB were recorded over a scan range of 200-1800 cm^{-1} using the Confocal Raman microscope (Alpha 300RA, WITec GmbH, Germany).

3.2.2.2.5. Differential Scanning Calorimetry (DSC) analysis

The melting behavior of the Lauric acid, Poloxamer-407, LA-SLN, and R-LA-SLN was studied by Differential Scanning Calorimetry (DSC) (Q20, TA Instruments,

USA). The samples of about 3 mg weight were placed in aluminium pans and it was hermetically sealed for DSC measurements. The samples were scanned at a rate of 10 ºC/min from 0 ºC to 100 ºC and cooled to 0 ºC at the same rate. An empty aluminium pan that was hermetically sealed was taken as the reference. By integrating the area under the transition peak, the melting enthalpy (ΔH) was calculated.

3.2.2.3. Entrapment efficiency and drug loading

The freshly prepared R-LA-SLN formulation (50 mL) was added to the Amicon stirred cell apparatus fitted with a 100 kDa membrane filter. To separate SLN from the aqueous phase, pressure-driven filtration, and magnetic stirring were given. The concentration of the free untrapped dye in the aqueous medium containing poloxamer-407 was measured to determine the entrapment efficiency (EE %). The aqueous phase was collected and the concentration of the free RhB in the filtrate was determined using fluorescence spectroscopy (Tecan infinite M200 microplate reader, $\lambda_{excitation}$ = 450 nm and $\lambda_{emission}$ = 580 nm). The unentrapped RhB was calculated from the standard curve plotted using different concentrations of RhB (linear in the range of 3.75-0.05 μg/mL with R^2 = 0.9989). The amount of RhB entrapped in the lipid is estimated as the drug loading. For this, the lyophilized R-LA-SLN loaded with different concentrations of RhB dye (1 mg, 5mg, and 10 mg) were taken and the RhB content was calculated using a calibration curve (linear in the range of 3.75-0.0018 μg/mL with R^2 = 0.9943).

The entrapment efficiency (EE) % and drug loading expressed in ($\mu g/mg$) were calculated using equations 4 and 5:

$$EE\% = \frac{Weight\ of\ the\ dye\ entrapped\ in\ SLN}{Initial\ weight\ of\ dye\ used} \times 100 \qquad Eqn.\ 4$$

$$Drug\ loading\ (\mu g/mg) = \frac{Weight\ of\ the\ dye\ entrapped\ in\ SLN\ (\mu g)}{Weight\ of\ the\ SLN\ (mg)} \qquad Eqn.\ 5$$

3.2.2.4. In vitro release of RhB from R-LA-SLN

The release of RhB from R-LA-SLN was estimated by diffusion dialysis technique. Lyophilized R-LA-SLN (20 mg) was dispersed into 2 mL of phosphate buffer saline (PBS, pH 7.4) and taken in a dialysis bag (molecular weight cutoff -14000 Da). The dialysis bag was sealed and placed into 10 mL PBS under continuous stirring at 37 °C. At different time intervals, 200 µL of the sample was pipetted out to estimate the amount of dye released. The same volume of the fresh buffer was replaced each time after sampling to keep the total volume constant. Fluorescence spectroscopy (Tecan infinite M200 microplate reader, $\lambda_{excitation}$= 450 nm and $\lambda_{emission}$= 580 nm) was used to measure the amount of released RhB. Blank LA-SLN was used as the control. Using DD solver, a Microsoft Excel add-in software program, the release data were fitted to various mathematical models, including zero order, first order, the Higuchi model, and the Korsmeyer-Peppas model, to examine the drug release kinetics.

3.2.2.5. Cellular interaction of LA-SLN with colorectal cancer cells

3.2.2.5.1. Cell viability studies with LA-SLN in colon cancer cells

MTT assay was used to determine the cytocompatibility of LA-SLN against HCT-116 and Caco-2 cells. The cells were exposed to a series of concentrations of LA-SLN (20, 40, 60, 80, 100, 200, 400, 600, and 800 µg/mL). The experiment was

carried out as detailed in the previous section 3.2.1.5.3. The cell viability was calculated using Eqn. 6:

$$Cell\ viability\ (\%) = ([Abs]sample/[Abs]\ control) \times 100 \qquad Eqn.\ 6$$

LIVE/DEAD assay was performed in both HCT-116 and Caco-2 cells after exposure to different concentrations of LA-SLN (20, 100, and 400 μg/mL) for 24 hours. An inverted fluorescence microscope (Olympus 1X70 DP73, Tokyo, Japan) was used to capture the fluorescence images.

3.2.2.5.2. Cellular uptake of R-LA-SLN and RhB dye by HCT-116 and Caco-2 cells

Confocal laser scanning microscopy (CLSM) was used to study the cellular uptake of R-LA-SLN and RhB dye in HCT-116 and Caco-2 cells. The cells were grown as detailed in section 3.2.1.5.1. The cells were then exposed to 100 μg/mL of fluorescent R-LA-SLN for different time intervals (0.5, 1, 2, and 4 hours). The same amount of RhB loaded in the LA-SLN was used for the cell uptake studies of RhB. After the incubation, the cells were rinsed with PBS and the cell nuclei were stained with DAPI and observed using CLSM. The cellular uptake was quantitatively evaluated by drawing ROI (as detailed in section 3.2.1.5.1.).

3.2.2.5.3. Cellular uptake studies of R-LA-SLN by Confocal Raman Mapping

The HCT-116 cells were treated with R-LA-SLN at two different time points (0.5 and 4 h) and investigated using a 50x Nikon (NA = 1.0) under the Confocal Raman Microscope. The protocol is similar to that detailed in section 3.2.1.5.2. The distribution of the chemical species on the HCT-116 cells was obtained from Hyper Spectral mapping. Here three different spectral groups for cells (cluster 1), RhB

(cluster 2), and the buffer (cluster 3) were separated using the cluster analysis function. The distribution of these three Raman spectra over the examined cells was color-coded and which indicates the uptake of RhB by the cells.

3.2.2.5.4. Effect of LA-SLN on Caco-2 cell TEER

Transepithelial electrical resistance (TEER) studies were carried out in Caco-2 cell monolayers based on a previously reported protocol (Rekha and Sharma, 2011). To study the effect of LA-SLN on the TEER of Caco-2 cell monolayer, cells were seeded on a polycarbonate insert membrane (Millipore) of pore size 0.4 μm at a density of 2.5 x 10^5 cells per well (figure 3.3.). Using a voltmeter with a chopstick electrode (Millicell ERS system), the integrity of the Caco-2 cell monolayer was evaluated for 21 days until a constant TEER was attained. After equilibration of the Caco-2 cell monolayer with Hank's Balanced Salt Solution (HBSS), the HBSS in the apical chamber was removed and replaced with fresh HBSS containing LA-SLN (400 μg/mL). The TEER of the cell monolayer was monitored at different time intervals at 37 ºC. The reduction in TEER was determined by calculating the change in TEER from the initial value using Eqn. 7:

$$TEER\ (\%) = \left[\frac{R_t - R_b}{R_0 - R_b}\right] \times 100 \qquad \textit{Eqn. 7}$$

Where R_t is the resistance at time t, R_0 is the initial resistance value, and R_b is the resistance when the cell monolayer is absent.

After the removal of the LA-SLN and replacing it with fresh media the TEER recovery was monitored at regular intervals for up to 24 hours.

3.2.2.5.5. RhB transport studies across Caco2 cell monolayer

For transport studies, the cells were grown and prepared as described in section 3.2.2.5.4. The experimental setup is shown in figure 3.3. After equilibration with HBSS for at least 2 hours, the apical chamber medium was replaced with fresh HBSS containing R-LA-SLN and RhB dye. Cells were incubated with R-LA-SLN at a concentration of 400 µg/mL and the same concentration of the RhB loaded in R-LA-SLN. At different time intervals, 100 µL aliquots were withdrawn from the basolateral chamber and the concentration of the sample was analyzed by a fluorescence Tecan infinite M200 microplate reader. The apparent permeability coefficient of the RhB was calculated using the Eqn. 8:

$$P_{app} = \frac{dQ/dt}{C_0 \times A} \qquad \textit{Eqn. 8}$$

Where dQ/dt is the permeability rate, A is the surface area of the membrane filter and C_0 is the initial concentration of the RhB in the apical chamber.

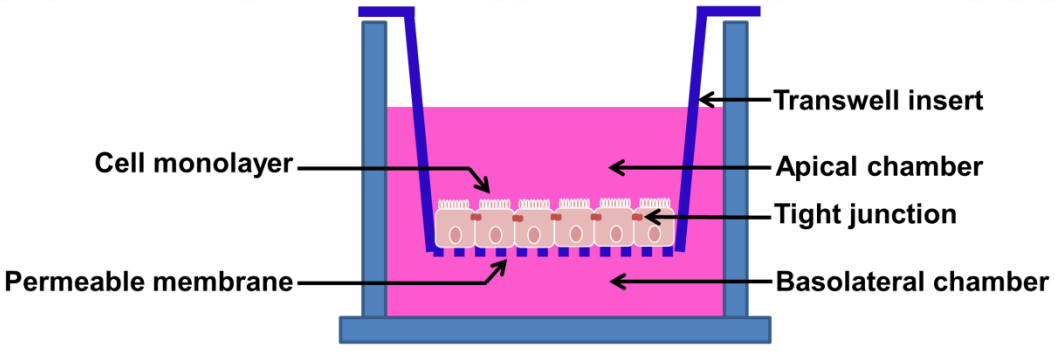

Figure 3.3. Schematic illustration of Caco-2 cell monolayer on a transwell plate.

3.2.2.5.6. Actin filament staining by rhodamine-phalloidin

The influence of LA-SLN on actin filaments of the Caco-2 cell monolayers was studied using a CLSM. For this experiment, Caco-2 cells were seeded on a coverslip

in a four-well plate at a density of 2.5 x 10^5 cells per well. The cells were used for transport experiments after 6 days of post-seeding. After the removal of the growth medium, the cell monolayer was equilibrated with HBSS for 2 hours before the transport experiment. Cells were incubated with LA-SLN at a concentration of 400 µg/mL for 1 hour. The LA-SLN was removed by washing the cells three times with PBS and then fixed with 250 µL of 4% formaldehyde in PBS for 20 minutes at room temperature. After fixing the cells were washed with PBS and then permeabilized using 250 µL of 0.2 % Triton X-100 [prepared in 1% Bovine Serum Albumin (BSA) in PBS] for 20 minutes. The permeabilized cells were washed thrice with PBS and incubated with 250 µL of 1% BSA for 30 minutes. The blocking solution was removed and the cells were incubated with 200 µL rhodamine phalloidin (5:200 in 1% BSA) for 20 minutes at room temperature. The cells were washed and treated with 1% BSA as before. The cell nucleus was stained with 200 µL DAPI (1:10,000) for 5 minutes. The cells were washed with PBS and the coverslips were removed from the PBS and the excess buffer was blotted and air-dried. The coverslips (cell side down) were mounted on clean microscope slides using DPX mountant. Images were obtained at 60X magnification using an Olympus FV300 confocal laser scanning microscope.

3.2.2.5.7. ZO-1 Tight junction staining

The influence of the LA-SLN on the tight junction of the Caco-2 monolayer was studied by CLSM. The Caco-2 cells were permeabilized and blocked with 1% BSA as mentioned in section 3.2.2.5.6. The blocking solution was removed and cells were incubated with 200 µL anti-ZO-1 antibody (1:60 in 1% BSA) overnight at 4 ºC. After

removing the primary antibody the cells were washed and treated again with 1% BSA for 30 minutes. The blocking solution was removed and the cells were incubated with 250 µL Texas Red labeled secondary antibody (1:200 in 1% BSA) for 1 hour at room temperature. The cells were washed and the nucleus was stained with 200 µL DAPI (1:10,000) for 5 minutes. The cells were then washed with PBS, air-dried, and mounted. Images were taken using CLSM.

3.2.2.6. Mucoadhesion studies by texture analyzer

Using a texture analyzer (TA.XT.plus, Stable Micro Systems, UK) equipped with a 50 kg load cell, mucoadhesion studies of LA-SLN were carried out. The source of the intestinal tissue was euthanized rats from a study approved by the Institutional Animal Ethics Committee (IAEC) [Approval No. SCT/IAEC-337/NOV/2019/104]. The rat intestinal segments were freshly excised, cut open, and then fixed on a mucoadhesive rig (figure 3.4). Using a double-sided adhesive tape, LA-SLN adhered to the surface of the 10 mm cylindrical probe. This cylindrical probe was then lowered onto the surface of the colon mucosa. The probe was moved vertically upward at a constant speed of 0.1 mm/s after applying a contact force of 50 g for 60 seconds. Exponent v6 software was used to record test data. The maximum force required to separate the probe from the intestinal tissue was taken as the mucoadhesive force (g). The area under the force versus distance curve is the work of adhesion (g. mm.).

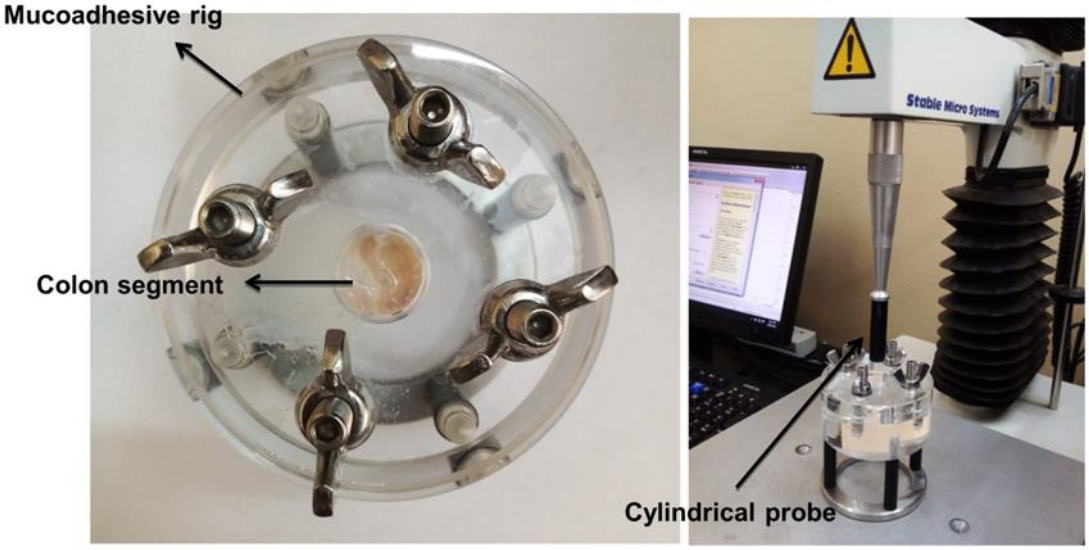

Figure 3.4. Experimental set-up used for the mucoadhesion studies of rat colon segment. The colon segment was cut open and placed on a mucoadhesive rig of the texture analyzer.

3.2.2.7. SDS PAGE- protein corona studies using pancreatin

3.2.2.7.1. Sample preparation for protein corona

Protein corona formation was studied based on the previously reported procedure (Wan et al., 2015). Different concentrations of LA-SLN (0.1, 0.25, 0.5, 1, 2.5, and 5 mg/mL) were incubated with 100 mg/mL pancreatin for 1 hour at 37 °C with continuous agitation. After incubation, the LA-SLN-protein complex was pelleted from excess protein by centrifugation at 14000g, 4 °C for 20 min. After discarding the supernatant, the pellet was resuspended in 500 µL PBS and centrifuged again to get the nanoparticle-protein complex. This washing procedure removes unbound and loosely bound (soft corona) proteins from LA-SLN. The washing step was repeated three times to obtain the hard corona-LA-SLN particles.

3.2.2.7.2. Identification of protein corona by SDS PAGE

To the protein-corona, SDS PAGE sample buffer and mercapto ethanol (reducing agent) were added and heated at 70°C for 10 min. The samples were then centrifuged at 14000g, 4°C for 20 min. The supernatant was then loaded into SDS PAGE 12% separating gel and run at a voltage of 200V. The SDS reagents and gel were prepared as given in Appendix A.1. The gel was stained with Coomassie Brilliant blue (Appendix A.2) and the images were taken using a luminescent image analyzer (Fujifilm LAS-4000, Tokyo).

3.2.3. System III: Chitosan and functionalized chitosan particles

Chitosan is a promising drug delivery carrier for therapeutics and diagnostics owing to its biocompatibility, biodegradability, low toxicity, and structural variability. The hydrophilicity of chitosan is due to the presence of –OH and $–NH_2$ groups. Chitosan polymers can be easily functionalized due to their reactive amino groups present in the polymer chain. To prepare different charge-based chitosan particles, chitosan polymers were functionalized with the amino acid lysine and maleic anhydride.

3.2.3.1. Determination of molecular weight of chitosan

The average molecular weight of the chitosan was determined by an Ubbelohde viscometer at a constant temperature of 24 ºC. A stock solution of chitosan was prepared in a mixture of solvent 0.1 M acetic acid/0.2 M NaCl (1/1, V/V). Briefly, 300 mg chitosan was dissolved in 30 mL of 0.1 M acetic acid and kept under stirring for 7 hours, then 30 mL of 0.2 M NaCl was added and continuously stirred overnight to dissolve chitosan completely. From the stock solution, five different concentrations of chitosan (0.05, 0.1, 0.15, 0.2, 0.25 g/dL) were prepared by diluting

it with the same solvent. The flow time through the capillary was measured for each concentration, including the solvent mixture as a reference. For each chitosan concentration, the following viscosities were calculated using the equations given below:

$$Relative\ viscosity, \eta_{rel} = \frac{t_i}{t_0} \qquad Eqn.\ 9$$

$$Specific\ viscosity, \eta_{sp} = \eta_{rel} - 1 \qquad Eqn.\ 10$$

$$Reduced\ viscosity, \eta_{red} = \frac{\eta_{sp}}{concentration} \qquad Eqn.\ 11$$

$$Inherent\ viscosoity, \eta_{inh} = \frac{ln\ \eta_{re1}}{concentration} \qquad Eqn.\ 12$$

The inherent viscosity and reduced viscosity were plotted against the chitosan concentration. By extrapolating the graph of reduced viscosity and inherent viscosity to zero concentration, it is possible to determine the intrinsic viscosity value. Mark–Houwink–Sakurada equation represents the intrinsic viscosity [η] as a function of the average molecular weight (M).

$$\eta = KM^{\propto} \qquad Eqn.\ 13$$

Where molecular weight is expressed in kDa, K, and α - the constants for the solvent system used (0.2 M NaCl and 0.1 M acetic acid = 1:1) - are 1.8×10^{-5} and 0.93, respectively (Suciati et al., 2018).

3.2.3.2. Degree of deacetylation of chitosan

The degree of deacetylation (DD) determines the free amino group content in the structure of chitosan. DD of chitosan was determined by UV spectrophotometry using the dual standard method (Liu et al., 2006). N-acetyl D-glucosamine and glucosamine hydrochloride were used as standards to represent N-acetyl D-glucosamine and glucosamine residues in chitosan. The standards and samples were dissolved in 0.1 M HCl. Standard solutions with varying concentrations of N-acetyl D glucosamine and glucosamine hydrochloride were prepared and their UV absorbance (λ_{max}= 201 nm) was measured (Table 3.2). The UV absorbance (A) of the chitosan solution is expressed as:

$$A = \varepsilon_a . c_a + \varepsilon_g \cdot c_g \qquad \textit{Eqn. 14}$$

Where ε_a and ε_g are the absorptivities of N-acetylglucosamine and glucosamine, c_a and c_g are the concentrations of N-acetylglucosamine and glucosamine in mmol/L.

The degree of acetylation (DA) of the admixture solution is the concentration of N-acetylglucosamine (c_a) divided by the total concentration of N-acetylglucosamine and glucosamine hydrochloride (c_g).

$$DA = \frac{c_a}{c_a + c_g} \qquad \textit{Eqn. 15}$$

c_t is the total concentration of N- acetyl glucosamine and glucosamine

$$\boldsymbol{c_t = c_a + c_g} \qquad \textit{Eqn. 16}$$

The relationship between A/c_t and DA is linear as indicated by the plot of A/c_t versus DA in figure 3.5. The equation obtained by linear regression is $A/c_t = 4.5DA + 0.0252$, $R^2 = 0.9854$.

Table 3.2. The absorption and A/c_t of the standard solutions

No.	c_a (mM)	c_g (mM)	c_t (mM)	DA	A	A/c_t
1	0.24	0.144	0.384	0.625	1.0119	2.635156
2	0.24	0.36	0.6	0.4	1.0255	1.709167
3	0.24	1.2	1.44	0.166667	1.054833	0.732523
4	0.18	0.168	0.348	0.517241	0.8496	2.441379
5	0.18	0.408	0.588	0.306122	0.839833	1.428288
6	0.18	1.68	1.86	0.096774	0.8599	0.462312
7	0.12	0.12	0.24	0.5	0.5906	2.460833
8	0.12	0.312	0.432	0.277778	0.6126	1.418056
9	0.12	1.68	1.8	0.066667	0.580567	0.322537
10	0.06	0.072	0.132	0.454545	0.2773	2.100758
11	0.06	0.216	0.276	0.217391	0.2521	0.913406
12	0.06	6	6.06	0.009901	0.3001	0.049521

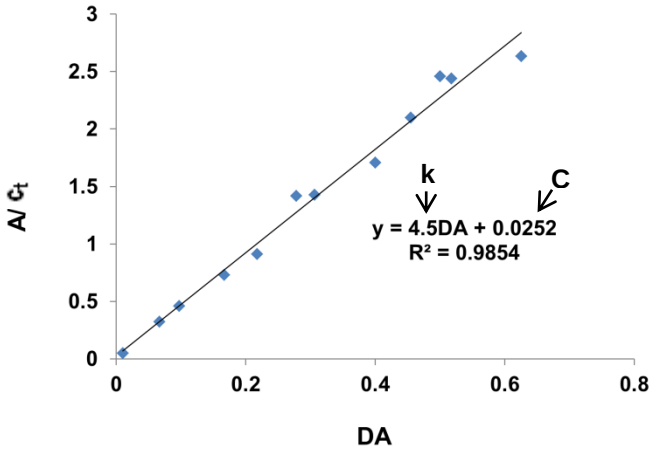

Figure 3.5. A/c_t versus DA of standards admixture solution.

The absorbance of chitosan was read at 201 nm and the DA was calculated using the Eqn. 17:

$$DA = \frac{161.1 \times A \times V - C \times m}{k \times m - 42.1 \times A \times V} \qquad \textit{Eqn. 17}$$

Where m is the weight of samples in milligrams, A is the absorbance of the sample at 201 nm, V is the volume of solution in liters, 161.1 is the molecular weight of glucosamine residue, and the values of k and C are obtained from the above graph.

The degree of deacetylation (DD) was calculated from the obtained degree of acetylation using the Eqn. 18:

$$DD = 1 - DA \times 100 \qquad \textit{Eqn. 18}$$

3.2.3.3. Synthesis of lysine chitosan (LCS) conjugate

LCS conjugate was synthesized using EDC chemistry. In 0.1M HCl, a 1% (w/v) chitosan solution was prepared, and the pH was raised to 4.5 using 2 M NaOH under vigorous stirring. L-Lysine monohydrochloride was added at a concentration of 0.75% (w/v) to the chitosan solution under stirring. About 500 mg EDC was dissolved in 5 mL distilled water and added dropwise to the chitosan solution (figure 3.6). The reaction was carried out for 12 hours, and the resulting solution was dialyzed four times against distilled water before being stored at 4 – 8 ºC.

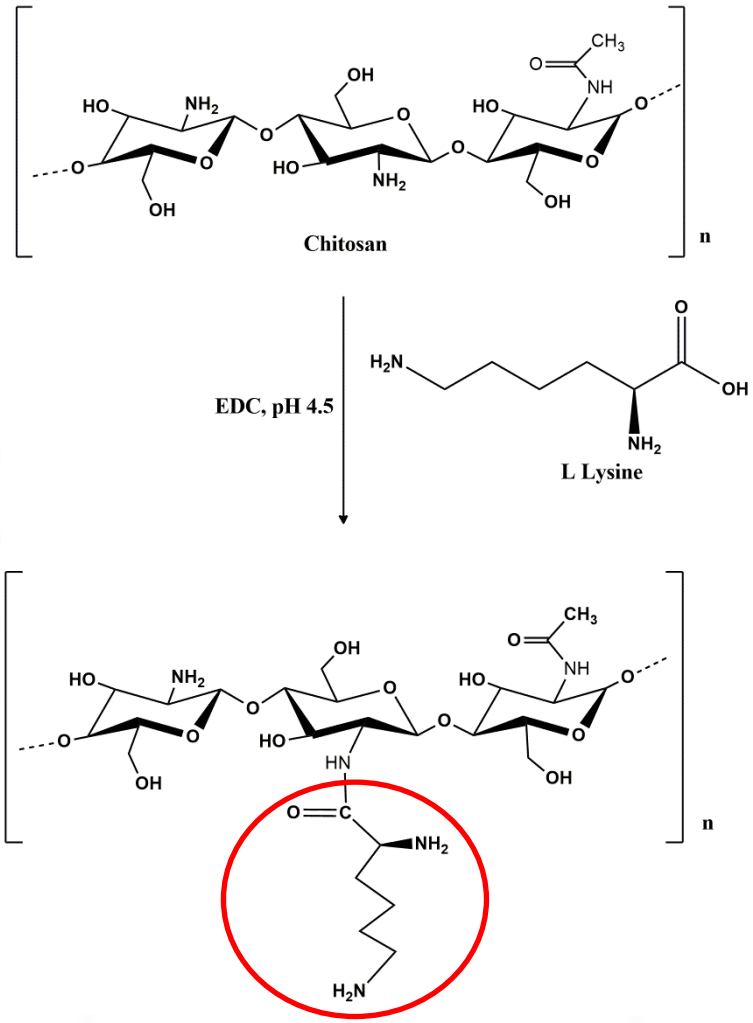

Figure 3.6. Scheme of the synthesis of LCS conjugate.

3.2.3.4. Synthesis of N-maleoyl chitosan (MCS) conjugate

For the synthesis of MCS conjugate, initially, chitosan solution (1%) was prepared in 2% (w/w) acetic acid. About 40 mL of this solution was taken and diluted with 150 mL methanol and stirred well. A known amount of maleic anhydride (800 mg) was dissolved in 8 mL acetone and added dropwise to the chitosan solution under stirring. After the addition of maleic anhydride, an immediate formation of gel was observed (figure 3.7). The reaction mixture was kept overnight at room temperature after which acetone was added to precipitate the gel and separated through a nylon

membrane. The precipitate was dissolved in water and the resultant solution was dialyzed four times against distilled water and stored at 4 - 8 ºC.

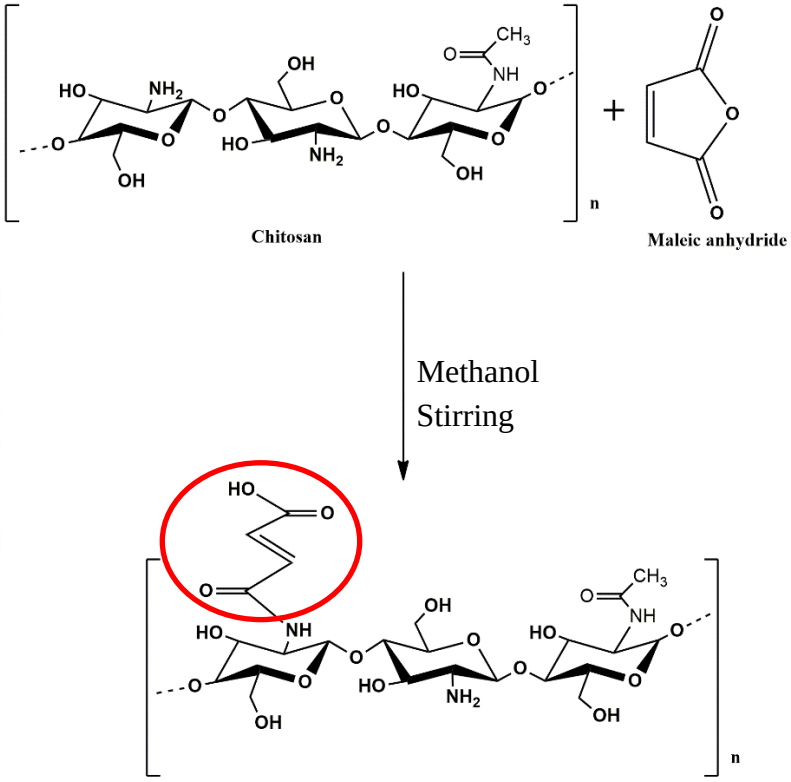

Figure 3.7. Scheme of the synthesis of MCS conjugate.

3.2.3.5. Characterization of the chitosan conjugates

3.2.3.5.1. Nuclear Magnetic Resonance (NMR) spectroscopy

^{1}H NMR spectra were recorded to verify the successful functionalization of chitosan. For NMR analysis, 1% chitosan solution was prepared in 0.1 M HCl and the solution was freeze-dried to ensure the solubility of chitosan in Deuterium oxide (D_2O). The ^{1}H NMR spectra of chitosan and chitosan conjugates (LCS and MCS) were recorded using a Bruker Avance 400 MHz FT-NMR Spectrometer. To acquire ^{1}H NMR analysis, chitosan and chitosan conjugates were dissolved in D_2O.

3.2.3.5.2. Fourier transform infrared (FTIR) spectroscopy

The FTIR spectra of native chitosan and chitosan conjugates (LCS and MCS) were recorded over an ATR (Attenuated Total Reflection) at a scan range of 500 - 4000 cm^{-1} using a Nicolet 5700 (Thermo Fischer Scientific, USA).

3.2.3.5.3. Determination of zeta potential of native chitosan and chitosan conjugates

To evaluate the change in surface charge of chitosan after modification, the zeta potential of the native chitosan and chitosan conjugates (LCS and MCS) were carried out at pH 6 using Malvern Zetasizer Nano ZS (Malvern Instruments, UK) at a temperature of 25 ºC.

3.2.3.5.4. Variation in amino content of native chitosan and chitosan conjugates

The amino content of chitosan conjugates was determined by the degree of deacetylation. The chitosan conjugates were dissolved in 0.1 M HCl and their absorbance was read at 201 nm and the degree of deacetylation was calculated from the equation as described in section 3.2.3.2. The free amino groups of native chitosan were compared with that of the chitosan conjugates to determine the variation in the amino group after modification.

3.2.3.5.5. Trinitrobenzenesulfonic acid assay

2,4,6-Trinitrobenzenesulfonic acid solution (TNBS) is a rapid and sensitive assay reagent for the determination of free amino groups. The degree of substitution or extent of derivatization was determined by TNBS assay. The change in amino groups of native chitosan after derivatization (LCS and MCS conjugates) was estimated. Samples were prepared at a concentration of 1mg/mL in water at pH 6. Briefly, 500 µL samples were incubated with 500 µL of 4 % (w/v) $NaHCO_3$ and 0.1 % (v/v)

TNBS reagent at 37 ºC for 1 hour. Then the reaction was stopped by adding 500 μL of 0.2 M HCl and recorded absorbance at 410 nm using a Cary® 50 UV-Vis spectrophotometer (Varian Inc., USA). Glucosamine was used as the standard. The amino group content of chitosan and chitosan conjugates (LCS and MCS) was calculated from the standard curve plotted using different concentrations of glucosamine (25, 50, 75, 100, 125, 150, 175, 200 μg/mL) with an R^2 value 0.995.

3.2.3.5.6. Thermogravimetric (TGA) analysis

Thermogravimetric analysis was performed using SDT Q 600 (TA Instruments, USA) to determine the mass loss of chitosan and chitosan conjugates (LCS and MCS). All the samples were heated from room temperature to 1000 ºC under a nitrogen atmosphere at a heating rate of 10 ºC/min. The data was collected as weight loss (%) on heating against temperature.

3.2.3.5.7. X-ray diffraction (XRD) analysis

The X-ray diffraction analysis was carried out to determine the crystallinity of native chitosan and chitosan conjugates (LCS and MCS). X-ray diffraction patterns were recorded over a 2-theta range from 10 to 80° using a Bruker D8 ADVANCE (Germany) diffractometer. The X-ray source used was Cu-Kα radiation with a wavelength of 1.54 Å.

3.2.3.6. Preparation of different charge-based chitosan particles

The different charge-based chitosan particles were prepared by the ionic gelation method using tripolyphosphate (TPP) as the crosslinker (figure 3.8). Particles were synthesized from native chitosan and chitosan conjugates (LCS and MCS).

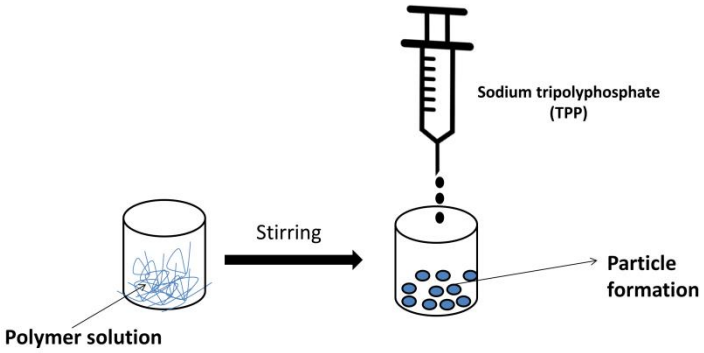

Figure 3.8. Schematics of chitosan and modified chitosan particle preparation.

3.2.3.6.1. Chitosan microparticles

For preparing chitosan microparticles, about 0.2% chitosan solution was prepared in 2% acetic acid and its pH was adjusted to 4.5 using 1M NaOH. TPP (6 mg/mL) was prepared and its pH was adjusted to 2 using 1 M HCl. From the above chitosan solution, 10 mL was taken and 30 mL water was added under stirring. About 10 mL TPP was then added dropwise over a period of 30 minutes under stirring at 1000 rpm to get crosslinked particles.

3.2.3.6.2. LCS microparticles

In order to prepare crosslinked LCS particles, 90 mL water was added to 10 mL LCS conjugate solution, and 15 mL TPP (6 mg/mL, pH 2) was added dropwise over a period of 30 minutes under stirring at 1000 rpm.

3.2.3.6.3. MCS microparticles

To prepare MCS particles, to 10 mL MCS conjugate solution 70 mL water was added, and under stirring (at 1000 rpm) 8 mL TPP (6 mg/mL, pH 2) was added dropwise over a period of 30 minutes.

The chitosan, LCS, and MCS particles formed were collected by centrifugation at 8000 rpm for 20 minutes. The particle pellet was washed by resuspending in distilled water to remove unreacted TPP and centrifuged again. This process was repeated thrice and the particles were resuspended in water and used for zeta potential analysis. The washed particles were then frozen at -20 ºC and then lyophilized (Labconco, Freezone 6plus, USA) and used for physicochemical characterization and all other studies.

3.2.3.7. Physicochemical characterization of particles

3.2.3.7.1. Zeta potential

The surface charge of the chitosan, LCS, and MCS microparticles in water and phosphate buffer saline (pH 7.4) was analyzed using Malvern Zetasizer Nano ZS (Malvern Instruments, UK).

3.2.3.7.2. FTIR spectra

The chitosan, LCS, and MCS microparticle formation were confirmed by the FTIR analysis. The FTIR spectra were recorded over an ATR scan range of 500-4000 cm^{-1} using a Nicolet 5700 spectrophotometer (Thermo Fischer Scientific, USA).

3.2.3.7.3. Scanning Electron Microscope (SEM) analysis

The morphology and appearance of the chitosan, LCS, and MCS microparticles were examined using a scanning electron microscope. The particles were sputter-coated with gold (Hitachi E1010, Japan) and analyzed by SEM (Hitachi S2400, Japan).

3.2.3.8. Water uptake studies of microparticles

The water uptake studies of the microparticles were carried out separately in three different pH buffers (1.2, 6.8, and 7.4) for 4 hours. The buffers were prepared as per United States Pharmacopeia (USP). For water uptake studies, 25 mg microparticles were incubated in a 5 mL buffer of respective pH. At specific time intervals, the samples were centrifuged at 8000 rpm for 5 minutes and the buffer was removed. The weight of the swollen particles was noted at 0.5, 1, 2, 3, and 4 hours. The water uptake (%) of the microparticles was calculated using the Eqn. 19:

$$Water\ uptake\ (\%) = \left[\frac{W_s - W_d}{W_d}\right] \times 100 \qquad \textit{Eqn. 19}$$

Where W_s is the weight of the swollen particles and W_d is the weight of the dry particles.

3.2.3.9. Drug loading and release studies of microparticles

3.2.3.9.1. Drug loading and entrapment efficiency

The microparticles were loaded with the drug, 5-fluorouracil (5-FU), by a remote loading process. The drug 5-FU was dissolved in phosphate buffer saline, pH 7.4 (10 mg/mL). The microparticles were loaded with 5-FU by diffusion filling and the particles were dried at 2-4 ºC. To calculate drug loading and entrapment efficiency, 50 mg microparticles were suspended in 10 mL HCl-KCl buffer of pH 1.2 (USP) and incubated overnight in the refrigerator with occasional stirring. The particle suspension was centrifuged at 8000 rpm for 20 minutes and the amount of 5-FU in the supernatant was measured by UV-Vis spectrophotometer (Cary® 50, Varian Inc., USA) at 266 nm. The amount of 5-FU loaded in the particle was calculated from the

standard curve plotted using different concentrations of 5-FU (2, 4, 6, 8, 10, 12) with an R^2 value = 0.9998.

The entrapment efficiency (EE) % and drug loading were calculated using the Eqn. 20 and 21:

$$EE\ (\%) = \frac{Weight\ of\ the\ drug\ entrapped}{Initial\ weight\ of\ drug\ used} \times 100 \qquad \textit{Eqn. 20}$$

$$Drug\ loading\ (\mu g/mg) = \frac{Weight\ of\ the\ drug\ entrapped\ \ (\mu g)}{Weight\ of\ the\ microparticle\ (mg)} \qquad \textit{Eqn. 21}$$

3.2.3.9.2. Energy Dispersive X-Ray Analysis (EDAX)

EDAX analysis was carried out on a Carl Zeiss EVO 18 Research (Germany) and employed to examine the elemental composition of the 5-FU loaded microparticles.

3.2.3.9.3. Drug release from microparticles

The drug release studies of the 5-FU loaded microparticles were done at pH 1.2 (HCl-KCl buffer; USP), 6.8, and 7.4 (phosphate buffer; USP) by dialysis method. The particles (50 mg) in 2 mL respective buffer were taken in a dialysis bag (Molecular cut-off =14000 Da) and the dialysis system was suspended in 8 mL buffer. Aliquots of 200 µL samples were taken at different time intervals for 24 hours and the released 5-FU was determined by UV-Vis spectrophotometer (Cary® 50, Varian Inc., USA) at 266 nm. The same volume of the fresh buffer was replaced each time after sampling. The amount of 5-FU released at different time points was calculated from the standard curve of 5-FU. Using DD solver, a Microsoft Excel add-in software program, the release data were fitted to various mathematical models,

including zero order, first order, the Higuchi model, and the Korsmeyer-Peppas model, to examine the drug release kinetics.

3.2.3.9.4. Drug release from Eudragit®S-100 coated particles

Eudragit coating on the microparticles was achieved by solvent evaporation technique. Initially, the microparticles were prepared by the procedure described in section 3.2.3.6. Then the microparticles were loaded with 5-FU drug and dried as mentioned in section 3.2.3.9.1. The 5-FU loaded particles (50 mg) were coated with 400 µL Eudragit®S100 (5%) dissolved in acetone and air dried to remove the solvent. The drug release studies of the dried Eudragit®S100 coated particles (50 mg/10mL) were carried out in different pH buffers to simulate the pH change along the gastrointestinal (GI) tract. The *in vitro* drug release experiments were carried out at pH 1.2 (HCl-KCl buffer; USP) for 2 hours, after which this buffer was replaced with pH 6.8 (phosphate buffer; USP) for 3 hours and finally, the pH 6.8 buffer was replaced with pH 7.4 (phosphate buffer; USP) for the next 19 hours. At regular time intervals, aliquots of 200 µL were withdrawn and absorbance was measured using a UV-Vis spectrophotometer (Cary® 50, Varian Inc., USA) at 266 nm. The same volume of the fresh buffer was replaced each time after sampling. The amount of 5-FU released at different time points was calculated from the standard curve plotted.

3.2.3.10. Cellular interaction of microparticles with colorectal cancer cells

3.2.3.10.1. Cell viability studies with chitosan and its conjugates in colon cancer cells

MTT assay was used to determine the cytocompatibility of chitosan and its conjugates (LCS and MCS) against HCT-116 and Caco-2 cells. The cells were

exposed to a series of concentrations of polymers (62.5, 125, 187.5, 250 μg/mL) and incubated at 37 °C for 24 hours. The experiment was carried out as detailed in the section 3.2.1.5.3. The cell viability was calculated using the equation given in section 3.2.2.5.1.

3.2.3.10.2. Cell viability studies with chitosan and chitosan conjugate particles in colon cancer cells.

The cell viability studies of crosslinked chitosan, LCS, and MCS microparticles against HCT-116 and Caco-2 cells were determined by MTT assay. The cells were exposed to a series of microparticle concentrations (62.5, 125, 187.5, and 250 μg/mL). The experiment was carried out as detailed in section 3.2.1.5.3. The cell viability was calculated using the equation given in section 3.2.2.5.1.

3.2.3.10.3. Cytotoxicity of drug and drug-loaded particles towards colon cancer cells

The cytotoxicity of the drug and drug-loaded microparticles against HCT-116 and Caco-2 cells was determined by MTT assay. The cells were seeded on 24-well plates at a density of 2.5 x 10^5 cells/well and cultured for 24 hours. The cells were exposed to different concentrations of 5-FU and 5-FU loaded microparticles (10, 100, 200, 800, 1200 μM) for 24, 48, and 72 hours. The experiment was carried out and cell cytotoxicity exhibited by the 5-FU and 5-FU loaded microparticles was calculated as detailed in section 3.2.1.5.3.

3.2.3.10.4. Effect of chitosan and modified chitosan particles on Caco-2 cell TEER

Transepithelial electrical resistance (TEER) studies were carried out in Caco-2 cell monolayers. The effect of chitosan, LCS, and MCS microparticles (5 mg/mL) on the

TEER of the Caco-2 cell monolayer was studied, as previously described in section 3.2.2.5.4.

3.2.3.10.5. Drug transport studies across caco2 cell monolayer

For drug transport studies, the cells were grown and prepared as mentioned above. After equilibration with HBSS for at least 2 hours, the apical chamber medium was replaced with fresh HBSS containing 5-FU loaded microparticles. Cells were incubated with 5-FU loaded microparticles for 1 hour. At different time intervals, 100 µL aliquots were withdrawn from the basolateral chamber and the concentration of the sample was analyzed by Cary® 50 UV-Vis spectrophotometer (Varian Inc., USA). The apparent permeability coefficient of the 5-FU was calculated using the equation given in section 3.2.2.5.5.

3.2.3.10.6. Actin filament staining by rhodamine-phalloidin

CLSM was used to study the influence of microparticles on actin filaments of the Caco-2 cell monolayers. Cells were incubated with microparticles at a concentration of 5 mg/mL for 1 hour. The experiment was carried out as described in section 3.2.2.5.6. Images were obtained at 60X magnification using an Olympus FV300 CLSM.

3.2.3.10.7. ZO-1 Tight junction staining

The influence of the microparticles on the tight junction of the Caco-2 monolayer was studied by CLSM. The Caco-2 cells were permeabilized and blocked with 1% BSA as mentioned in 3.2.2.5.6. The blocking solution was removed and cells were incubated with 200 µL anti-ZO-1 antibody FITC (60:1000 in 1% BSA) overnight at 4

ºC. After removing the antibody, the cells were washed 3 times with PBS. The cell nucleus was stained with 200 µL DAPI (1:10,000) for 5 minutes. The cells were then washed with PBS, air-dried, and images were taken using CLSM at 60X magnification.

3.2.3.11. Mucin binding studies

For mucin binding studies, 25 mg microparticles were incubated in 1 mL of mucin solution [Mucin (5 mg/mL) dissolved in phosphate buffer saline (PBS, pH 7.4)] under stirring at 100 rpm at 37 ºC in a shaker incubator. After 2 hours of incubation, the dispersions were centrifuged at 6000 rpm for 15 minutes. About 100 µL supernatant was taken and the protein estimation was done by the Lowry method. The amount of mucin adsorbed by the microparticles was determined from the difference between its initial concentration and the concentration found in the supernatant after incubation and centrifugation. The calculations were made based on a standard curve plotted using different mucin concentrations (0.5, 1, 1.5, 2, and 2.5 mg/mL) with the R^2 value = 0.9983.

3.2.3.12. Mucoadhesion studies of microparticles

Mucoadhesion studies of native chitosan and functionalized chitosan particles were carried out in both the small intestinal region as well as the colon region of the rat intestine by two methods.

3.2.3.12.1. In vitro mucoadhesion studies

The experiment was carried out based on a previously reported procedure (Rekha and Sharma, 2011). Freshly excised intestinal tissue of approximately 5 cm in length was taken and flushed with normal saline to remove the free mucus and cut open

longitudinally. The tissue was then fixed on semicylindrical polypropylene support and washed with saline. A known quantity of the microparticle (25 mg) was spread on the intestinal tissue and kept in a humidity chamber for 5 minutes for microparticle mucosal interaction (figure 3.9). The tissue was placed at an angle of 45º and then washed with phosphate buffer saline, (pH 7.4) at a flow rate of 120 mL/hour for 60 minutes. The microparticles dislodged from tissue were collected, dried and weight was noted. The mucoadhesive capacity is calculated as the percentage of the dry particles retained by the mucosal tissue compared to the initial weight of the microparticles applied.

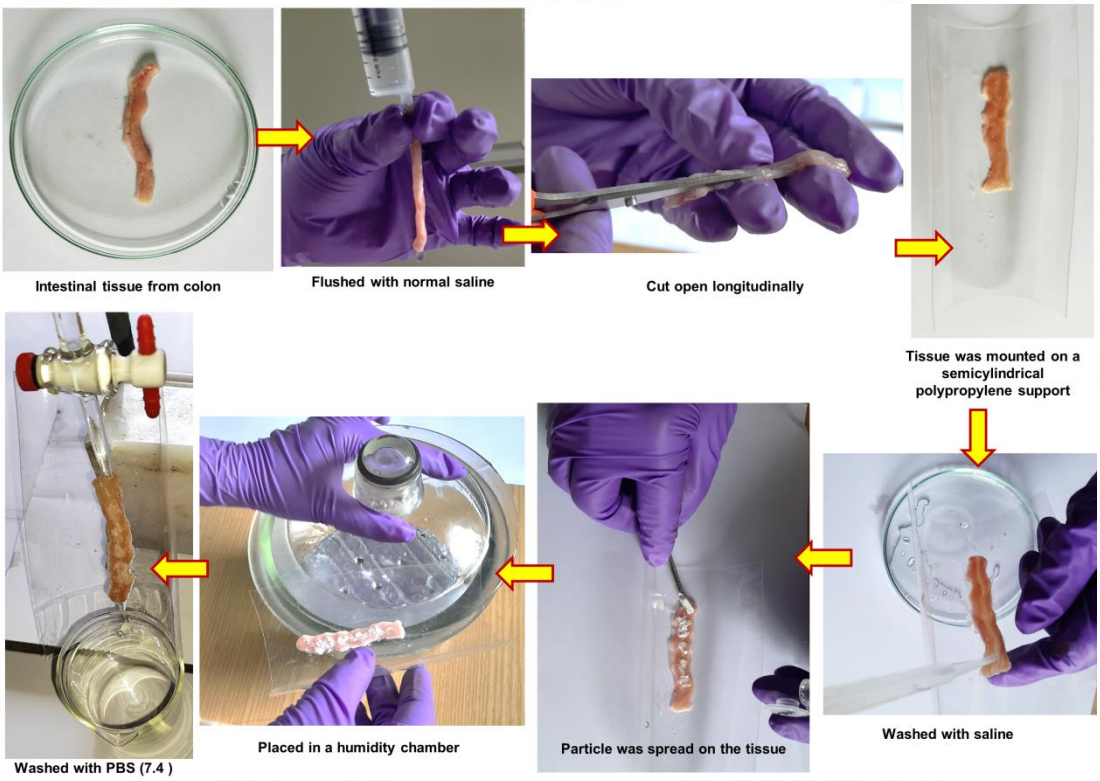

Figure 3.9. Procedure for *in vitro* mucoadhesion studies in rat intestine.

3.2. 3.12.2. Mucoadhesion studies by texture analyzer

The mucoadhesion studies of microparticles were carried out in rat intestinal colon segments as described in section 3.2.2.6.

3.2.3.13. SDS PAGE- protein corona studies using pancreatin

3.2.3.13.1. Sample preparation for protein corona

Two different quantities of microparticles (2 and 5 mg) were incubated with 100 µL pancreatin (100 mg/mL) for 1 hour at 37 °C with continuous agitation. The experiment was done as described in section 3.2.2.7.1.

3.2.3.13.2. Identification of protein corona by SDS PAGE

The separated hard corona-bound microparticles were heated in reducing sample buffer and separated by 12% SDS PAGE. The procedure was carried out as detailed in section 3.2.2.7.2.

3.2.4. Statistical analysis

The measurements were repeated at least thrice and the data were expressed as mean ± standard deviation (SD). The data were statistically evaluated by student's t-test using Microsoft Excel software. A p-value less than 0.05 was considered to be statistically significant. Where p-value ≤ 0.0001 is denoted as four asterisks; p-value ≤ 0.001 is given three asterisks; p-value ≤ 0.01 is given two asterisks; p-value ≤ 0.05 is given one asterisk and p-value > 0.05 is considered as statistically not significant and given as 'ns'.

4 RESULTS AND DISCUSSION

The main focus of the work was to study the interactions of nano and micro drug delivery carriers with the simulated intestinal microenvironment. For achieving this objective, we synthesized three different particle systems. Chitosan and functionalized chitosan particles are the micro-drug delivery systems selected for the study. Curcumin silver nanoparticle conjugate and lauric acid solid lipid nanoparticles are the nano-drug delivery systems used for the study.

4.1. System I: Curcumin-silver nanoparticle conjugate

Curcumin-silver nanoparticle conjugate (CUR-AgNP) is a metallic nano-drug delivery system. Dulbecco and Savarino reported that curcumin is hydrolytically unstable in intestinal pH (7.4) leading to poor bioavailability (Dulbecco and Savarino, 2013). Therefore, curcumin was conjugated with silver nanoparticles, and evaluated its stability at intestinal pH 7.4 and also studied its interactions with colon cancer cells.

4.1.1. Synthesis of curcumin-silver nanoparticle conjugate

For the synthesis of the CUR-AgNP, we adopted a green chemistry approach without the involvement of any harsh chemical reducing agents or organic solvents at room temperature (28°C). There exists a plethora of literature on the green synthesis of the CUR-AgNP (Jaiswal and Mishra, 2018; Khan et al., 2019; Loo et al., 2016; Shameli et al., 2012). Some of these studies reported the quick green synthesis of the CUR-AgNP in an alkaline environment (Jaiswal and Mishra, 2018; Khan et al., 2019). Under alkaline pH conditions (pH 9-10) curcumin is unstable and undergoes rapid

degradation (Esatbeyoglu et al., 2012). In this study, the synthesis of the CUR-AgNP was carried out at pH 7 to prevent or minimize the degradation of curcumin.

4.1.2. Physicochemical characterization

4.1.2.1. UV-Visible absorption and fluorescence spectroscopy

By monitoring the UV-Visible absorption spectra and fluorescence spectra as a function of time, the formation of the CUR-AgNP was confirmed (Figure 4.1). As depicted in figure 4.1 A & B, the UV-Visible spectra of the CUR-AgNP gave a prominent peak at around 420 nm due to the surface plasmon resonance (SPR) of spherical silver nanoparticles (Shameli et al., 2012). Additionally, the absorption spectra of curcumin exhibit two strong absorption bands, one in the visible range with maximum absorption at 420 nm and another band in the UV region with maximum absorption at 260 nm (Priyadarsini, 2014).

In the present study when CUR solution was added to silver nitrate solution, the absorbance at 420 nm due to the presence of unconjugated CUR was found to be decreased as time progressed. This decrease in the concentration of free CUR confirms the successful synthesis of the CUR-AgNP. As evident in the spectra (figure 4.1A) from the second to the fifth day, there was no significant variation in the absorbance of the CUR-AgNP. After the addition of CUR to silver nitrate solution, the formation of CUR-AgNP was studied for a shorter duration of up to 150 minutes (figure 4.1.B). The findings showed that the CUR-AgNP formation occurs within hours. Therefore, this can be used as a reliable method for the green synthesis of the CUR-AgNP.

Fluorescence spectroscopy was also used to monitor the formation of the CUR-AgNP (figure 4.1C). At an excitation wavelength of 420 nm, the emission spectra were recorded from 430 nm to 720 nm. CUR showed a broad maximum at 540 nm, when both solutions of CUR and silver nitrate were mixed the peak intensity suddenly decreased. When the measurements were taken after 30 minutes of mixing both solutions, the fluorescence maximum was shifted to 564 nm. On the second day, the fluorescence emission maxima were found to be blue-shifted to 548 nm, indicating the formation of the CUR-AgNP. As the time progressed, the fluorescence intensity tended to decrease further. It has been reported that due to the strong electromagnetic field the fluorescence of a chromophore close to the surface of metal nanoparticles would be strongly affected (Mooradian, 1969). Therefore, the quenching of fluorescence is an indication of the complexation of CUR with AgNP. Singh et al. reported a similar trend in gold nanoparticles surface functionalized with curcumin (Singh et al., 2013). The oxidized curcumin molecules on the surface of the nanoparticles interact electronically with the surface to donate electrons to the metal, thus quenching the fluorescence through non-radiative pathways available in the metal nanoparticles. The quenching of fluorescence is a clear indication of the conjugation of CUR with AgNPs and the formation of a more stable CUR-AgNP with lower vibrational energy levels.

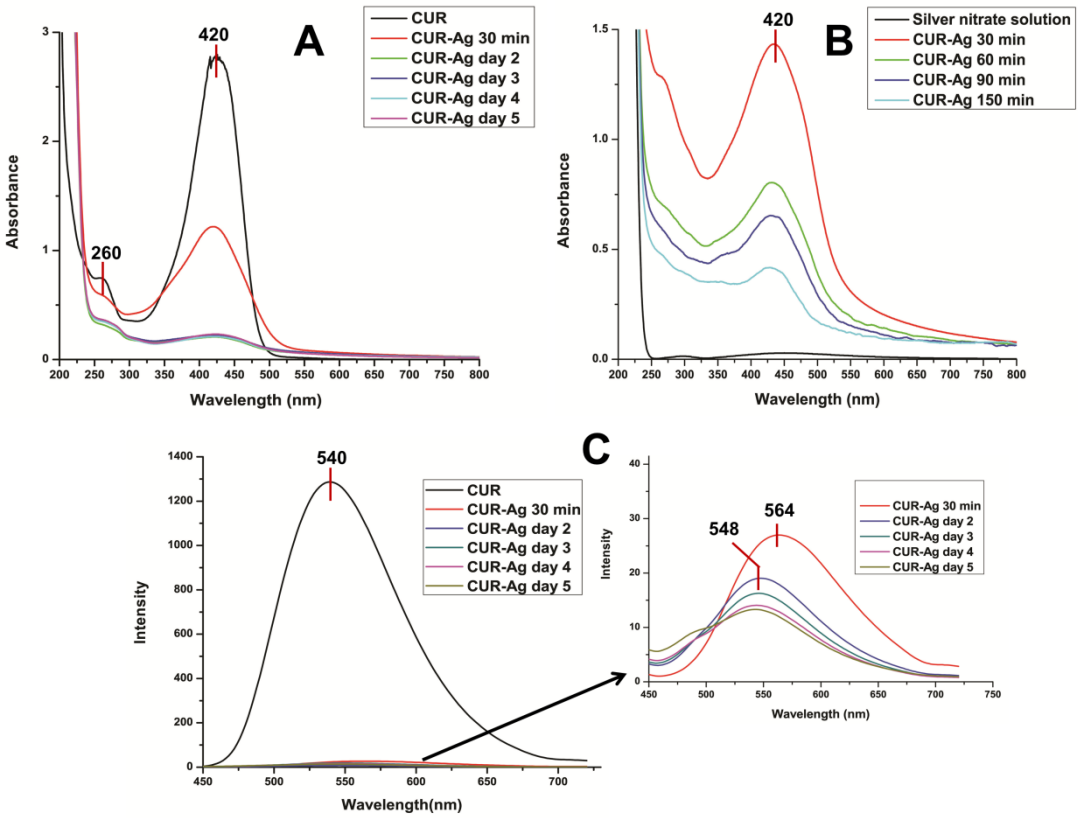

Figure 4.1. A & B: UV-Vis spectra depicting the formation of the CUR-AgNP as a function of time; C: Fluorescence spectra showing the formation of the CUR-AgNP as a function of time; A & C were recorded after the addition of curcumin solution into silver nitrate solution except for 'CUR'. For CUR and CUR-AgNP, the curcumin concentration was the same.

4.1.2.2. Determination of particle size and zeta potential

The hydrodynamic diameter of the CUR-AgNP suspension was found to be 12.45 ± 2.61 nm (figure 4.2A, n=3), and the polydispersity index (PDI) was 0.44 ± 0.007 (n=3). The zeta potential of the CUR-AgNP suspension was -28.5 ± 0.52 mV (figure 4.2B). These results are in close range to the previously reported zeta potential (-27.9 mV) for AgNPs reduced using curcumin (Song et al., 2019). The stability of nanoparticle dispersion was directly related to the zeta potential value (Gupta et al., 2020). Luo et al. reported that higher negative values of zeta potential represent greater electrostatic repulsion and, therefore, greater nanoparticle stability (Luo et al.,

2015). The surface charge of the nanoparticles in the biological system is expected to be simulated by the zeta potential of the CUR-AgNP in phosphate buffer (pH 7.4). In 0.1X phosphate buffer saline (pH 7.4) the zeta potential of the CUR-AgNP was -22.9 ± 0.2 mV. The zeta potential of the CUR-AgNP in PBS (pH 7.4) was found to be less negative due to the increased concentration of counter ions in PBS (Midekessa et al., 2020).

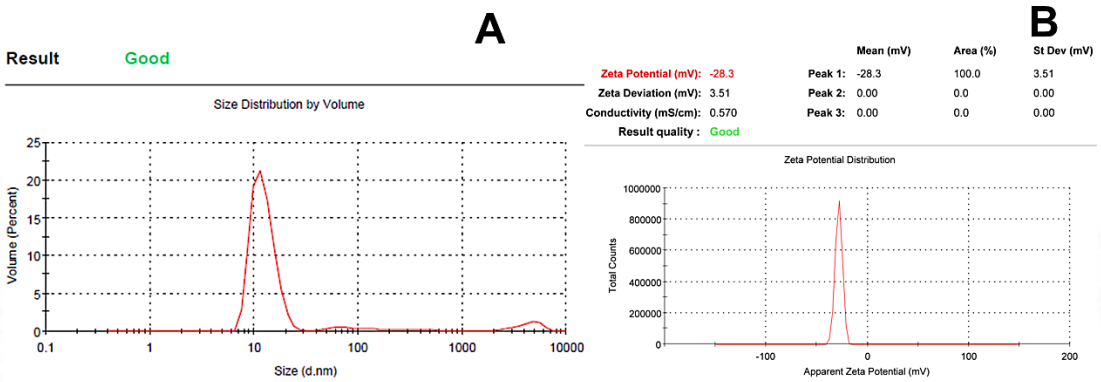

Figure 4.2. A: Size distribution of CUR-AgNP; B: Zeta potential of CUR-AgNP suspension.

4.1.2.3. X-ray diffraction (XRD) analysis

By using XRD analysis, the phase purity of the synthesized CUR-AgNP was evaluated (figure 4.3). The different peaks in the XRD spectra of the CUR-AgNP correspond to the face-centered cubic structure of metallic silver. The Joint Committee on Powder Diffraction Standards (JCPDS) card number of silver 04-0783 matched perfectly with the 2θ values (38°, 44°, 64°, 77°, and 81°) corresponding to the planes (1 1 1), (2 0 0), (2 2 0), (3 1 1) and (2 2 2) (Park et al., 2011; Shu et al., 2020). The crystalline nature of the CUR-AgNP was evident from the XRD pattern.

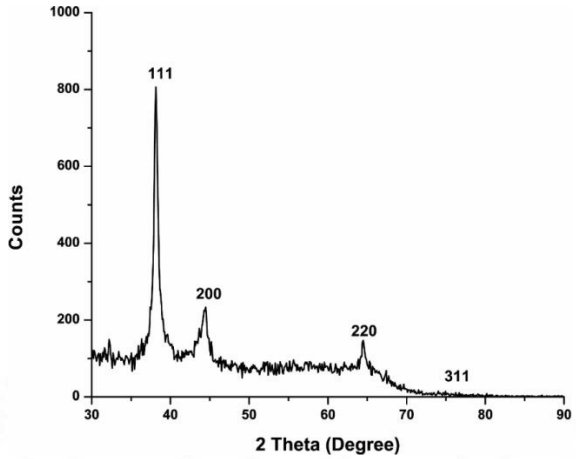

Figure 4.3. XRD spectra of CUR-AgNP

4.1.2.4. Transmission electron microscopy (TEM) analysis

The morphology of the CUR-AgNP was found to be spherical according to TEM analysis (figure 4.4). The CUR-AgNP was found to be in the size range of 10-15 nm as revealed by the TEM image. No visible aggregation of the CUR-AgNP was observed under TEM.

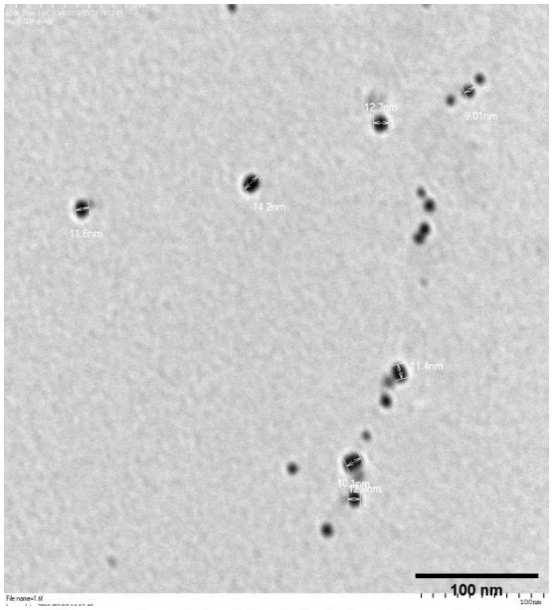

Figure 4.4. Transmission electron microscopy image of CUR-AgNP.

4.1.2.5. FTIR analysis

FTIR spectra of the CUR and CUR-AgNP are shown in Figures 4.5 A & B. FTIR spectra of the CUR-AgNP revealed characteristic peaks at 3506, 1628, 1602, 1509, and 1272 cm^{-1} (Mohan et al., 2012). The peak at 3506 cm^{-1} was attributed to the stretching vibrations of the −OH group in the CUR and a peak at 1628 cm^{-1} was assigned primarily to mixed C=C and C=O bonds. Another peak, at 1602 cm^{-1} corresponds to C=C (benzene ring) symmetric aromatic ring stretching vibrations. Moreover, the peak at 1509 cm^{-1} corresponds to C=O vibration, and enol peaks of C-O were found at 1272 cm^{-1}.

In the case of the CUR-AgNP, the −OH peak was found to be broad and shifted to 3422 cm^{-1} compared to CUR. The result was similar to the reports that had been previously published (Jaiswal and Mishra, 2018; Loo et al., 2016). The CUR-AgNP showed a new peak at 1382 cm^{-1}, which may be due to the capping of CUR over the silver nanoparticles, which was bound either by the C=O group or via the phenolic –OH group (Jaiswal and Mishra, 2018; Kundu and Nithiyanantham, 2013).

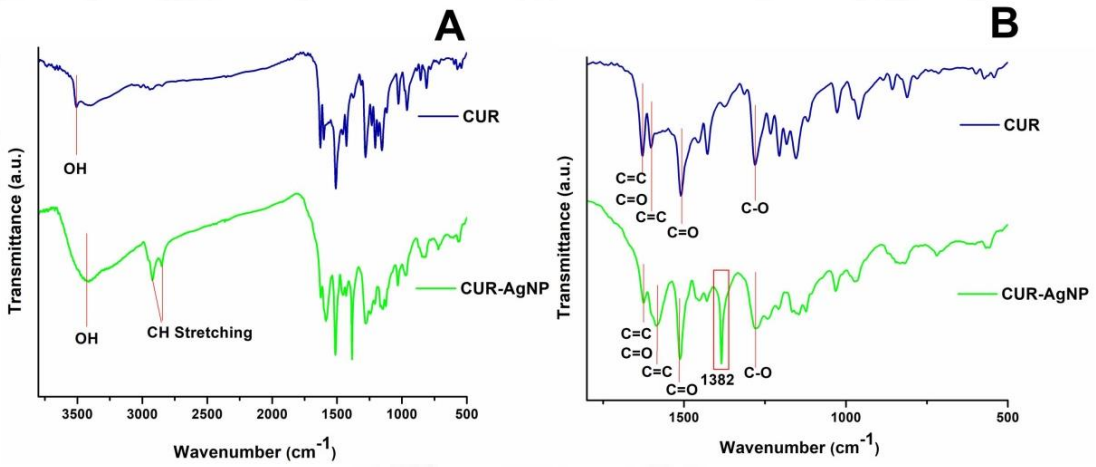

Figure 4.5. FTIR spectra of CUR and CUR-AgNP: (A) 3800-500 cm^{-1} range; (B) 1800-500 cm^{-1} range.

4.1.2.6. Inductively coupled plasma optical emission spectroscopy (ICP-OES) analysis

ICP-OES analysis was used to evaluate the silver ion release from the CUR-AgNP. The silver ion release from the CUR-AgNP was found to be 0.527 ppm. Silver ion release from silver nanoparticles has been associated with toxicity (Bhubhanil et al., 2021). In the present study, the silver ion release from CUR-AgNP was found to be very less therefore the associated toxicity was also expected to be less.

4.1.2.7. X-ray photoelectron spectroscopy (XPS) analysis

Using X-ray photoelectron spectroscopy (XPS), the nature of the binding interaction between CUR and AgNPs was investigated. For CUR and CUR-AgNP, XPS analysis for the core-level electrons of carbon, oxygen, and silver atoms was carried out (figure 4.6). In CUR, the XPS peak of the carbon atom (C1s) centered at a binding energy of 284.77 eV, may be deconvoluted into three peaks at energies 284.72, 286.23, and 288.28 eV corresponding to sp^3 carbon, C-O, and C=O, respectively (figure 4.6A). When the carbon atom (C1s) peak of the CUR-AgNP was de-convoluted, it was found that the peaks corresponding to the sp^3 and C-O carbons didn't deviate much from their positions in comparison to CUR (figure 4.6C). But intriguingly, the peak for C=O was downshifted to 288.08 eV, showing that the carbonyl group was involved in the binding interaction with AgNPs (Khandelwal et al., 2018).

The deconvolution of the XPS peak for oxygen atoms (O1s) further strengthens this observation. In CUR, the oxygen peak can be deconvoluted into two peaks at 531.18 and 532.77 eV corresponding to C-O and C=O peaks, respectively (figure 4.6B).

These peaks were found to be shifted to 532.48 and 533.61 eV, upon binding with AgNPs indicating the involvement of carbonyl functionality of CUR in the binding. (figure 4.6D).

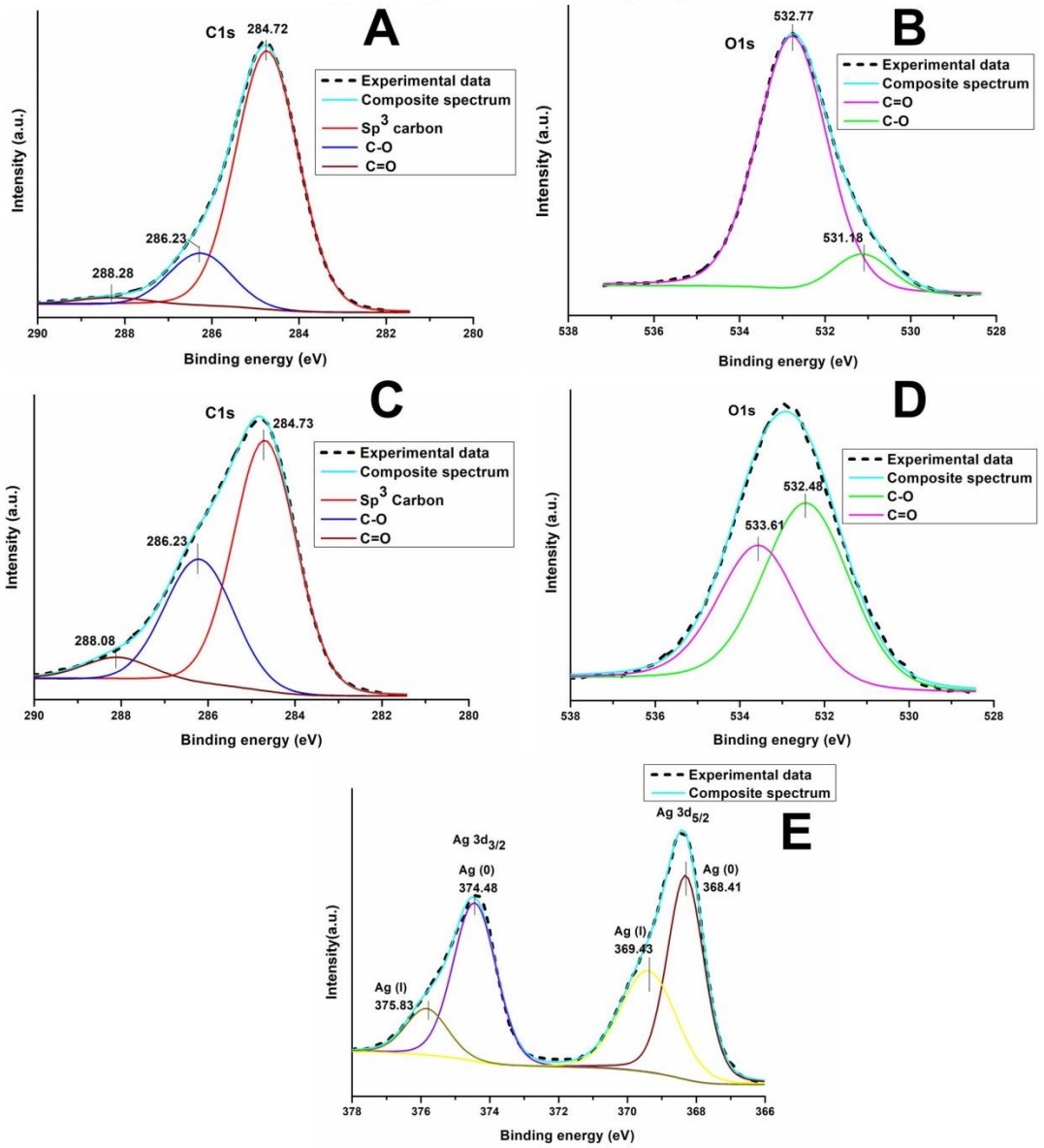

Figure 4.6. Deconvoluted XPS spectra of: (A & B). CUR and (C-E). CUR-AgNP. The C1s core-level electrons are represented by the XPS spectra 'A' and 'C'; the O1s core-level electrons are represented by 'B' and 'D', and the Ag3d core-level electrons are represented by 'E'.

The XPS spectrum for Ag atoms revealed two broad peaks for Ag 3d5/2 and Ag 3d3/2 at binding energies of 368.41 and 374.48 eV, respectively (Lyu et al., 2020).

Each of these peaks splits into two peaks when they are deconvoluted (figure 4.6E), indicating the presence of silver in two different oxidation states Ag(0) and Ag(I) (Carmona et al., 2017).

The FTIR and XPS data indicate that CUR binds to silver nanoparticles with its diketo moiety. In figure 4.7A, the binding of a curcuminoid molecule (curcumin, demethoxycurcumin, or bisdemethoxycurcumin) to a silver nanoparticle is illustrated schematically.

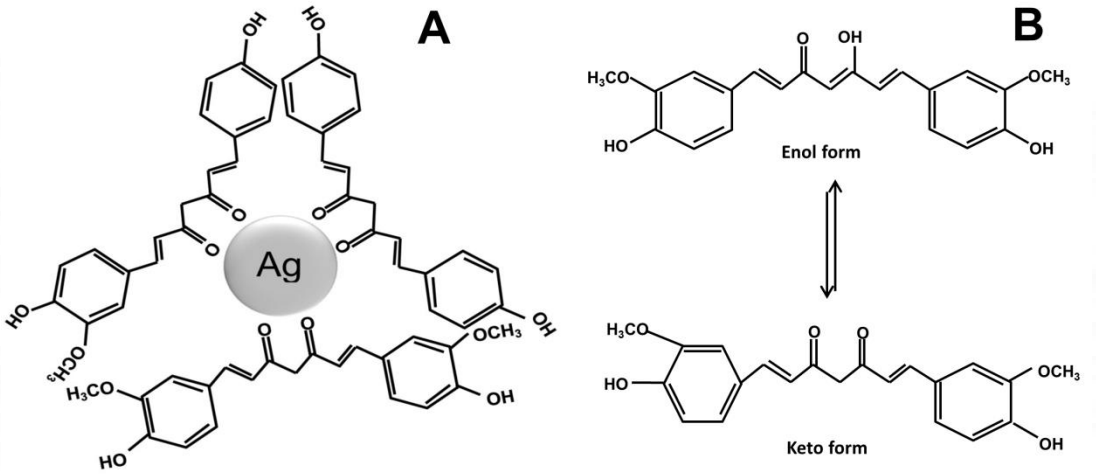

Figure 4.7. (A) Schematic representation of curcuminoids attached to silver nanoparticles; (B) Keto-enol tautomerism of curcumin.

The diketo moiety of curcumin displays the keto-enol tautomerism which is shown in figure 4.7B (Angelini et al., 2020). In acidic and neutral pH, curcumin exists in its keto form, and in alkaline pH conditions, curcumin exists in its enol form (Wanninger et al., 2015).

Curcumin acts as a monobasic bidentate ligand in which the α,β-unsaturated β-diketo moiety functions as a chelating agent for complexation with metal ions (Ferrari et al., 2014). Banerjee and Chakravarty reported that curcumin stabilizes itself in transition metal complexes by binding to transition metal ions through its monoanionic enol

form (Banerjee and Chakravarty, 2015). The degradation of curcumin at physiological pH leads to two types of degradation products which include alkaline hydrolysis products and autoxidation products (Gordon et al., 2015; Griesser et al., 2011). The alkaline hydrolysis products (ferulic acid, vanillin, ferulaldehyde, and feruloyl methane) are formed by hydroxyl ion (-OH) mediated hydrolysis reaction (Wang et al., 1997). In the hydroxyl ion mechanism, the hydroxyl ion (-OH) attacks the carbonyl group of curcumin leading to the degradation of the molecule. The autoxidation products such as bicyclopentadione are formed through a radical-mediated process where hydrogen dissociation from the phenol group forms a phenolic radical, which then migrates to the conjugated heptadienedione chain and initiates a chain reaction of curcumin degradation (Gordon et al., 2015; Griesser et al., 2011). The alkaline hydrolysis of the diketone group resulted in the degradation of curcumin (Zhu et al., 2017). CUR-AgNPs are formed through the enolic group, where the enolic proton is replaced by the metal ion and the O-methoxy phenolic group remains intact (Priyadarsini, 2014). When the diketo moiety binds to metal ions the degradation of CUR under physiological conditions could be prevented.

4.1.3. Estimation of the curcumin content in CUR-AgNP

The active phenolic pigment of turmeric is a mixture of curcumin, demethoxycurcumin, and bisdemethoxycurcumin, collectively known as curcuminoids. They were estimated and found to be in the ratio 79:18:3 by HPLC estimation. Peaks corresponding to curcumin, demethoxycurcumin, and bisdemethoxycurcumin were well separated in the HPLC chromatogram at various retention times of 24.9, 28.6, and 32.7 (Figure 4.8A). The curcumin content in the

CUR-AgNP was also assessed by HPLC. The concentration of curcumin bound to the nanoparticle was found to be 210 ± 3.2 µg/mg of CUR-AgNP, after being extracted in ethanol.

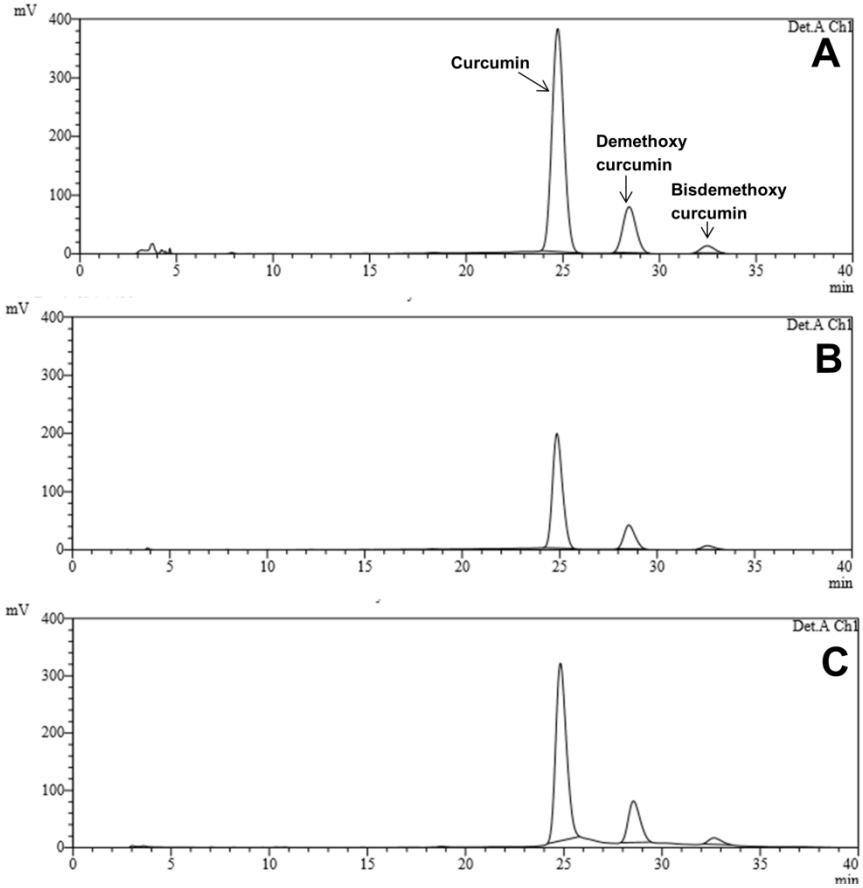

Figure 4.8. Chromatogram of CUR and stability of CUR in PBS: (A) HPLC traces of individual curcuminoids in the CUR control; (B) HPLC traces of CUR (control) after 30 minutes incubation in PBS (pH 7.4); and (C) HPLC traces of CUR bound to CUR-AgNP after 30 minutes exposure in PBS (pH 7.4).

4.1.4. *In vitro* degradation studies of curcumin

Figure 4.9 depicts the UV–Vis spectroscopy data of the degradation induced by phosphate buffer of pH 7.4 on CUR and CUR bound on the CUR-AgNP. A significant reduction in the intensity of the peak at 420 nm and a simultaneous increase in peak height at 260 nm was observed for CUR after 30 minutes of

incubation in phosphate buffer (pH 7.4). This result agreed well with the previously published reports (Gordon et al., 2015; Jaiswal and Dongre, 2020). The increase in peak height at 260 nm was attributed to the formation of smaller aromatic compounds due to the chemical degradation of curcumin (Cañamares et al., 2006). Conversely, CUR bound to the CUR-AgNP was found to be stable in phosphate buffer (pH 7.4) without much variation in the peak height at 260 nm and 420 nm. In the case of CUR, the peak height ratio decreased significantly indicating its fast degradation in phosphate buffer. However, the peak ratio for bound CUR in the CUR-AgNP was almost constant, indicating that it was more stable in the phosphate buffer (pH 7.4). The ratio of peak heights at 420 nm and 260 nm was used to calculate the extent of degradation (%), and the results are shown in Table 4.1.

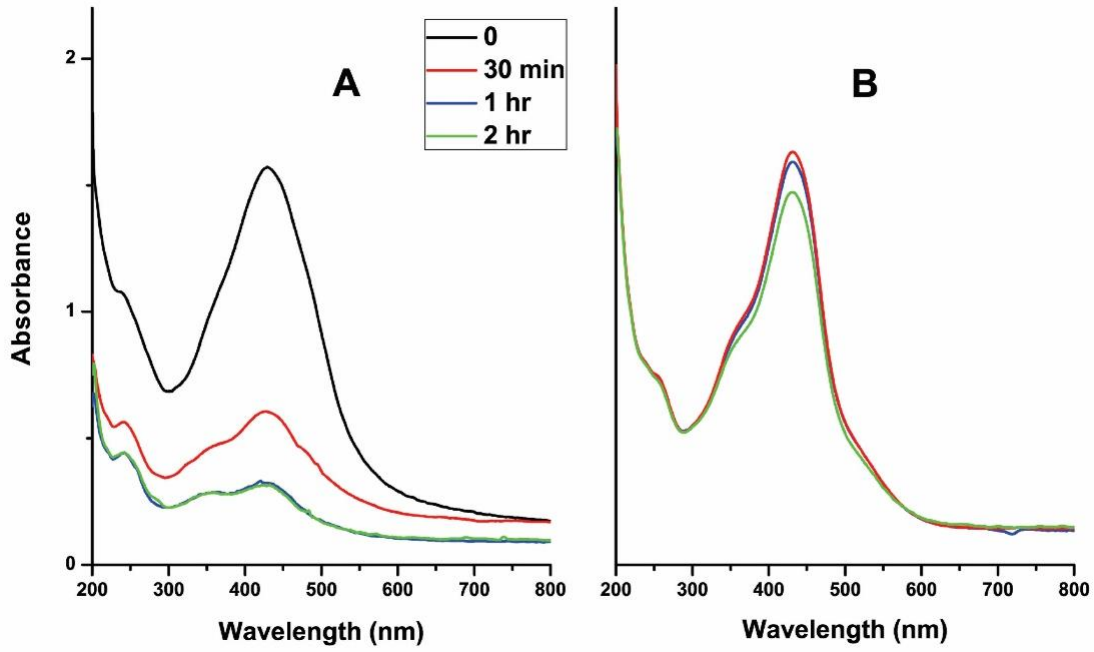

Figure 4.9. Stability/degradation studies using UV–Vis absorption spectroscopy: (A) CUR and (B) CUR-AgNP at different time periods in phosphate buffer of pH 7.4.

Table 4.1. Degradation (%) of CUR and CUR-AgNP calculated from UV-Vis spectra

Samples	CUR		CUR-AgNP	
Time (Hours)	Peak height ratio (A_{420}/A_{260})	Degradation (%)	Peak height ratio (A_{420}/A_{260})	Degradation (%)
0	32.19	0	38.53	0
0.5	8.19	75	38.19	0
1	3.56	89	38.73	0
2	3.27	90	38.55	0

HPLC analysis was carried out to further confirm the stability of CUR and CUR-AgNP in phosphate buffer (pH 7.4). After 30 minutes of incubation in phosphate buffer (pH 7.4), CUR exhibited significant degradation (figure 4.8B). It has been reported that more than 90% of curcumin gets degraded within 30 minutes under physiological conditions (Wang et al., 1997). While CUR bound to the CUR-AgNP indicated no significant degradation (figure 4.8C) revealing that CUR bound to the CUR-AgNP is stable in the physiological medium. The stability of curcumin complexed with divalent metal ions such as Zn^{2+}, Cu^{2+}, Mg^{2+}, and Se^{2+} was reported to have higher stability *in vitro* compared to native curcumin (Zebib et al., 2010).

The degradation (%) of CUR and CUR bound to the CUR-AgNP was studied for an extended period of up to 24 hours and the data is given in figure 4.10. The degradation of native curcumin (CUR) at 24 hours was found to be 59.8 %, while curcumin bound to the CUR-AgNP exhibited only 28 % degradation. In the CUR and CUR-AgNP, demethoxycurcumin degraded by about 44 % and 29 %, respectively at 24 hours. Bisdemethoxycurcumin in CUR and CUR-AgNP exhibited 42 % and 27 % of degradation at 24 hours. In the CUR-AgNP, the degradation

pattern of curcuminoids was found to be similar and the initial degradation of curcumin, demethoxycurcumin, and bisdemethoxycurcumin at 4 hours was found to be 9.6 %, 11.4 %, and 10.6 %, respectively. In contrast, the curcuminoids in CUR exhibited a distinct pattern of degradation and the initial degradation at 4 hours was observed to be 49.6 % for curcumin, 42.7 % for demethoxycurcumin, and 38.3 % for bisdemethoxycurcumin, respectively. The rate of degradation of three curcuminoids in CUR was found to be greater at the initial 4 hours and curcumin was found to degrade faster than the other two curcuminoids. Compared to curcumin, one methoxy group is absent in demethoxycurcumin and this significantly slows the hydrogen abstraction, although the loss of the methoxy group and hydrogen abstraction occur on opposite ends of the molecule (Schneider et al., 2015). Consequently, the rate of degradation was less for demethoxycurcumin compared to curcumin. Among the curcuminoids, bisdemethoxycurcumin showed lesser degradation at physiological pH of 7.4 compared to curcumin and demethoxycurcumin. Bisdemethoxycurcumin lacks both methoxy groups which confers stability toward autoxidation (Schneider et al., 2015). The degradation profile was found to be similar to that of a previously published report (Esatbeyoglu et al., 2012).

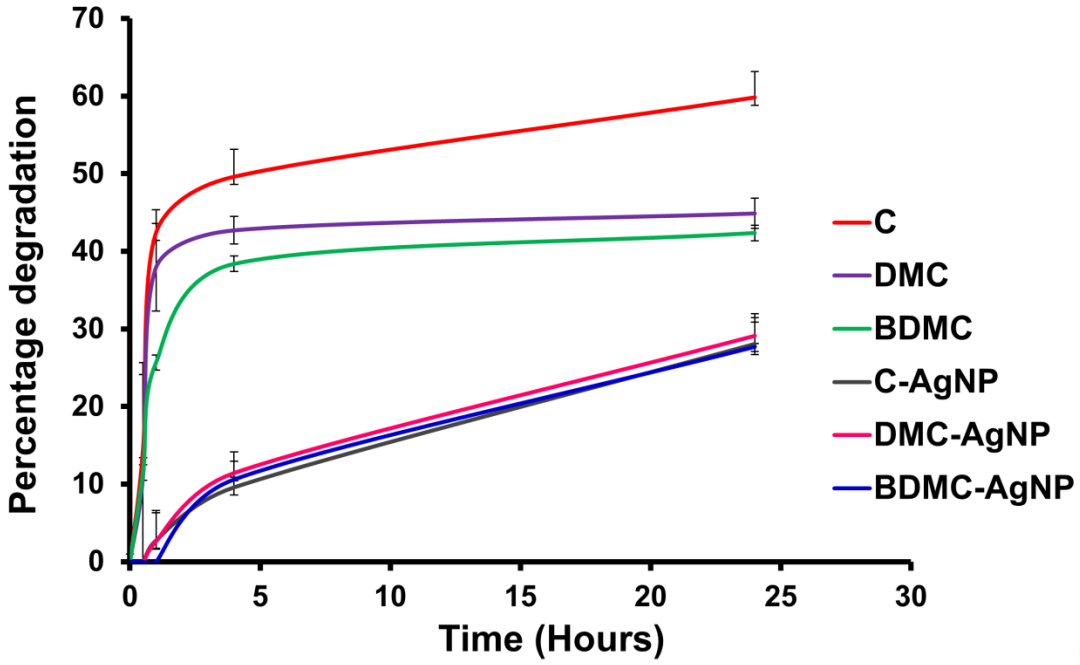

Figure 4.10. Degradation (%) of individual curcuminoids present in the CUR and CUR-AgNP (C – Curcumin; DMC – Demethoxycurcumin; BDMC - Bisdemethoxy-curcumin).

4.1.5. Cellular interaction of CUR-AgNP with colorectal cancer cells

4.1.5.1. Cellular uptake of CUR-AgNP by HCT-116 and Caco-2 cells

The cellular uptake and localization of the chemotherapeutic agent in particular cellular components are very crucial to understand its efficacy (Coogan and Fernández-Moreira, 2014). The green fluorescence of curcumin is being exploited to qualitatively study the cellular uptake and localization of the CUR-AgNP in the HCT-116 and Caco-2 cells using confocal laser scanning microscopy (CLSM). The excitation wavelength used for the CUR-AgNP was 488 nm and the emission was monitored through 525 nm filters. At this excitation wavelength, no fluorescence was observed in untreated cells (figure 4.11A and 4.13A). This was done to avoid background autofluorescence which can lead to the misinterpretation of image data and the generation of false positive results. While doing CLSM, it is always

important to check autofluorescence under the same conditions used to observe an introduced fluorochrome. The untreated cells help to claim that the observed fluorescence was due to the added fluorochrome (Wayne, 2019). Figure 4.11 shows the fluorescence images obtained when the HCT-116 cells were incubated with CUR-AgNP for 0.5, 1, 2, and 4 hours, respectively. Figure 4.13 shows the fluorescence images obtained when the Caco-2 cells were incubated with CUR-AgNP for 0.5, 1, 2, and 4 hours. Within the initial 0.5 hours, the CUR-AgNP was observed as green fluorescence in the cytoplasm of both HCT-116 and Caco-2 cells (figure 4.11B and 4.13B). The CUR-AgNP fluorescence appeared after 0.5 hours in HCT-116 cells and reached the maximum fluorescence diffusion at 1 hour itself and was observed decreasing after 4 hours (figure 4.12). The decrease in fluorescence at 4 hours was due to the exocytosis of the CUR-AgNP from the cells. In the case of Caco-2 cells, CUR-AgNP fluorescence appeared after a very short contact time (0.5 hours), and reached the maximum fluorescence diffusion at 2 hours (figure 4.14).

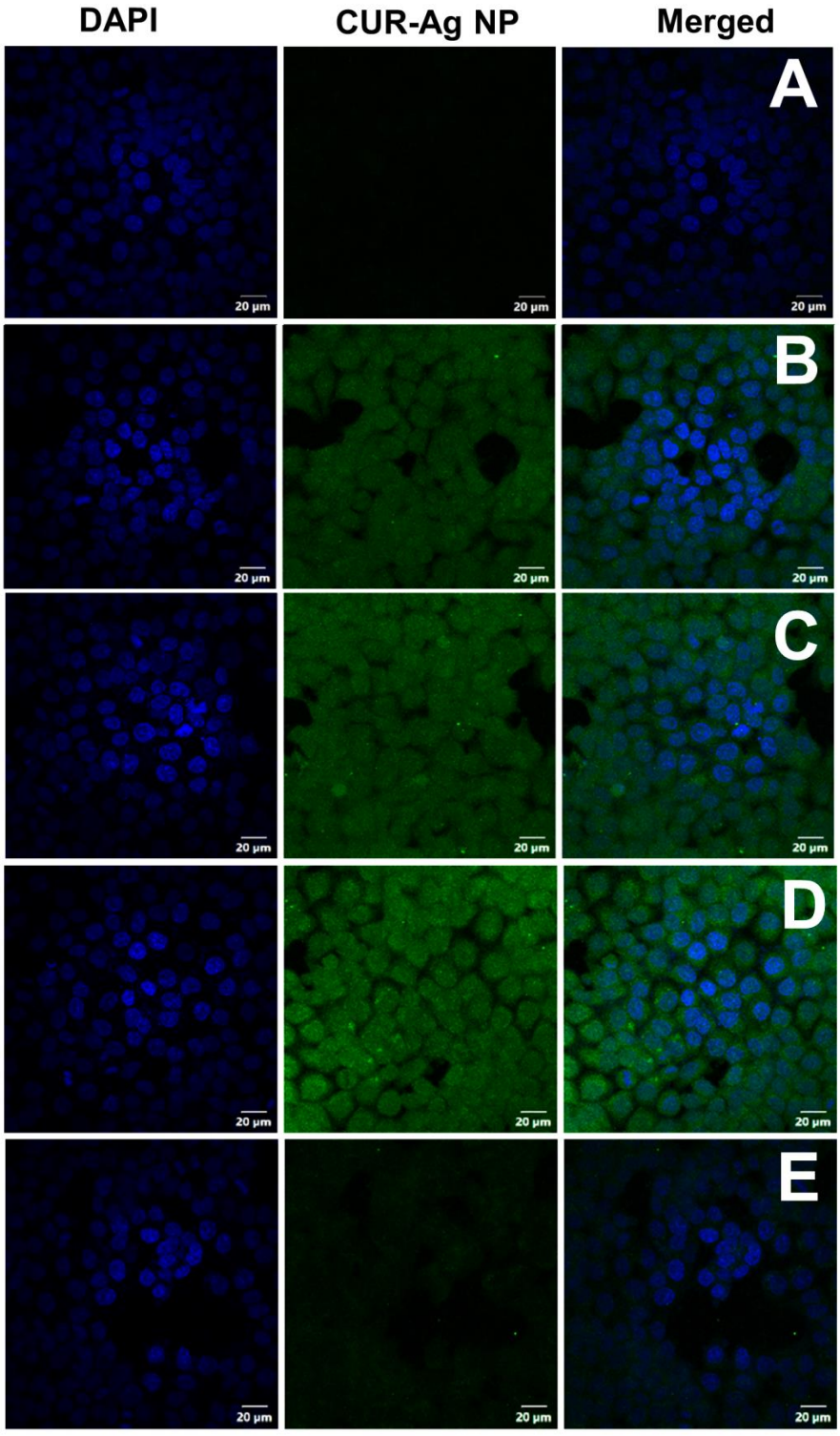

Figure 4.11. Uptake of CUR-AgNP (Green) by HCT-116 at different time periods studied with CLSM: (A) Untreated cells; (B-E) Cellular uptake of CUR-AgNP at 0.5, 1, 2, and 4 hours in HCT-116 cells. DAPI was used for nuclear staining (blue).

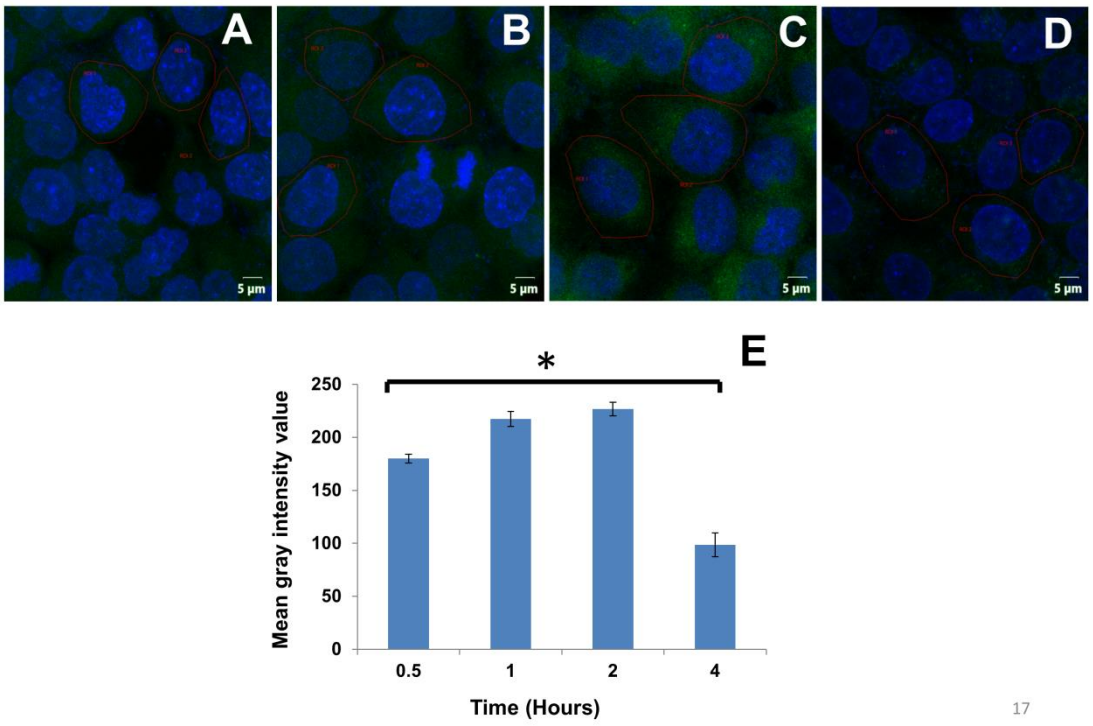

Figure 4.12. Uptake of CUR-AgNP by HCT-116 cells: (A-D) Confocal images showing the uptake of CUR-AgNP at 0.5, 1, 2, and 4 hours. DAPI was used for nuclear staining (blue); (E) Cellular uptake (indicated by mean gray intensity) was estimated by drawing ROI. p-value < 0.05 was considered statistically significant and indicated with one asterisk.

Using ROI analysis, the cellular uptake of the CUR-AgNP was calculated in both HCT-116 and Caco-2 cells (Figures 4.13 and 4.15). The results indicate that the cellular uptake of the CUR-AgNP was time-dependent in both HCT-116 and Caco-2 cells.

The increased cellular uptake of curcumin metal complexes has been extensively reported in the literature (Prasad et al., 2021). Rubagotti et al. reported that gallium–curcumin complex and gallium-diacetyl curcumin exhibited higher uptake by colorectal carcinoma (HT29) and lymphoma (K562) cell lines than in lymphocytes (Rubagotti et al., 2017). Cobalt (III) binds to curcumin and increases the hydrolytic

stability of curcumin and increases the cellular uptake and bioactivity compared to free curcumin (Garai et al., 2016).

In HCT-116 and Caco-2 cells the CUR-AgNP was found to be localized in the cytoplasm. Sarkar et al. reported that the iron (III) complex of curcumin localized in cytoplasm makes the cytosolic organelles as the potential targets (Sarkar et al., 2016). Curcumin is reported to induce anticancer activity by interfering with the function of the transcription factor NF-κB, which is a protein complex involved in the transcription of DNA (Aggarwal et al., 2007; Anand et al., 2008; Dhillon et al., 2008). In colorectal cancer cells, curcumin induces apoptosis through multiple target molecules and associated signaling pathways (Ismail et al., 2019). Sharma et al. reported that curcumin-stabilized silver nanoparticles significantly inhibit NF-κB nuclear expression (Sharma et al., 2017).

The mechanism of apoptosis induced by curcumin in colorectal cells is detailed as follows: Curcumin inhibits the nuclear factor kappa light chain enhancer of activated B cells (NF-κB) and cyclooxygenase-2 (COX-2), down-regulates transcription factor catenin and activating protein-1 (AP-1), suppresses the anti-apoptotic proteins and increases the levels of reactive oxygen species (ROS), superoxide dismutase (SOD), and pro-apoptotic proteins, as well as Fas and death receptor 5 (DR5) receptor (Ismail et al., 2019).

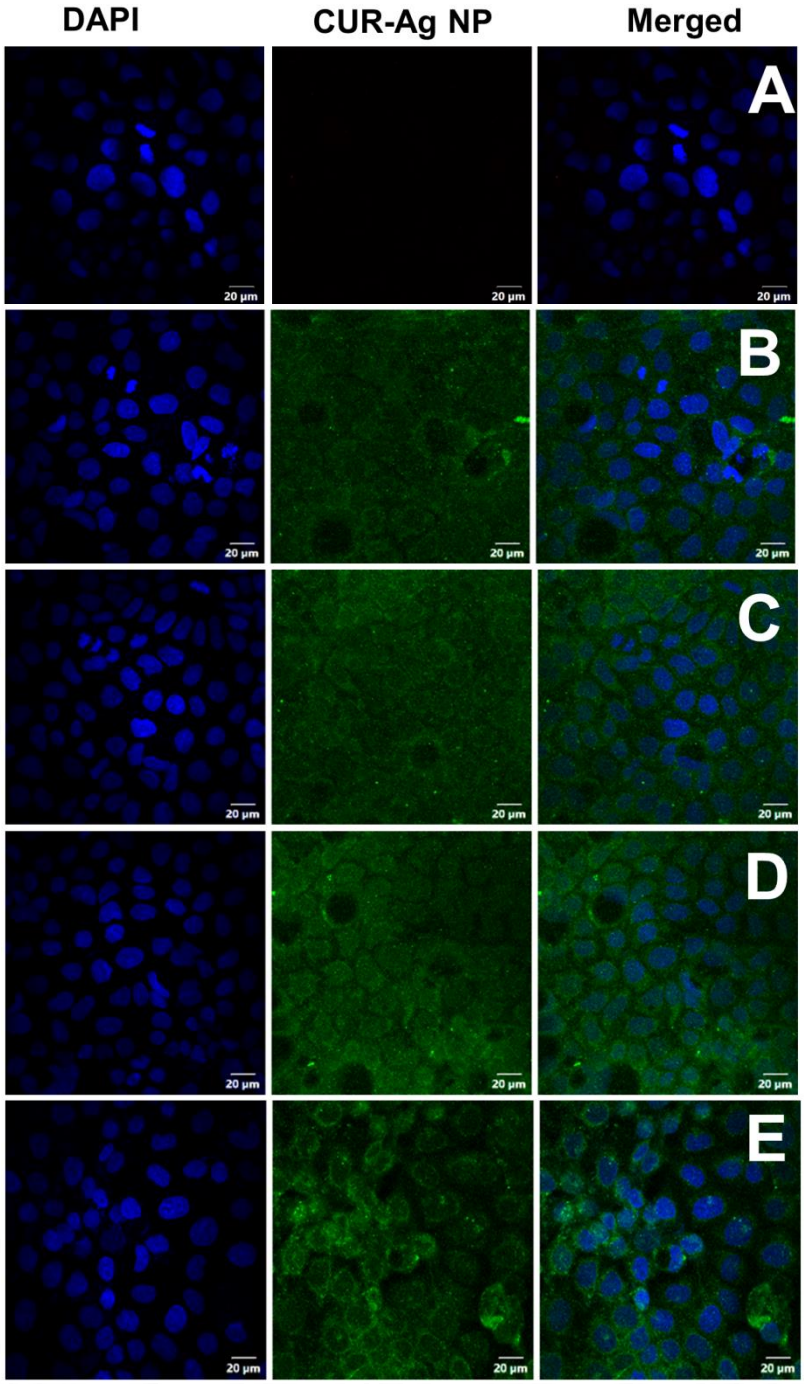

Figure 4.13. Uptake of CUR-AgNP (Green) by Caco-2 cells at different time periods studied with CLSM: (A) untreated cells; (B-E) Cellular uptake of CUR-AgNP at 0.5, 1, 2, and 4 hours in Caco-2 cells. DAPI was used for nuclear staining (blue).

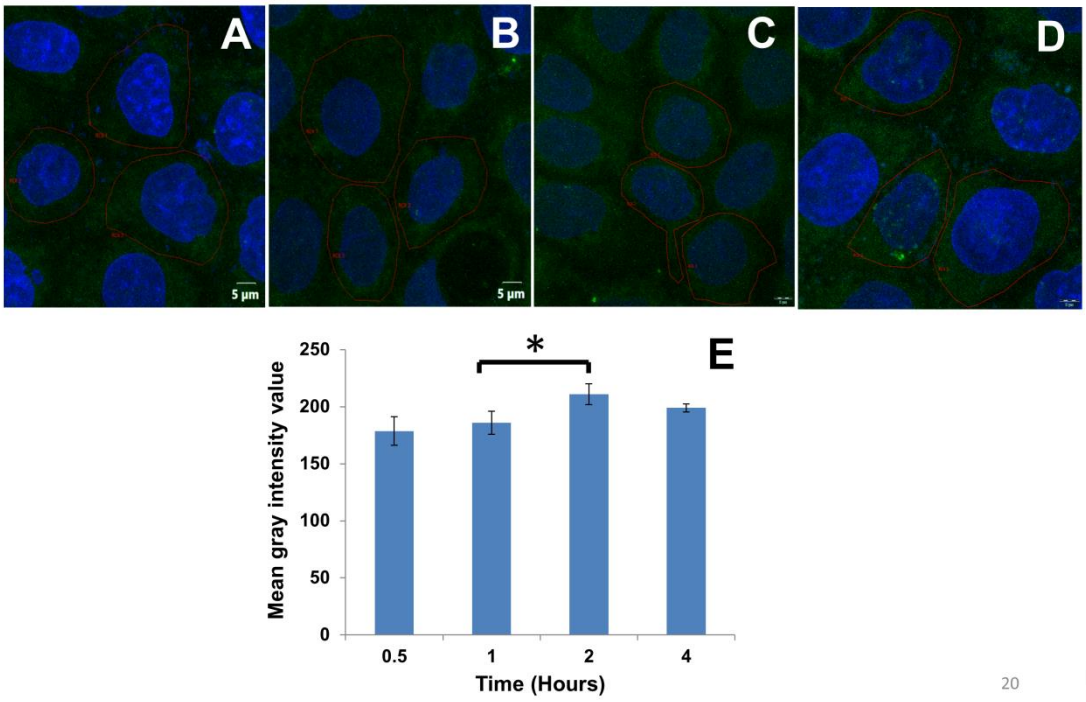

Figure 4.14. Uptake of CUR-AgNP by Caco-2 cells: (A-D) Confocal images showing the uptake of CUR-AgNP at 0.5, 1, 2, and 4 hours. DAPI was used for nuclear staining (blue); (E) Cellular uptake (indicated by mean gray intensity) was estimated by drawing ROI. p-value < 0.05 was considered statistically significant and indicated with one asterisk.

4.1.5.2. Cellular uptake studies of CUR-AgNP by Confocal Raman Mapping

Raman mapping has been used as a method to get details on the chemical fingerprints of distinct subcellular compartments. Based on the distinctive chemical characteristics the nucleus, cytoplasm, and other cellular organelles can be visualized. Confocal Raman microscopy was used to measure the dynamics of cellular uptake and localization of the CUR-AgNP with nanoscale resolution in HCT- 116 cells. The cellular uptake was evaluated at two different time points (2 hours and 4 hours) and are shown in figure 4.15 B & D. Figures 4.15 A & C indicate the white light image of HCT-116 cells treated with CUR-AgNP for 2 hours and 4 hours, where the white box represents the region selected for Raman mapping. The cells were mapped utilizing the absorption of the C-H stretching bands at 2800–3000

cm^{-1} (figure 4.15E). The prominent peaks at 2928 cm^{-1} and 2887 cm^{-1} are attributed to the –CH stretching modes of protein and lipid groups (Talari et al., 2015). The peak at 1653 corresponds to the carbonyl stretch (C=O) of amide I and C=C stretching of lipids (Talari et al., 2015). Another peak, at 1442 cm^{-1} was assigned to the $–CH_2$ bending mode of proteins and lipids (Talari et al., 2015). The presence and distribution of the CUR-AgNP were mapped utilizing the fluorescence of the CUR-AgNP (figure 4.15 B & D). At 2 hours, the cells showed higher uptake of the CUR-AgNP compared to 4 hours, where the CUR-AgNP was found to be distributed throughout the cytoplasm. The result obtained in confocal Raman mapping supports the CLSM data.

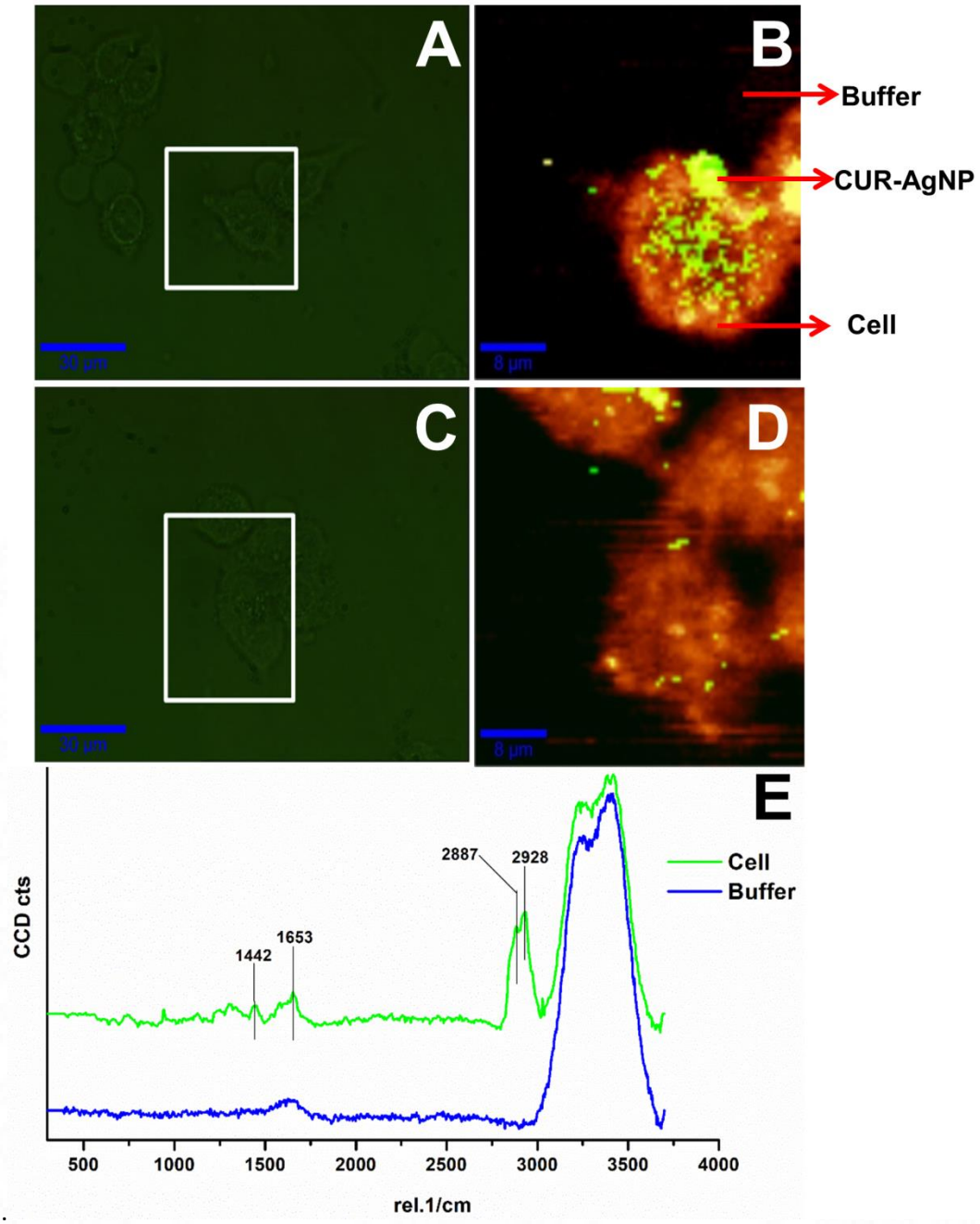

Figure 4.15. Raman chemical spectral map of HCT-116 cells treated with CUR-AgNP for 2 hours (B) and 4 hours (D) showing the uptake of CUR-AgNP; White light image of HCT-116 cells treated with CUR-AgNP for 2 hours (A) and 4 hours (C) where the white box represents the region selected for Raman mapping. (Yellow – Cells mapped utilizing the intensity in the C-H stretching band at the range 2800 – 3000 cm^{-1}; Green – distribution of CUR-AgNP in the cytoplasm mapped by fluorescence of CUR-AgNP). Raman spectra of the cell cluster and buffer cluster demixed from the hyperspectral chemical map. (E) Spectra for the range 4000-300 cm^{-1}.

4.1.5.3. Cytotoxicity of curcumin and CUR-AgNP toward colon cancer cells

The *in vitro* cytotoxicity of curcumin and CUR-AgNP against the colon cancer cells, HCT-116 and Caco-2 were evaluated by MTT assay (figure 4.16A & B). Curcumin and CUR-AgNP exhibit dose-dependent cytotoxicity in both HCT-116 and Caco-2 cells. The IC_{50} values of curcumin towards HCT-116 and Caco-2 cells were found to be 13 μg/mL and 15 μg/mL. The IC_{50} values of the CUR-AgNP towards HCT-116 were found to be 73 μg/mL. While in the case of Caco-2 cells, the IC_{50} was achieved at a higher concentration of 204 μg/mL. HCT-116 cells were more sensitive toward the cytotoxic activity of the CUR-AgNP, while Caco-2 cells were found to be resistant to the cytotoxic activity. A similar trend was reported by Abd-Elnaby et al. and Shawkey et al. for silver nanoparticles prepared from the marine actinomycete and *Citrullus colocynthis*, where the nanoparticles were found to be sensitive towards HCT-116 cells and resistant towards Caco-2 cells (Abd-Elnaby et al., 2016; Shawkey et al., 2013). Compared to curcumin the CUR-AgNP was found to be less effective in achieving cytotoxicity against colorectal cancer cells. So, a higher concentration of CUR-AgNP was required to achieve cytotoxicity against colorectal cancer cells.

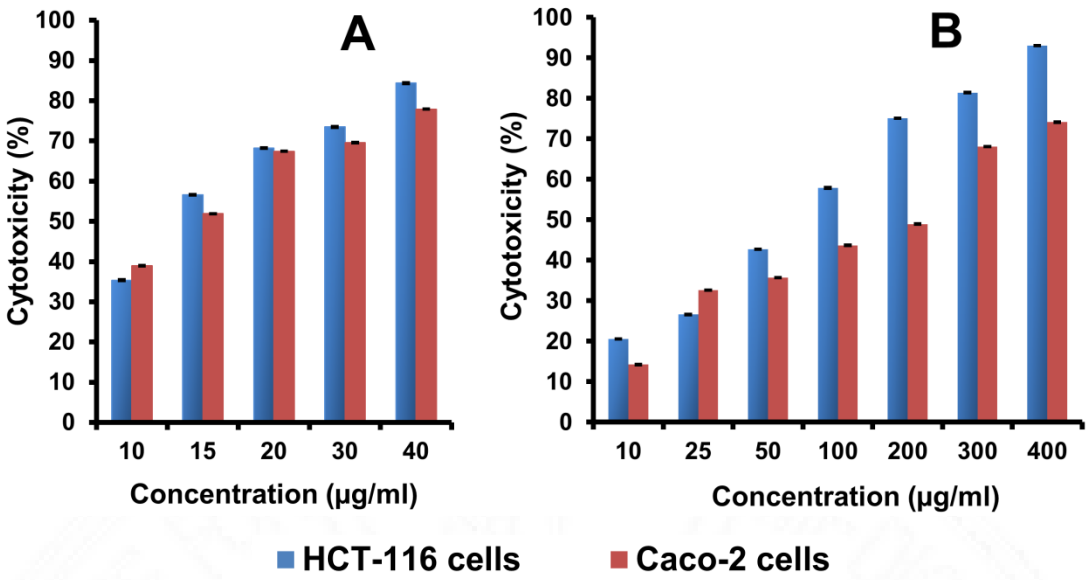

Figure 4.16. Cytotoxicity exhibited by: (A) curcumin and (B) CUR-AgNP on HCT-116 and Caco-2 cells.

4.1.6. Limitation of CUR-AgNP system

Curcumin bound to the CUR-AgNP was able to exhibit substantial stability in intestinal pH (7.4) compared to free curcumin. However, a higher concentration of CUR-Ag NP is required to elicit cytotoxicity in colorectal cancer cells. This limits the application of CUR-AgNP for colorectal cancer treatment. Due to this reason, we haven't further proceeded with this system and have not carried out the interactions of CUR-AgNP with the simulated intestinal microenvironment.

4.2. System II: Lauric acid solid lipid nanoparticles

Solid lipid nanoparticles (SLN) have gained more interest owing to their non-toxicity, biocompatibility, and biodegradability. Lauric acid (LA), a medium-chain saturated fatty acid that possesses high intestinal absorption was selected for the synthesis of solid lipid nanoparticles (LA-SLN). A fluorescent lipophilic dye rhodamine B (RhB) was incorporated into LA-SLN as a model drug. The interactions of LA-SLN with the intestinal microenvironment (protein corona and mucus) were

studied. The cellular uptake of RhB-loaded LA-SLN and free RhB dye was studied to evaluate the efficacy of LA-SLN as a carrier for intracellular drug delivery.

4.2.1. Physicochemical characterization

4.2.1.1. Determination of particle size and zeta potential

The hydrodynamic diameter of LA-SLN and R-LA-SLN were found to be 21.42 ± 1.83 nm and 21.70 ± 1.09 nm, respectively, as revealed by particle size analysis (n=3, figure 4.17 A & B). The polydispersity index (PDI) of LA-SLN and R-LA-SLN was found to be 0.297 ± 0.006 and 0.293 ± 0.001, respectively (n=3). The particle size and PDI, also known as size distribution are the two key factors that affect drug release and can also influence therapeutic efficacy (Ahmed et al., 2020). Since lyophilized R-LA-SLN was used for cell uptake studies, the dispersibility of the R-LA-SLN after lyophilization was evaluated by the dynamic light scattering technique. The hydrodynamic size of the redispersed lyophilized R-LA-SLN was 19.59 ± 0.2 nm, with a PDI of 0.275 ± 0.009 (n = 3), indicating that the lyophilized R-LA-SLN had been redispersed successfully (figure 4.17C). It is interesting to note that after freeze-drying and encapsulation the particle size and PDI did not change much.

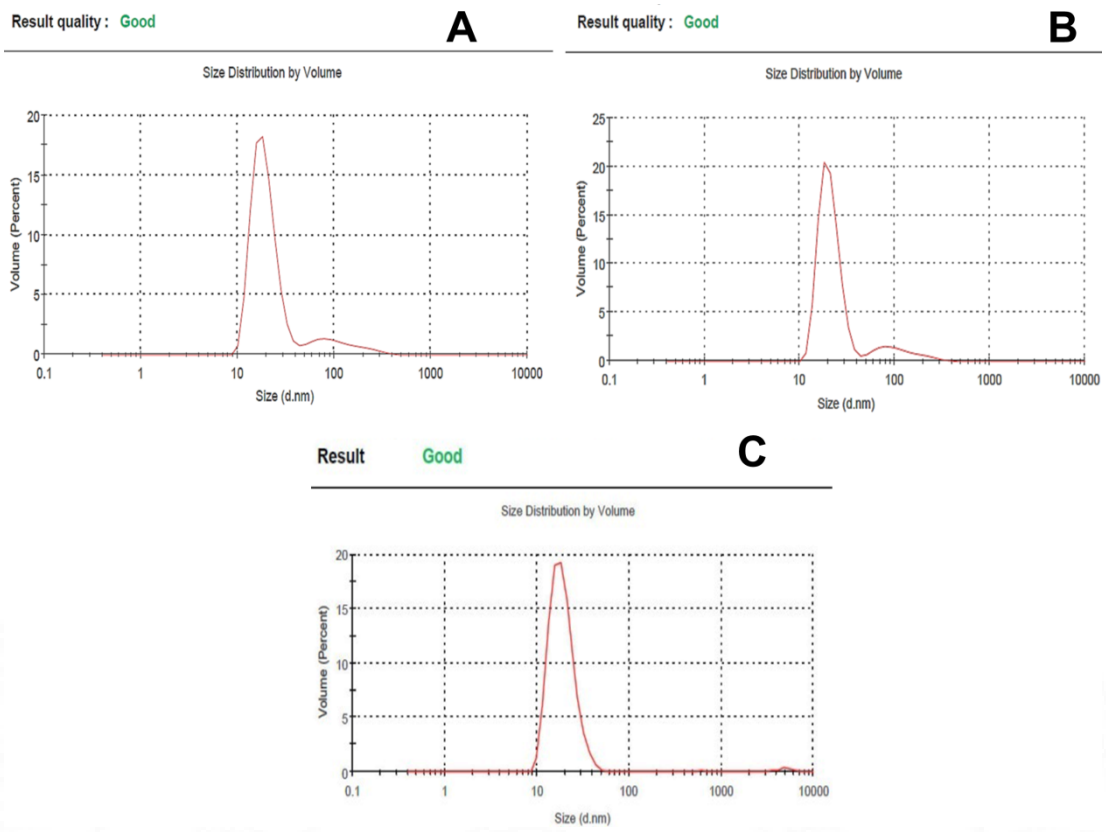

Figure 4.17. Representative data displaying the hydrodynamic diameter of: (A) LA-SLN; (B) R-LA-SLN and (C) Resuspended lyophilized R-LA-SLN.

Oral drug delivery carriers should pass through the various pH conditions of the GI tract. So, it is critical to assess their stability at various pH conditions of the GI tract. Dynamic light scattering (DLS) was used to study the stability of LA-SLN and R-LA-SLN in different pH conditions of the GI tract (pH 1.2 - stomach; pH 6.8 - small intestine; and pH 7.4 - colon). DLS was used not only to determine the size of nanoparticles in suspension but also to determine their stability under various pH conditions (Carvalho et al., 2018). PDI is a critical parameter that gives an idea of the physical stability of nanosuspension (Mura et al., 2021). The particle size distribution of the samples, given as PDI, is a measure of sample heterogeneity (Onugwu et al., 2022). The hydrodynamic diameters and PDI of LA-SLN at pHs 1.2, 6.8, and 7.4 were found to be 27.83 ± 0.48 nm (PDI = 0.30 ± 0.002), 26.54 ± 2.17 nm (PDI =

0.456 ± 0.003), and 25.14 ± 0.47 nm (PDI = 0.472 ± 0.002), respectively (figure 4.18). The hydrodynamic diameters and PDI of R-LA-SLN at pHs 1.2, 6.8, and 7.4 were 28.11 ± 1.47 (PDI = 0.47 ± 0.11), 24.29 ± 2.93 nm (PDI = 0.49 ± 0.07), and 26.19 ± 0.42 nm (0.456 ± 0.0007), respectively (figure 4.18). Slight changes in particle sizes were noted for LA-SLN and R-LA-SLN at different pH conditions. Comparing LA-SLN and R-LA-SLN suspensions, the PDI values tend to increase with an increase in pH. This increase in PDI denotes slight aggregation of the particles. However, Cho et al. stated that PDI values less than 0.3 are considered optimal, while values less than 0.5 are within acceptable limits (Cho et al., 2013). The PDI of the LA-SLN and R-LA-SLN were found to be within acceptable limits in different pH conditions (1.2, 6.8, and 7.4).

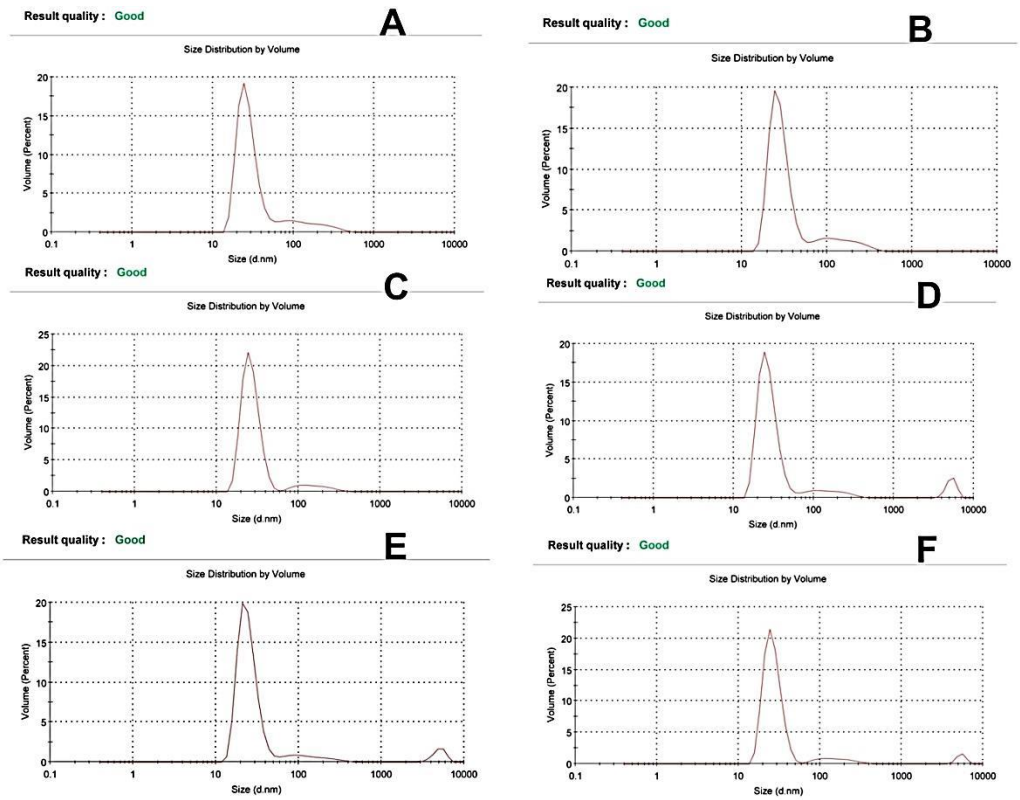

Figure 4.18. Representative data displaying the hydrodynamic diameters of LA-SLN in different pH conditions: (A). pH 1.2, (C). pH 6.8 and (E). pH 7.4. The hydrodynamic sizes of R-LA-SLN in different pH conditions: (B). pH 1.2, (D) pH 6.8, and (F). pH 7.4.

Zeta potential represents the surface charge of a particle in a given environment. It is a key factor that indicates the stability of the nanoparticle suspension. LA-SLN suspension in the water had a zeta potential of -29.6 ± 0.78 mV (n = 3) whereas R-LA-SLN suspension had a zeta potential of -22.36 ± 0.96 mV (n = 3). This difference indicates that the positively charged RhB dye got successfully incorporated within the R-LA-SLN (Figure 4.19 A & B).

The repulsion among the negatively charged LA-SLN provides stability and avoids nanoparticle aggregation (Honary and Zahir, 2013). The charge of the SLN in the biological system was anticipated to be simulated by the zeta potential of LA-SLN suspended in phosphate buffer (pH 7.4). The zeta potential is mainly affected by pH,

ionic strength, and solution composition (Zhu et al., 2007). The zeta potential of LA-SLN changed to -9.4 ± 0.62 mV (n = 3) when they were taken in 0.01 M phosphate buffer saline (pH 7.4). The increased counterion concentration in 0.01 M PBS may be the reason for this change in zeta potential. The ionic environment of the LA-SLN was affected by the higher conductivity, due to the presence of counterions. The electrical double layer can be more strongly held by excess counter ions, which causes the electrical double layer to shrink. The ionic strength of the surrounding medium was reported to be inversely proportional to the thickness of the electrical double layer around the particle (Midekessa et al., 2020). The repulsive forces between LA-SLN were reduced when the conductivity of the dispersion medium increased. This led to greater inter-particulate interactions due to van der Waals forces and interfered with the stability of the LA-SLN colloidal system resulting in an increased zeta potential value.

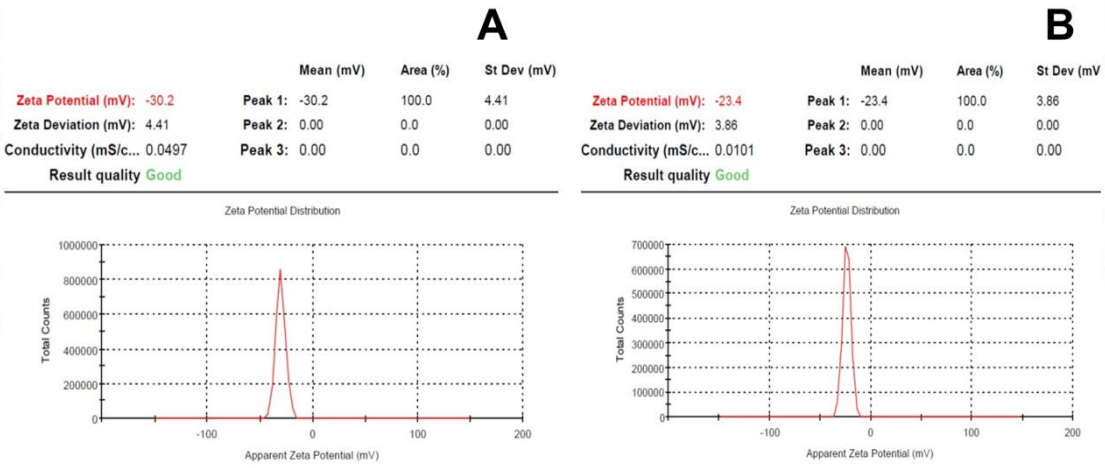

Figure 4.19. Representative data displaying the zeta potential of: (A) LA-SLN and (B) R-LA-SLN.

4.2.1.2. Transmission electron microscopy (TEM) analysis

TEM analysis showed that morphologically LA-SLN and R-LA-SLN were spherical (figure 4.20). The majority of the particles were in the 10-25 nm range, with a few particles up to a size of 40 nm, which is consistent with DLS data. Under TEM, no visible aggregation of the LA-SLN and R-LA-SLN was observed (Figure 4.20 A & B).

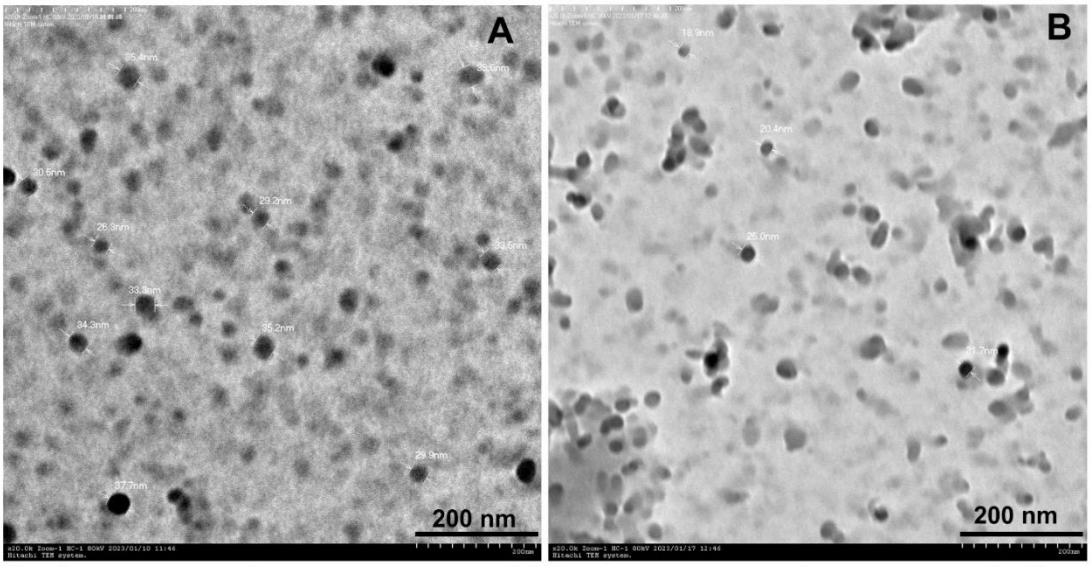

Figure 4.20. TEM images of: (A) LA-SLN and (B) R-LA-SLN

4.2.1.3. FTIR analysis

Poloxamer 407 was the surfactant used for the preparation of the LA-SLN and R-LA-SLN. The solid lipid core of the SLN was stabilized by a layer of surfactant. To confirm the presence of the surfactant layer the IR spectrum of poloxamer 407 was compared with the spectra of R-LA-SLN and LA-SLN. Figure 4.21A displays the FTIR spectra of the LA, Poloxamer 407, and LA-SLN. The FTIR spectrum of LA displayed distinctive peaks at 2921, 2853, 1702, 1299, 936, and 724 cm^{-1}. The peaks at 2921 cm^{-1} and 2853 cm^{-1} were attributed to stretching vibrations of the $–CH_2$ and $–CH_3$ groups, respectively. The carbonyl group C=O was responsible for the peak at

1702 cm^{-1}, whereas the stretching vibrations of C–O were responsible for the peak at 1299 cm^{-1}. The peak at 936 cm^{-1} denotes the wagging vibration of the –OH functional group of LA whereas the peak at 724 cm^{-1} indicates the out-of-plane bending vibration of the C–H groups. The result obtained was similar to that of a previously published report (Sarı et al., 2009). The FTIR spectrum of the surfactant, Poloxamer 407, exhibited distinctive peaks at 2896, 1346, and 1109 cm^{-1}. The peak at 2896 cm^{-1} denotes the C–H stretching of the aliphatic chain whereas the peaks at 1346 and 1109 cm^{-1} are related to in-plane O–H bend and C–O stretch (Karolewicz et al., 2017).

Figure 4.21B displays the FTIR spectra of the LA-SLN, R-LA-SLN, and RhB. LA-SLN and R-LA-SLN displayed distinctive peaks of LA with slight shifts at 2923 cm^{-1}, 2854 cm^{-1}, and 1733 cm^{-1}. In the spectrum of LA-SLN, the characteristic peaks of the surfactant, poloxamer 407, were found at 2896 cm^{-1}, 1346 $cm^{-1,}$ and 1109 cm^{-1}, respectively. This reveals that the stability of the LA-SLN was contributed by the surfactant layer on their surfaces. The LA-SLN and R-LA-SLN were found to have identical FTIR spectra (figure 4.21C). The concentration of RhB dye loaded in the R-LA-SLN was very low. As a result, the prominent RhB peaks were not well evident in the spectrum after RhB encapsulation in LA-SLN. However, a detailed examination of the FTIR spectra revealed a small broad peak at 1583 cm^{-1} in R-LA-SLN that is absent in LA-SLN, confirming the presence of RhB in R-LA-SLN. The band at 1583 cm^{-1} in RhB is attributed to the vibrational motion of the phenyl group (Sharma, 2018).

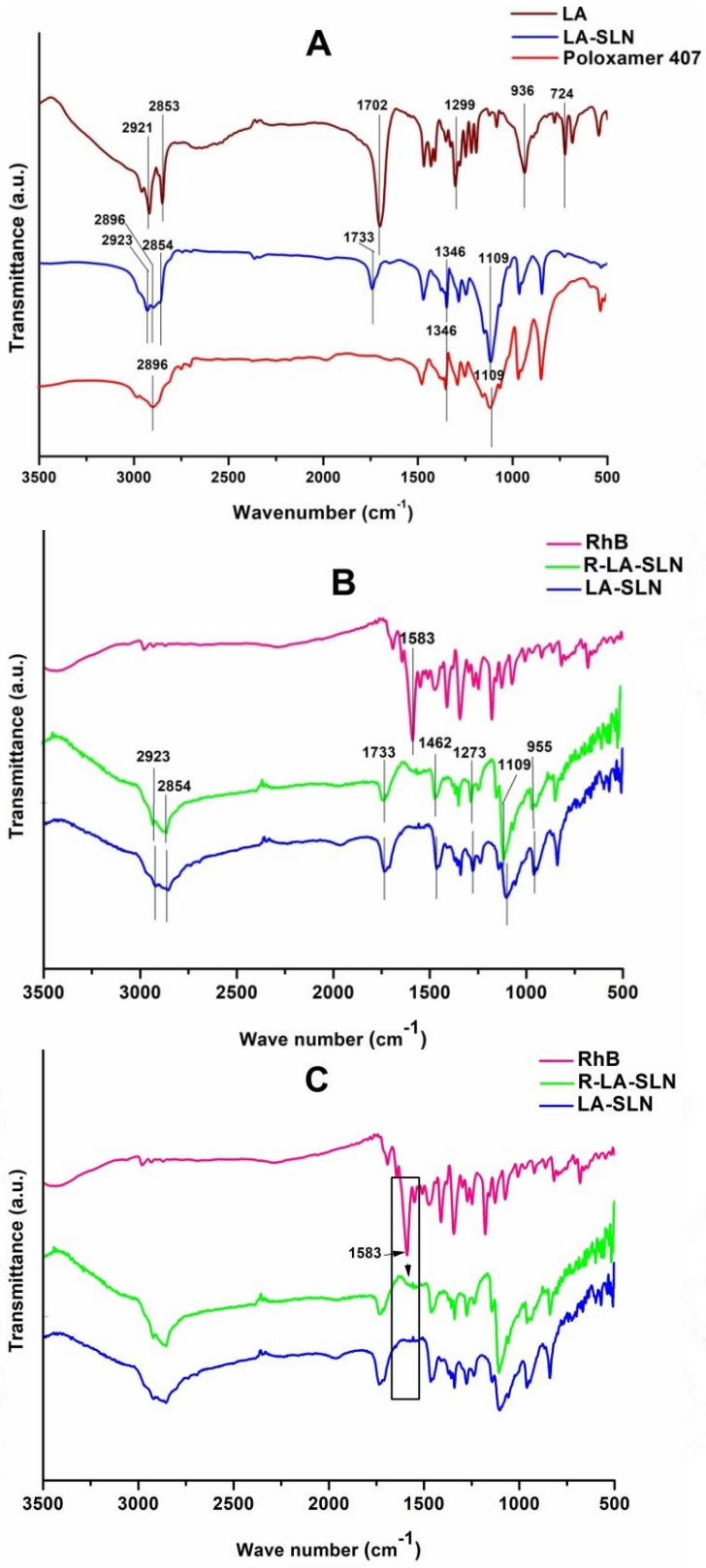

Figure 4.21. (A) FTIR spectra of LA, Poloxamer 407, and LA-SLN; (B & C) FTIR spectra of RhB, R-LA-SLN, and LA-SLN.

4.2.1.4. Confocal Raman Microscope analysis

Figure 4.22 displays the Raman spectra of RhB, LA-SLN, and R-LA-SLN. The distinctive peaks of LA (1481, 1290, 1145, 1081, 926, and 856 cm^{-1}) were found in both LA-SLN and R-LA-SLN. The peak at 1481 cm^{-1} was assigned to the $–CH_2$ scissoring vibration and the peak at 1290 cm^{-1} was attributed to the $–CH_2$ twisting vibration. The peaks at 1145 and 1081 cm^{-1} were attributed to C–C stretching vibrations. The doublet peaks at 856 and 926 cm^{-1} correspond to $–CH_2$ rocking vibrations. The Raman spectra obtained for LA were found to be similar to that of a previously published report (De Gelder et al., 2007). In LA-SLN, the presence of a peak at 1688 cm^{-1} was attributed to the stretching vibration of the carbonyl (C=O) group. In the case of R-LA-SLN, peak shifts were found at 1662 cm^{-1}, 1473 cm^{-1}, and 933 cm^{-1}, and additional peaks were observed at 541 cm^{-1} and 588 cm^{-1} showing the successful incorporation of RhB in the R-LA-SLN. The peak at 1651 cm^{-1} in RhB was attributed to aromatic C=C stretching and C–C bending. The peaks in RhB and R-LA-SLN from 580 to 420 cm^{-1} are associated with both in-plane and out-of-plane deformations of the benzene ring. In RhB, the peak at 1516 cm^{-1} was assigned to aromatic C-H bending, and the peak at 1360 cm^{-1} was due to aromatic C–C bending. The peaks at 1291 and 1205 cm^{-1} were attributed to the C–C bridge band stretching and aromatic C–H bending. The peak at 632 cm^{-1} was assigned to xanthene ring puckering as reported by Lin et al. (Lin et al., 2015).

In the case of Raman spectra, no evident peak of RhB was observed in R-LA-SLN at 1360 cm^{-1} since the concentration of RhB is low. Interestingly, after the incorporation of RhB into LA-SLN the peak at 1357 cm^{-1} was shifted to 1354 cm^{-1}.

Furthermore, the broad peak in LA-SLN (1357 cm^{-1}) tends to become sharper in R-LA-SLN (1354 cm^{-1}). This could be due to the overlapping of the RhB peak 1360 cm^{-1}.

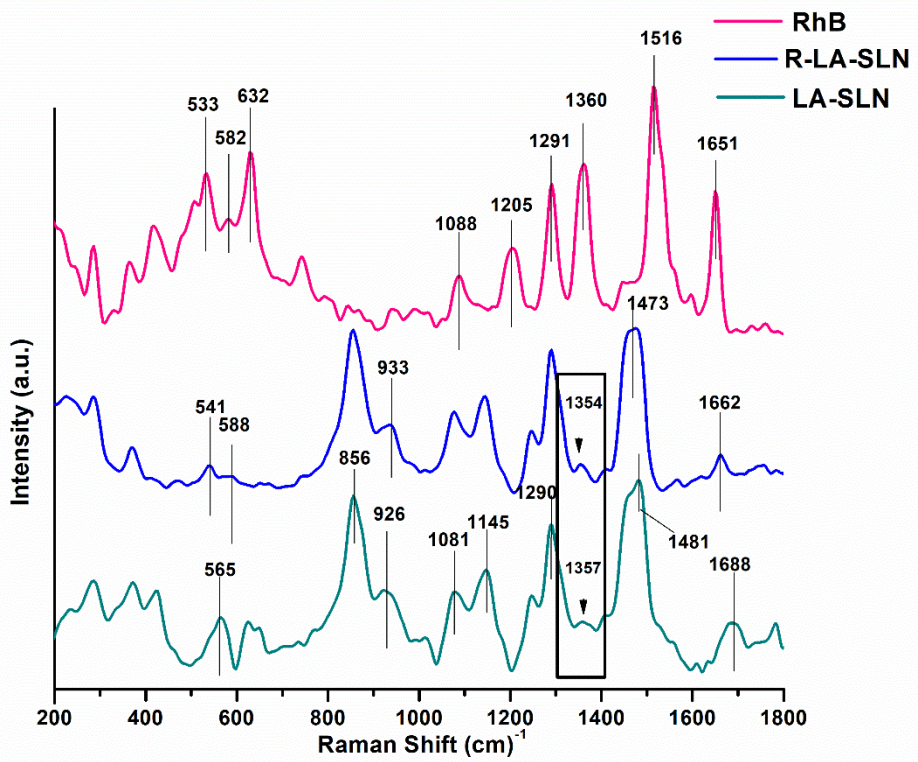

Figure 4.22. Raman spectra of LA-SLN, R-LA-SLN, and RhB.

4.2.1.5. Differential Scanning Calorimetry (DSC) analysis

Table 4.2 summarizes the melting and enthalpy data for LA, Poloxamer 407, LA-SLN, and R-LA-SLN obtained by Differential Scanning Calorimetry. LA displayed a sharp endothermic peak at 45.18 °C owing to its melting and the melting point of Poloxamer 407 was observed at 55.62 °C (figure 4.23 A & B). The melting temperatures of LA and its SLN were found to be different when the thermograms of the two were compared. The increased melting point of LA-SLN compared to LA could be due to the adsorbed Poloxamer 407 surfactant molecules. A similar trend was previously reported in the literature (Patel et al., 2020). The sharp endothermic

peak of LA displays fast melting with a large enthalpy change (figure 4.23A). Conversely, SLN formulations tend to melt slowly with lower enthalpy changes (figure 4.23 C & D). This may be due to the presence of polydispersed nanoparticles, that is particles with different dimensions, leading them to melt at a slightly higher temperature (Shah et al., 2014). The melting points of both LA-SLN and R-LA-SLN were observed to be very close signifying the fact that RhB dye has little interaction with the LA-SLN. These systems can effectively be used as drug carriers as they have melting points that are significantly higher than 40 °C so they can remain solid at body temperature.

Additionally, DSC analysis provides information regarding crystallization behavior and lipid crystal disorder. The lipid crystals disorder was estimated using the melting temperature range, which was calculated from the difference between the melting (T_m) and the onset of melting temperatures (T_o) (Peres et al., 2016).

$$Lipid\ crystal\ disorder = T_m - T_o \qquad Eqn.\ 22$$

Increased (T_m - T_o) values indicate more disorder in the lipid crystals (Severino et al., 2011). The value of (T_m - T_o) for LA was 1.9, whereas the values for LA-SLN and R-LA-SLN were 6.09 and 4.71, respectively. The increase in the T_m - T_o value of LA-SLN and R-LA-SLN indicates that the crystal order in the normal lipid got disturbed during the SLN formation. The crystallinity of LA (χ_c) was calculated using the equation given below (Peres et al., 2016):

$$\chi_c = \frac{\Delta H_m}{\Delta H_{pure\ LA}} \times 100 \qquad Eqn.\ 23$$

Where the melting enthalpies of the sample and pure LA are denoted by ΔH_m and $\Delta H_{Pure\ LA}$, respectively. Pure LA had an enthalpy of 178.3 J/g which was taken as 100% crystalline. In LA-SLN, the crystallinity of LA was 36.3 % (ΔH_m= 64.81 J/g), while it was 43 % in R-LA-SLN (ΔH_m= 78.24 J/g). The method employed to prepare the SLN formulation can partially impede the crystallization of LA (Peres et al., 2016). Barbosa et al. reported that the lipid within the SLN can undergo considerable rearrangement during the preparation process, resulting in a less ordered structure (Barbosa et al., 2018).

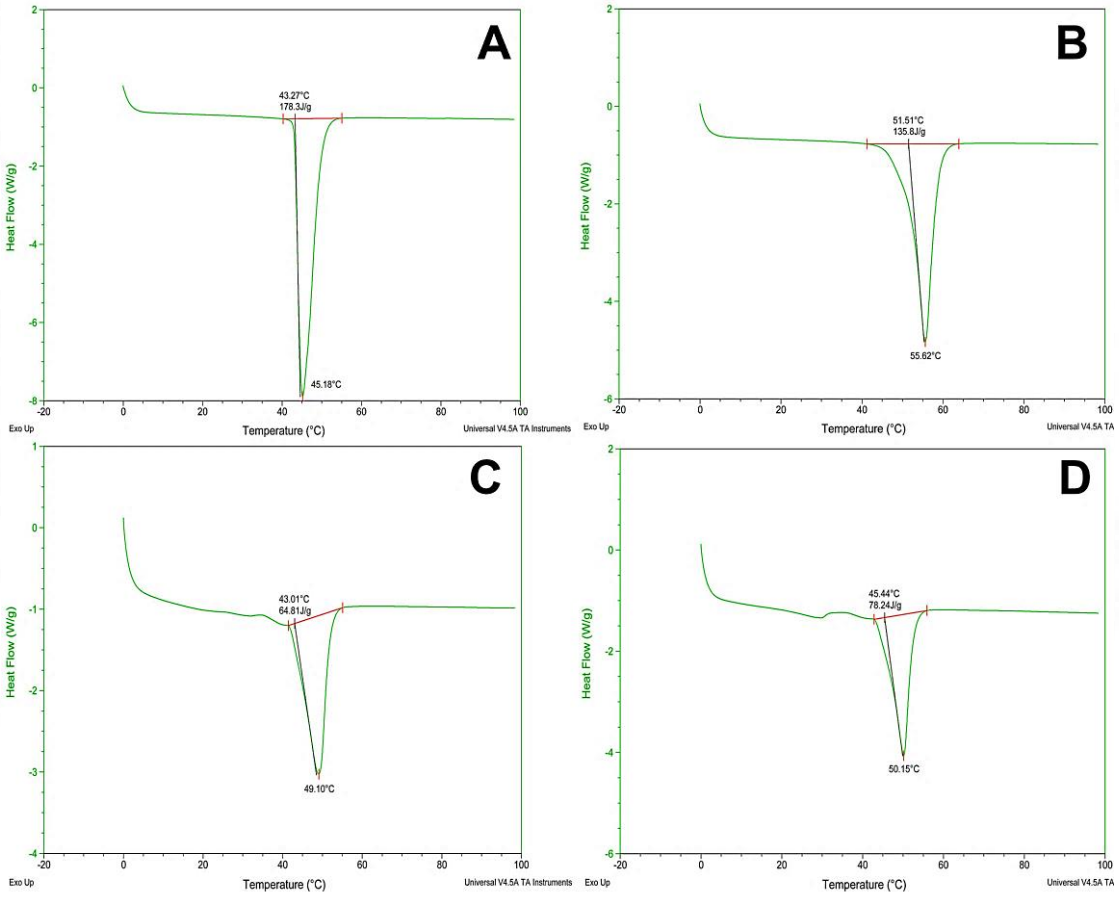

Figure 4.23. Differential Scanning Calorimetry thermograms of: (A) LA; (B) Poloxamer 407; (C) LA-SLN, and (D) R-LA-SLN.

Table 4.2. Melting parameters of LA, LA-SLN, R-LA-SLN, and Poloxamer 407

Sample	Melting Point (°C) T_m	Onset Temperature (°C) T_o	Enthalpy (J/g)
LA	45.18	43.27	178.3
LA-SLN	49.10	43.01	64.81
R-LA-SLN	50.15	45.44	78.24
Poloxamer 407	55.62	51.51	135.8

4.2.2. Drug loading and entrapment efficiency

Solid lipid nanoparticles can entrap both hydrophilic and hydrophobic drugs (Rivolta et al., 2011). The important factor to consider while designing SLN for drug encapsulation is lipid crystallinity (Peres et al., 2016). The loading of R-LA-SLN with different concentrations of RhB dye (1 mg, 5 mg, and 10 mg) was found to be 10.2, 42.6, and 59.7 μg/mg lipid. Increased dye concentration may have a negative impact on the cells and cellular uptake studies. As a result, R-LA-SLN loaded with 1 mg RhB was used in all studies. R-LA-SLN had an entrapment efficiency of 80.31 ± 0.18 % with RhB loading of 10.2 ± 0.02 μg/mg lipid. The greater entrapment efficiency of the SLN could be attributed to its lower crystallinity and less ordered matrix. The decreased crystallinity of the lipid favors a reduction in the rate of drug loss from the carrier during storage, which in turn enhances its shelf life (Pardeike et al., 2009). Galvao et al. reported that a less-ordered matrix has more voids and vacancies that can hold a large number of drug molecules in its lattice structure (Galvão et al., 2020). Another factor that leads to improved entrapment efficiency is the lipophilic nature of the RhB, therefore it interacts strongly with the lipid matrix (Parvez et al., 2020).

4.2.3. *In vitro* release of RhB from R-LA-SLN

The release profile of RhB from R-LA-SLN was evaluated for 24 hours at pH 7.4 (figure 4.24A). As shown in figure 4.24A, the dye release was only 39 % in the first hour and it increased to 52 % in the fourth hour. The maximum drug release (71.9 %) was observed at the 10^{th} hour. The drug release from LA-SLN was biphasic, with an initial burst release (25.7 ± 4.2 %) occurring in the first 0.25 hours followed by a sustained release until the 10^{th} hour. The remaining RhB was found to be entrapped within the SLN. The presence of adsorbed RhB on the surface of the SLN may have contributed to the initial burst release (Kushwaha et al., 2013). The sustained release pattern would aid in keeping an effective amount of the drug within the therapeutic window at the microenvironment intended for release. This release pattern also serves to reduce the potential harmfulness of drugs to healthy cells (Din et al., 2017). It has been also reported that due to the limited mobility of molecules in the solid state, SLN can more accurately regulate the release of their therapeutic payloads (Tenchov et al., 2021).

The drug release kinetics were studied by fitting the release data to different mathematical models such as zero order, first order, Higuchi model, and Korsmeyer-Peppas model using DD solver, an MS Excel add-in software package. Table 4.3 lists the coefficient of determination (R^2) calculated for the different mathematical models. The Korsmeyer-Peppas model fits best with an R^2 value of 0.985 (figure 4.24B). The diffusion exponent 'n' in the Korsmeyer-Peppas equation explains the transport mechanism of the drug. Duong et al. reported that when $n \leq 0.5$, it denotes Fickian diffusion, $0.5 < n \leq 0.9$ denotes anomalous or non-Fickian diffusion, and $n \geq$

1 denotes case-II transport (Duong et al., 2019). Fickian diffusion has no boundaries, whereas non-Fickian diffusion has a sharp boundary separating the region of the loaded drug (Albayati and Abd Alkadir, 2019). The calculated value of 'n' in this case was 0.222, indicating that the release mechanism was Fickian diffusion in PBS at pH 7.4. The mechanism of release appears to be controlled by diffusion (Silva et al., 2012).

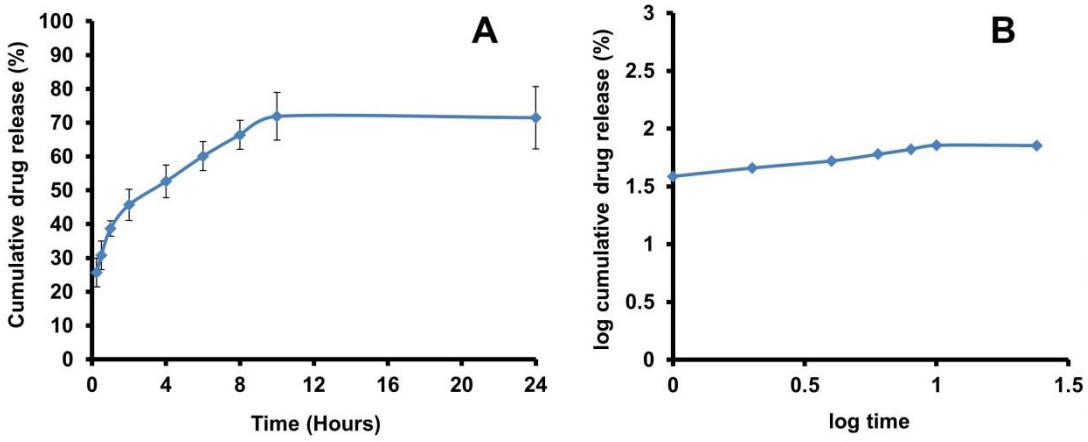

Figure 4.24. RhB release profile from R-LA-SLN in phosphate buffer of pH 7.4 (A); Drug release kinetics fitting the Korsmeyer-Peppas model (B).

Table 4.3. Parameters of various mathematical models after fitting the release kinetics of RhB from R-LA-SLN

Zero order		First order		Higuchi		Korsmeyer-Peppas		
R^2	K	R^2	K	R^2	K	R^2	K	n
0.7250	2.3130	0.4517	0.0341	0.8999	20.72	**0.985**	39.075	0.222

4.2.4. Cellular interaction of LA-SLN with colorectal cancer cells

4.2.4.1. Cell viability studies with LA-SLN in colon cancer cells

The cell viability was investigated in two different colon cancer cells, HCT-116, and Caco-2 cells. The cytotoxic response of LA-SLN against HCT-116 and Caco-2 cells evaluated by MTT assay is shown in figure 4.25 A & B. The results showed that when the concentration of LA-SLN was 20 µg/mL in HCT-116 cells, the cell

survival rate was close to 100 %. The cell viability reduced from 95 ± 0.04 % to 87 ± 0.02 % as the LA-SLN concentration increased from 40 µg/mL to 100 µg/mL. In the case of Caco-2 cells, a significant reduction in cell viability was observed only at 800 µg/mL and found to be more resistant to LA-SLN treatment. Even at a higher concentration of 800 µg/mL, both cells were found to be non-toxic to LA-SLN. The results revealed that LA-SLN can be used as a good carrier for drug delivery applications.

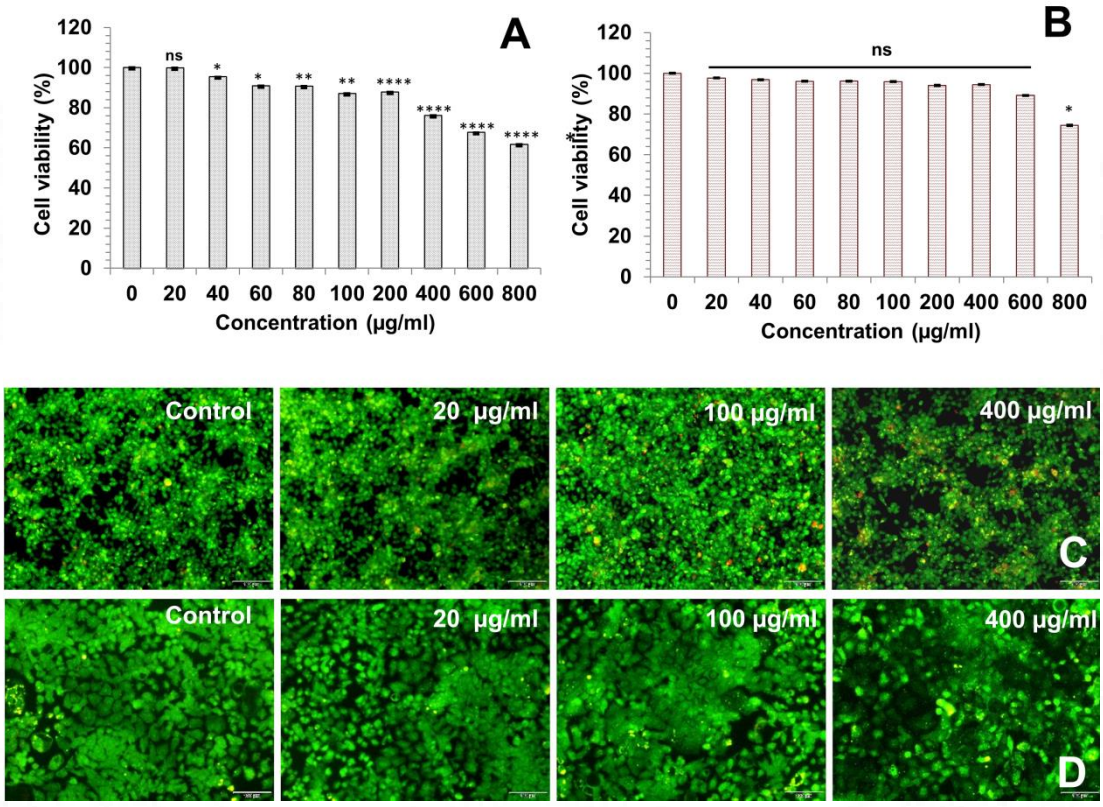

Figure 4.25. Cell viability assessment using MTT assay for studying the response of different concentrations of LA-SLN to HCT-116 cells (A) and Caco-2 cells (B). LIVE/DEAD assay - fluorescent images of HCT-116 (panel C) and Caco-2 cells (panel D) following treatment with various concentrations of LA-SLN. In LIVE/DEAD staining acridine orange stains all nucleated live cells green and ethidium bromide stains all dead cells red (scale bar-100 µm). P value < 0.05 is considered statistically significant; p-value ≤ 0.0001 is denoted with four asterisks; p-value ≤ 0.05 is denoted with one asterisk; p-value > 0.05 is statistically not significant and denoted as 'ns'.

LIVE/DEAD assay further supports the MTT assay. Figure 4.25 C & D show representative images of the responses of different doses of LA-SLN on HCT-116 and Caco-2 cells. In the LIVE/DEAD cell viability assay, acridine orange penetrates all cells and stains the nuclei green. On the other hand, ethidium bromide only enters cells when the cytoplasmic membrane integrity is compromised, leaving the nuclei stained red. At a higher concentration of LA-SLN (400 μg/mL), the number of dead cells was found to be lower in both HCT-116 and Caco-2 cells, confirming the low cytotoxicity of LA-SLN.

4.2.4.2. Cellular uptake of R-LA-SLN and RhB dye by HCT-116 and Caco-2 cells

Figure 4.26 depicts the morphological features of the colon cancer cells HCT-116 and Caco-2 cells used for the study. The cells were stained with rhodamine-phalloidin (red) for F-actin and DAPI (blue) for the nucleus. The distribution of actin filaments in HCT-116 (figure 4.26 A & B) and Caco-2 (figure 4.26 C) cells was studied using a confocal laser scanning microscope (CLSM).

CLSM was used to assess the cellular uptake of R-LA-SLN and free RhB qualitatively. Figure 4.27 shows the fluorescence images obtained after incubating HCT-116 cells and Caco-2 cells with R-LA-SLN for 0.5, 1, 2, and 4 hours, respectively. Figure 4.28 shows fluorescence images obtained after incubating HCT-116 and Caco-2 cells with free RhB dye for 0.5, 1, 2, and 4 hours.

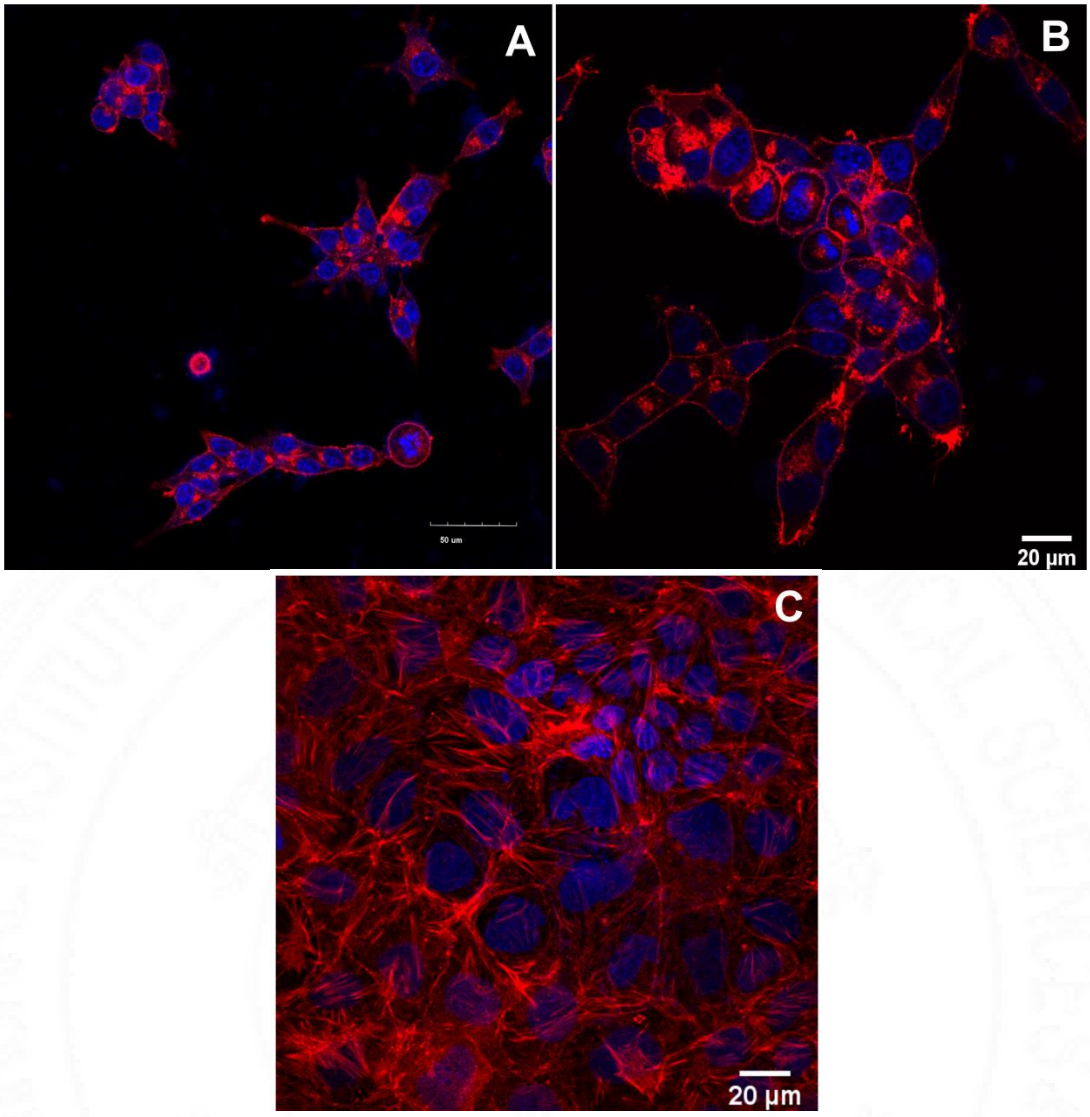

Figure 4.26. Morphological features observed for (A) HCT-116 cells at a magnification of 40X, (B) Caco-2 cells at a magnification of 60X, and (C) colon cancer cells at a magnification of 60X used in the study under a confocal laser scanning microscope. Cells were stained with Rhodamine phalloidin for F-actin (red) and DAPI for nuclear staining (blue).

R-LA-SLN was observed as distinct red dots in the cytoplasm of both HCT-116 and Caco-2 cells within the initial 0.5 hours of incubation (figure 4.27 A-H). Whereas the red fluorescence was found to be distributed throughout the intracellular space in the case of free RhB dye (figure 4.28 A-H).

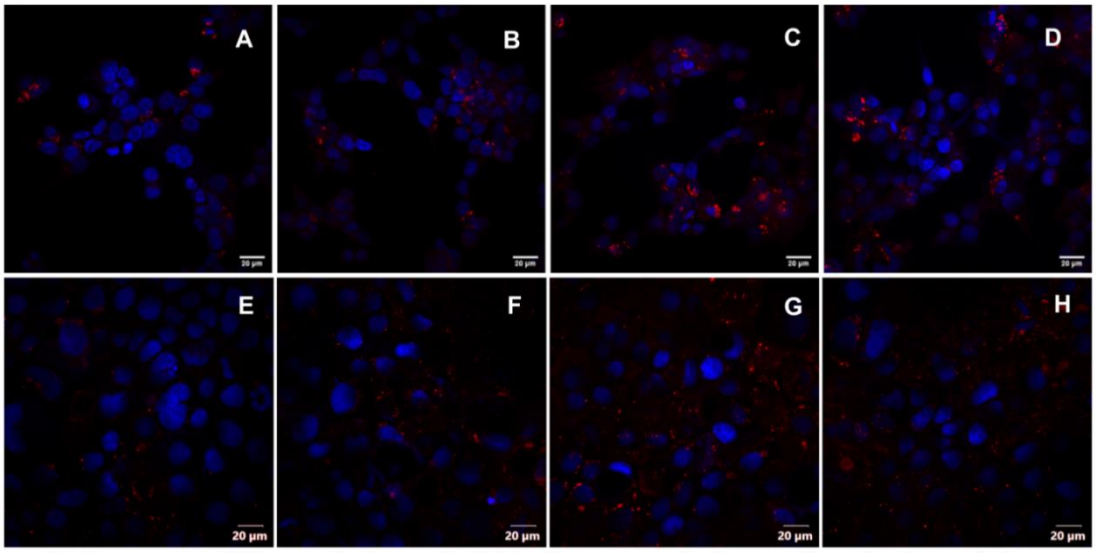

Figure 4.27. CLSM analysis of R-LA-SLN (Red) uptake by HCT-116 and Caco-2 cells over time. (A-D): Cellular uptake of R-LA-SLN in HCT-116 cells at 0.5, 1, 2, and 4 hours; (E-H): Cellular uptake of R-LA-SLN in Caco-2 cells at 0.5, 1, 2, and 4 hours. DAPI was used to stain the nucleus (blue).

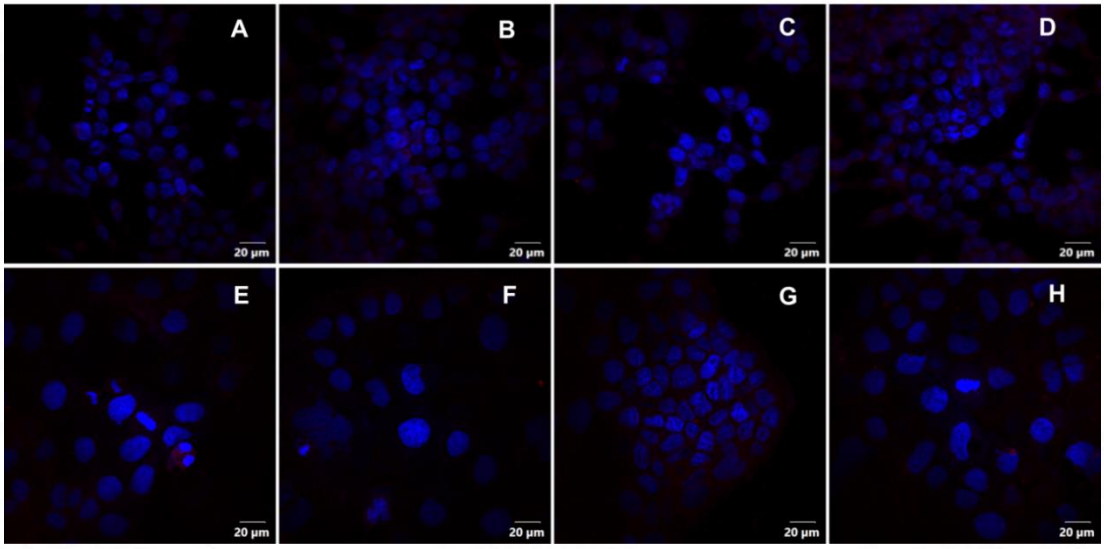

Figure 4.28. CLSM analysis of free Rhodamine B dye (Red) uptake by HCT-116 and Caco-2 cells over time. (A-D): Cellular uptake of free RhB dye in HCT-116 cells at 0.5, 1, 2, and 4 hours; (E-H): Cellular uptake of free RhB dye in Caco-2 cells at 0.5, 1, 2, and 4 hours. DAPI was used to stain the nucleus (blue).

The cellular uptake of R-LA-SLN and free RhB dye in HCT-116 and Caco-2 cells was calculated using ROI analysis (figures 4.29 and 4.30). The results show that R-LA-SLN cellular uptake is time-dependent in both HCT-116 and Caco-2 cells. The

fluorescence of R-LA-SLN occurred after a very short contact time (0.5 hours), reached its maximum fluorescence intensity at 2 hours, and was found to decrease after 4 hours of incubation (figure 4.29I). This could be due to R-LA-SLN exocytosis from the cells. Whilst free RhB dye displayed little fluorescence inside the cells indicating poor uptake by both HCT-116 and Caco-2 cells (figure 4.28). Cellular uptake of R-LA-SLN was twice in HCT-116 cells, at 0.5 and 2 hours compared to that of free RhB dye (figure 4.29I). Cellular uptake of R-LA-SLN was 2.5 times higher in Caco-2 cells at 0.5 hours and 5 times higher at 2 hours compared to free RhB dye (figure 4.30I).

The lipophilic nature of the SLN may be attributed to the increased cellular uptake of R-LA-SLN. The affinity between the fatty acid and the cell membrane was determined by the melting point of the fatty acid as well as the length and degree of carbon chain saturation (Tranchant et al., 1997). The cellular uptake of R-LA-SLN with a melting point of 50.15 ºC was found to be higher as cells favor the uptake of materials with a low melting point. Yuan et al. reported that monostearin SLN having a melting point of 55-60 ºC was found to have better cellular uptake compared to stearic acid SLN (melting point = 67 - 69 ºC) and ATO888 SLN (melting point = 68 ºC) (Yuan et al., 2008). It has also been reported that as the length of the carbon chain increased by two carbons, the rate of diffusion decreased by around 100 times (Hamilton, 1998). Since LA is a saturated medium-chain fatty acid with 12 carbons, it can diffuse more quickly across the cell membrane via a "flip-flop" mechanism.

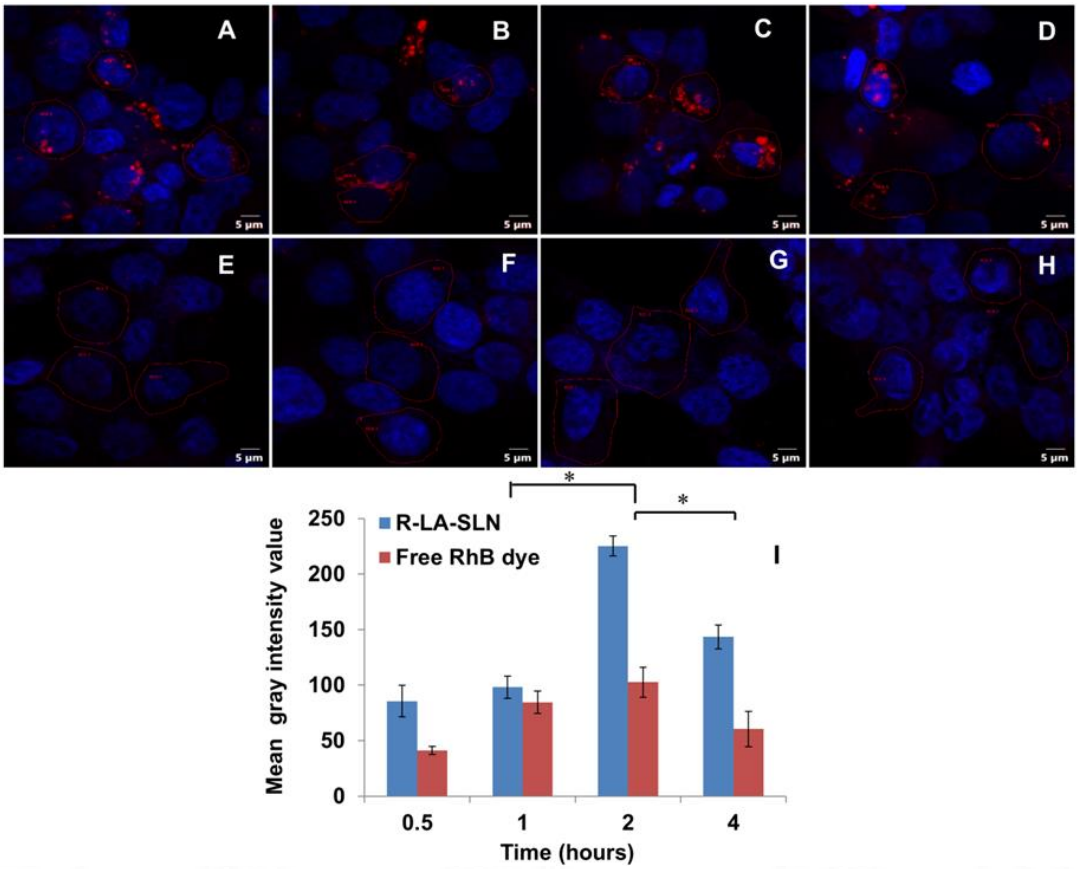

Figure 4.29. Cellular uptake of R-LA-SLN and free RhB by HCT-116 cells. (A-D): Confocal images of R-LA-SLN uptake at 0.5, 1, 2, and 4 hours. (E-H): Confocal images of free RhB dye uptake at 0.5, 1, 2, and 4 hours. DAPI was used to stain the nucleus (blue). I: Cellular uptake (indicated by mean gray intensity) estimated by drawing ROI. A p-value < 0.05 was considered statistically significant and is indicated with an asterisk.

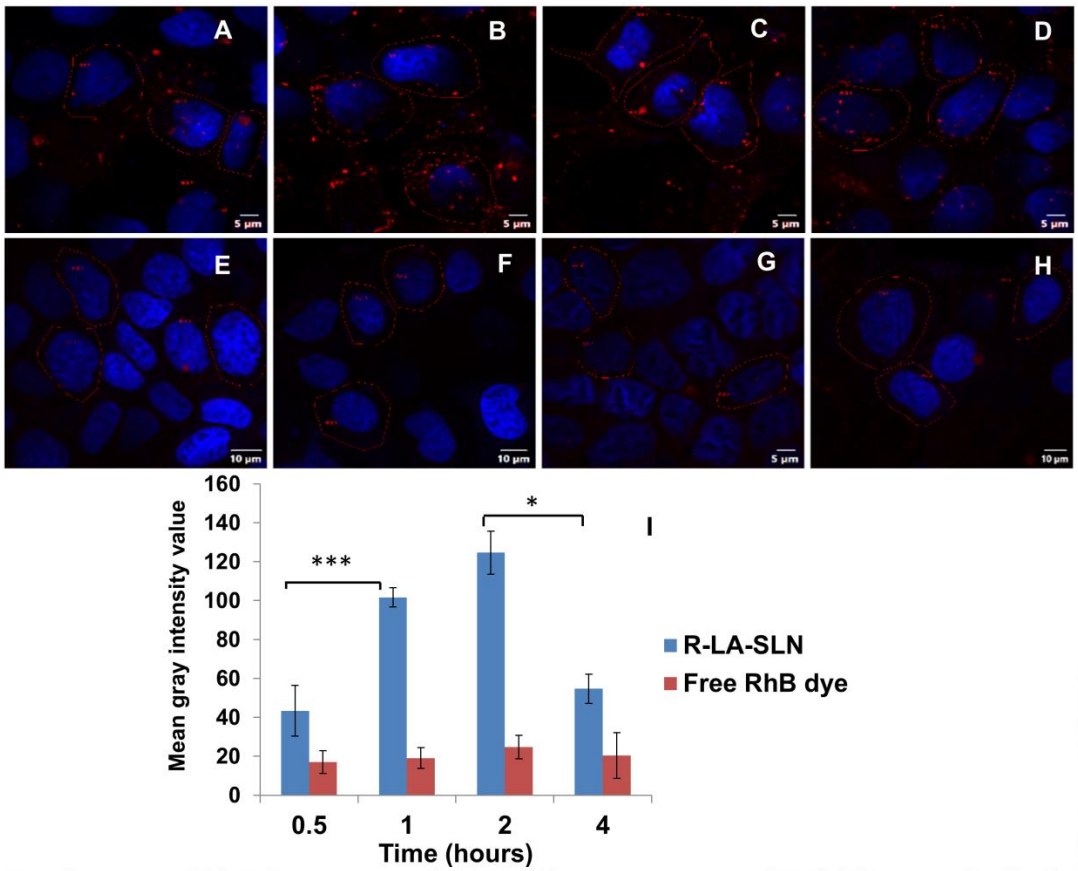

Figure 4.30. Cellular uptake of R-LA-SLN and free RhB by Caco-2 cells. (A-D): Confocal images of R-LA-SLN uptake at 0.5, 1, 2, and 4 hours. (E-H): Confocal images of free RhB dye uptake at 0.5, 1, 2, and 4 hours. DAPI was used to stain the nucleus (blue). I: Cellular uptake (indicated by mean gray intensity) estimated by drawing ROI. A p-value < 0.05 was considered statistically significant and is indicated with an asterisk, whereas a p-value ≤ 0.001 is indicated with three asterisks.

Makeen et al. reported that zeta potential also plays an important role in the interaction of nanocarriers with cells (Makeen et al., 2020). Usually, nanoparticles show a higher affinity to the cellular membrane due to electrostatic interactions (Wilhelm et al., 2003). The cell membrane possesses large negatively charged domains which should repel the negatively charged nanoparticles (Patil et al., 2007). Aside from large negatively charged domains, cell membranes also have positive sites. To counteract the repulsive interaction of large negatively charged domains, negatively charged nanoparticles bind to positive sites in clusters. This binding

results in localized membrane neutralization and gelation, which improves endocytosis and cellular uptake (Foroozandeh and Aziz, 2018). The first reason proposed for the higher cellular uptake of negatively charged SLN was the non-specific process of SLN adsorption on the cell membrane and the next reason was the formation of SLN clusters (Patil et al., 2007).

CLSM was used to evaluate the intracellular distribution of the internalized SLN. The fluorescence was primarily localized in the cytoplasm after incubating the cells with R-LA-SLN, indicating that the fluorescent R-LA-SLN accumulated in the cytoplasm. The findings were consistent with previously published literature on SLN prepared with different materials (Yuan et al., 2008). Therefore, LA-SLN can be used as effective carriers for delivering chemotherapeutic agents that target microtubules in the cytoplasm. Novais et al. reported that microtubule targeting agents (taxanes and vinca alkaloids) disrupt microtubules and activate the spindle assembly checkpoint, which causes a prolonged delay in mitosis and is expected to induce cell death (Novais et al., 2021).

4.2.4.3. Cellular uptake studies of R-LA-SLN by Confocal Raman Mapping

Figure 4.31 A & B display Raman chemical mapping by hyperspectral imaging done on R-LA-SLN treated cells at 0.5 hours and 4 hours. The cell was mapped using the absorption of the C-H stretching band at 2800-3000 cm^{-1}. The presence and distribution of RhB were mapped using the RhB characteristic peak at 1516 cm^{-1} (figure 4.31 C & D). The chemical map revealed an increased presence of RhB in the cytoplasm. The presence of RhB in the cytoplasm within the first 0.5 hours after R-LA-SLN incubation with HCT-116 cells was confirmed by Raman mapping.

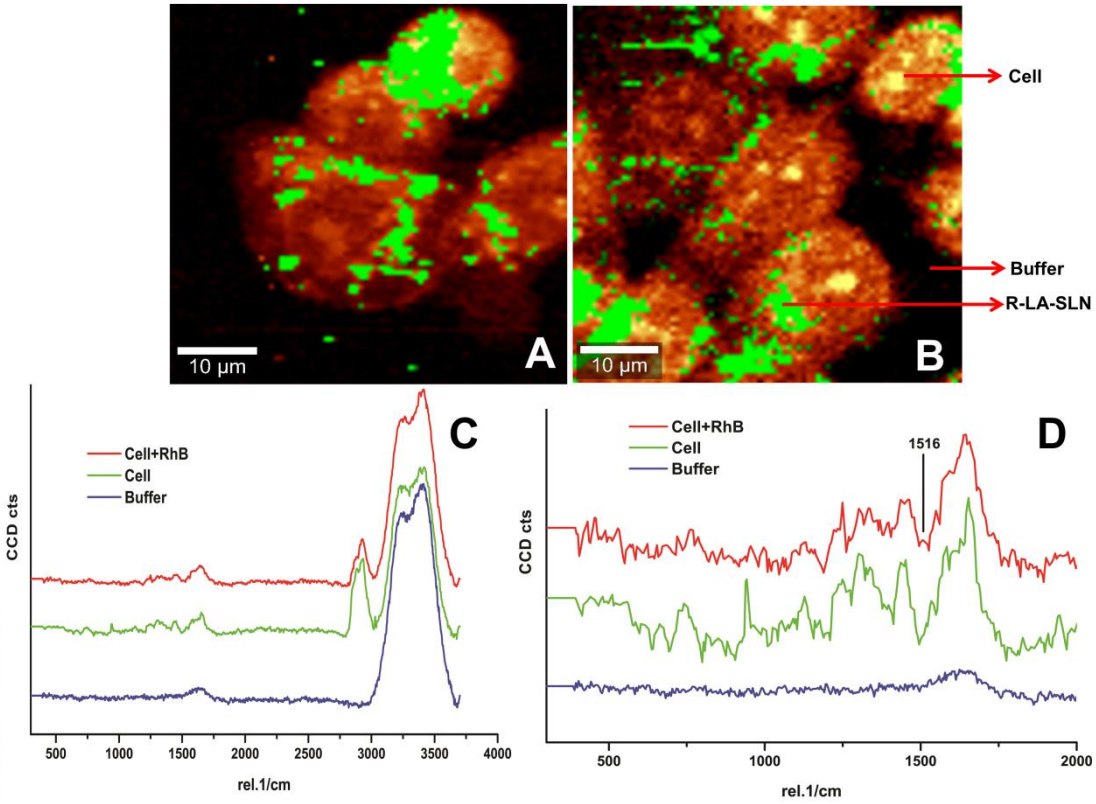

Figure 4.31. Raman chemical spectral map of HCT-116 cells incubated with R-LA-SLN for (A) 0.5 hours and (B) 4 hours demonstrating RhB uptake. (Yellow – Cells were mapped using the intensity in the C-H stretching band at the range 2800 – 3000 cm^{-1}; Green – RhB distribution in the cytoplasm was mapped using the band at 1516 cm^{-1}). Raman spectra were demixed from the hyperspectral chemical map of the Cell+RhB cluster, Cell cluster, and buffer cluster. (C) Spectra in the 4000-300 cm^{-1} range; (D). Spectra for the wavelength range 2000-500 cm^{-1}.

4.2.4.4. Effect of LA-SLN on Caco-2 cell TEER

Tight junctions are multifunctional protein complexes composed of transmembrane proteins such as claudins and occludin, as well as cytosolic proteins (Suzuki, 2013). Tight junctions form a seal between neighboring epithelial cells near the apical surface, preventing ion and molecule transport paracellularly (Farquhar and Palade, 1963). Tight junction appears as a continuous apical belt around the cell periphery, and these proteins are closely linked with the plasma membrane in an intact cell tight junction (Denker and Nigam, 1998). Transepithelial electrical resistance (TEER) is

used to evaluate the integrity and permeability of the tight junction barrier in intestinal tissues and cells (Suzuki, 2013). The effect of LA-SLN on Caco-2 cell monolayer TEER is shown in figure 4.32. The TEER values of the control cell monolayers remained constant throughout the study period. Whereas after LA-SLN treatment, the TEER values decreased by around 80% after the first 60 minutes and did not decrease further (figure 4.32A). LA has been previously reported to reduce the TEER rapidly in Caco-2 cells (Suzuki, 2013). The decrease in TEER value indicates a loss of tight junction integrity, which leads to a loss of barrier properties and ion flux across the monolayer (Rekha and Sharma, 2011). To increase drug permeability across the intestinal epithelium and improve the oral bioavailability of poorly absorbed drugs, the tight junction must be opened quickly, efficiently, and reversibly (Wallace et al., 2014). As a result, it is critical to determine whether Caco-2 cell monolayers can "reseal" the tight junction after the removal of the LA-SLN. From the result, it is clear that the TEER value returned to its original value within 24 hours (figure 4.32B).

Lauric acid (C12), a medium-chain fatty acid known to be a drug absorption enhancer via the tight junction pathway, also increases paracellular permeability (Lindmark et al., 1998). LA increases tight junction permeability in Caco-2 cells by activating protein kinase C and myosin light-chain kinase. In response to myosin light chain kinase, the perijunctional actomyosin ring contracts, resulting in increased paracellular permeability (Suzuki, 2013).

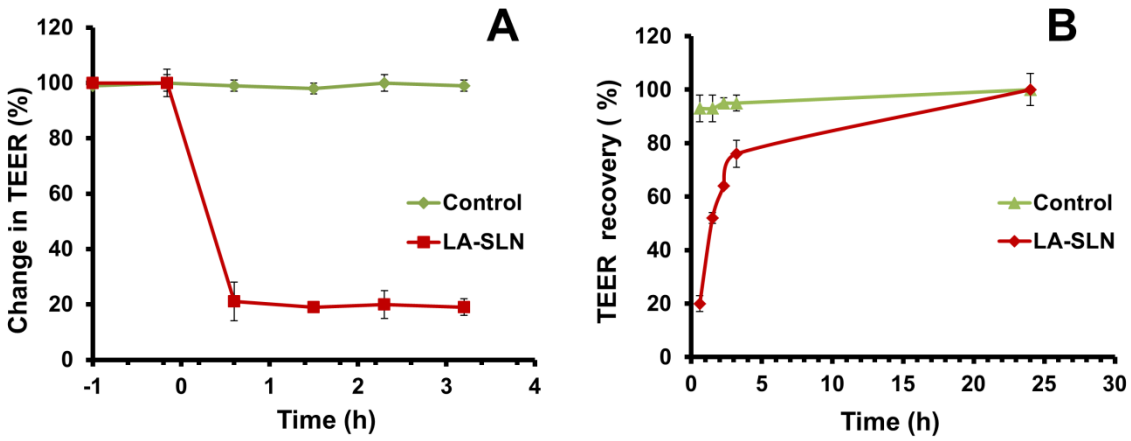

Figure 4.32. Transepithelial electrical resistance (TEER). (A) Effect of LA-SLN on Caco-2 cell monolayer TEER; (B). TEER recovery.

4.2.4.5. RhB transport studies across Caco2 cell monolayer

The transport of free RhB dye and R-LA-SLN across the Caco-2 cell monolayer was monitored as a function of time (figure 4.33). RhB loaded in R-LA-SLN had an apparent permeability of 6.6 x 10^{-6} cms^{-1}, while free RhB dye had an apparent permeability of 1.0 x 10^{-6} cms^{-1}. The permeability of RhB loaded in R-LA-SLN was found to be 6 times greater than that of free RhB dye alone. The LA-SLN with the highest reduction of TEER values was found to be more effective in inducing the permeation of RhB across the cell monolayer than the free RhB dye alone.

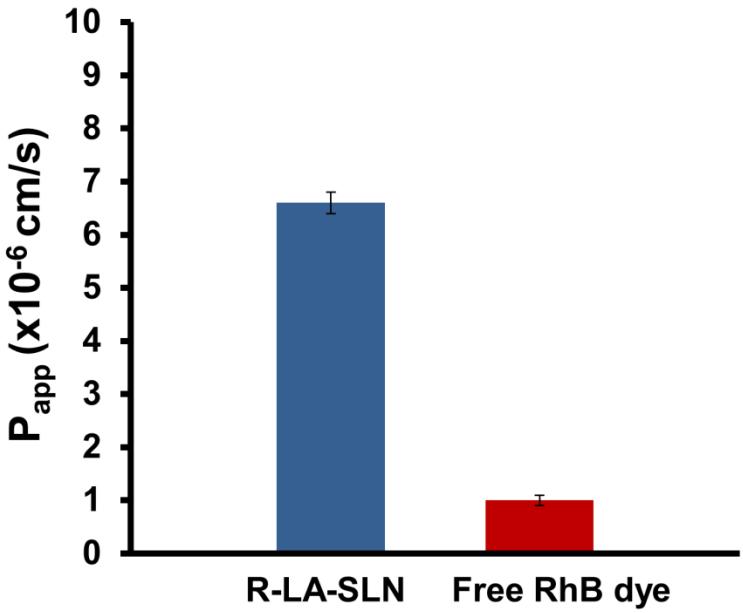

Figure 4.33. Apparent permeability coefficient (Papp) of RhB dye loaded in LA-SLN (R-LA-SLN) and free RhB dye.

4.2.4.6. Actin filament staining by rhodamine-phalloidin

A ring of filamentous actin encircles every epithelial cell at the level of the apical junctional complex and physically interacts with the tight junction in addition to the specific tight junction proteins (Madara et al., 1987). Wang et al. reported that tight junction proteins such as claudin-4 are connected to the actin cytoskeleton through transcellular adaptor proteins, including ZO-1 and actin, which is the major protein in the cell cortex (Wang et al., 2017).

The effect of LA-SLN on actin filaments was evaluated by rhodamine-phalloidin staining (figure 4.34B). The staining pattern of LA-SLN treated cells (figure 4.34B) revealed the disruption of actin filaments when compared to the untreated control cells (figure 4.34A). Actin depolymerization indicates that the tight junction has been disrupted and its barrier properties have been lost.

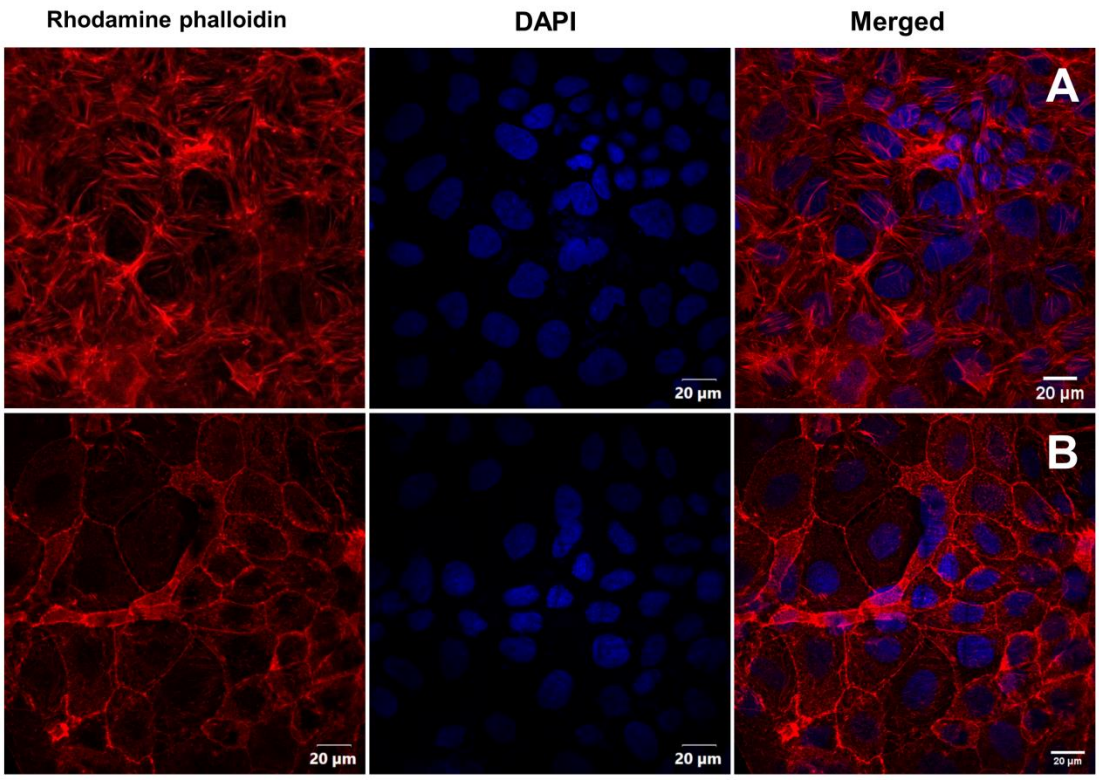

Figure 4.34. filament staining of Caco-2 cell monolayer: (A) Control and (B) after LA-SLN treatment. Confocal images at 60X magnification.

4.2.4.7. ZO-1 Tight junction staining

The effect of LA-SLN on tight junction protein ZO-1 was evaluated by Anti-ZO-1 immunofluorescent staining. In untreated control cells, ZO-1 appears as smooth lines at cell-cell junctions (figure 4.35A). The immunofluorescent staining intensity of LA-SLN treated cells was found to be weaker compared to that of the control cells, indicating that ZO-1 had been lost from cell-cell contact sites (figure 4.35B). The loss of ZO-1 immunofluorescence from conserved regions of the membrane indicates a loss of tight junction integrity and consequently barrier properties (Smith et al., 2004).

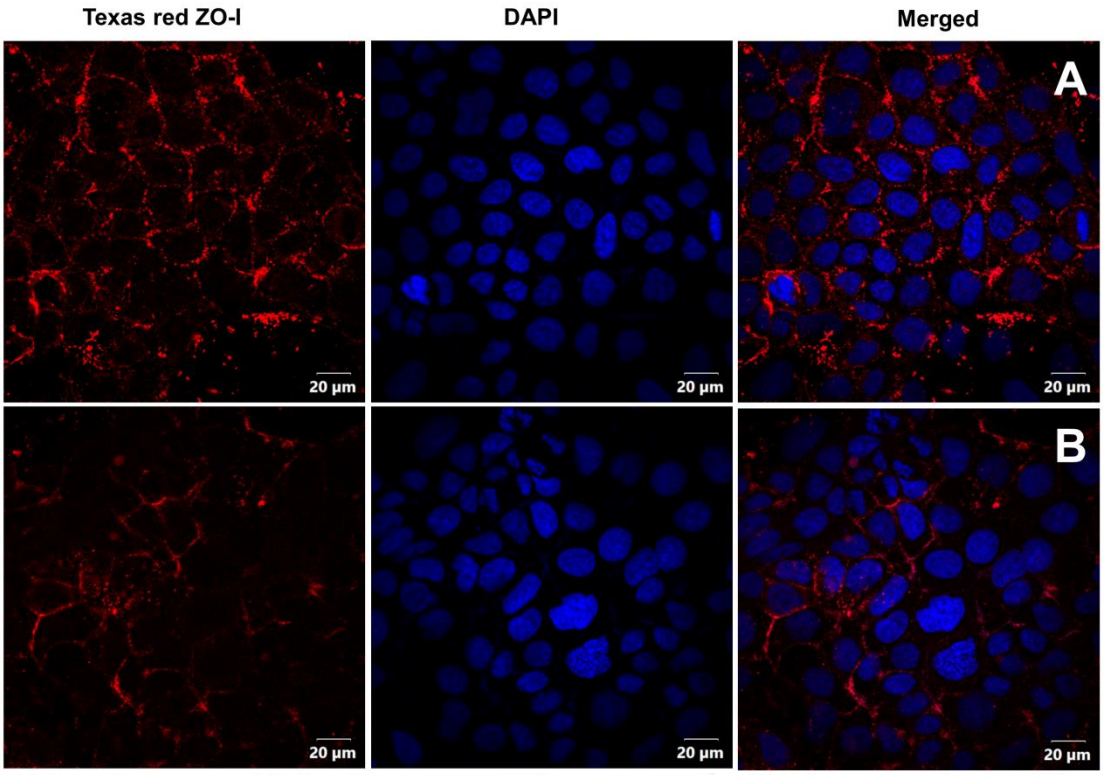

Figure 4.35. Tight junction ZO-1 staining of Caco-2 cell monolayer: (A) Control and (B) after LA-SLN treatment. Confocal images at 60X magnification.

4.2.5. Mucoadhesion studies by texture analyzer

Mucoadhesion is an important factor to consider when developing oral drug delivery carriers. Strong mucoadhesion indicates improved contact with the absorption site, resulting in effective absorption. Mucoadhesion studies of LA-SLN were carried out in the rat intestinal colon mucosa using a texture analyzer. Mucoadhesion was evaluated using this technique by measuring the maximum force required to separate the particle or dosage form from the surface of the substrate after contact for a specified time and force. Maximum detachment force (Fmax) and work of adhesion (Wad) are the two parameters obtained from texture analysis, used to compare the mucoadhesive nature (Thirawong et al., 2007). Chitosan microparticles with a surface charge of +13.3 ± 0.17 mV were used as control particles in mucoadhesion

studies. The mucoadhesive force exerted by LA-SLN was 1.7 times greater than that of chitosan particles, a material well known for its mucoadhesive behavior. The mucoadhesive force revealed by LA-SLN and chitosan particles was found to be 18.3 ± 0.2 g and 10.5 ± 0.1 g, respectively (Table 4.4). The work of adhesion of LA-SLN (12.8 ± 2.7 g.mm) was found to be significantly greater than that of chitosan particles (4.4 ± 0.94 g.mm). Higher Fmax and Wad values indicate a more mucoadhesive nature. Both of these findings demonstrated that LA-SLN is more mucoadhesive than chitosan particles (figure 4.36). Nanoparticles with smaller particle sizes and higher surface area-to-volume ratios increase the interface available for mucoadhesive interactions (Gómez-Guillén and Montero, 2021). Furthermore, the SLN's hydrophobic nature interacts with mucin's hydrophobic domains, and native mucus lipids contribute to the mucoadhesive property (Chayed and Winnik, 2007). This suggests that the LA-SLN would have more residence time in the colon. This, in turn, can lead to drug release over longer periods, ensuring a better therapeutic effect.

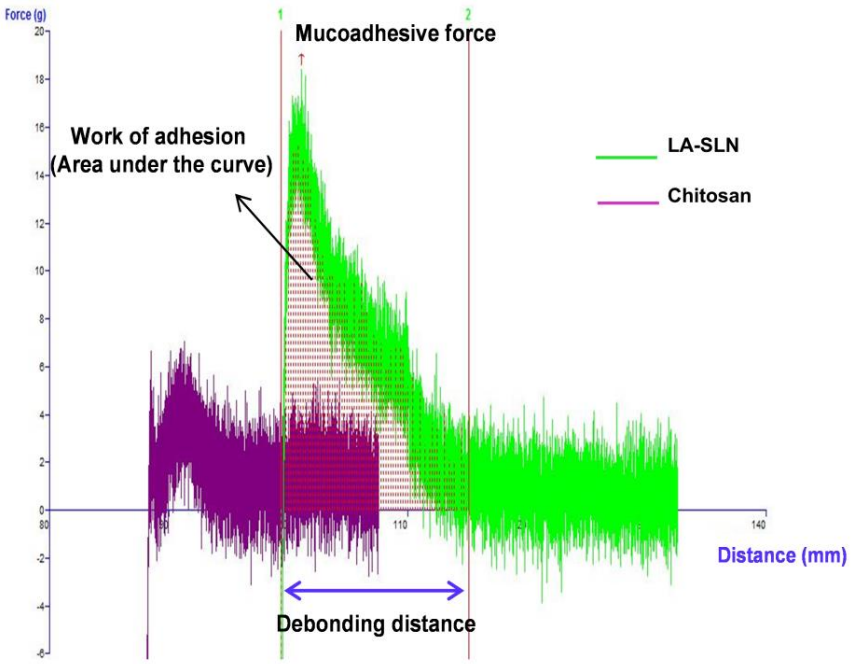

Figure 4.36. Mucoadhesive force exhibited by chitosan particles and LA-SLN evaluated by texture analyzer.

Table 4.4. Mucoadhesive force displayed by chitosan particles (control) and LA-SLN

Sample type	Work of Adhesion, g.mm	Debonding Distance, mm	Mucoadhesive force, g
Chitosan particles	4.4 ± 0.94	1.8 ± 1.0	10.5 ± 0.1
LA - SLN	12.8 ± 2.7	1.4 ± 0.1	18.3 ± 0.2

4.2.6. SDS PAGE- protein corona studies using pancreatin

This study was carried out to explore the interactions of LA-SLN with proteins in the GI environment. Different concentrations of the LA-SLN (0.1, 0.25, 0.5, 1, 2.5, 5 mg) were incubated with pancreatin and the tightly bound proteins termed “hard corona” were eluted and analyzed by SDS-PAGE (figure 4.37). Pancreatin from the exocrine cells of the porcine pancreas is a mixture of several digestive enzymes including amylase, trypsin, lipase, ribonuclease, and protease. The molecular weight

of amylase, lipase protease, trypsin, and ribonuclease was reported as 45 kDa, 38 kDa, 23.8 kDa, 20 kDa, and 13.7 kDa, respectively (Shen et al., 2013). The major protein bound to the LA-SLN was found to be ribonuclease.

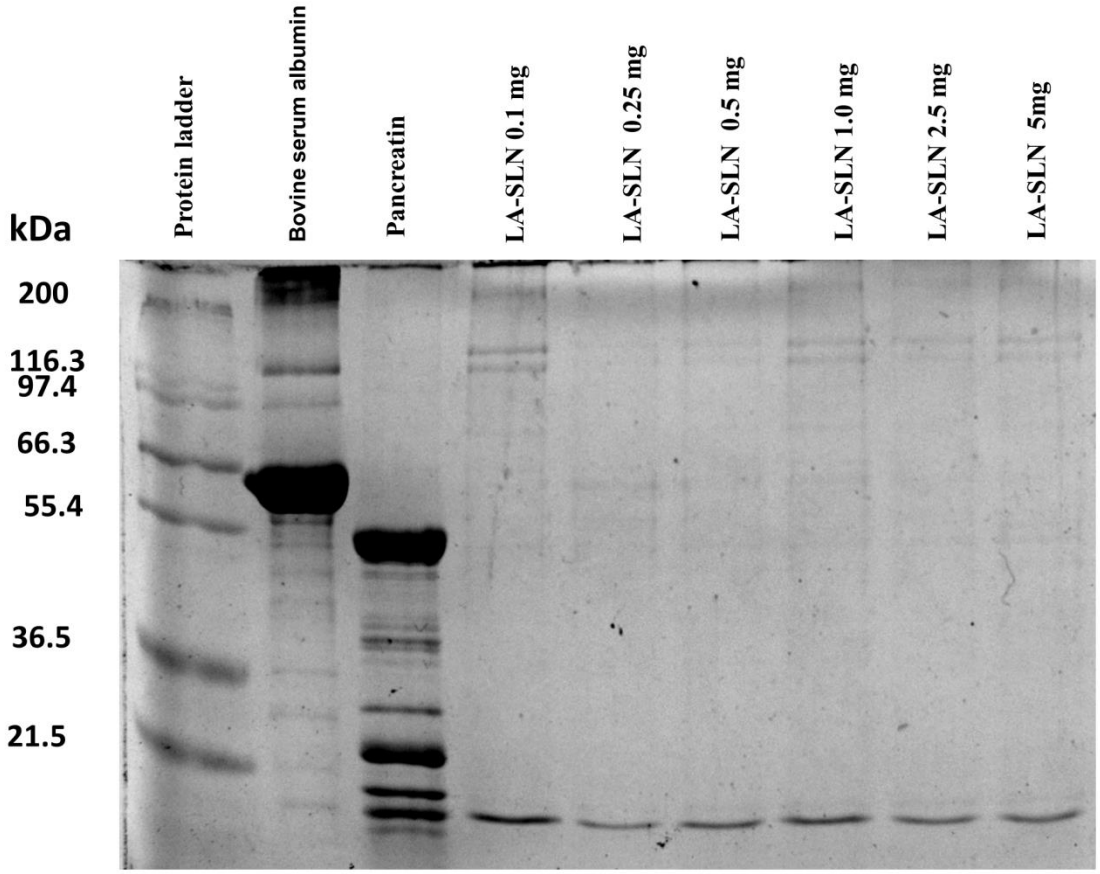

Figure 4.37. Protein corona formation in LA-SLN evaluated by SDS-PAGE.

4.3. System III: Chitosan and functionalized chitosan particles

Chitosan is a polycationic biopolymer composed of D-glucosamine and N-acetyl-D -glucosamine units and it is obtained by the partial deacetylation of chitin, the second most abundant polymer in nature. It has been widely exploited for biomedical applications owing to its nontoxicity, biodegradability, hydrophilicity, and biocompatibility. The reactive amino groups and hydroxyl groups present in chitosan

can be easily modified under mild reaction conditions to prepare modified chitosan with desired properties (Rekha and Sharma, 2011). The determination of molecular weight and degree of deacetylation of chitosan is very important as they decide the physical and biological properties of chitosan (Yuan et al., 2011).

4.3.1. Determination of molecular weight of chitosan

The average molecular weight of chitosan was determined by an Ubbelohde viscometer. From the Mark-Houwink-Sakurada equation, the molecular weight of the chitosan used for the study was calculated and found to be 566 ± 36.3 kDa. Based on the molecular weight, chitosan can be classified into low molecular weight (<100 kDa), medium molecular weight (100-1000 kDa), and high molecular weight (>1000 kDa) (Santoso et al., 2020). According to this classification, the chitosan selected for this work goes with the medium molecular weight category.

4.3.2. Degree of deacetylation of chitosan

Commercially, chitosan is prepared by the deacetylation of chitin. Deacetylation is the process of removal of acetyl groups from chitin and substitution of reactive amino groups ($-NH_2$). Degree of deacetylation (DD) determines the content of free amino groups in the structure of chitosan (ul-Islam and Butola, 2018). DD is one of the most significant chemical properties, which could influence the performance of chitosan in many applications (Hosseinnejad and Jafari, 2016). By the dual standard method, the degree of deacetylation of chitosan was calculated and was found to be 83.16 ± 2.7 %. This indicates that chitosan has 17 % of acetyl groups and 83% of amino groups in its chain. The presence of free amino groups in chitosan makes it more subjective to modification under mild conditions.

4.3.3. Lysine chitosan conjugate

L-lysine is a natural alkaline amino acid that has three reactive groups (α-carboxyl group, α-amino group, and ε-amino group), making chemical modification possible (Xiao and Zhou, 2008). Figure 4.38A depicts the molecular structure and pKa values of the amine and carboxyl groups of lysine. Lysine chitosan (LCS) conjugate was synthesized by EDC coupling reaction between the amino groups of chitosan and the carboxylic group of lysine (Figure 4.38B). The carbodiimide reacts with the carboxylic group of lysine and activates them, then it reacts with the primary amines of chitosan forming an amide bond (Crescenzi et al., 2003). Lysine chitosan conjugate formation was further confirmed by physicochemical characterization.

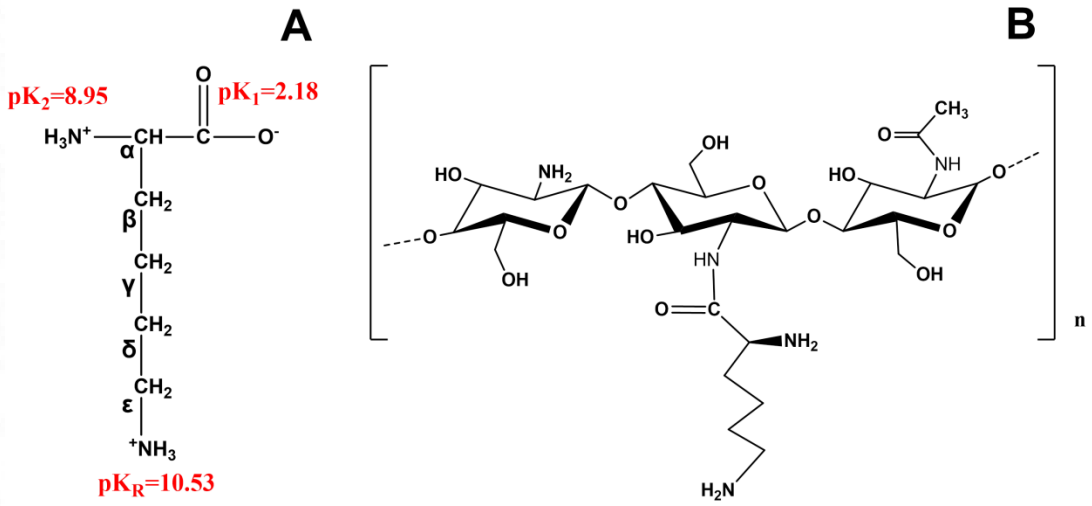

Figure 4.38. Schematic representation of: (A) lysine; (B) LCS conjugate

4.3.4 N-maleoyl chitosan conjugate

N-maleoyl chitosan (MCS) conjugate was synthesized by the conjugation of maleic anhydride to the chitosan backbone via a ring-opening reaction mechanism. Here MCS conjugate formation takes place through the acylation process between the amino group of chitosan and the electrophilic carbonyl group from maleic anhydride,

forming the amide bond (Figure 4.39) with the opening of the anhydride ring (Pasaribu et al., 2018). The MCS conjugate formation was confirmed by physicochemical characterization.

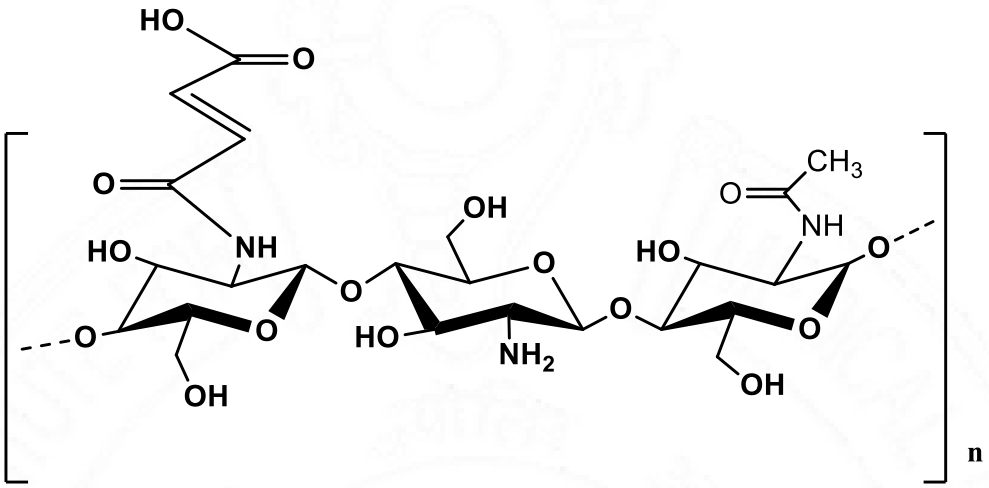

Figure 4.39. Schematic representation of MCS conjugate

4.3.5. Characterization of the chitosan conjugates

4.3.5.1. NMR analysis

The structures of acetylated and deacetylated monomers of chitosan are shown in figure 4.40. ^{1}H NMR spectra of native chitosan and chitosan conjugates (LCS and MCS) are given in figure 4.41. Chemical shifts (δ) were given using tetramethylsilane as the internal reference. The solvent proton resonates at 4.7 ppm. The chemical shifts of the ^{1}H signals of native chitosan are shown in figure 4.41.A. The acetyl protons (H-Ac) of the acetylated monomer resonate at 1.977 ppm, H2 protons of the deacetylated monomer (H-2D) resonate at 3.098 ppm. The signals at 3.4-3.8 ppm are attributed to H3-H6 pyranose ring protons of both monomers and H2 protons of acetylated monomer [H2, H3, H4, H5, and H6 (H2/6)]. The H1 protons of the acetylated monomer (H-1A) and deacetylated monomer (H-1D) resonate at 5.10

and 5.36 ppm. The ^{1}H NMR spectra of chitosan agree well with the previously published reports (Hao, 2007; Lavertu et al., 2003).

The chemical shifts of the ^{1}H signals of LCS conjugate are shown in figure 4.41B. The acetyl protons (H-Ac) and protons of the lysine chitosan unit (H-8B) resonate at 1.982 ppm. The H11 proton of the lysine chitosan unit (H11B) appears at 3.262 ppm (Haijun Yu et al., 2007) and H2 protons of the deacetylated monomer (H-2D) resonate at 2.906 ppm. The ring protons (H2/6) and H7 protons of the chitosan lysine unit (H7B) resonate between 3.5-3.8 ppm. The result observed was in agreement with a previously published report (Hao, 2007). The intensity of the peak at 1.982 ppm increased in LCS conjugate compared to chitosan due to the increase in the number of alkyl groups. The additional peak at 3.262 ppm in LCS conjugate is due to $CH\text{-}NH_2$ in the alkyl chain of lysine. The ^{1}H NMR spectra of LCS conjugate confirm the successful conjugation of lysine to chitosan.

The chemical shifts of the ^{1}H signals of the MCS conjugate are shown in figure 4.41C. The acetyl protons (H-Ac) resonate at 1.999 ppm, H2 protons of the deacetylated monomer (H-2D) resonate at 2.939 ppm. The peaks arising at 6.2-6.5 ppm and 5.7-5.8 ppm are assigned to N-maleoyl alkene protons (Zhou et al., 2018). The appearance of these peaks confirms the maleoyl substitution of chitosan. In detail, the peaks at 6.2-6.5 ppm correspond to =CH-COOH (maleoylated group), 5.7-5.8 ppm corresponds to −NH-CO=CH (maleoylated group) and 3.2-3.6 ppm correspond to ring protons of chitosan backbone (H2/6) (Ravishankar et al., 2018).

There is a significant difference between the NMR spectra of native chitosan and chitosan conjugates (LCS and MCS). Chitosan conjugates, MCS and LCS show

additional peaks of the maleoyl group and lysine. In addition, the peak at 2.9 ppm corresponds to H-2(D) proton in LCS and MCS conjugate found to almost disappeared, which indicates that most of the $–NH_2$ group of chitosan was reacted with lysine and maleic anhydride (Zhou et al., 2018).

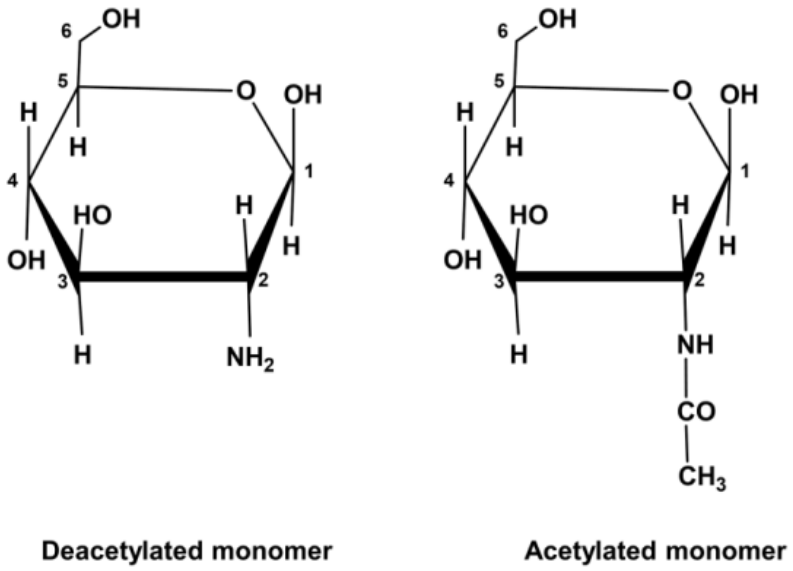

Figure 4.40. Deacetylated and acetylated monomers of chitosan

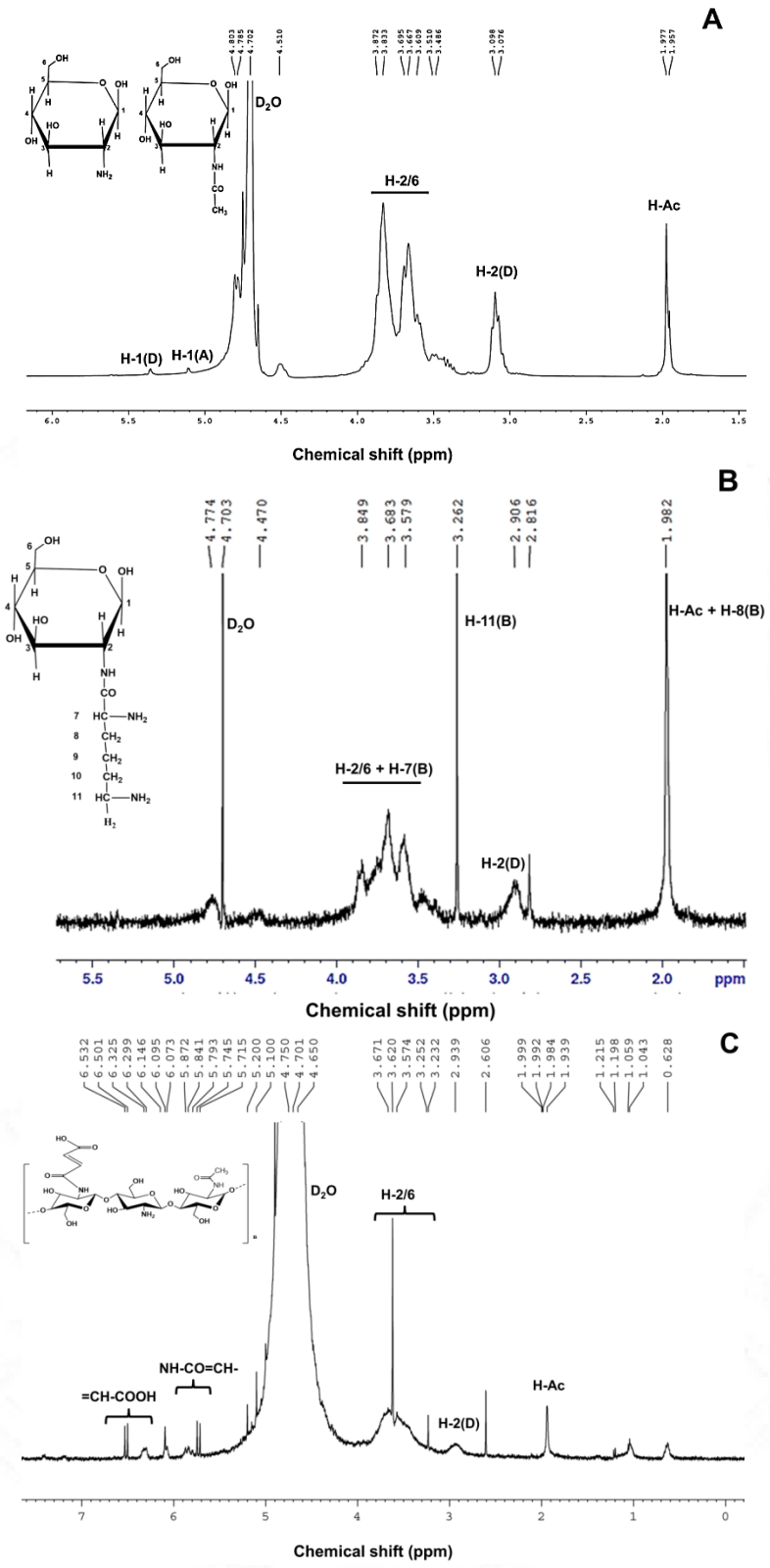

Figure 4.41. ^{1}H NMR spectra of (A) native chitosan, (B) LCS conjugate, and (C) MCS conjugate.

4.3.5.2. FTIR analysis

FTIR analysis of native chitosan and chitosan conjugates (LCS and MCS) are given in figure 4.42. The FTIR spectrum of chitosan is shown in figure 4.42A. A strong band at 3412 cm^{-1} is associated with the stretching vibrations of –OH and –NH as well as inter- and intramolecular hydrogen bonding. The –OH and –NH peaks overlapped due to inter and intramolecular traces of water, which resulted in a wide band formation (Mittal et al., 2022). The peaks at 2926 and 2882 cm^{-1} were assigned to the C-H symmetric and asymmetric stretching vibrations. The presence of N-acetyl groups was confirmed by the peaks at 1650 cm^{-1} (C=O stretching of amide I), 1585 cm^{-1} (N-H bending of amide II), and 1257 cm^{-1} (C-N stretching of amide III). The peak at 1585 cm^{-1} also corresponds to the N-H bending of primary amines. The peaks at 1423 and 1383 cm^{-1} are associated with $–CH_2$ bending and symmetrical deformations of $–CH_3$. The peak at 1319 cm^{-1} was assigned to the C-H in the pyranose ring. The peaks at 1154 cm^{-1} can be attributed to asymmetric stretching of the C-O-C bridge. The C-O-C asymmetrical stretching in the phase ring was observed at 1083 cm^{-1}. The peak at 1030 cm^{-1} corresponds to the C-O asymmetrical stretching of the primary and secondary alcohol. The stretching of the glucosamine ring was detected at 897 cm^{-1}. The peaks at 663 and 606 cm^{-1} correspond to -NH and -OH out of the plane respectively. The peaks obtained for chitosan are similar to those reported in the literature (Mittal et al., 2022; Queiroz et al., 2014; Zvezdova, 2010).

The FTIR spectra of the LCS conjugate are shown in figure 4.42B. There was a considerable shift in the absorption peaks of the LCS conjugate compared to that of

native chitosan. The chitosan peaks at 3412, 1650, 1585, and 1257 cm^{-1} underwent significant shifts to 3299, 1635, 1535, and 1261 cm^{-1} in LCS conjugate (Table 4.5). In the spectrum of LCS conjugate, the peaks at 1635 cm^{-1} (C=O, amide I) are stronger than that of chitosan. The peak at 1535 cm^{-1} (N-H of $–NH_2$ and amide II) becomes a well-demarcated peak compared to that of chitosan. It should be noted that the spectrum of LCS conjugate was particularly sharper in comparison with the spectrum of chitosan, supporting the fact that most of the amino groups of chitosan were substituted by lysine (Hao, 2007). This indicates that L lysine has reacted with chitosan and gave rise to additional $–NH_2$ and $–CH_2$ groups in LCS conjugate (Xiao and Zhou, 2008).

The FTIR spectra of the MCS conjugate are shown in figure 4.42C. The peaks at 3412, 1650, 1585, and 1257 cm^{-1} of chitosan were shifted to 3265, 1623, 1555, and 1237 cm^{-1}, respectively, in MCS conjugate (Table 4.5). The peak at 1555 cm^{-1} became a well-demarcated peak compared to that of chitosan due to the amide bond formation. The amide groups of chitosan shifted to lower numbers after being modified with maleic anhydride, this might be due to the increased hydrogen bonding with the substituted maleic acid (Don and Chen, 2004). After maleoylation, the FTIR spectrum of MCS conjugate showed additional peaks at 3098, 1714, 1656, and 852 cm^{-1} which are indicative of carbon-hydrogen bonding (vinyl group), carbonyl group (C=O from maleic anhydride), C=C stretching and a double bond (vinyl, C=C bending) in maleoyl group (Zhou et al., 2018). This confirms the anhydride ring opening, which leads to the formation of an amic acid (Ravishankar et

al., 2018). These results demonstrated the successful incorporation of the carboxylic functional group into chitosan.

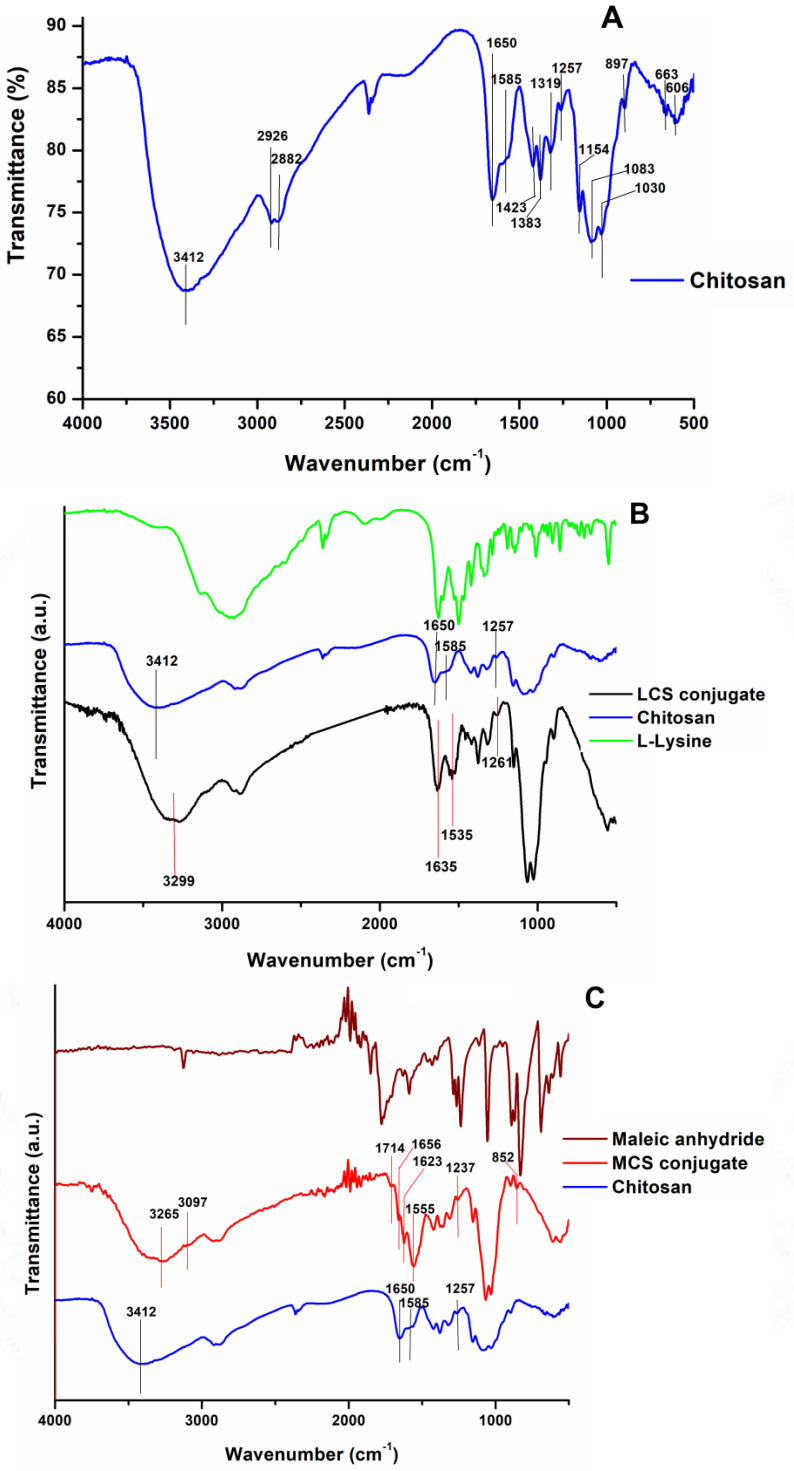

Figure 4.42. FTIR spectra of: (A) native chitosan, (B) LCS conjugate, and (C) MCS conjugate

Table 4.5. Characteristic peaks of the functional groups in chitosan, LCS conjugate, and MCS conjugate

Peak	**Wavenumber (cm^{-1})**						
Functional group	**NH_2/OH stretch**	**C=O stretch**	**C=C stretch**	**Amide I**	**Amide II**	**Amide III**	**C=C bend**
Chitosan	3412	…….	…….	1650	1585	1257	….....
LCS Conjugate	3299	…….	…….	1635	1535	1261	…….
MCS conjugate	3265	1714	1656	1623	1555	1237	852

4.3.5.3. Determination of zeta potential of native chitosan and chitosan conjugates

The changes in the surface chemistry of the chitosan during the lysine and maleic anhydride modification were characterized by zeta potential measurements. Figure 4.43 shows the zeta potential of chitosan, LCS conjugate, and MCS conjugate measured at pH 6. The surface charge of chitosan was found to be 38.77 ± 2.6.1 mV. Native chitosan exhibits a cationic surface charge due to the presence of amino groups. After modification with lysine (LCS conjugate), the zeta potential of chitosan was increased from 38.77 ± 2.61 mV to 58.15 ± 3.25 mV. This is due to the increased number of $–NH_2$ groups contributed by lysine as it has two amino groups in its side chain (Figure 4.38). At pH 6 both the amino groups of lysine get protonated (Nolting et al., 2007). This confirms the successful conjugation of lysine with chitosan. Compared to native chitosan the zeta potential of maleic anhydride-modified chitosan (MCS conjugate) was found to decrease from 38.77 ± 2.61 mV to 18.23 ± 2.67 mV. This is attributed to the reduction in the number of free amino groups in chitosan and the incorporation of carboxyl groups from maleic anhydride. Most of the amino groups present in the chitosan were involved in the acylation process with the carbonyl group from maleic anhydride, forming the amide bond (Figure 4.39).

This confirms the successful conjugation of the maleoyl group of maleic anhydride with chitosan.

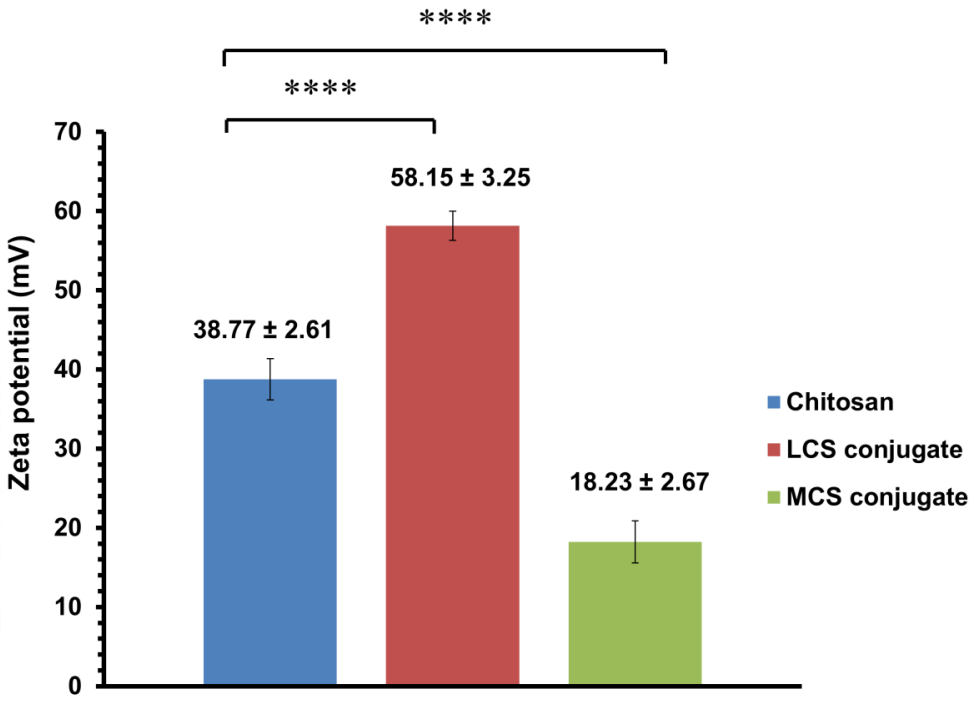

Figure 4.43. Zeta potential of chitosan and chitosan conjugates at pH 6

4.3.5.4. Variation in amino content of native chitosan and chitosan conjugates

The degree of deacetylation (DD) determines the free amino group content in the structure of chitosan. The free amino groups of native chitosan were compared with that of the chitosan conjugates to determine the variation in the amino group after modification (figure 4.44). The amino group content of chitosan was 83.16 ± 2.7 %. After modification with lysine, the percentage amino group increased from 83.16 ± 2.7 % to 89.23 ± 1.7 %. This is due to the $–NH_2$ groups contributed by lysine. This reveals the successful conjugation of lysine with chitosan. After modification with the maleoyl group of maleic anhydride, the free amino group content of chitosan decreased from 83.16 ± 2.7 % to 45.7 ± 2.1 %. The amino groups (%) of MCS

conjugate decreased due to the involvement of free amino groups of chitosan in the amide bond formation with the carbonyl group from maleic anhydride. This confirms the successful conjugation of the maleoyl group of maleic anhydride with chitosan.

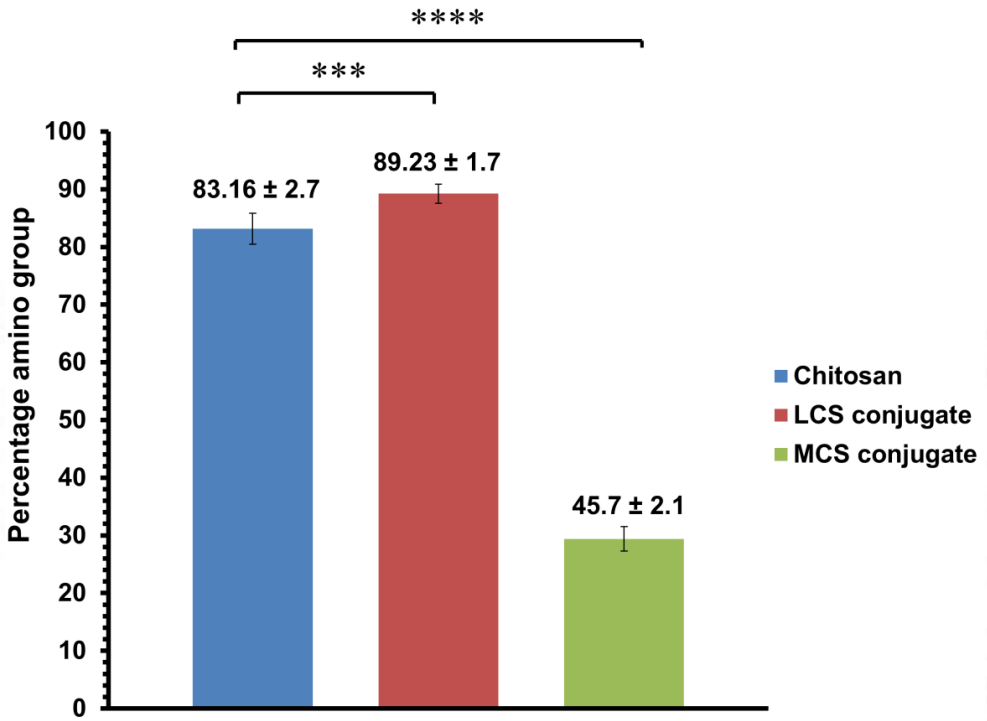

Figure 4.44. Amino group content of chitosan and chitosan conjugates

4.3.5.5. Trinitrobenzenesulfonic acid assay

Trinitrobenzenesulfonic acid (TNBS) reacts with primary amines to give an orange-colored complex that can be readily measured at 410 nm (Figure 4.45). The degree of substitution/extent of derivatization was calculated by determining the remaining underivatized primary amino groups in chitosan (Sonia et al., 2011). The free amino groups in chitosan were assumed to be 100 % and the percentage of free amino groups in the chitosan conjugates was calculated based on this. The free amino groups in the LCS conjugate were expected to be increased after lysine conjugation to chitosan. However, the amino groups in LCS conjugate remained the same as that

of chitosan (Figure 4.46). This is because TNBS reacts only with the primary amines (ε amino group) of lysine, not with the α amino group of lysine (Figure 4.45). Trinitrobenzenesulfonic acid specifically binds with the ε amino group of proteins (Sashidhar et al., 1994).

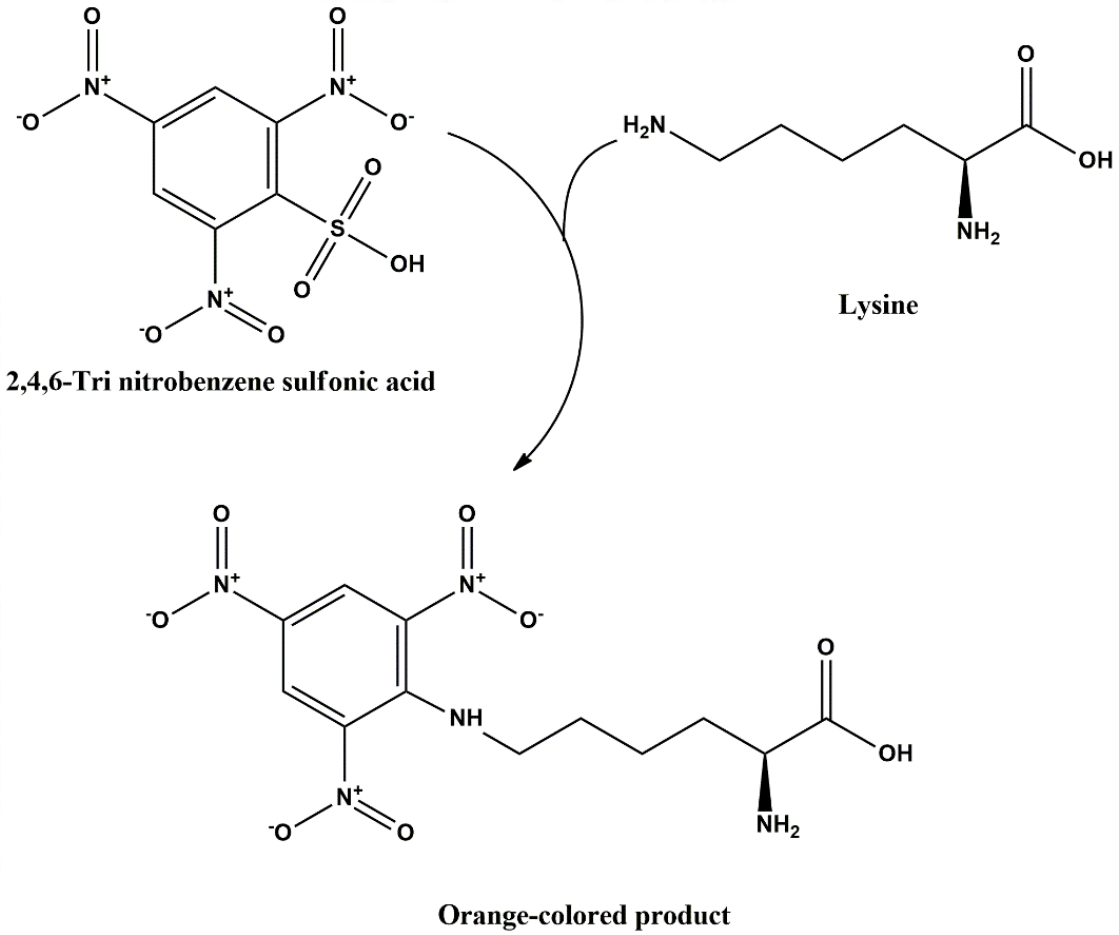

Figure 4.45. TNBS reaction with the primary amine of lysine

Trinitrobenzenesulfonic acid assay results of MCS conjugate showed a significant reduction in the percentage of free amino groups. The percentage of free amino groups in the MCS conjugate was found to be 49.67 ± 5.1 (Figure 4.46). The reduction in free amino groups is due to the involvement of free amino groups of chitosan in amide bond formation with the carbonyl group from maleic anhydride.

This again confirms the successful conjugation of the maleoyl group of maleic anhydride with chitosan.

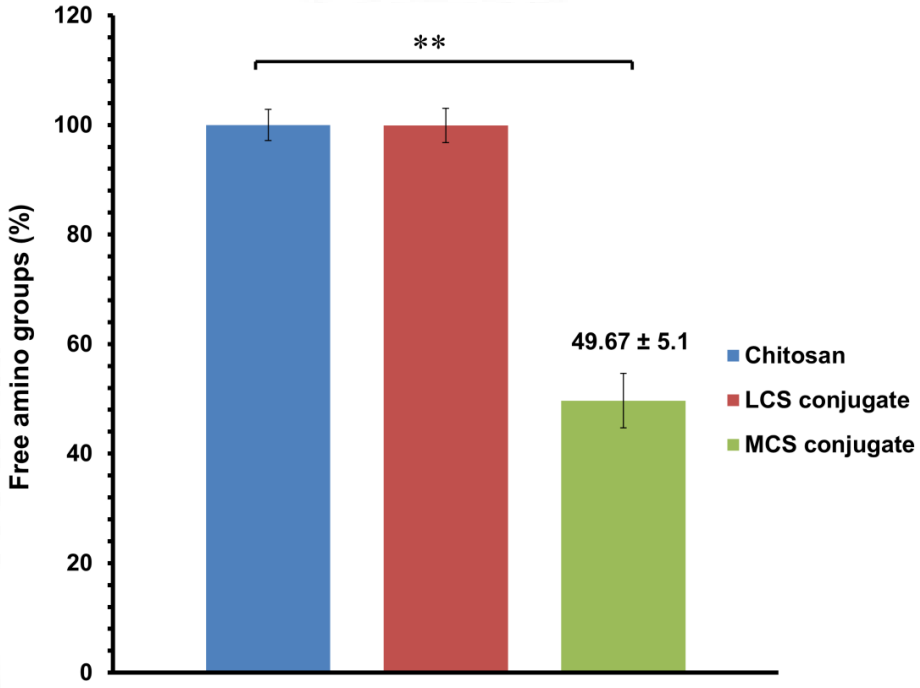

Figure 4.46. Free amino groups (%) in chitosan, LCS conjugate, and MCS conjugate. (The amino groups in chitosan were assumed to be 100%).

4.3.5.6. Thermogravimetric (TGA) analysis

The thermal degradation behavior of chitosan, LCS conjugate, and MCS conjugate are shown in figure 4.47. The first region of weight loss almost immediately after the start of heating in chitosan, LCS conjugate, and MCS conjugate is due to the removal of absorbed water from the hydrophilic polysaccharide structure and no degradation of polymer is assumed to take place at this point (Corazzari et al., 2015). The degradation of chitosan starts at 125.44 °C. In the case of LCS and MCS conjugates, the degradation starts at 117.78 and 96.18 °C. The conjugates start degrading at a lower temperature compared to chitosan. This indicates that the conjugates have less thermal stability compared to chitosan. On the other hand, this confirms the

successful modification of chitosan. The second weight loss in the range of 233-382 °C in chitosan is due to the dehydration of the saccharide ring, depolymerization, and decomposition of acetylated and deacetylated units (Moussout et al., 2016; Sirviö et al., 2021). From TGA, 50% weight loss of chitosan occurred at 315.09 °C which is decreased to 292.91 °C in the case of LCS conjugate indicating the decreased stability of chitosan after modification with lysine. In MCS conjugate the degradation from 96.18 °C to 247.93 °C was found to be 5.82 %. On modification with maleic anhydride the temperature at which 50 % weight loss occurred was higher than other systems (344.82 °C). This might be due to increased hydrogen bonding and charged complex formation between the substituted carboxylic groups and the remaining amino groups (Fan et al., 2009).

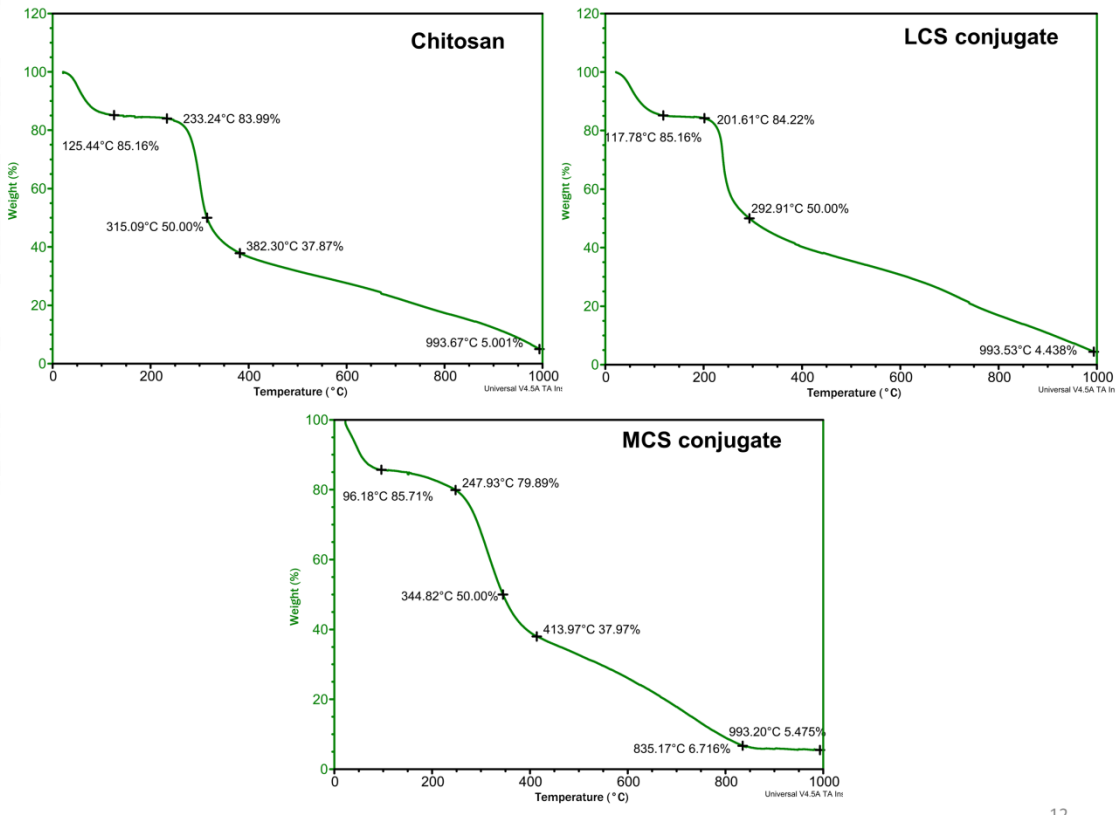

Figure 4.47. TGA thermograms of chitosan, LCS conjugate and MCS conjugate

4.3.5.7. X-ray diffraction (XRD) analysis

The changes in crystallinity of chitosan upon modification were analyzed by X-ray diffraction analysis. X-ray diffraction patterns of chitosan, LCS, and MCS are given in figure 4.48. The XRD analysis of chitosan showed a sharp crystalline peak at 20° which corresponds to the (110) plane. Compared to chitosan, XRD spectra of LCS and MCS conjugate showed a broad single peak pattern at 2θ values of 20º and 30°. The LCS and MCS conjugate becomes substantially more amorphous due to the deformation of strong hydrogen bonds in the chitosan backbone as the amino groups were functionalized by the lysine and maleoyl group (Hou et al., 2017). The crosslinked glucosamine units prevent the crystallization of the polysaccharide sequence which leads to the amorphous nature of the conjugates (Xiao and Zhou, 2008).

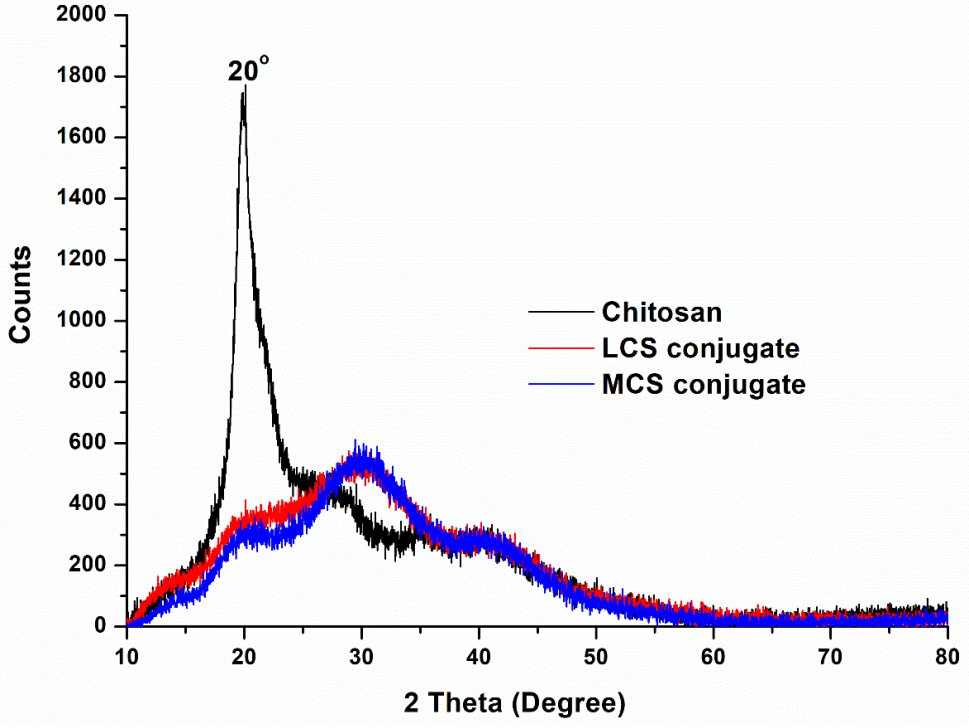

Figure 4.48. XRD spectra of chitosan and chitosan conjugates

4.3.6. Crosslinked chitosan microparticles

The chitosan, LCS, and MCS microparticles were crosslinked by the ionic gelation method (Figure 4.49). Tripolyphosphate (TPP) was used as the crosslinker for the chitosan particles owing to its advantages including small molecular weight with a triple negative charge, low toxicity, and quick gelling ability (Dehousse et al., 2010). Through ionic interaction, the negatively charged phosphate groups of TPP can form ionic links with positively charged amino groups of chitosan (Karimi et al., 2013).

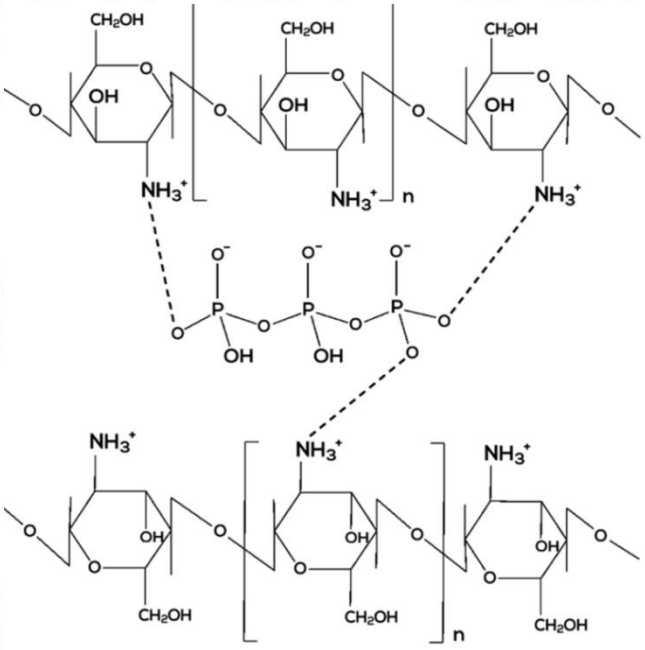

Figure 4.49. Schematic representation of ionic interaction in crosslinked chitosan microparticles (Othman et al., 2018)

Since the charge densities of chitosan and TPP are pH-dependent, pH plays a significant role in the ionic interaction between TPP and chitosan. Chitosan has a pKa value of approximately 6.5, which means that most of its amino groups are positively charged in the pH range of 3.5 to 5.5 (Karimi et al., 2013). This is why the pH of the chitosan solution was adjusted to 4.5 before chitosan particle preparation. When dissolved in water sodium tripolyphosphate ($Na_5P_3O_{10}$) dissociates to give

both hydroxyl and phosphoric ions. When the pH of the TPP was adjusted to 3 only phosphoric ions were present but at pH 9, both OH^- and phosphoric ions were present and may compete with each other to interact with the $–NH_3^+$ of chitosan (Bhumkar and Pokharkar, 2006). The chitosan-TPP complex at lower pH (pH 2) was formed by the ionic interaction between the positively charged chitosan and negatively charged phosphoric ions. The pKa value of TPP was 2.3 (pKa_3=2.3) and its charge density increases as the pH increases (at pH = 3 approximately 20% of the molecules are only doubly charged). Therefore, the addition of TPP in a higher pH range results in more efficient formation of chitosan microparticles (Karimi et al., 2013).

4.3.7. Physicochemical characterization of microparticles

4.3.7.1. Zeta potential

The zeta potentials of chitosan, LCS, and MCS microparticles in water are shown in figure 4.50. The zeta potentials of chitosan, LCS, and MCS particles were +13.3 ± 0.17, +23.7 ± 0.58 and -9.54 ± 0.79 mV, respectively. The zeta potentials of chitosan, LCS conjugate, and MCS conjugates were found to be decreasing after particle formation (figure 4.43). Sadeghi et al. found that the value of zeta potential tends to decrease when chitosan and its quaternized derivatives are converted from their free soluble forms to nanoparticles by the ionic gelation method (Sadeghi et al., 2008). The reduction in zeta potential observed with the addition of TPP was because the TPP occupies some of the positive charges of chitosan (NH_3^+) due to crosslinking (Jonassen et al., 2012). The negative zeta potential of the MCS microparticles is due to the presence of carboxyl groups of maleic anhydride.

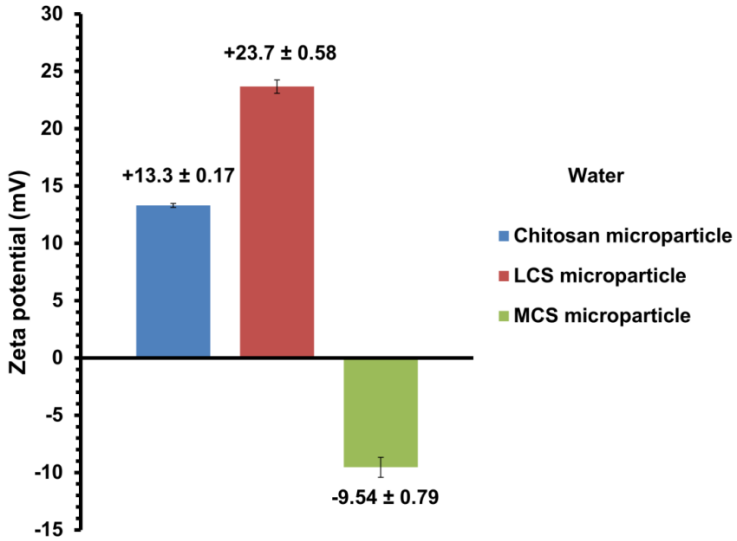

Figure 4.50. Zeta potential of chitosan, LCS and MCS microparticles in water

The zeta potential of chitosan, LCS, and MCS particles in phosphate buffer saline (PBS, pH 7.4) is shown in figure 4.51. It is expected that the zeta potential of particles suspended in phosphate buffer (pH 7.4) would mimic the charge of the particles in the biological system. The respective zeta potentials of chitosan, LCS, and MCS microparticles in PBS (7.4) were found to be -0.40 ± 0.15, +0.67 ± 0.04, and -6.96 ± 0.79 mV. The zeta potentials of chitosan and LCS microparticles were much lower and the zeta potential of MCS microparticles became less negative when they were suspended in PBS compared to the values obtained when they were taken in water. This change in the zeta potential is due to the increased concentration of counterions in PBS (Midekessa et al., 2020).

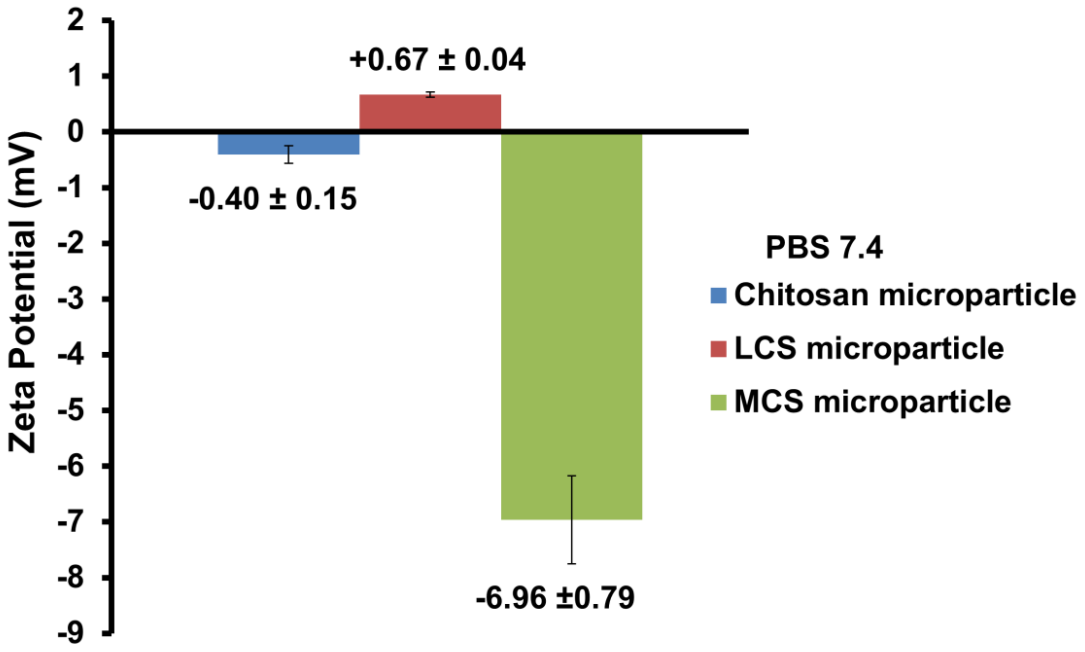

Figure 4.51. Zeta potential of chitosan, LCS and MCS particles in PBS (7.4)

4.3.7.2. FTIR spectra

The chitosan, LCS, and MCS microparticle formation were confirmed by the FTIR analysis. The FTIR spectra of chitosan, LCS, and MCS microparticles are shown in figure 4.52. The FTIR spectra of chitosan, LCS, and MCS microparticles were compared with that of native chitosan, LCS conjugates, and MCS conjugates (Table 4.2). The characteristic absorption peaks of chitosan were found to be shifted on ionic crosslinking of chitosan and TPP (Oh et al., 2019). The same trend was observed for LCS and MCS microparticles when it was compared with LCS and MCS conjugate (Table 4.6). The shift in amide I and II peaks in microparticles is caused by the interaction between the NH_3^+ group of chitosan and the phosphate groups of TPP (Lustriane et al., 2018). The disappearance of the peaks at 1423 and 1319 cm^{-1} was observed for chitosan microparticles. A similar trend was followed by LCS microparticles. In the case of MCS microparticles, the disappearance of the

peak at 1656 cm^{-1} was evident and a well-evident peak at 1424 cm^{-1} became a shoulder peak at 1417 cm^{-1} after particle formation. These changes are due to the complexation of chitosan with TPP. The spectral difference in the range from 2000-4000 cm^{-1} was assigned to the diversities in the hydrogen bonding intensities among chitosan and TPP (Gao et al., 2021).

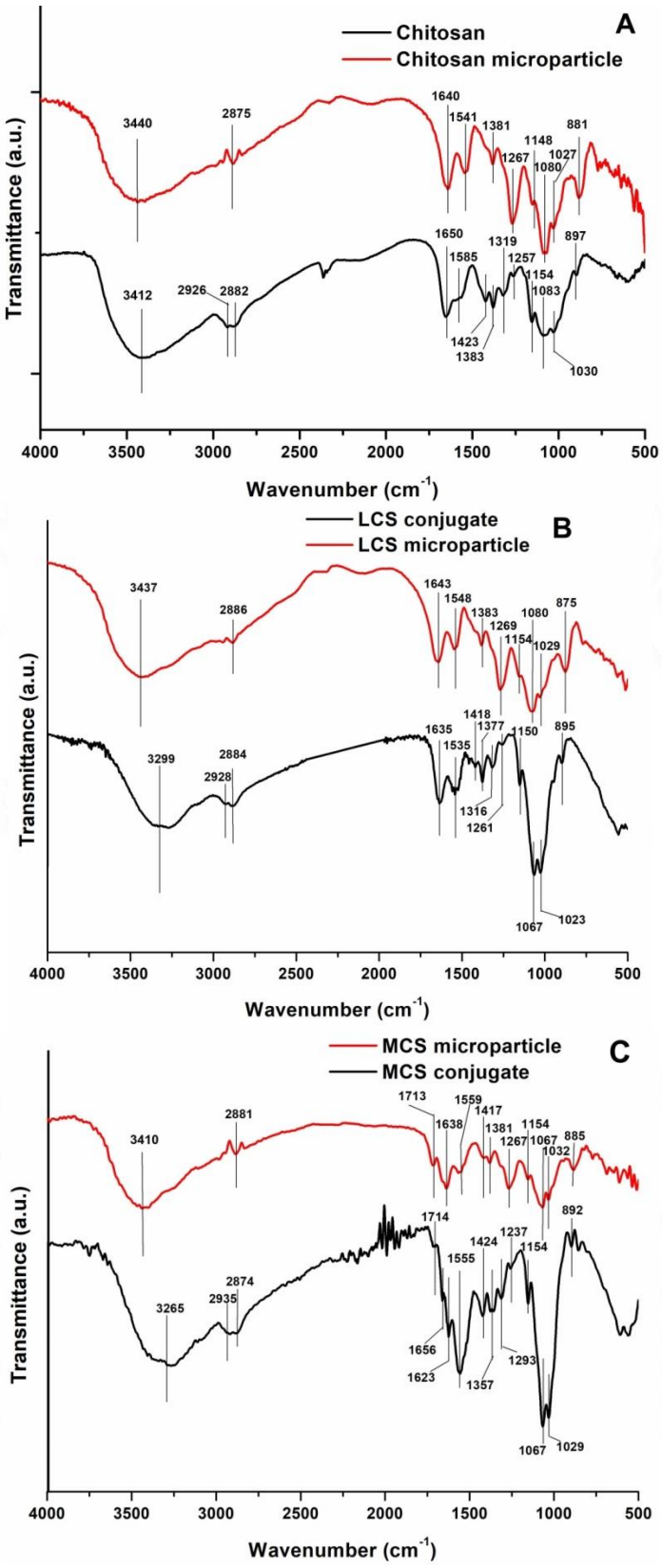

Figure 4.52. FTIR spectra of (A) chitosan; (B) LCS and (C) MCS microparticles

Table 4.6. Characteristic peaks of the functional groups in chitosan, LCS, and MCS microparticles

Wavenumber (cm^{-1})						
Functional groups	**Chitosan**	**Chitosan particle**	**LCS conjugate**	**LCS particle**	**MCS conjugate**	**MCS particle**
NH_2/OH stretch	3412	3440	3299	3437	3265	3410
C-H stretch	2926 2882	2875	2928 2884	2886	2935 2874	2881
C=O stretch	……..	……..	……..	…….	1714	1713
C=C stretch	……..	……..	……..	…….	1656	…….
Amide I	1650	1640	1635	1643	1623	1638
Amide II	1585	1541	1535	1548	1555	1559
CH_2 bending	1423	…….	1418	……	1424	1417
CH_3 deformation	1383	1381	1377	1383	1357	1381
C-H in pyranose ring	1319	……	1316	……..	1293	…….
Amide III	1257	1267	1261	1269	1237	1267
C-O-C	1154	1148	1150	1154	1154	1154
C-O-C	1083	1080	1067	1080	1067	1067
C-O primary alcohol	1030	1027	1023	1029	1029	1032
Pyranose ring	897	881	895	875	892	885

4.3.7.3. Scanning Electron Microscope (SEM) analysis

The morphology and appearance of the chitosan, LCS, and MCS microparticles were examined using a scanning electron microscope. SEM images of chitosan, LCS conjugate, and MCS conjugate are displayed at higher and lower magnifications as shown in figure 4.53. Scanning electron microscopy images were recorded at magnifications (1000X, 5000X, and 20000X). Morphologically the microparticles were observed as irregularly shaped large particles in an agglomerated state. The surface morphology of the MCS microparticles was found to be different from chitosan and LCS microparticles. The highly folded wrinkled surface of the MCS

microparticles is evident in figure 4.53I. The specific surface area and hydrophilicity of the microspheres were significantly affected by the wrinkled surface. The microspheres with wrinkled surfaces have a large surface area (Liang et al., 2019). The formation of wrinkled surfaces is associated with the cross-linking nature of the polymeric network (Zhao and Qiu, 2011).

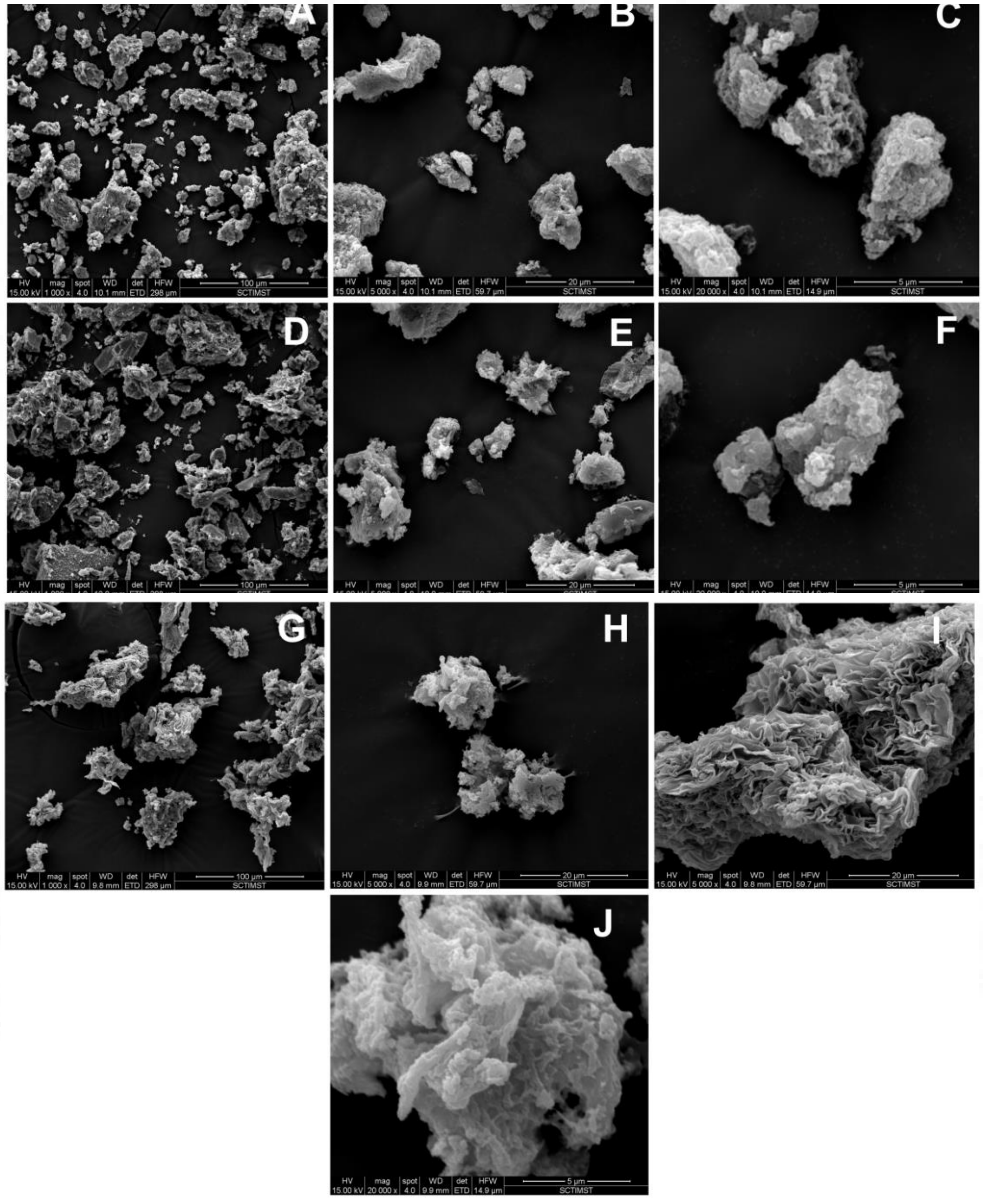

Figure 4.53. SEM images of chitosan (A-C); LCS (D-F) and MCS (G-J) microparticles. Scale bar 100 μm (A, D, G); scale bar 20 μm (B, E, H, I) and scale bar 5 μm (C, F, J).

4.3.8. Water uptake studies of microparticles

The water uptake studies of the microparticles were carried out separately in three different pH buffers (1.2, 6.8, and 7.4) for 4 hours (Figure 4.54). To mimic the GI tract the water uptake studies were carried out at pH 1.2, 6.8, and 7.4, where pH 1.2 represents the pH of the stomach, 6.8 and 7.4 phosphate buffer represents the intestinal pH. Chitosan microparticles exhibit a higher degree of water uptake at pH 1.2 (Figure 4.54A). The protonation of amino groups ($-NH_2$) of chitosan to ammonium ions ($-NH_3^+$) leads to swelling at acidic pH (Ghauri et al., 2021). At lower pH, due to the presence of more ionic groups (ammonium ions) charge repulsion and a decrease in osmotic pressure occur leading to an increase in water uptake and swelling (Gierszewska et al., 2018). At pH 1.2, the particles show water uptake very quickly (588 ± 17.7 %, 2 hours) and after 2 hours the water uptake was found to be decreased due to the dissolution of the chitosan particles. If the chitosan microparticles are more tightly crosslinked with TPP it does not swell as much as loosely crosslinked chitosan microparticles. The loosely crosslinked chitosan-TPP particles have a high hydrodynamic free volume to accommodate more solvent molecules thereby it induces a higher degree of swelling and also undergoes dissolution (Parize et al., 2012). When the pH was increased to 6.8 and 7.4 the water uptake was found to decrease. At higher pH, deprotonation of ammonium ions takes place leading to a decrease in swelling due to fewer polymer chain interactions.

LCS microparticles exhibit higher water uptake at pH 1.2 (706 ± 62 %, 1 hour) and the water uptake was found to be higher than that of chitosan microparticles (Figure 4.54B). The increased water uptake is due to the protonation of additional amino

groups contributed by lysine in LCS microparticles. At lower pH, both the amino groups of lysine get protonated and lead to swelling of the particle by charge repulsion. The water uptake of LCS microparticles was found to be decreased at pH 6.8 and 7.4 due to the deprotonation of ammonium ions.

Due to the presence of both amino and carboxylate groups (COO^{-}), the sensitivity of the MCS microparticles toward different pH buffers is of great interest. MCS conjugate shows higher water uptake at pH 1.2 (Figure 4.54C). At acidic pH (1.2) the protonated amino groups are responsible for the higher water uptake. MCS is anionic with a hydrophilic carboxylate group in the molecular chain. At pH 7.4 the electrostatic repulsion between carboxylate groups (COO^{-}) forms a loose network structure leaving more water molecules to diffuse easily into the network and thus demonstrating a higher water uptake compared to that at pH 6.8 (Zhou et al., 2018). On the other hand, the electrostatic interaction between the $-NH_3^+$ and the COO^- groups as well as the interactions between the free amino ($-NH_2$) and free carboxyl (-COOH) groups should be responsible for decreased water uptake at pH 6.8 (Vanichvattanadecha et al., 2008).

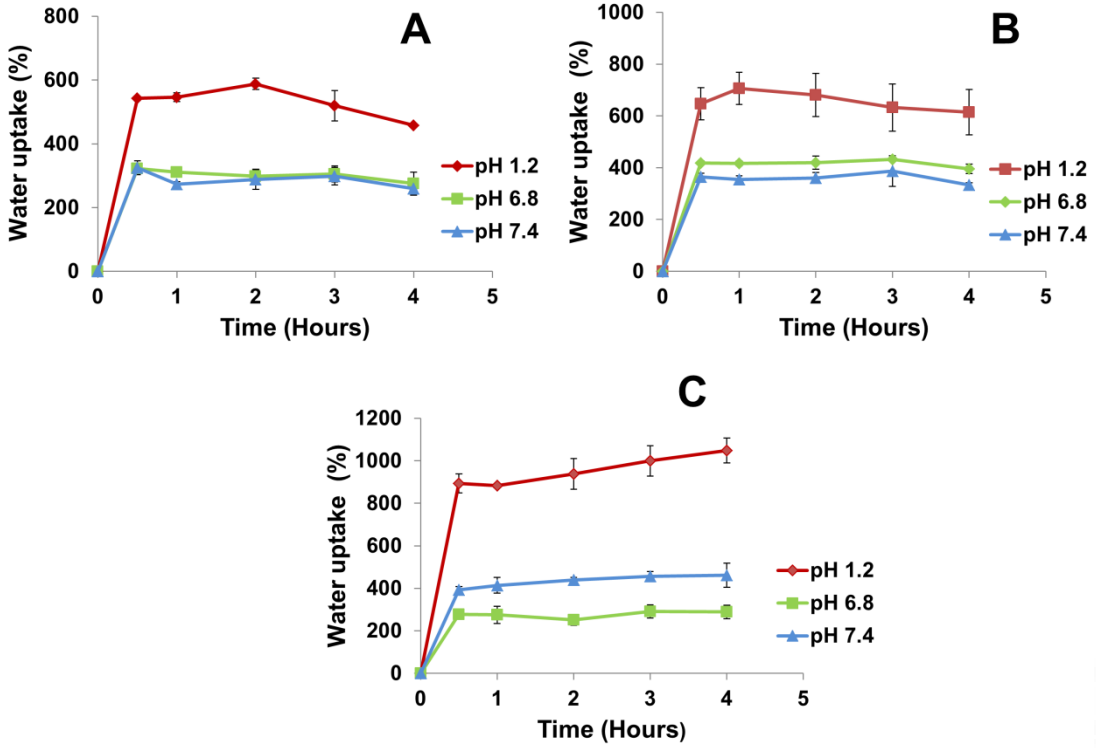

Figure 4.54. Water uptake (%) of: (A) chitosan, (B) LCS and, (C) MCS microparticles in different pH buffers as a function of time.

4.3.9. Drug loading and release studies of microparticles

4.3.9.1. Drug loading and entrapment efficiency

The microparticles were loaded with the anti-cancer drug 5-fluorouracil (5-FU). The encapsulation efficiency and drug loading in microparticles were calculated (figure 4.55). The encapsulation efficiency and drug loading of chitosan microparticles were 77.7 ± 3 % and 28.87 ± 2.1 µg/mg particle. For LCS microparticles the encapsulation efficiency and drug loading and were found to be 92.2 ± 3.1 % and 19.6 ± 0.6 µg/mg particle. In the case of MCS particles, the encapsulation efficiency and drug loading were observed as 87.5 ± 0.4 % and 32.9 ± 1.8 µg/mg particles. The drug loading was found to be higher for MCS microparticles compared to that of chitosan particles (figure 4.55B). This might be due to the increased surface area of the MCS microparticles owing to their wrinkled surface. LCS microparticles exhibit less drug

loading compared to both MCS and chitosan particles. The drug entrapment efficiency of both LCS and MCS microparticles was found to be higher than that of chitosan microparticles (figure 4.55A).

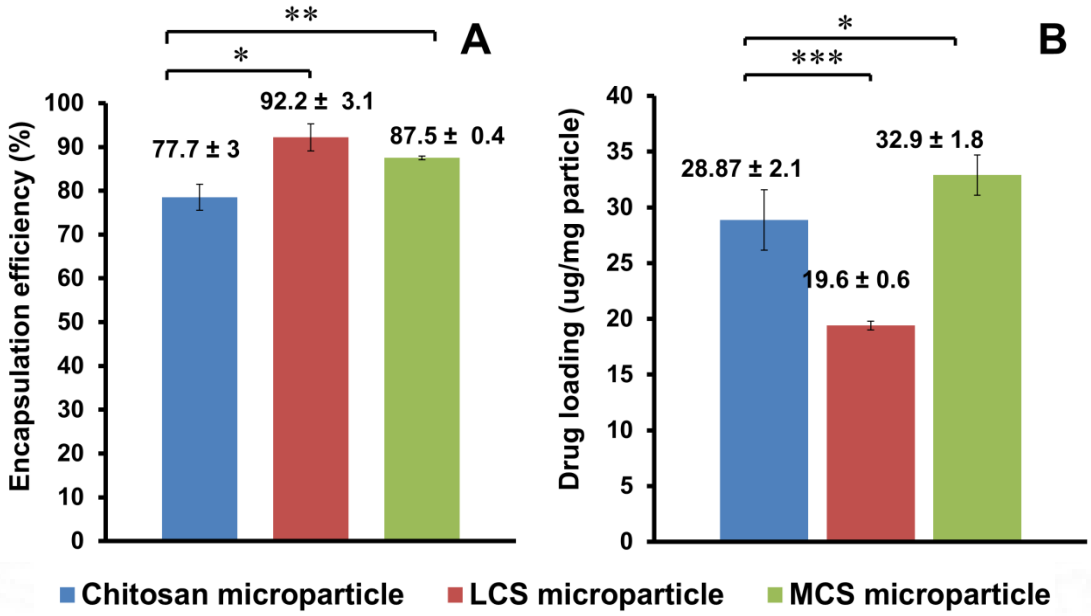

Figure 4.55. Encapsulation efficiency (A) and drug loading (B) of microparticles

4.3.9.2. Energy Dispersive X-Ray Analysis (EDAX)

The EDAX spectrum of 5-FU loaded chitosan, LCS, and MCS microparticles are shown in figure 4.56. The EDAX spectrum obtained for chitosan, LCS and MCS microparticles showed the presence of carbon (C), oxygen (O), phosphorous (P), and fluorine (F). Carbon and oxygen belong to the polymer, F comes from 5-FU whereas phosphorous is attributed to the crosslinking agent TPP showing that the microparticle development was successful (de Pinho Neves et al., 2014). The presence of fluorine confirms the encapsulation of 5-FU into the microparticles (E A K et al., 2020) even though its percentage weight was found to be less. The

microparticles were loaded with 5-FU dissolved in PBS (7.4). So the presence of potassium as well as phosphorous is also contributed by the components of PBS.

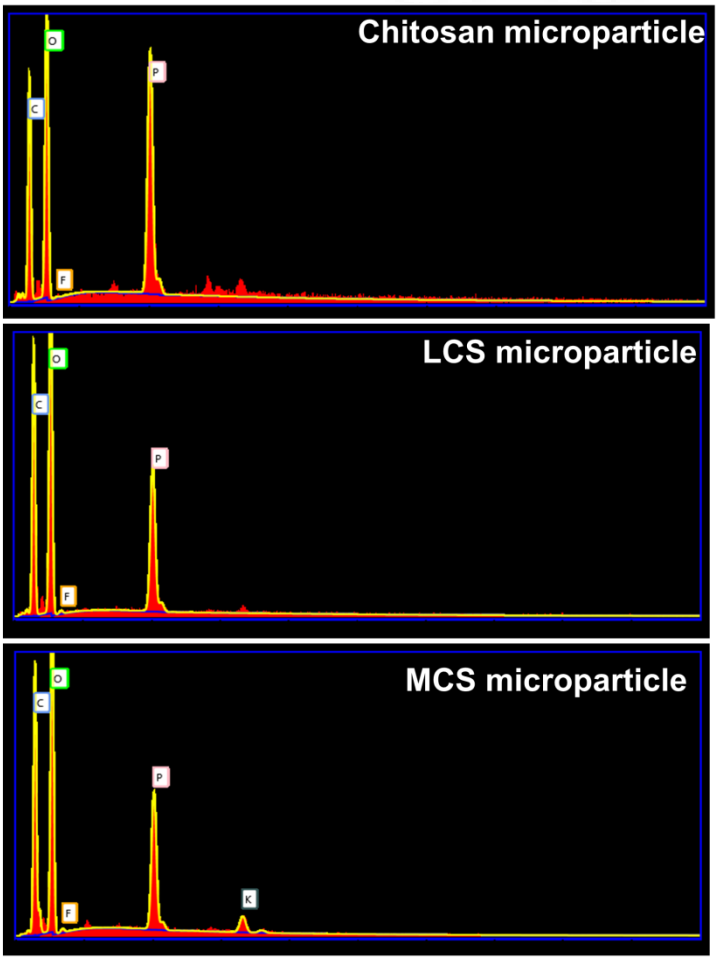

Element	Weight %	Atomic %
C K	44.29	54.98
O K	40.33	37.58
F K	0.12	0.10
P K	15.26	7.35

Element	Weight %	Atomic %
C K	45.49	54.94
O K	44.20	40.07
F K	0.52	0.40
P K	9.80	4.59

Element	Weight %	Atomic %
C K	44.66	54.47
O K	43.76	40.07
F K	0.59	0.45
P K	9.06	4.29
K K	1.94	0.73

Figure 4.56. EDX spectrum of 5-FU loaded microparticles

4.3.9.3. Drug release from microparticles

The drug release studies of the 5-FU loaded microparticles were carried out on pH 1.2, 6.8, and 7.4 to evaluate the release of the drug under the simulated GI tract conditions (Figure 4.57). For drug release, nonenzymatic dissolution conditions were selected where pH 1.2 represents the simulated gastric fluid, 6.8 and 7.4 phosphate buffers represent the intestinal fluid. The drug released from chitosan, LCS, and MCS microparticles at pH 1.2 was found to be 78.5 %, 80.17 %, and 77.5 %,

respectively, at the initial one-hour (figure 4.57 A, C, E). At pH 1.2 chitosan and MCS, microparticles showed a maximum drug release of 96.9 % and 93.4 % in 5 hours, whereas LCS microparticles exhibited 99.6% drug release in 4 hours. At pH 6.8, chitosan microparticles released about 69.09 % 5-FU in the first hour. In the case of LCS and MCS microparticles, 65.02 % and 57.40% of 5-FU were released in the first hour. The maximum drug release exhibited by microparticles at pH 6.8 was found to be 80.09%, (chitosan, 6 hours), 77.37 %, (LCS, 2 hours), and 80.05 % (MCS, 6 hours). At pH 7.4, about 59.62 % of 5-FU was released from chitosan microparticles and about 65.94% and 60.40% of 5-FU from LCS and MCS microparticles at the first hour. The maximum drug release exhibited by microparticles at pH 7.4 was found to be 71.74 %, (chitosan, 6 hours), 82.19 %, (LCS, 3 hours), and 86.4%, (MCS, 5 hours).

The drug release from the microparticles can be explained based on the swelling of the microparticles. The drug release from the chitosan, LCS, and MCS microparticles was higher at pH 1.2 compared to that at pH 6.8 and 7.4. At pH 1.2, the free $–NH_2$ groups will be completely protonated and result in matrix swelling due to hydration and intermolecular repulsion (Sonia et al., 2011). At higher pH (6.8 and 7.4), the deprotonation of ammonium ions takes place and leads to a decrease in the swelling of microparticles which results in a decrease in drug release. The burst release of the drug observed at the initial hour might be due to the release of the drug adsorbed on the surface of the microparticles.

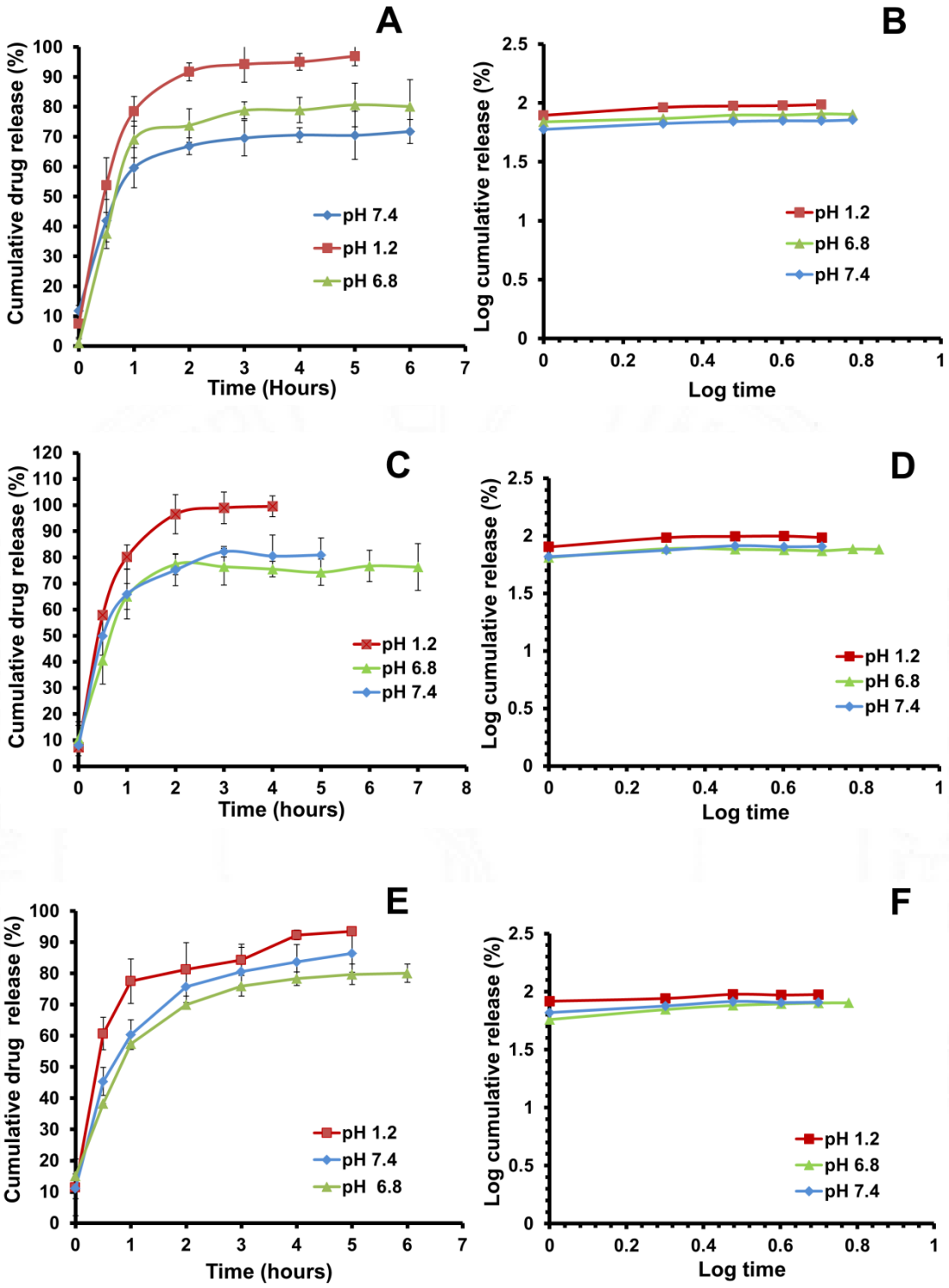

Figure 4.57. Drug release profile of 5-FU from: (A) chitosan, (C) LCS, and (E) MCS microparticles; Drug release kinetics fitting to Korsmeyer-Peppas model - (B) chitosan, (D) LCS, and (F) MCS microparticles.

The drug release data were fitted to different mathematical models such as zero order, first order, Higuchi model, and Korsmeyer-Peppas model, using the DD solver, a Microsoft Excel add-in software package, to study the drug release kinetics (figure 4.57 B, D, F). To identify the best-fit model the coefficient of determination (R^2) for the different models was determined and is shown in Table 4.3. The Korsmeyer-Peppas model was found to fit best for all microparticles at pH 1.2, 6.8, and 7.4 as it had the highest R^2 value compared to other models (Table 4.7). Permanadewi et al. reported that the Korsmeyer-Peppas model was a simple model that describes drug release from a polymeric system (Permanadewi et al., 2019). This model describes several release mechanisms simultaneously including the diffusion of water into the matrix, matrix swelling, and matrix dissolution (Korsmeyer et al., 1983). The diffusion exponent (n) value is an indicator of the mechanism of drug release. The "n" value for the microparticles at pH 1.2, 6.8, and 7.4 was found to be less than 0.5. If "n=0.5" then the samples follow a simple Fickian diffusion but here "n" values lie below 0.5 indicating that the mechanism of drug release is the complex Fickian diffusion through a swollen matrix and water-filled pores (Bacaita et al., 2012).

Table 4.7. Parameters of different mathematical models after fitting the release kinetics of 5-FU from microparticles

Sample	pH	Zero-order	First order	Higuchi	Korsmeyer-Peppas	
		R^2	R^2	R^2	R^2	*n*
Chitosan	**1.2**	0.7835	0.6577	0.9260	**0.9829**	**0.208**
	6.8	0.7474	0.5900	0.8966	**0.9671**	**0.209**
	7.4	0.7251	0.6355	0.8834	**0.9733**	**0.152**
LCS	**1.2**	0.7626	0.6441	0.9142	**0.9810**	**0.194**
	6.8	0.7250	0.6247	0.8605	**0.9520**	**0.159**
	7.4	0.7766	0.6559	0.9233	**0.9882**	**0.189**
MCS	**1.2**	0.7515	0.6622	0.9068	**0.9875**	**0.145**
	6.8	0.8438	0.7517	0.9553	**0.9742**	**0.247**
	7.4	0.8566	0.7299	0.9671	**0.9902**	**0.256**

4.3.9.4. Drug release from Eudragit®S-100 coated particles

Eudragit®S-100 is an anionic copolymer based on methyl methacrylate and methacrylic acid. The pH-responsive behavior of the Eudragit®S-100 is due to the presence of weakly acidic carboxyl groups (Figure 4.58A). In an acidic environment, carboxyl groups are uncharged whereas, at pH greater than their pKa (pKa ~ 4), the polymer chains begin to disentangle due to the electrostatic repulsion between the negatively charged carboxyl groups (Vinner et al., 2017).

The drug release profile of the Eudragit®S-100 coated microparticles was carried out at pH 1.2 followed by pH 6.8 and 7.8 to reflect intestinal pH conditions. Eudragit®S-100 coated microparticles can prevent the loss of 5-FU in the acidic environment of the stomach. From figure 4.58B it is clear that the Eudragit®S-100 coating can prevent the release of 5-FU from the microparticles at pH 1.2. The coating also helped in controlling the release profile of 5-FU at pH 6.8 and 7.4, the initial burst release was nullified. It was observed that the uncoated chitosan, LCS, and MCS

microparticles at pH 1.2, 6.8, and 7.4 showed a significantly higher 5-FU release at initial hours itself (figure 4.57).

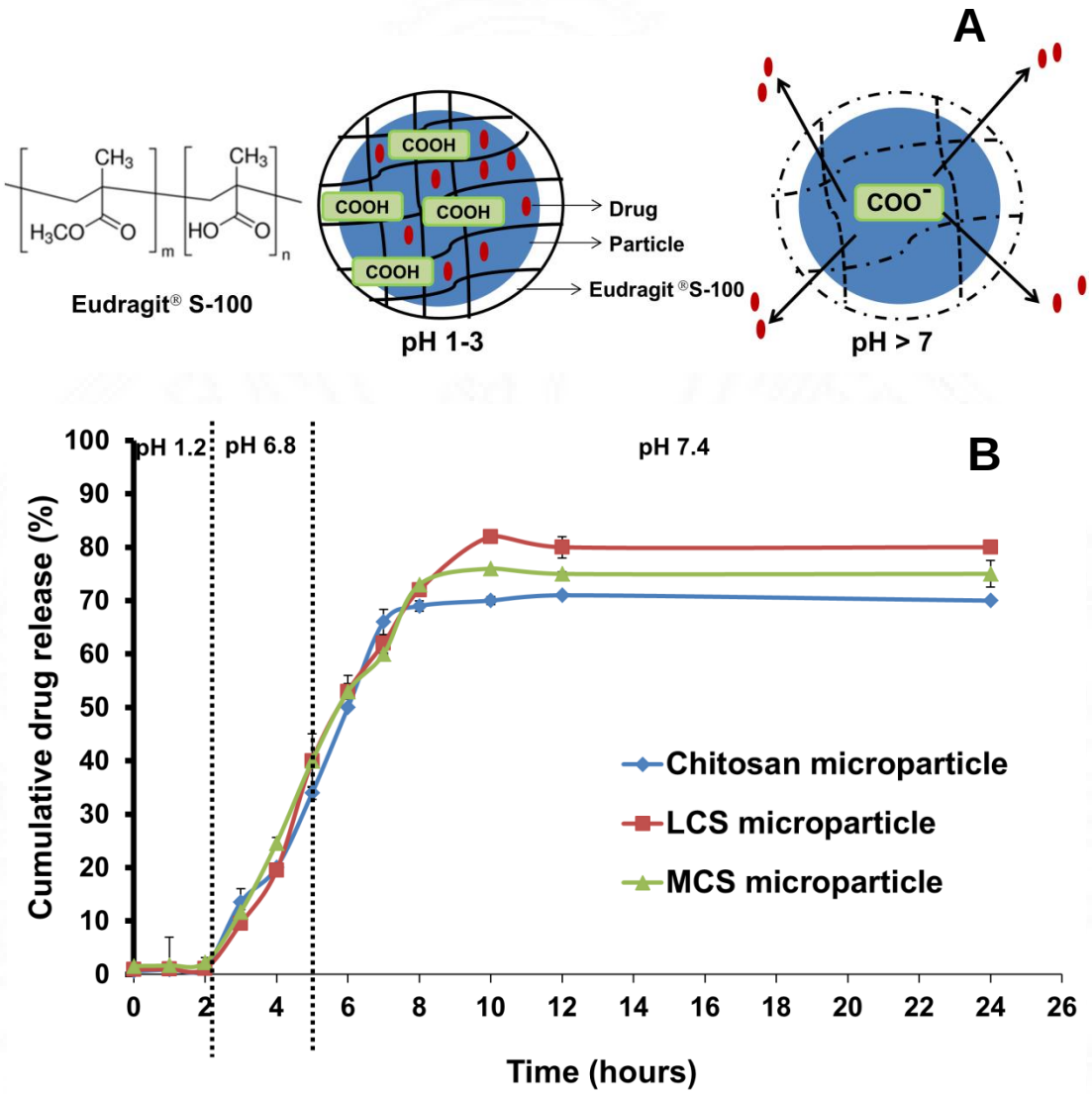

Figure 4.58. Schematic representation of Eudragit® S-100 at different pH (A); Drug release from Eudragit®S-100 coated microparticles (B).

4.3.10. Cellular interaction of microparticles with colorectal cancer cells

4.3.10.1. Cell viability studies with chitosan and its conjugates in colon cancer cells

The cytotoxic response of chitosan, LCS conjugate, and MCS conjugate was evaluated in HCT-116 and Caco-2 colon cancer cells by using an MTT assay. As shown in figure 4.59 the cell viability following exposure to chitosan, LCS

conjugate, and MCS conjugate for 24 hours at the highest concentration (250 µg/mL) was found to be greater than 80% in both HCT-116 and Caco-2 cells. In the case of HCT-116 cells at 250 µg/mL concentration, the cell viability of chitosan, LCS conjugate, and MCS conjugate was found to be 82.04 ± 0.19 %, 96.43 ± 0.14 %, and 85.44 ± 0.06 %. At 250 µg/mL concentration, the cell viability of chitosan, LCS conjugate, and MCS conjugate against Caco-2 cells was found to be 88.95 ± 0.01%, 85.71 ± 0.01%, and 87.34 ± 0.05%, respectively. The results revealed that the chitosan and modified chitosan polymers are non-toxic to both cells even at higher concentrations.

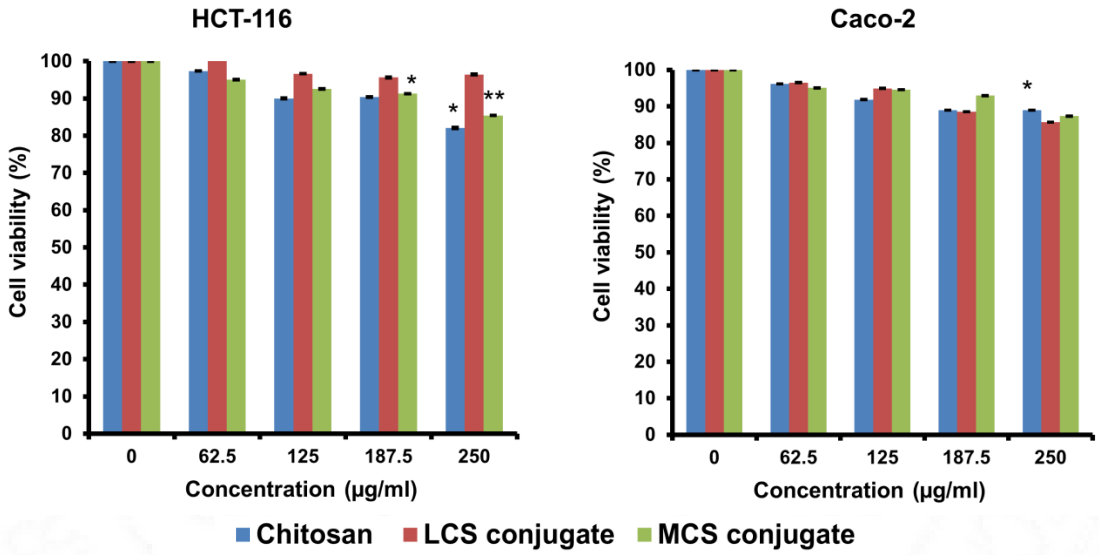

Figure 4.59. Cell viability in response to different concentrations of native chitosan, LCS conjugate, and MCS conjugate performed by MTT assay towards HCT-116 and Caco-2 cells.

4.3.10.2. Cell viability studies with chitosan and chitosan conjugate particles in colon cancer cells.

The cytotoxic response of chitosan, LCS, and MCS microparticles against HCT-116 and Caco-2 colon cancer cells was evaluated by MTT assay (figure 4.60). In HCT-116 cells, the cell viability of chitosan, LCS, and MCS microparticles at 250 µg/mL

concentration was found to be 88.4 ± 0.03%, 93.77 ± 0.03%, and 95.84 ± 0.04%, respectively. In the case of Caco-2 cells, the cell viability of chitosan, LCS, and MCS microparticles at 250 µg/mL concentration was found to be 85.2 ± 0.06 %, 89.9 ± 0.06%, and 83.3 ± 0.06%, respectively. In all instances, the cell viability was observed to be greater than 80%. It has been reported that the cell viability exhibited by native chitosan and glutamine chitosan particles was above 80 % when the Caco-2 cells were treated with 5mg/mL particles (Rekha and Sharma, 2011). The results indicate that chitosan, LCS and MCS microparticles are nontoxic to both cells even at higher concentrations. Being nontoxic these microparticles can be used as a carrier for oral drug delivery applications.

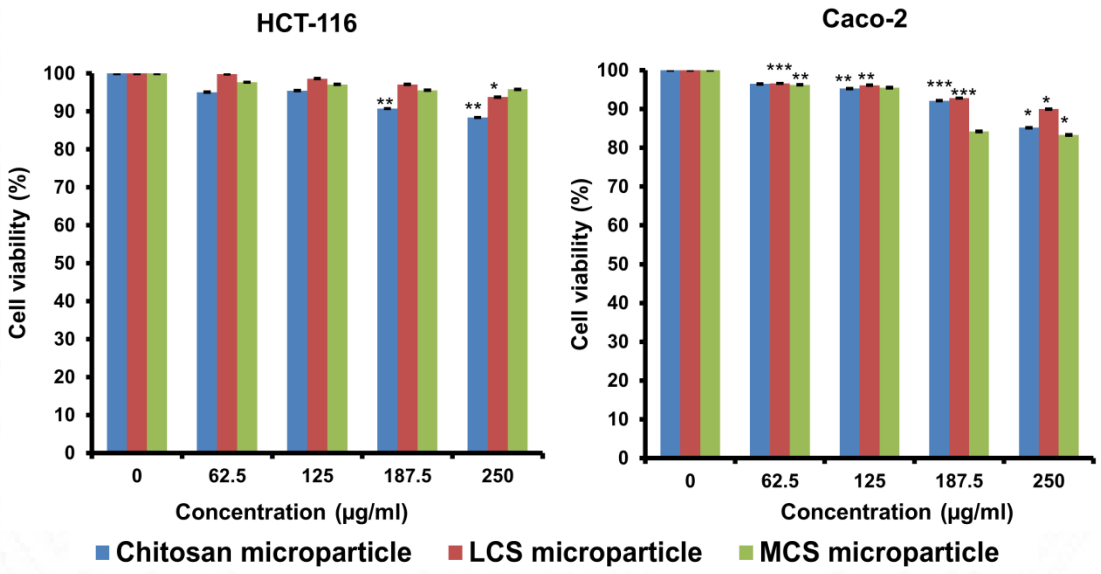

Figure 4.60. Cell viability in response to different concentrations of chitosan, LCS, and MCS microparticles performed by MTT assay towards HCT-116 and Caco-2 cells.

4.3.10.3. Cytotoxicity of drug and drug-loaded particles toward colon cancer cells.

The *in vitro* cytotoxicity of free 5-FU and 5-FU loaded chitosan, LCS, and MCS microparticles on HCT-116 and Caco-2 cells was evaluated by MTT assay. The

HCT-116 and Caco-2 cells were exposed to different concentrations of 5-FU and 5FU- loaded in microparticles (10, 100, 200, 800, and 1200 μM) at different periods (24, 48 and 72 hours) are shown in figures 4.61 and 4.62.

The IC_{50} value of 5-FU after 24 hours of exposure to HCT- 116 was around 557 μM (Figure 4.61). After 48 and 72 hours of single-dose exposure, the cell viability was reduced to 50 % at 188 μM and 166 μM concentrations of 5-FU (Table 4.8). The IC_{50} values of 5-FU loaded in chitosan, LCS, and MCS microparticles after 24 hours of exposure were found to be 726, 258, and 293 μM. After 48 hours of incubation, the IC_{50} values of 5-FU loaded in chitosan, LCS, and MCS microparticles were found to be 99.2, 98, and 128 μM. The IC_{50} values of 5-FU loaded in chitosan, LCS, and MCS microparticles after 72 hours of exposure were found to be 31.95, 15.5, and 21.2 μM, respectively.

The IC_{50} value of 5-FU after 24 hours of exposure to Caco-2 was around 1118 μM (Figure 4.62). In the case of Caco-2 cells after 48 and 72 hours of single-dose exposure, the cell viability was reduced to 50 % at 884 μM and 552 μM concentrations of 5-FU (Table 4.9). The IC_{50} values of 5-FU loaded in LCS, and MCS microparticles after 24 hours of exposure were found to be 1065 and 1091 μM while IC_{50} was not reached for 5-FU loaded in chitosan microparticles. After 48 hours of incubation, the IC_{50} values of 5-FU loaded in chitosan, LCS, and MCS microparticles were found to be 517, 452, and 439 μM. The IC_{50} values of 5-FU loaded in chitosan, LCS, and MCS microparticles after 72 hours of exposure were found to be 200, 177, and 200 μM, respectively.

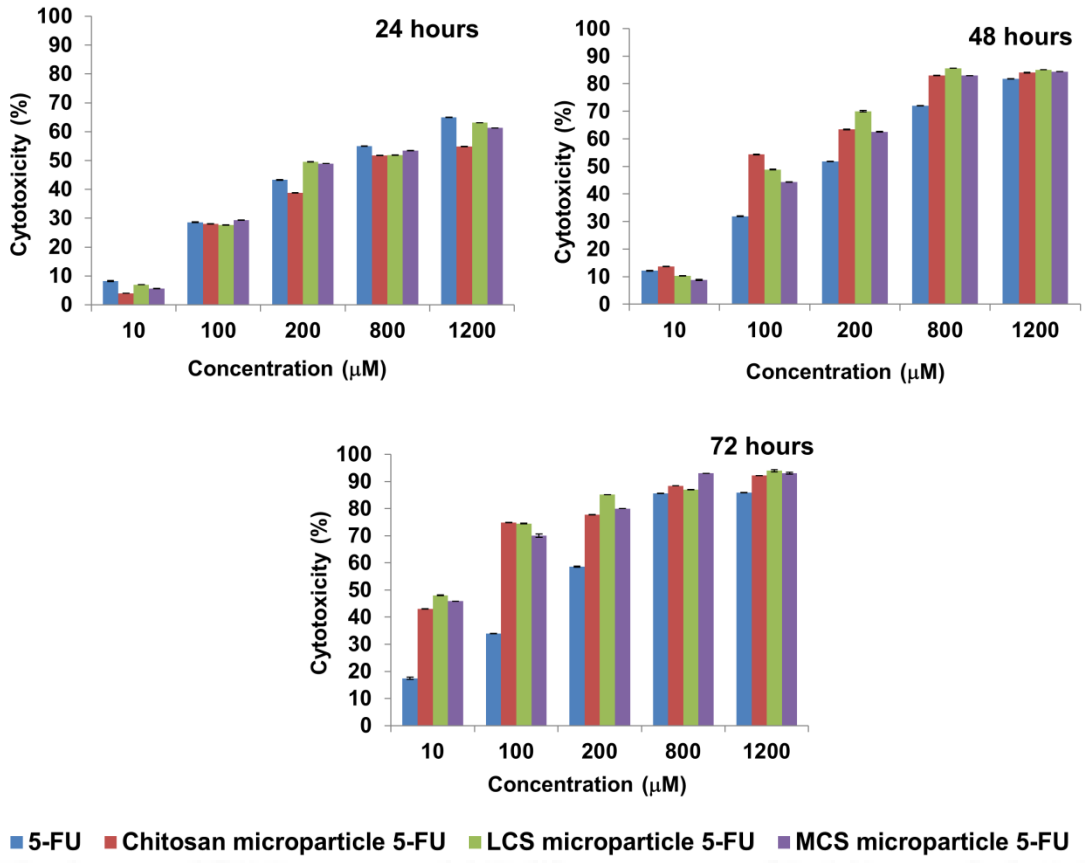

Figure 4.61. Cytotoxicity of 5-FU and 5-FU loaded microparticles towards HCT-116 cells at different time intervals.

Table 4.8. IC_{50} values of 5-FU and 5-FU loaded in microparticles toward HCT-116 cells

Microparticles	***IC*** $_{50}$ **(µM)**		
Time (hours)	**24**	**48**	**72**
5-FU	557	188	166
Chitosan 5-FU	726	99.2	31.95
LCS 5-FU	258	98	15.5
MCS 5-FU	293	128	21.2

After 48 hours of single-dose exposure, a remarkably lower concentration was observed to reduce cell viability to 50% in both HCT-116 and Caco-2 cells. Furthermore, a very low concentration of 5-FU was sufficient to reduce 50% cell viability after 72 hours of exposure. The results revealed that HCT-116 and Caco-2

cells respond to the 5-FU and 5-FU loaded in microparticles in a dose-dependent and time-dependent manner. The time factor demonstrated more influence on 5-FU activity compared to the observed dose dependency. Tawfik et al. reported a similar trend after treating HCT-116 and HT-29 colon cancer cells with 5-FU. These results suggest that the cytotoxic effect exhibited by 5-FU is more dependent on prolonged exposure to cells rather than the availability of higher concentrations with short-time exposure (Tawfik et al., 2017). It has also been reported that 5-FU-induced autophagy is time-dependent in HCT-116 cells and Caco-2 cells (Thant et al., 2008; Yang et al., 2018).

It was observed that the Caco-2 cells were less sensitive to 5-FU compared to HCT-116 cells. This indicates that prolonged exposure to 5-FU can enhance the desired toxicity. Thant et al. reported that Caco-2 cells with mutant p53 failed to activate caspase -8, −9, −7, and −3 and with hypermethylated caspase-8 are resistant to 5-FU (Thant et al., 2008).

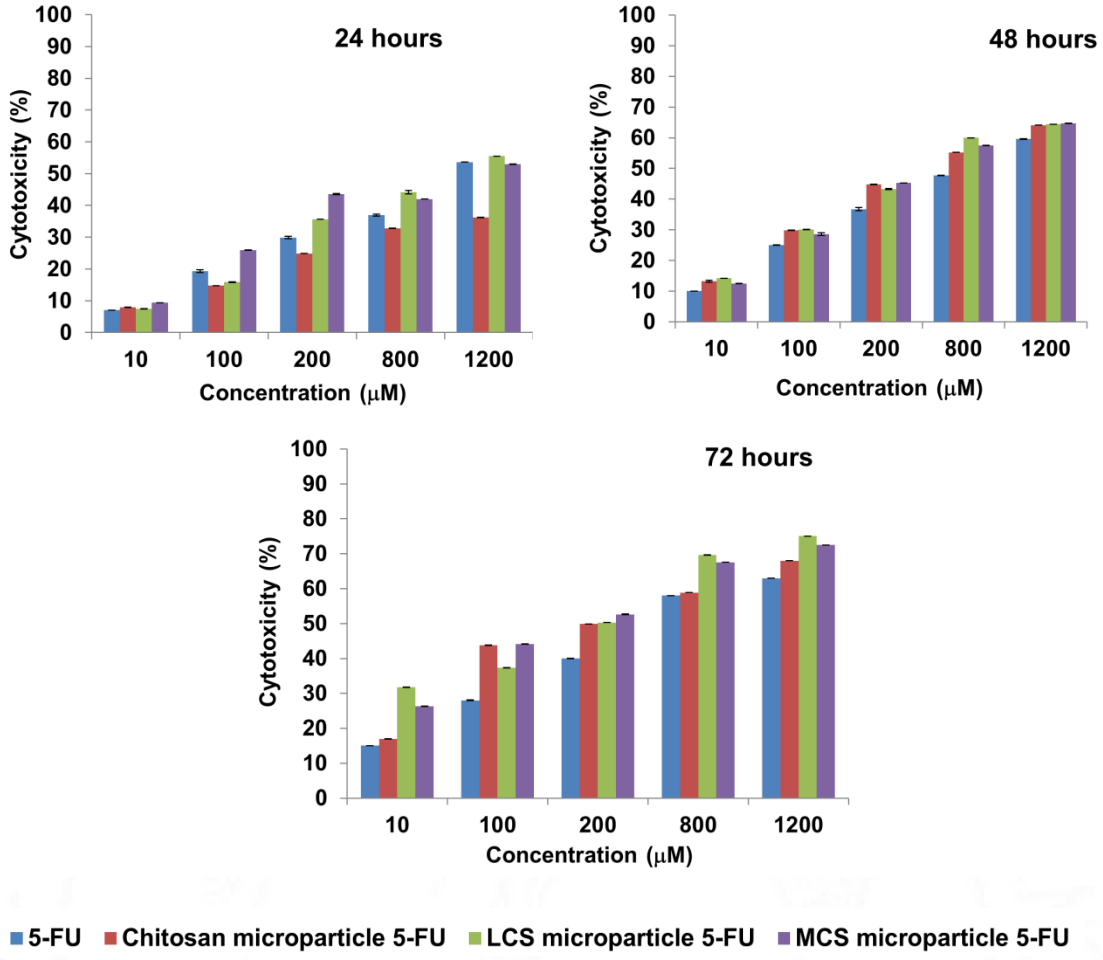

Figure 4.62. Cytotoxicity of 5-FU and 5-FU loaded microparticles towards Caco-2 cells at different time intervals.

Table 4. 9. IC_{50} values of 5-FU and 5-FU loaded microparticles toward Caco-2 cells

Microparticles	*IC 50* (μM)		
Time (hours)	**24**	**48**	**72**
5-FU	1118	884	552
Chitosan 5-FU	Not reached	517	200
LCS 5-FU	1065	452	177
MCS 5-FU	1091	439	200

4.3.10.4. Effect of chitosan and modified chitosan particles on Caco-2 cell TEER

The human epithelial cell line Caco-2 was used as a model of the intestinal epithelial barrier. When grown on transwell membrane filters, Caco-2 cells spontaneously form tight junctions and markers of intestinal epithelial cell differentiation (Buzza et al., 2010). Tight junctions are multifunctional protein complexes made up of a variety of cytosolic proteins like zonula occludens (ZO)-1, ZO-2, ZO-3, and cingulin and transmembrane proteins like claudins, occludins and junctional adhesion molecules (JAMs) (Cereijido et al., 2000). Tight junctions form the continuous intercellular barrier between epithelial cells, which is necessary to separate tissue spaces and control the selective movement of solutes across the epithelium (Anderson and Van Itallie, 2009). Transepithelial electrical resistance (TEER) is a very sensitive and reliable method to confirm the integrity and permeability of cellular monolayer by measuring the electrical resistance across it (Srinivasan et al., 2015).

The effect of chitosan, LCS, and MCS microparticles on the transepithelial electrical resistance of Caco-2 cell monolayers is shown in figure 4.63A. Throughout the study period, the TEER values of the control cell monolayers remained constant. After chitosan and LCS microparticle treatment, the TEER values of Caco-2 cells were found to be decreased by around 75% and 80% whilst in the case of MCS microparticles the TEER was reduced by about 40 %. The TEER did not decrease much further in any of the three cases after the initial 60 minutes. The reduction in TEER value indicates the loss of tight junction integrity which leads to the loss of barrier properties and causes the influx of ions across the monolayer (Rekha and Sharma, 2011). It has been also reported that the reduction in TEER was not due to

the cytotoxic effects but due to the transient opening of tight junctions (Sadeghi et al., 2008). The tight junction opening was found to be higher for positively charged LCS and chitosan microparticles compared to negatively charged MCS microparticles. The TEER reduction was found to be in the order LCS > chitosan > MCS microparticles. Sadeghi et al. reported that in comparison to the free-soluble polymers, nanoparticles based on chitosan and its quaternized derivatives had a much lower effect on TEER reduction (Sadeghi et al., 2008). This is due to the reduction in the available amount of positive charge at the surface of the nanoparticles, compared to the soluble form of chitosan. In a study by Schipper et al., the tight junction-modulating effects of chitosan were shown to be mediated by its cationic surface charge (Schipper et al., 1997).

The surface charge of the particles plays an important role in the opening of the tight junction. It is very important to understand the mechanism of tight junction opening by particles. The mechanism underlying tight junction opening is different for positive and negatively charged particles. Chitosan-mediated tight junction disruption activates integrin receptors on cell membranes which initiate the cascade of tight junction opening (Hsu et al., 2012). The chitosan-induced tight junction opening is mediated through the tyrosine kinase signaling pathway. The regulatory proteins focal adhesion kinase (FAK) and steroid receptor coactivator (Src) mediate signals to the actin cytoskeleton (Quintela-Fandino et al., 2010). Chitosan molecules interact with integrin $\alpha_v\beta_3$ through electrostatic interaction between the $-NH_3^+$ groups of chitosan and $-COO^-$ groups on the integrin $\alpha_v\beta_3$ forming a chitosan-integrin $\alpha_v\beta_3$ complex, phosphorylation of FAK and Src tyrosine kinase, and regulation of tight

junction permeability via the redistribution of claudin-4 from cell membrane to cytosol (Hsu et al., 2012). After chitosan treatment other junctional proteins such as ZO-1, JAM-1, and occludin were also reported to be downregulated (Lin et al., 2007; Ranaldi et al., 2002; Smith et al., 2005; Sonaje et al., 2012). The mechanism of tight junction opening is the same for both chitosan and LCS (cationic) microparticles.

The chelation of extracellular or tight junctional calcium (Ca^{2+}) by charged carboxylate groups of MCS (anionic) microparticles leads to temporary disruption of tight junctions and thereby facilitating paracellular transport (Li et al., 2006). Ca^{2+} is important for the cadherins at adherens junctions, which is essential for the induction and maintenance of tight junction assembly (Su et al., 2012).

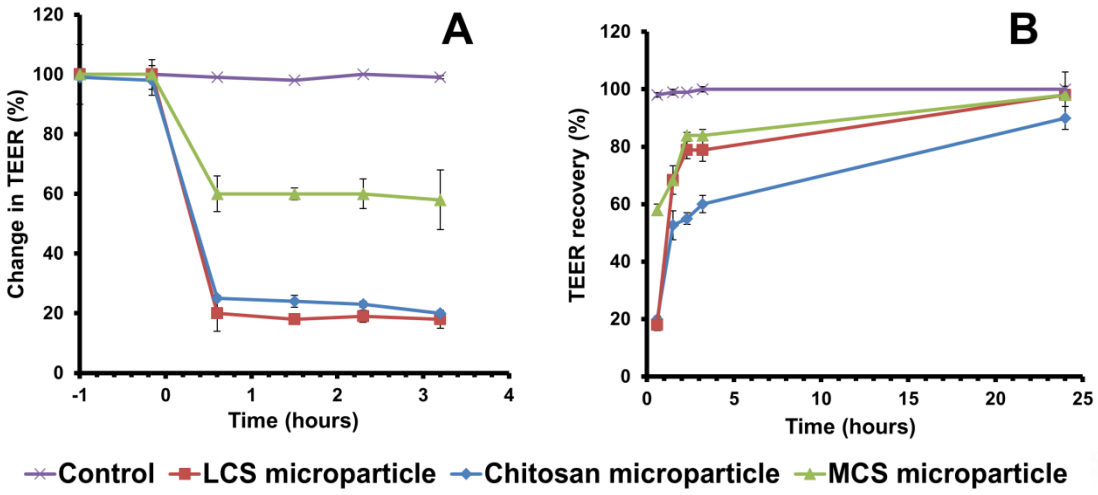

Figure 4.63. Effect of chitosan, LCS, and MCS microparticles on Caco-2 cell TEER (A); TEER recovery (B).

After the removal of the microparticles, the TEER values came back to that of the control cell monolayers within 24 hours (figure 4.63B). This indicates that the tight junctions of the Caco-2 cell monolayers were resealed and barrier properties were recovered after the microparticle removal.

4.3.10.5. Drug transport studies across caco-2 cell monolayer

The transport of the drug 5-FU and 5-FU loaded in microparticles across the Caco-2 cell monolayers was monitored as a function of time (figure 4.64). The apparent permeability of 5-FU loaded in chitosan, LCS, and MCS microparticles was found to be 7.60 ± 0.63, 9.20 ± 0.80, and 3.20 ± 0.21 cms^{-1}. According to figure 4.64, the LCS microparticles offered the highest permeability of 5-FU, and MCS microparticles showed the least influence on the transport of 5-FU across the Caco-2 cell monolayer. The apparent permeability of the 5-FU was found to be in the order LCS > chitosan > MCS. The result correlates well with the results obtained from the TEER measurements. The LCS microparticles with the highest reduction of TEER values were found to be effective in inducing the permeation of 5-FU across the cell monolayer. In contrast, the MCS microparticles that had the smallest reduction on the TEER resulted in the least permeation of 5-FU across the Caco-2 cell monolayer. A similar trend was reported by Sadeghi et al. for the permeability of human insulin where trimethyl chitosan (TMC) nanoparticles having a higher zeta potential showed a slightly higher ability to transport insulin than chitosan and other derivatives (Sadeghi et al., 2008).

The free drug 5-FU alone was found to have less permeation across the Caco-2 cell monolayer with an apparent permeability of 2.5 ± 0.11 cms^{-1}. The permeability of 5-FU was found to be 3.7-fold higher for LCS microparticles compared to the free drug 5-FU. The chitosan and MCS microparticles showed a 3-fold and 1.28-fold increase in the apparent permeability of 5-FU compared to 5-FU alone. This result revealed that the microparticles play an important role in tight junction opening and promote

paracellular transport of 5-FU. The tight junction opening facilitates the absorption of hydrophilic drugs like 5-fluorouracil across the intestinal epithelium.

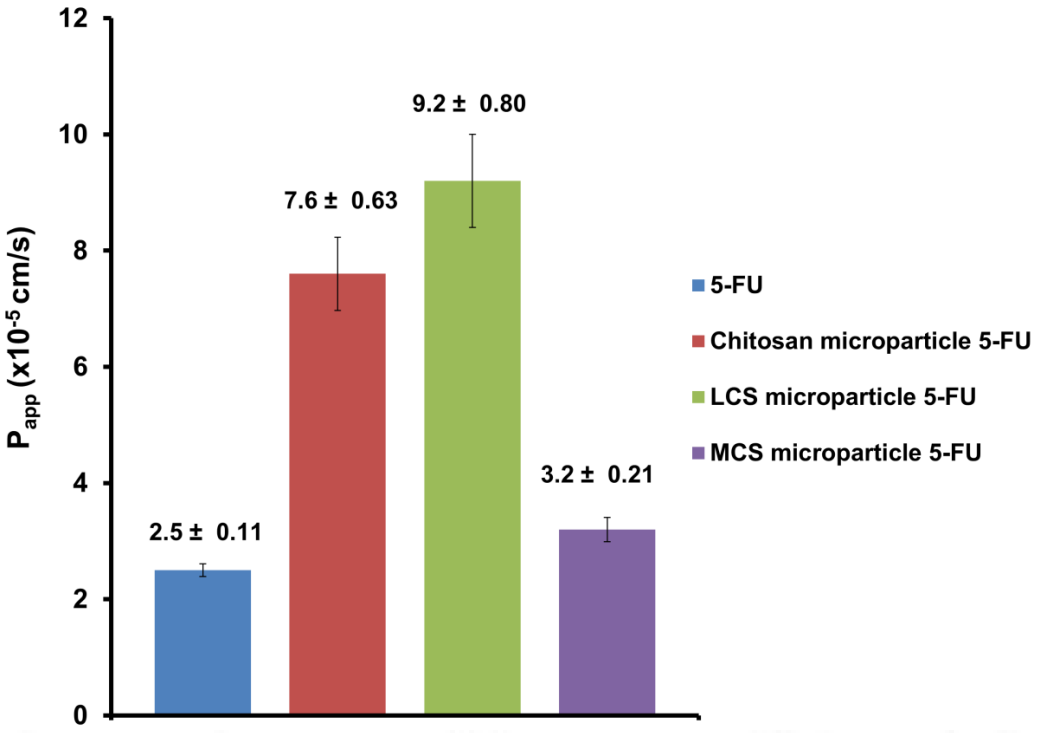

Figure 4.64. Apparent permeability coefficient (P_{app}) of 5-FU and 5-FU loaded in microparticles.

4.3.10.6. Actin filament staining by rhodamine-phalloidin

A ring of filamentous actin encircles every epithelial cell at the level of the apical junctional complex and physically interacts with the tight junction in addition to the specific tight junction proteins (Madara, 1987). Wang et al. reported that tight junction proteins such as claudin-4 are connected to the actin cytoskeleton through transcellular adaptor proteins, including ZO-1 and actin, which is the major protein in the cell cortex (Wang et al., 2017). The cytoskeletal and tight junction disruption is associated with altered cell shape, retraction of microfilaments from the plasma

membrane, local accumulation of condensed actin, and the disruption of the parallel strands that include the tight junction (Madara et al., 1986; Meza et al., 1982).

The effect of chitosan, LCS, and MCS microparticles on actin filaments was evaluated by rhodamine-phalloidin staining (figure 4.65). The disruption of the actin filaments was observed from the staining pattern in the case of microparticle-treated cells (figure 4.65B, C, D) compared to the control cells (figure 4.65A). Actin filaments in the case of LCS microparticle-treated cells (figure 4.65C) were observed to be more discontinuous and disrupted compared to chitosan (figure 4.65B) and MCS (figure 4.65D) microparticles. The order of actin filament disruption was found to be LCS > chitosan > MCS. TEER measurement data was further supported by actin filament staining. The TEER reduction was found to be higher for LCS microparticles compared to chitosan and MCS microparticles. This indicates that the tight junction opening is in the order LCS > chitosan > MCS microparticles. Actin depolymerization is an indication of the tight junction disruption and the loss of its barrier properties (Shen and Turner, 2005).

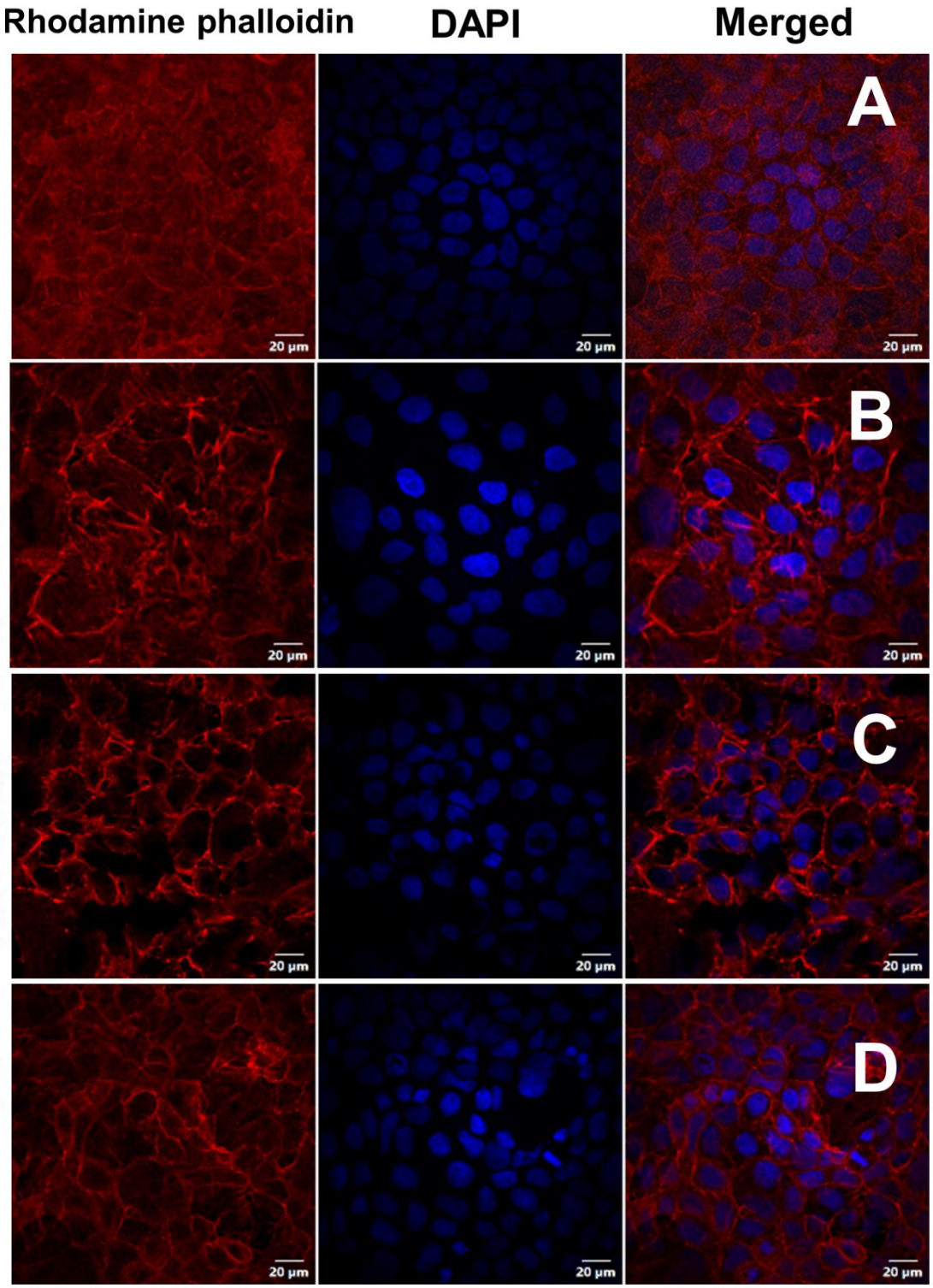

Figure 4.65. Actin filament staining of Caco-2 cells: (A) control; (B) chitosan; (C) LCS, and (D) MCS microparticle treatment. Magnification of the Confocal images was 60X.

4.3.10.7. ZO-1 Tight junction staining

The effect of chitosan, LCS, and MCS microparticles on tight junction protein ZO-1 was evaluated by Anti-ZO-1 immunofluorescent staining. In untreated control cells, ZO-1 appears as smooth lines at cell-cell junctions (figure 4.66A). The immunofluorescent staining intensity of chitosan, LCS, and MCS particle-treated cells was found to be weaker compared to the control this indicates the loss of ZO-1 from sites of cell-cell contact (figure 4.66 B, C, D). The loss of ZO-1 immunofluorescence from conserved regions of the membrane indicates a loss of tight junction integrity and consequently barrier properties (Smith et al., 2004). The ZO-1 staining intensity was found to be the least in the LCS microparticle-treated cells (figure 4.66C). The order of ZO-1 loss was found to be LCS > chitosan > MCS microparticles. This data further confirms the tight junction opening on microparticle treatment. It has been also reported that chitosan-mediated tight junction disruption is due to the translocation of tight junction protein (ZO-1) from the plasma membrane to the cytoskeleton (Rekha and Sharma, 2011). The cationic microparticles (LCS and chitosan) were found to open the tight junction more efficiently compared to anionic (MCS) microparticles (figure 4.66D).

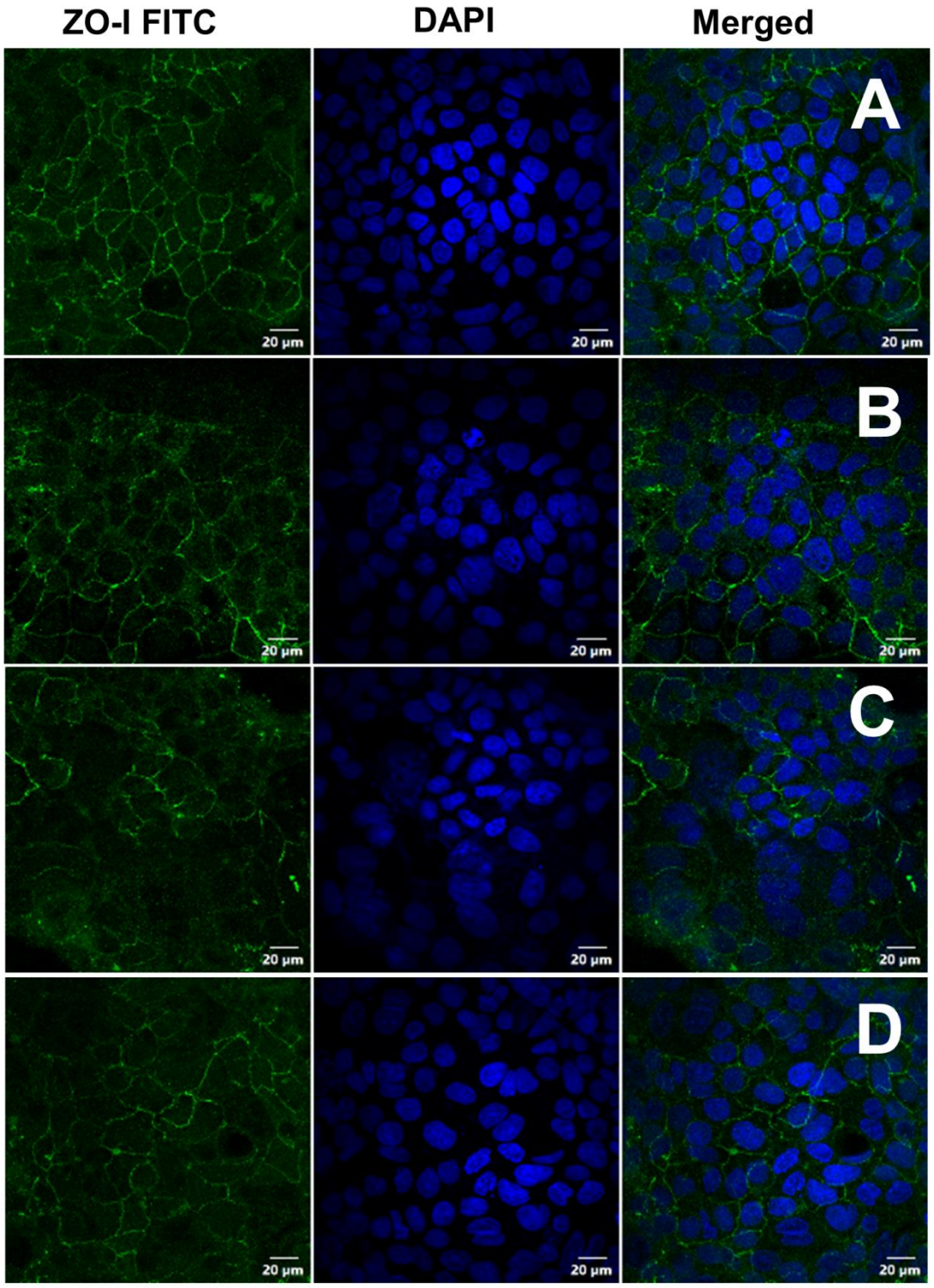

Figure 4.66. Tight junction (ZO-1) staining of Caco-2 cells: (A) control; (B) chitosan; (C) LCS and (D) MCS microparticle treatment. Confocal images were taken at 60X magnification.

4.3.11. Mucin binding studies

Mucin is the primary functional component of the mucus layer. Mucins are extracellular glycoproteins with a high molecular weight (0.5-20 MDa) containing about 80% carbohydrates attached to the protein core mostly through O-glycosylation (Szilágyi et al., 2020). Mucins are involved in the adhesion of the unstirred layer to the cell surface and also serve as a physical barrier in which pathogens and nanoparticles are trapped (Cone, 2009). Collado-González et al. reported that the interactions of chitosan and mucin determine the behavior and fate of chitosan-based nanosystems. The simplest hypothesis is that these biomaterials either adsorbed at the mucus layer, shed with the mucus, or go through this layer and reach the cell surface (Collado-González et al., 2019). The tenacious and sticky network of mucin fibers prevents the diffusion of foreign particles by trapping and steric hindrance (Liu et al., 2015). Mucus turnover can dynamically eliminate these entrapped particles through constant secretion and shedding (Liu et al., 2021). The mucin binding percentage of chitosan, LCS, and MCS microparticles was found to be 32.8 ± 0.2 %, 32.1 ± 0.1 %, and 30.7 ± 0.1 % (Table 4.10). Irrespective of charge all the microparticles exhibit less interaction with mucin. So, the microparticles can efficiently overcome the mucus barrier and avoid rapid clearance.

Table 4.10. Mucin binding percentage of microparticles

Samples	Mucin Binding (%)
Chitosan microparticles	32.8 ± 0.2
LCS microparticles	32.1 ± 0.1
MCS microparticles	30.7 ± 0.1

4.3.12. Mucoadhesion studies of microparticles

The adhesion between two materials, at least one of which is a mucosal surface, is generally referred to as mucoadhesion (Shaikh et al., 2011). Mucoadhesion enhances the bioavailability of a drug by prolonging its residence time close to the absorbing tissue (Schattling et al., 2017). While developing oral drug delivery carriers mucoadhesion is an important factor to take into account. Mucoadhesion studies of native chitosan and functionalized chitosan particles were carried out in both the small intestinal region as well as the colon region of the rat intestine by two methods.

4.3.12.1. In vitro mucoadhesion studies

The percentage mucoadhesion of the chitosan, LCS, and MCS microparticles in the small intestine region was found to be 95.0 ± 0.9 %, 97.4 ± 0.83 %, and 97.6 ± 1.44 % (figure 4.67A). The mucoadhesion was found to be significantly higher for LCS and MCS microparticles compared to chitosan microparticles. The mucoadhesion in the small intestine region was in the order MCS = LCS > chitosan microparticles.

In the colon region, the mucoadhesion exhibited by chitosan, LCS, and MCS microparticles was found to be 84.8 ± 4.2 %, 95.2 ± 2.22 %, and 93.6 ± 3.79 %, respectively (figure 4.67B). The mucoadhesion was found to be higher for LCS microparticles compared to MCS and chitosan particles. The mucoadhesion in the colon region follows the order LCS > MCS > chitosan microparticles.

Compared to chitosan microparticles the positive charge is higher for LCS microparticles which could be due to the availability of amino groups from lysine which can remain protonated at physiological pH. The increased mucoadhesion of

LCS microparticles compared to chitosan is due to the electrostatic interaction between the negatively charged mucus and positively charged amines of LCS microparticles (Schattling et al., 2017). The increased mucoadhesion by MCS microparticles compared to chitosan microparticles is due to its anionic nature, where hydrogen bonds formed between the mucus and carboxylic group of anionic MCS microparticles increased the mucoadhesive property (Schattling et al., 2017). The mucoadhesive nature of modified chitosan particles was found to be higher than chitosan microparticles.

The mucoadhesion of the microparticles was found to be higher in the small intestine region compared to the colon region. Atuma et al. reported that the thickness of the mucus layer varies from the stomach to the colon region in the rat (Atuma et al., 2001). The thickness of the mucus layer in the colon is higher (≈ 830 μm) compared to the duodenum (≈170 μm) and jejunum (≈ 123 μm) region of the small intestine. The firmly adherent mucus layer was reported to be 116 μm in the colon and in the small intestine, it was very thin (≈ 20 μm) or absent. The thinner mucus layer in the small intestine leads to less mucin interaction with microparticles which results in higher mucoadhesion.

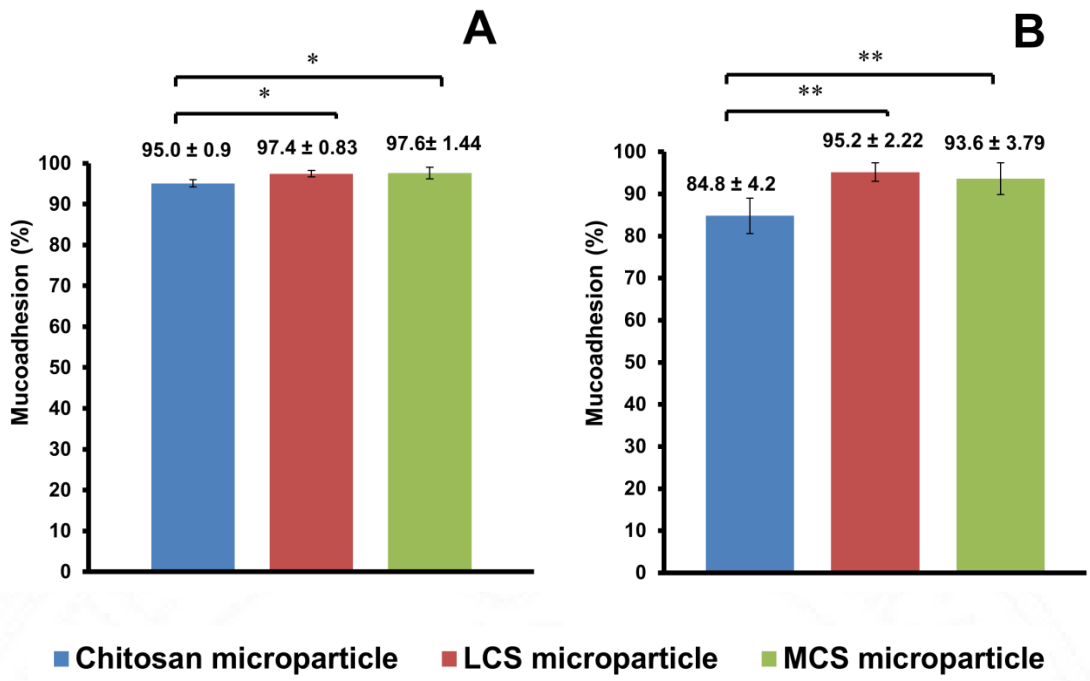

Figure 4.67. Mucoadhesion of microparticles in the small intestine (A) and Colon (B) regions of the rat intestine.

4.3.12.2. Mucoadhesion studies by texture analyzer

Mucoadhesion studies of microparticles were carried out in the rat small intestine and colon regions using a texture analyzer (figure 4.68). In the small intestine, the mucoadhesive force exhibited by chitosan, LCS, and MCS microparticles were found to be 38.7 ± 4.1 g, 45.7 ± 6.9 g, and 53.3 ± 5.7 g, respectively (Table 4.11). The mucoadhesive force (Fmax) follows the order MCS > LCS > chitosan microparticles (figure 4.68A). The mucoadhesive force exerted by MCS microparticles was found to be 1.3-fold higher compared to chitosan microparticles. In the case of LCS microparticles, the mucoadhesive force was found to be 1.1-fold higher than chitosan microparticles. The work of adhesion (Wad) of MCS microparticles was found to be substantially greater than LCS and chitosan microparticles (Table 4.11).

Table 4.11. Correlation between zeta potential and mucoadhesive strength on small intestine region

Particles	Zeta Potential (mV)	Work of adhesion (g.mm)	Mucoadhesive Force (g)
Chitosan	+13.3 ± 0.17	47.4 ± 4.7	38.7 ± 4.1
LCS	+23.7 ± 0.58	48.1 ± 12.8	45.7 ± 6.9
MCS	-9.54 ± 0.79	67.9 ± 13.9	53.3 ± 5.7

In the colon, the mucoadhesive force exhibited by chitosan, LCS, and MCS microparticles was found to be 16.41 ± 1.00 g, 26.73 ± 1.14 g, and 23.17 ± 2.10 g, respectively (Table 4.12). The mucoadhesive force (Fmax) exhibited by microparticles follows the order LCS > MCS > chitosan (figure 4.68B). The mucoadhesive force exhibited by LCS microparticles was found to be higher than MCS and chitosan microparticles. The mucoadhesive force exerted by LCS microparticles was found to be 1.5-fold higher than chitosan microparticles. In the case of MCS microparticles, the mucoadhesive force was found to be 1.2-fold higher than chitosan particles. The Wad of LCS microparticles were found to be higher than MCS and chitosan microparticles.

Table 4.12. Correlation between zeta potential and mucoadhesive strength on colon region

Particles	Zeta Potential (mV)	Work of adhesion (g.mm)	Mucoadhesive Force (g)
Chitosan	+13.3 ± 0.17	4.4 ± 0.94	16.41 ± 1.00
LCS	+23.7 ± 0.58	18.1 ± 2.2	26.73 ± 1.14
MCS	-9.54 ± 0.79	7.6 ± 0.49	23.17 ± 2.10

Greater mucoadhesive force and work of adhesion indicate a higher mucoadhesive nature. The modified LCS and MCS microparticles exhibit higher mucoadhesion

compared to chitosan microparticles in both the small intestine and colon regions. The increased mucoadhesive nature contributed to longer residence time in the intestine and can release drugs over longer periods thereby ensuring better therapeutic effects.

The mucoadhesive nature of the microparticles evaluated by the texture analyzer was in good agreement with that of the *in vitro* mucoadhesion studies reported in section *4.3.12.1*. The increased mucoadhesion of LCS microparticles compared to chitosan was attributed to the electrostatic interaction between the negatively charged mucus and positively charged amines of LCS microparticles (Schattling et al., 2017). The increased mucoadhesion by MCS microparticles compared to chitosan microparticles could be due to the hydrogen bond formation between the mucus and carboxylic group of anionic MCS microparticles (Schattling et al., 2017).

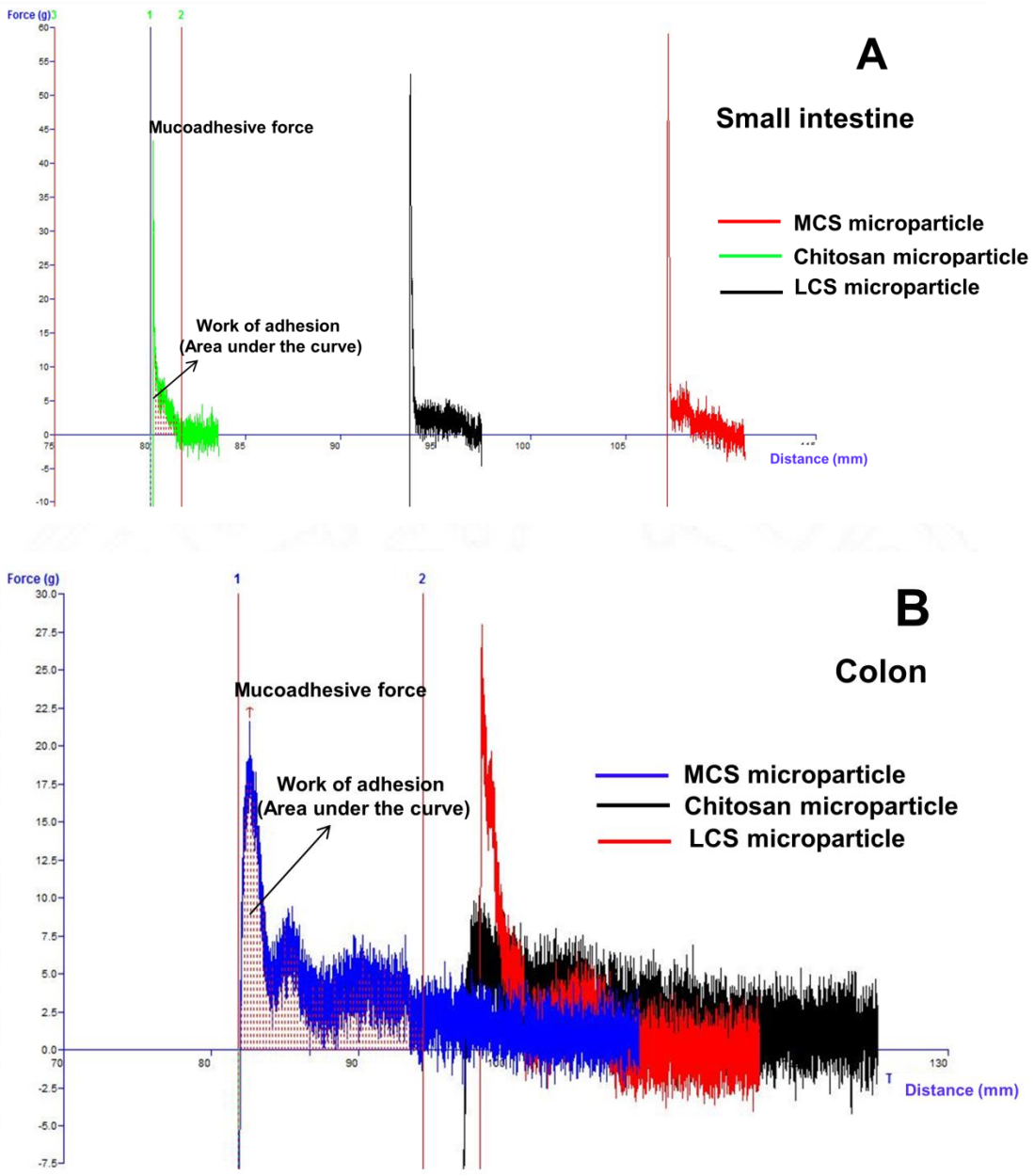

Figure 4.68. Mucoadhesive force exhibited by microparticles evaluated by texture analyzer.

4.3.13. SDS PAGE- protein corona studies using pancreatin mix

This study was carried out to explore the interactions of microparticles with proteins in the GI environment. The biological fate of the particles is largely determined by how they interact with the proteins in their environment. Two different quantities (2 mg and 5 mg) of the microparticles were incubated with pancreatin and the tightly

bound proteins termed “hard corona” were eluted and analyzed by SDS-PAGE (figure 4.69). Pancreatin from the exocrine cells of the porcine pancreas is a mixture of several digestive enzymes including amylase, trypsin, lipase, ribonuclease, and protease. The molecular weight of amylase, lipase protease, trypsin, and ribonuclease was reported as 45 kDa, 38 kDa, 23.8 kDa, 20 kDa, and 13.7 kDa, respectively (Shen et al., 2013).

The major protein bound to the microparticles was found to be ribonuclease. Irrespective of the charge, ribonuclease binds to both the cationic (chitosan and LCS) and anionic (MCS) microparticles. The intensity of the band corresponding to ribonuclease was found to be decreased after incubating with 5 mg microparticle. Zhang et al. reported that the protein adsorption capacity, that is the amount of protein adsorbed on each particle, is inversely proportional to the nanoparticle exposure concentration regardless of the zeta potential or material properties (Wei et al., 2015; Zhang et al., 2017). Higher concentrations of nanoparticles have a lower potential to adsorb proteins when the protein concentration is relatively constant and fewer protein molecules are available for each particle (Zhang et al., 2021, 2017). This indicates that fewer protein molecules get adsorbed onto each microparticle when the particle concentration increases.

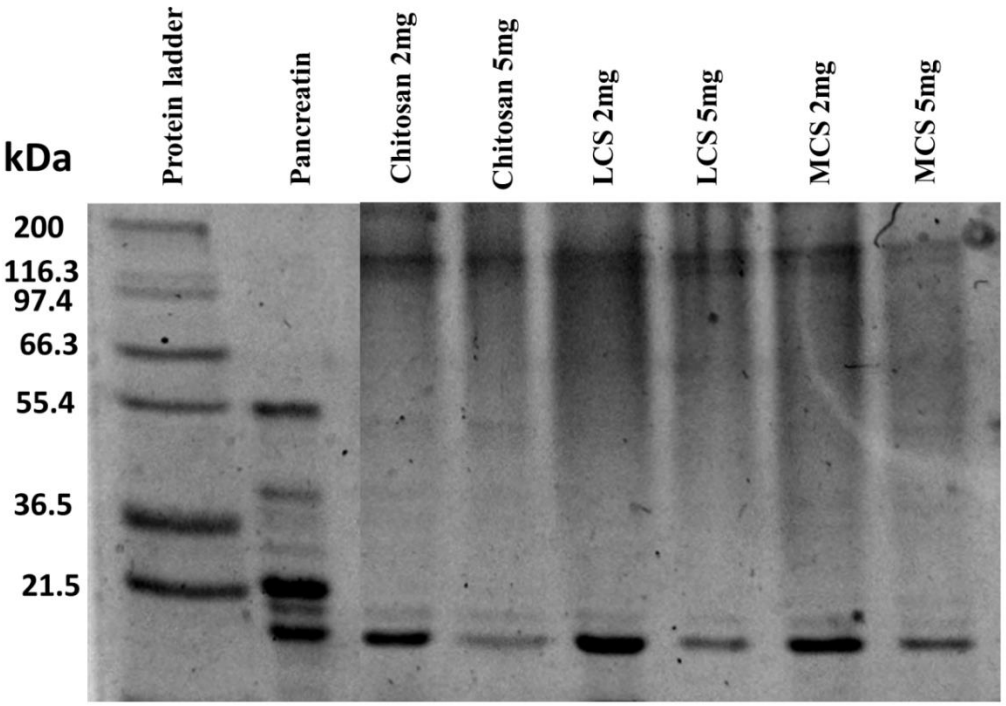

Figure 4.69. Protein corona formation in microparticles evaluated by SDS-PAGE

5 SUMMARY AND CONCLUSION

The focus of the work was to study the interactions of nano and micro drug delivery carriers with the simulated intestinal microenvironment. The drug carriers used in this study belonged to three different categories based on the material used to generate them: lipid-based nanocarriers, nanoparticles of metal-drug conjugates, and microparticles of chitosan and its derivatives. These drug carriers had different surface chemistry and size (metallic, hydrophobic, and hydrophilic) and varied in their interactions with simulated intestinal microenvironments and drug-delivering efficacy. Chitosan and functionalized chitosan particles were the microparticle-based drug delivery systems used for the study. Curcumin-silver nanoparticle conjugate (CUR-AgNP) and lauric acid solid lipid nanoparticles (LA-SLN) were the nano-drug delivery systems used for the study.

CUR-AgNP was synthesized by using curcumin as the reducing agent, and its successful formation was confirmed by analytical techniques. The cellular uptake of CUR-AgNP was found to be time-dependent and the particles were found to be localized in the cytoplasm of the cells. The curcumin bound to the CUR-AgNP was able to exhibit substantial stability in intestinal pH (7.4) compared to native curcumin. However, higher concentrations of CUR-AgNP were required to elicit cytotoxicity in colorectal cancer cells compared to native curcumin. Caco-2 cells were found to be more resistant to CUR-AgNP compared to HCT-116 cells. This limits the application of CUR-AgNP for colorectal cancer treatment. Due to this reason, we haven't further proceeded with this system and have not carried out the interactions of CUR-AgNP with the simulated intestinal microenvironment.

The second system, LA-SLN was prepared by the hot homogenization method. A fluorescent lipophilic dye, Rhodamine B (RhB), was incorporated into the LA-SLN (R-LA-SLN) as a model drug. R-LA-SLN had an entrapment efficiency of 80.31 ± 0.18 % with a drug loading of 10.2 ± 0.02 μg/mg lipid. The *in vitro* release studies of R-LA-SLN revealed a biphasic release pattern and released about 71.9 % dye in 10 hours at pH 7.4. Rhodamine B-loaded LA-SLN exhibited higher cellular uptake compared to free RhB dye. The R-LA-SLN was found to be localized in the cytoplasm of the cells. Lauric acid solid lipid nanoparticle induces tight junction opening and also increases the paracellular transport of the dye. Lauric acid solid lipid nanoparticles were found to be cytocompatible even at higher concentrations and also showed a substantially higher mucoadhesive property. It has the potential to be used as a drug carrier for oral drug delivery. The major protein bound to the LA-SLN upon incubation with pancreatin was ribonuclease. However, the drug-loading capacity of the LA-SLN was found to be poor.

In the case of the third system, chitosan polymers were functionalized with lysine and maleic anhydride and prepared chitosan particles with different zeta potentials. The zeta potential of the chitosan, LCS, and MCS microparticles were found to be +13.3 ± 0.17, +23.7 ± 0.58, and -9.54 ± 0.79 mV, respectively. Chitosan, LCS, and MCS microparticles were found to be cytocompatible even at higher concentrations. On drug-loading, these microparticles exhibited significant cytotoxicity toward colon cancer cells in a dose-dependent and time-dependent manner revealing their potential for colorectal cancer treatment.

The interactions of microparticles with the simulated intestinal microenvironment (different pH conditions of the gastrointestinal (GI) tract, mucin, mucoadhesion, and intestinal tight junction opening) were carried out. The chitosan, LCS, and MCS microparticles exhibited higher percentages of water uptake and drug release at pH 1.2. To prevent the loss of the drug in the acidic conditions of the stomach the microparticles were coated with Eudragit®S-100. The coating also helped in controlling the release profile of 5-fluorouracil (5-FU) at pH 6.8 and 7.4, with little initial burst release.

To evaluate the interactions of microparticles with proteins in the GI tract, particles were incubated with pancreatin (composed of amylase, lipase, trypsin, protease, and ribonuclease), and hard corona formed on the surface of the particles were separated by SDS-PAGE. The major protein bound to the microparticles was ribonuclease.

Mucin is the primary functional component of the mucus layer. The tenacious and sticky network of mucin fibers prevents the diffusion of foreign particles by trapping and these entrapped particles are eliminated through constant secretion and shedding of mucus. Chitosan, LCS, and MCS microparticles were found to exhibit less interaction with mucin which is advantageous for oral drug delivery systems. So, the microparticles can efficiently overcome the mucus barrier and reach the intestinal epithelium.

The modified LCS and MCS particles showed significantly higher mucoadhesion compared to native chitosan microparticles. The mucoadhesion of the microparticles was found to be higher in the small intestine region compared to the colon region.

The hydrophilicity of 5-FU limits its oral therapeutic efficacy due to poor intestinal permeability and GI tract absorption. Tight junctions act as a barrier that prevents the permeability of hydrophilic drugs. The tight junction opening is associated with the surface charge of the drug delivery carriers incorporated with 5-FU. Based on the observations the cationic LCS and chitosan microparticles exhibited better tight junction opening and 5-FU drug transport across the Caco-2 cell monolayer compared to anionic MCS particles. Among the chitosan systems, lysine chitosan microparticles were found to be the most suitable carrier for colon drug delivery.

The future perspective of this work includes:

1. To study the effect of protein corona on nanoparticle cellular uptake and drug release.
2. *In vivo* studies to assess the suitability of the drug-loaded chitosan and modified chitosan particles in colon-targeted drug delivery.

6 REFERENCES

1. Abd-Elnaby, H.M., Abo-Elala, G.M., Abdel-Raouf, U.M., Hamed, M.M., 2016. Antibacterial and anticancer activity of extracellular synthesized silver nanoparticles from marine Streptomyces rochei MHM13. Egypt. J. Aquat. Res. 42, 301–312. https://doi.org/10.1016/j.ejar.2016.05.004
2. Adib, Z.M., Ghanbarzadeh, S., Kouhsoltani, M., Khosroshahi, A.Y., Hamishehkar, H., 2016. The effect of particle size on the deposition of solid lipid nanoparticles in different skin layers: a histological study. Adv. Pharm. Bull. 6, 31.
3. Aggarwal, B.B., Harikumar, K.B., 2009. Potential therapeutic effects of curcumin, the anti-inflammatory agent, against neurodegenerative, cardiovascular, pulmonary, metabolic, autoimmune and neoplastic diseases. Int. J. Biochem. Cell Biol. 41, 40–59.
4. Aggarwal, B.B., Sundaram, C., Malani, N., Ichikawa, H., 2007. Curcumin: the Indian solid gold. Mol. Targets Ther. Uses Curcumin Health Dis. 1–75.
5. Ahadian, S., Finbloom, J.A., Mofidfar, M., Diltemiz, S.E., Nasrollahi, F., Davoodi, E., Hosseini, V., Mylonaki, I., Sangabathuni, S., Montazerian, H., Fetah, K., Nasiri, R., Dokmeci, M.R., Stevens, M.M., Desai, T.A., Khademhosseini, A., 2020. Micro and nanoscale technologies in oral drug delivery. Adv. Drug Deliv. Rev. 157, 37–62. https://doi.org/10.1016/j.addr.2020.07.012
6. Ahmad, N., Albassam, A.A., Faiyaz Khan, M., Ullah, Z., Mohammed Buheazah, T., Salman AlHomoud, H., Ali Al-Nasif, H., 2022. A novel 5-Fluorocuracil multiple-nanoemulsion used for the enhancement of oral bioavailability in the treatment of colorectal cancer. Saudi J. Biol. Sci. 29, 3704–3716. https://doi.org/10.1016/j.sjbs.2022.02.017
7. Ahmed, M.M., Fatima, F., Anwer, M.K., Aldawsari, M.F., Alsaidan, Y.S.M., Alfaiz, S.A., Haque, A., Az, A., Alhazzani, K., 2020. Development and characterization of Brigatinib loaded solid lipid nanoparticles: In-vitro cytotoxicity against human carcinoma A549 lung cell lines. Chem. Phys. Lipids 233, 105003. https://doi.org/10.1016/j.chemphyslip.2020.105003

8. Albayati, T.M., Abd Alkadir, A.J., 2019. Synthesis and characterization of mesoporous materials as a carrier and release of prednisolone in drug delivery system. J. Drug Deliv. Sci. Technol. 53, 101176.
9. Alqahtani, M.S., Kazi, M., Alsenaidy, M.A., Ahmad, M.Z., 2021. Advances in Oral Drug Delivery. Front. Pharmacol. 12, 618411. https://doi.org/10.3389/fphar.2021.618411
10. Al-Remawi, M., 2015. Application of N-hexoyl chitosan derivatives with high degree of substitution in the preparation of super-disintegrating pharmaceutical matrices. J. Drug Deliv. Sci. Technol. 29, 31–41. https://doi.org/10.1016/j.jddst.2015.06.001
11. Amara, S., Bourlieu, C., Humbert, L., Rainteau, D., Carrière, F., 2019. Variations in gastrointestinal lipases, pH and bile acid levels with food intake, age and diseases: Possible impact on oral lipid-based drug delivery systems. Adv. Drug Deliv. Rev. 142, 3–15. https://doi.org/10.1016/j.addr.2019.03.005
12. Anand, P., Thomas, S.G., Kunnumakkara, A.B., Sundaram, C., Harikumar, K.B., Sung, B., Tharakan, S.T., Misra, K., Priyadarsini, I.K., Rajasekharan, K.N., Aggarwal, B.B., 2008. Biological activities of curcumin and its analogues (Congeners) made by man and Mother Nature. Biochem. Pharmacol., Special Issue: Apoptosis World 2008 76, 1590–1611. https://doi.org/10.1016/j.bcp.2008.08.008
13. Anderson, A.M., Mitchell, M.S., Mohan, R.S., 2000. Isolation of Curcumin from Turmeric. J. Chem. Educ. 77, 359. https://doi.org/10.1021/ed077p359
14. Anderson, J.M., Van Itallie, C.M., 2009. Physiology and Function of the Tight Junction. Cold Spring Harb. Perspect. Biol. 1, a002584. https://doi.org/10.1101/cshperspect.a002584
15. Angelini, G., Pasc, A., Gasbarri, C., 2020. Curcumin in silver nanoparticles aqueous solution: Kinetics of keto-enol tautomerism and effects on AgNPs. Colloids Surf. Physicochem. Eng. Asp. 603, 125235. https://doi.org/10.1016/j.colsurfa.2020.125235
16. Arruebo, M., Sebastian, V., 2020. Chapter 11 - Batch and microfluidic reactors in the synthesis of enteric drug carriers, in: Martins, J.P., Santos, H.A. (Eds.),

Nanotechnology for Oral Drug Delivery. Academic Press, pp. 317–357. https://doi.org/10.1016/B978-0-12-818038-9.00008-9

17. Attama, A.A., Momoh, M.A., Builders, P.F., 2012. Lipid nanoparticulate drug delivery systems: a revolution in dosage form design and development. Recent Adv. Nov. Drug Carr. Syst. 5, 107–140.
18. Atuma, C., Strugala, V., Allen, A., Holm, L., 2001. The adherent gastrointestinal mucus gel layer: thickness and physical state in vivo. Am. J. Physiol. Gastrointest. Liver Physiol. 280, G922-929. https://doi.org/10.1152/ajpgi.2001.280.5.G922
19. Auffan, M., Rose, J., Bottero, J.-Y., Lowry, G.V., Jolivet, J.-P., Wiesner, M.R., 2009. Towards a definition of inorganic nanoparticles from an environmental, health and safety perspective. Nat. Nanotechnol. 4, 634–641. https://doi.org/10.1038/nnano.2009.242
20. Augustine, R., Ashkenazi, D.L., Arzi, R.S., Zlobin, V., Shofti, R., Sosnik, A., 2018. Nanoparticle-in-microparticle oral drug delivery system of a clinically relevant darunavir/ritonavir antiretroviral combination. Acta Biomater. 74, 344–359. https://doi.org/10.1016/j.actbio.2018.04.045
21. Auría-Soro, C., Nesma, T., Juanes-Velasco, P., Landeira-Viñuela, A., Fidalgo-Gomez, H., Acebes-Fernandez, V., Gongora, R., Almendral Parra, M.J., Manzano-Roman, R., Fuentes, M., 2019. Interactions of Nanoparticles and Biosystems: Microenvironment of Nanoparticles and Biomolecules in Nanomedicine. Nanomaterials 9, 1365. https://doi.org/10.3390/nano9101365
22. Bacaita, E.S., Ciobanu, B.C., Popa, M., Agop, M., Desbrieres, J., 2012. Phases in temporal multiscale evolution of drug release mechanism from IPN-type chitosan based hydrogels. Phys. Chem. Chem. Phys. 12.
23. Banerjee, S., Chakravarty, A.R., 2015. Metal complexes of curcumin for cellular imaging, targeting, and photoinduced anticancer activity. Acc. Chem. Res. 48, 2075–2083.
24. Barbosa, D.M., Ribeiro, L.N., Casadei, B.R., Da Silva, C.M., Queiróz, V.A., Duran, N., De Araújo, D.R., Severino, P., De Paula, E., 2018. Solid lipid nanoparticles for dibucaine sustained release. Pharmaceutics 10, 231.

25. Bhubhanil, S., Talodthaisong, C., Khongkow, M., Namdee, K., Wongchitrat, P., Yingmema, W., Hutchison, J.A., Lapmanee, S., Kulchat, S., 2021. Enhanced wound healing properties of guar gum/curcumin-stabilized silver nanoparticle hydrogels. Sci. Rep. 11, 21836. https://doi.org/10.1038/s41598-021-01262-x
26. Bhumkar, D.R., Pokharkar, V.B., 2006. Studies on effect of pH on cross-linking of chitosan with sodium tripolyphosphate: A technical note. AAPS PharmSciTech 7, E138–E143. https://doi.org/10.1208/pt070250
27. Boddupalli, B.M., Mohammed, Z.N.K., Nath, R.A., Banji, D., 2010. Mucoadhesive drug delivery system: An overview. J. Adv. Pharm. Technol. Res. 1, 381–387. https://doi.org/10.4103/0110-5558.76436
28. Boegh, M., Nielsen, H.M., 2015. Mucus as a Barrier to Drug Delivery – Understanding and Mimicking the Barrier Properties. Basic Clin. Pharmacol. Toxicol. 116, 179–186. https://doi.org/10.1111/bcpt.12342
29. Boushra, M., Tous, S., Fetih, G., Korzekwa, K., Lebo, D.B., Xue, H.Y., Wong, H.L., 2016. Development and evaluation of viscosity-enhanced nanocarrier (VEN) for oral insulin delivery. Int. J. Pharm. 511, 462–472. https://doi.org/10.1016/j.ijpharm.2016.07.016
30. Bravo-Osuna, I., Vauthier, C., Farabollini, A., Palmieri, G.F., Ponchel, G., 2007. Mucoadhesion mechanism of chitosan and thiolated chitosan-poly(isobutyl cyanoacrylate) core-shell nanoparticles. Biomaterials 28, 2233–2243. https://doi.org/10.1016/j.biomaterials.2007.01.005
31. Brown, T.D., Whitehead, K.A., Mitragotri, S., 2019. Materials for oral delivery of proteins and peptides. Nat. Rev. Mater. 5, 127–148. https://doi.org/10.1038/s41578-019-0156-6
32. Buzza, M.S., Netzel-Arnett, S., Shea-Donohue, T., Zhao, A., Lin, C.-Y., List, K., Szabo, R., Fasano, A., Bugge, T.H., Antalis, T.M., 2010. Membrane-anchored serine protease matriptase regulates epithelial barrier formation and permeability in the intestine. Proc. Natl. Acad. Sci. U. S. A. 107, 4200–4205. https://doi.org/10.1073/pnas.0903923107
33. Çağdaş, M., Sezer, A.D., Bucak, S., 2014. Liposomes as potential drug carrier systems for drug delivery. Appl. Nanotechnol. Drug Deliv. 1, 1–50.

34. Cañamares, M.V., Garcia-Ramos, J.V., Sanchez-Cortes, S., 2006. Degradation of curcumin dye in aqueous solution and on Ag nanoparticles studied by ultraviolet–visible absorption and surface-enhanced raman spectroscopy. Appl. Spectrosc. 60, 1386–1391.
35. Cao, X., Han, Y., Li, F., Li, Z., McClements, D.J., He, L., Decker, E.A., Xing, B., Xiao, H., 2019. Impact of protein-nanoparticle interactions on gastrointestinal fate of ingested nanoparticles: Not just simple protein corona effects. NanoImpact 13, 37–43. https://doi.org/10.1016/j.impact.2018.12.002
36. Carmona, E.R., Benito, N., Plaza, T., Recio-Sánchez, G., 2017. Green synthesis of silver nanoparticles by using leaf extracts from the endemic Buddleja globosa hope. Green Chem. Lett. Rev. 10, 250–256.
37. Carvalho, P.M., Felício, M.R., Santos, N.C., Gonçalves, S., Domingues, M.M., 2018. Application of Light Scattering Techniques to Nanoparticle Characterization and Development. Front. Chem. 6.
38. Cereijido, M., Shoshani, L., Contreras, R.G., 2000. Molecular Physiology and Pathophysiology of Tight Junctions I. Biogenesis of tight junctions and epithelial polarity. Am. J. Physiol.-Gastrointest. Liver Physiol. 279, G477–G482. https://doi.org/10.1152/ajpgi.2000.279.3.G477
39. Chang, Y.-N., Liang, Y., Xia, S., Bai, X., Zhang, J., Kong, J., Chen, K., Li, J., Xing, G., 2020. The High Permeability of Nanocarriers Crossing the Enterocyte Layer by Regulation of the Surface Zonal Pattern. Mol. Basel Switz. 25, 919. https://doi.org/10.3390/molecules25040919
40. Chayed, S., Winnik, F.M., 2007. In vitro evaluation of the mucoadhesive properties of polysaccharide-based nanoparticulate oral drug delivery systems. Eur. J. Pharm. Biopharm. Off. J. Arbeitsgemeinschaft Pharm. Verfahrenstechnik EV 65, 363–370. https://doi.org/10.1016/j.ejpb.2006.08.017
41. Chen, X., Zou, L.-Q., Niu, J., Liu, W., Peng, S.-F., Liu, C.-M., 2015. The stability, sustained release and cellular antioxidant activity of curcumin nanoliposomes. Molecules 20, 14293–14311.

42. Cho, E.J., Holback, H., Liu, K.C., Abouelmagd, S.A., Park, J., Yeo, Y., 2013. Nanoparticle Characterization: State of the Art, Challenges, and Emerging Technologies. Mol. Pharm. 10, 2093–2110. https://doi.org/10.1021/mp300697h
43. Clogston, J.D., Patri, A.K., 2011. Zeta potential measurement. Methods Mol. Biol. Clifton NJ 697, 63–70. https://doi.org/10.1007/978-1-60327-198-1_6
44. Collado-González, M., González Espinosa, Y., Goycoolea, F.M., 2019. Interaction Between Chitosan and Mucin: Fundamentals and Applications. Biomimetics 4, 32. https://doi.org/10.3390/biomimetics4020032
45. Collins, F.L., Rios-Arce, N.D., Atkinson, S., Bierhalter, H., Schoenherr, D., Bazil, J.N., McCabe, L.R., Parameswaran, N., 2017. Temporal and regional intestinal changes in permeability, tight junction, and cytokine gene expression following ovariectomy-induced estrogen deficiency. Physiol. Rep. 5, e13263. https://doi.org/10.14814/phy2.13263
46. Cone, R.A., 2009. Barrier properties of mucus. Adv. Drug Deliv. Rev. 61, 75–85. https://doi.org/10.1016/j.addr.2008.09.008
47. Coogan, M.P., Fernández-Moreira, V., 2014. Progress with, and prospects for, metal complexes in cell imaging. Chem Commun 50, 384–399. https://doi.org/10.1039/C3CC45229H
48. Corazzari, I., Nisticò, R., Turci, F., Faga, M.G., Franzoso, F., Tabasso, S., Magnacca, G., 2015. Advanced physico-chemical characterization of chitosan by means of TGA coupled on-line with FTIR and GCMS: Thermal degradation and water adsorption capacity. Polym. Degrad. Stab. 112, 1–9. https://doi.org/10.1016/j.polymdegradstab.2014.12.006
49. Crescenzi, V., Francescangeli, A., Taglienti, A., Capitani, D., Mannina, L., 2003. Synthesis and Partial Characterization of Hydrogels Obtained via Glutaraldehyde Crosslinking of Acetylated Chitosan and of Hyaluronan Derivatives. Biomacromolecules 4, 1045–1054. https://doi.org/10.1021/bm0340669
50. Cui, X., Bao, L., Wang, X., Chen, C., 2020. The nano–intestine interaction: understanding the location-oriented effects of engineered nanomaterials in the intestine. Small 16, 1907665.

51. Dayrit, F.M., 2015. The properties of lauric acid and their significance in coconut oil. J. Am. Oil Chem. Soc. 92, 1–15.
52. De Gelder, J., De Gussem, K., Vandenabeele, P., Moens, L., 2007. Reference database of Raman spectra of biological molecules. J. Raman Spectrosc. Int. J. Orig. Work Asp. Raman Spectrosc. High. Order Process. Also Brillouin Rayleigh Scatt. 38, 1133–1147.
53. de Pinho Neves, A.L., Milioli, C.C., Müller, L., Riella, H.G., Kuhnen, N.C., Stulzer, H.K., 2014. Factorial design as tool in chitosan nanoparticles development by ionic gelation technique. Colloids Surf. Physicochem. Eng. Asp. 445, 34–39. https://doi.org/10.1016/j.colsurfa.2013.12.058
54. De, R., Kundu, P., Swarnakar, S., Ramamurthy, T., Chowdhury, A., Nair, G.B., Mukhopadhyay, A.K., 2009. Antimicrobial activity of curcumin against Indian Helicobacter pylori and also during mice infection. Antimicrob. Agents Chemother.
55. Dehousse, V., Garbacki, N., Jaspart, S., Castagne, D., Piel, G., Colige, A., Evrard, B., 2010. Comparison of chitosan/siRNA and trimethylchitosan/siRNA complexes behaviour in vitro. Int. J. Biol. Macromol. 46, 342–349. https://doi.org/10.1016/j.ijbiomac.2010.01.010
56. Denker, B.M., Nigam, S.K., 1998. Molecular structure and assembly of the tight junction. Am. J. Physiol. 274, F1-9. https://doi.org/10.1152/ajprenal.1998.274.1.F1
57. Derjaguin, B.V., Toporov, Y.P., Muller, V.M., Aleinikova, I.N., 1977. On the relationship between the electrostatic and the molecular component of the adhesion of elastic particles to a solid surface. J. Colloid Interface Sci. 58, 528–533.
58. Dhanisha, S.S., Guruvayoorappan, C., Drishya, S., Abeesh, P., 2018. Mucins: Structural diversity, biosynthesis, its role in pathogenesis and as possible therapeutic targets. Crit. Rev. Oncol. Hematol. 122, 98–122. https://doi.org/10.1016/j.critrevonc.2017.12.006
59. Dhillon, N., Aggarwal, B.B., Newman, R.A., Wolff, R.A., Kunnumakkara, A.B., Abbruzzese, J.L., Ng, C.S., Badmaev, V., Kurzrock, R., 2008. Phase II trial of

curcumin in patients with advanced pancreatic cancer. Clin. Cancer Res. 14, 4491–4499.

60. Din, F. ud, Aman, W., Ullah, I., Qureshi, O.S., Mustapha, O., Shafique, S., Zeb, A., 2017. Effective use of nanocarriers as drug delivery systems for the treatment of selected tumors. Int. J. Nanomedicine 12, 7291–7309. https://doi.org/10.2147/IJN.S146315
61. Don, T.-M., Chen, H.-R., 2004. Modification of Chitosan with Maleic Anhydride and Synthesis of Chitosan-g-Poly (N-isopropylacrylamide), in: Asian Pacific Confederation of Chemical Engineering Congress Program and Abstracts Asian Pacific Confederation of Chemical Engineers Congress Program and Abstracts. The Society of Chemical Engineers, Japan, pp. 661–661.
62. Dos Santos, A.M., Carvalho, S.G., Meneguin, A.B., Sábio, R.M., Gremião, M.P.D., Chorilli, M., 2021. Oral delivery of micro/nanoparticulate systems based on natural polysaccharides for intestinal diseases therapy: Challenges, advances and future perspectives. J. Controlled Release 334, 353–366.
63. Dulbecco, P., Savarino, V., 2013. Therapeutic potential of curcumin in digestive diseases. World J. Gastroenterol. WJG 19, 9256–9270. https://doi.org/10.3748/wjg.v19.i48.9256
64. Duong, V.-A., Maeng, H.-J., Chi, S.-C., 2019. Data on optimization and drug release kinetics of nanostructured lipid carriers containing ondansetron hydrochloride prepared by cold high-pressure homogenization method. Data Brief 26, 104475.
65. E A K, N., S, B., Martin, C.A., J, R.R., A, S., V, N., B S, L., Frank-Kamenetskaya, O.V., Radhakrishnan, S., S, N.K., 2020. A competent bidrug loaded water soluble chitosan derivative for the effective inhibition of breast cancer. Sci. Rep. 10, 3991. https://doi.org/10.1038/s41598-020-60888-5
66. EFSA Panel on Food Additives and Flavourings (FAF), Younes, M., Aquilina, G., Castle, L., Engel, K.-H., Fowler, P., Frutos Fernandez, M.J., Fürst, P., Gundert-Remy, U., Gürtler, R., Husøy, T., Manco, M., Mennes, W., Moldeus, P., Passamonti, S., Shah, R., Waalkens-Berendsen, I., Wölfle, D., Corsini, E., Cubadda, F., De Groot, D., FitzGerald, R., Gunnare, S., Gutleb, A.C., Mast, J.,

Mortensen, A., Oomen, A., Piersma, A., Plichta, V., Ulbrich, B., Van Loveren, H., Benford, D., Bignami, M., Bolognesi, C., Crebelli, R., Dusinska, M., Marcon, F., Nielsen, E., Schlatter, J., Vleminckx, C., Barmaz, S., Carfí, M., Civitella, C., Giarola, A., Rincon, A.M., Serafimova, R., Smeraldi, C., Tarazona, J., Tard, A., Wright, M., 2021. Safety assessment of titanium dioxide (E171) as a food additive. EFSA J. 19, e06585. https://doi.org/10.2903/j.efsa.2021.6585

67. El Khoury, E., Abiad, M., Kassaify, Z.G., Patra, D., 2015. Green synthesis of curcumin conjugated nanosilver for the applications in nucleic acid sensing and anti-bacterial activity. Colloids Surf. B Biointerfaces 127, 274–280. https://doi.org/10.1016/j.colsurfb.2015.01.050
68. Elieh-Ali-Komi, D., Hamblin, M.R., 2016. Chitin and Chitosan: Production and Application of Versatile Biomedical Nanomaterials. Int. J. Adv. Res. 4, 411–427.
69. El-Kattan, A., Varma, M., El-Kattan, A., Varma, M., 2012. Oral Absorption, Intestinal Metabolism and Human Oral Bioavailability, Topics on Drug Metabolism. IntechOpen. https://doi.org/10.5772/31087
70. El-Maghawry, E., Tadros, M.I., Elkheshen, S.A., Abd-Elbary, A., 2020. Eudragit®-S100 Coated PLGA Nanoparticles for Colon Targeting of Etoricoxib: Optimization and Pharmacokinetic Assessments in Healthy Human Volunteers. Int. J. Nanomedicine 15, 3965. https://doi.org/10.2147/IJN.S244124
71. Ensign, L.M., Cone, R., Hanes, J., 2012. Oral drug delivery with polymeric nanoparticles: the gastrointestinal mucus barriers. Adv. Drug Deliv. Rev. 64, 557–570. https://doi.org/10.1016/j.addr.2011.12.009
72. Esatbeyoglu, T., Huebbe, P., Ernst, I.M., Chin, D., Wagner, A.E., Rimbach, G., 2012. Curcumin—from molecule to biological function. Angew. Chem. Int. Ed. 51, 5308–5332.
73. Eyres, L., Eyres, M.F., Chisholm, A., Brown, R.C., 2016. Coconut oil consumption and cardiovascular risk factors in humans. Nutr. Rev. 74, 267–280. https://doi.org/10.1093/nutrit/nuw002
74. Fan, J., Chen, J., Yang, L., Lin, H., Cao, F., 2009. Preparation of dual-sensitive graft copolymer hydrogel based on N-maleoyl-chitosan and poly(N-

isopropylacrylamide) by electron beam radiation. Bull. Mater. Sci. 32, 521–526. https://doi.org/10.1007/s12034-009-0077-x

75. Fan, Y., Yi, J., Zhang, Y., Yokoyama, W., 2017. Improved chemical stability and antiproliferative activities of curcumin-loaded nanoparticles with a chitosan chlorogenic acid conjugate. J. Agric. Food Chem. 65, 10812–10819.
76. Farhadi, A., Banan, A., Fields, J., Keshavarzian, A., 2003. Intestinal barrier: an interface between health and disease. J. Gastroenterol. Hepatol. 18, 479–497. https://doi.org/10.1046/j.1440-1746.2003.03032.x
77. Farooq, U., Khan, S., Nawaz, S., Ranjha, N.M., Haider, M.S., Khan, M.M., Dar, E., Nawaz, A., 2017. Enhanced gastric retention and drug release via development of novel floating microspheres based on Eudragit E100 and polycaprolactone: synthesis and in vitro evaluation. Des. Monomers Polym. 20, 419–433. https://doi.org/10.1080/15685551.2017.1326702
78. Farquhar, M.G., Palade, G.E., 1963. Junctional complexes in various epithelia. J. Cell Biol. 17, 375–412. https://doi.org/10.1083/jcb.17.2.375
79. Ferrari, E., Benassi, R., Sacchi, S., Pignedoli, F., Asti, M., Saladini, M., 2014. Curcumin derivatives as metal-chelating agents with potential multifunctional activity for pharmaceutical applications. J. Inorg. Biochem. 139, 38–48.
80. Flora, G., Gupta, D., Tiwari, A., 2013. Nanocurcumin: a promising therapeutic advancement over native curcumin. Crit. Rev. Ther. Drug Carr. Syst. 30.
81. Foroozandeh, P., Aziz, A.A., 2018. Insight into cellular uptake and intracellular trafficking of nanoparticles. Nanoscale Res. Lett. 13, 1–12.
82. Galvão, J.G., Santos, R.L., Lira, A.A.M., Kaminski, R., Sarmento, V.H., Severino, P., Dolabella, S.S., Scher, R., Souto, E.B., Nunes, R.S., 2020. Stearic acid, beeswax and carnauba wax as green raw materials for the loading of carvacrol into nanostructured lipid carriers. Appl. Sci. 10, 6267.
83. Gao, Xiaoyi, Liu, N., Wang, Z., Gao, J., Zhang, H., Li, M., Du, Y., Gao, Xiang, Zheng, A., 2021. Development and Optimization of Chitosan Nanoparticle-Based Intranasal Vaccine Carrier. Mol. Basel Switz. 27, 204. https://doi.org/10.3390/molecules27010204

84. Garai, A., Pant, I., Banerjee, S., Banik, B., Kondaiah, P., Chakravarty, A.R., 2016. Photorelease and Cellular Delivery of Mitocurcumin from Its Cytotoxic Cobalt(III) Complex in Visible Light. Inorg. Chem. 55, 6027–6035. https://doi.org/10.1021/acs.inorgchem.6b00554
85. Garti, N., 2008. Delivery and controlled release of bioactives in foods and nutraceuticals. Elsevier.
86. Ghauri, Z.H., Islam, A., Qadir, M.A., Gull, N., Haider, B., Khan, R.U., Riaz, T., 2021. Development and evaluation of pH-sensitive biodegradable ternary blended hydrogel films (chitosan/guar gum/PVP) for drug delivery application. Sci. Rep. 11, 21255. https://doi.org/10.1038/s41598-021-00452-x
87. Gierszewska, M., Ostrowska-Czubenko, J., Chrzanowska, E., 2018. pH-responsive chitosan/alginate polyelectrolyte complex membranes reinforced by tripolyphosphate. Eur. Polym. J. 101, 282–290. https://doi.org/10.1016/j.eurpolymj.2018.02.031
88. Gómez-Guillén, M.C., Montero, M.P., 2021. Enhancement of oral bioavailability of natural compounds and probiotics by mucoadhesive tailored biopolymer-based nanoparticles: A review. Food Hydrocoll. 118, 106772. https://doi.org/10.1016/j.foodhyd.2021.106772
89. Gordon, O.N., Luis, P.B., Sintim, H.O., Schneider, C., 2015. Unraveling curcumin degradation: autoxidation proceeds through spiroepoxide and vinylether intermediates en route to the main bicyclopentadione. J. Biol. Chem. 290, 4817–4828.
90. Griesser, M., Pistis, V., Suzuki, T., Tejera, N., Pratt, D.A., Schneider, C., 2011. Autoxidative and cyclooxygenase-2 catalyzed transformation of the dietary chemopreventive agent curcumin. J. Biol. Chem. 286, 1114–1124. https://doi.org/10.1074/jbc.M110.178806
91. Gupta, A., Briffa, S.M., Swingler, S., Gibson, H., Kannappan, V., Adamus, G., Kowalczuk, M., Martin, C., Radecka, I., 2020. Synthesis of Silver Nanoparticles Using Curcumin-Cyclodextrins Loaded into Bacterial Cellulose-Based Hydrogels for Wound Dressing Applications. Biomacromolecules 21, 1802–1811. https://doi.org/10.1021/acs.biomac.9b01724

92. Hägerström, H., Edsman, K., Strømme, M., 2003. Low-frequency dielectric spectroscopy as a tool for studying the compatibility between pharmaceutical gels and mucous tissue. J. Pharm. Sci. 92, 1869–1881. https://doi.org/10.1002/jps.10451
93. Haijun Yu, †, Xuesi Chen, †, Tiancheng Lu, †, Jing Sun, †, Huayu Tian, †, Jun Hu, †, Yu Wang, †, Peibiao Zhang, † and, Xiabin Jing*, †, 2007. Poly(l-lysine)-Graft-Chitosan Copolymers: Synthesis, Characterization, and Gene Transfection Effect [WWW Document]. ACS Publ. https://doi.org/10.1021/bm060910u
94. Halwani, A.A., 2022. Development of Pharmaceutical Nanomedicines: From the Bench to the Market. Pharmaceutics 14, 106. https://doi.org/10.3390/pharmaceutics14010106
95. Hamilton, J.A., 1998. Fatty acid transport: difficult or easy? J. Lipid Res. 39, 467–481.
96. Han, Y., Gao, Z., Chen, L., Kang, L., Huang, W., Jin, M., Wang, Q., Bae, Y.H., 2019. Multifunctional oral delivery systems for enhanced bioavailability of therapeutic peptides/proteins. Acta Pharm. Sin. B 9, 902–922. https://doi.org/10.1016/j.apsb.2019.01.004
97. Hao, L., 2007. Preparation and Characterization of a Novel Magnetic Nano-Gene Vector. Acta Phys.-Chim. Sin. 23, 1857–1863. https://doi.org/10.1016/S1872-1508(07)60090-4
98. Heger, M., van Golen, R.F., Broekgaarden, M., Michel, M.C., 2014. The molecular basis for the pharmacokinetics and pharmacodynamics of curcumin and its metabolites in relation to cancer. Pharmacol. Rev. 66, 222–307. https://doi.org/10.1124/pr.110.004044
99. Homayun, B., Lin, X., Choi, H.-J., 2019. Challenges and Recent Progress in Oral Drug Delivery Systems for Biopharmaceuticals. Pharmaceutics 11, 129. https://doi.org/10.3390/pharmaceutics11030129
100. Honary, S., Zahir, F., 2013. Effect of zeta potential on the properties of nano-drug delivery systems-a review (Part 1). Trop. J. Pharm. Res. 12, 255–264.

101.Hosseinnejad, M., Jafari, S.M., 2016. Evaluation of different factors affecting antimicrobial properties of chitosan. Int. J. Biol. Macromol. 85, 467–475. https://doi.org/10.1016/j.ijbiomac.2016.01.022

102.Hou, X., Zhang, W., He, M., Lu, Y., Lou, K., Gao, F., 2017. Preparation and characterization of β-cyclodextrin grafted N-maleoyl chitosan nanoparticles for drug delivery. Asian J. Pharm. Sci. 12, 558–568. https://doi.org/10.1016/j.ajps.2017.07.007

103.Hsu, L.-W., Lee, P.-L., Chen, C.-T., Mi, F.-L., Juang, J.-H., Hwang, S.-M., Ho, Y.-C., Sung, H.-W., 2012. Elucidating the signaling mechanism of an epithelial tight-junction opening induced by chitosan. Biomaterials 33, 6254–6263. https://doi.org/10.1016/j.biomaterials.2012.05.013

104.Huang, G.-Q., Zhang, Z.-K., Cheng, L.-Y., Xiao, J.-X., 2019. Intestine-targeted delivery potency of O-carboxymethyl chitosan-coated layer-by-layer microcapsules: An in vitro and in vivo evaluation. Mater. Sci. Eng. C Mater. Biol. Appl. 105, 110129. https://doi.org/10.1016/j.msec.2019.110129

105.Immordino, M.L., Dosio, F., Cattel, L., 2006. Stealth liposomes: review of the basic science, rationale, and clinical applications, existing and potential. Int. J. Nanomedicine 1, 297–315.

106.Ingersoll, K.S., Cohen, J., 2008. The impact of medication regimen factors on adherence to chronic treatment: a review of literature. J. Behav. Med. 31, 213–224. https://doi.org/10.1007/s10865-007-9147-y

107.Iqbal, J., Shahnaz, G., Perera, G., Hintzen, F., Sarti, F., Bernkop-Schnürch, A., 2012. Thiolated chitosan: development and in vivo evaluation of an oral delivery system for leuprolide. Eur. J. Pharm. Biopharm. Off. J. Arbeitsgemeinschaft Pharm. Verfahrenstechnik EV 80, 95–102. https://doi.org/10.1016/j.ejpb.2011.09.010

108.Ismail, N.I., Othman, I., Abas, F., H. Lajis, N., Naidu, R., 2019. Mechanism of Apoptosis Induced by Curcumin in Colorectal Cancer. Int. J. Mol. Sci. 20, 2454. https://doi.org/10.3390/ijms20102454

109.Iyer, M.A., Eddington, D.T., 2019. Storing and releasing rhodamine as a model hydrophobic compound in polydimethylsiloxane microfluidic devices. Lab. Chip 19, 574–579.

110.Jaiswal, S., Mishra, P., 2018. Antimicrobial and antibiofilm activity of curcumin-silver nanoparticles with improved stability and selective toxicity to bacteria over mammalian cells. Med. Microbiol. Immunol. (Berl.) 207, 39–53.

111.Jaiswal, V.D., Dongre, P.M., 2020. Biophysical interactions between silver nanoparticle-albumin interface and curcumin. J. Pharm. Anal.

112.Johansson, M.E.V., Sjövall, H., Hansson, G.C., 2013. The gastrointestinal mucus system in health and disease. Nat. Rev. Gastroenterol. Hepatol. 10, 352–361. https://doi.org/10.1038/nrgastro.2013.35

113.Jonassen, H., Kjøniksen, A.-L., Hiorth, M., 2012. Effects of ionic strength on the size and compactness of chitosan nanoparticles. Colloid Polym. Sci. 290, 919–929. https://doi.org/10.1007/s00396-012-2604-3

114.Kahai, P., Mandiga, P., Wehrle, C.J., Lobo, S., 2022. Anatomy, Abdomen and Pelvis, Large Intestine, StatPearls [Internet]. StatPearls Publishing.

115.Karimi, M., Avci, P., Ahi, M., Gazori, T., Hamblin, M.R., Naderi-Manesh, H., 2013. Evaluation of Chitosan-Tripolyphosphate Nanoparticles as a p-shRNA Delivery Vector: Formulation, Optimization and Cellular Uptake Study. J. Nanopharmaceutics Drug Deliv. 1, 266–278. https://doi.org/10.1166/jnd.2013.1027

116.Karolewicz, B., Gajda, M., Górniak, A., Owczarek, A., Mucha, I., 2017. Pluronic F127 as a suitable carrier for preparing the imatinib base solid dispersions and its potential in development of a modified release dosage forms. J. Therm. Anal. Calorim. 130, 383–390. https://doi.org/10.1007/s10973-017-6139-1

117.Kavianinia, I., Plieger, P.G., Kandile, N.G., Harding, D.R.K., 2015. Preparation and characterization of an amphoteric chitosan derivative employing trimellitic anhydride chloride and its potential for colon targeted drug delivery system. Mater. Today Commun. Complete, 78–86. https://doi.org/10.1016/j.mtcomm.2015.03.002

118.Kawashima, Y., Yamamoto, H., Takeuchi, H., Kuno, Y., 2000. Mucoadhesive DL-lactide/glycolide copolymer nanospheres coated with chitosan to improve oral delivery of elcatonin. Pharm. Dev. Technol. 5, 77–85. https://doi.org/10.1081/pdt-100100522

119.Khalil, N.M., do Nascimento, T.C.F., Casa, D.M., Dalmolin, L.F., de Mattos, A.C., Hoss, I., Romano, M.A., Mainardes, R.M., 2013. Pharmacokinetics of curcumin-loaded PLGA and PLGA-PEG blend nanoparticles after oral administration in rats. Colloids Surf. B Biointerfaces 101, 353–360. https://doi.org/10.1016/j.colsurfb.2012.06.024

120.Khan, H.U., Aamir, K., Jusuf, P.R., Sethi, G., Sisinthy, S.P., Ghildyal, R., Arya, A., 2021. Lauric acid ameliorates lipopolysaccharide (LPS)-induced liver inflammation by mediating TLR4/MyD88 pathway in Sprague Dawley (SD) rats. Life Sci. 265, 118750. https://doi.org/10.1016/j.lfs.2020.118750

121.Khan, M.J., Shameli, K., Sazili, A.Q., Selamat, J., Kumari, S., 2019. Rapid green synthesis and characterization of silver nanoparticles arbitrated by curcumin in an alkaline medium. Molecules 24, 719.

122.Khandelwal, P., Alam, A., Choksi, A., Chattopadhyay, S., Poddar, P., 2018. Retention of Anticancer Activity of Curcumin after Conjugation with Fluorescent Gold Quantum Clusters: An in Vitro and in Vivo Xenograft Study. ACS Omega 3, 4776–4785. https://doi.org/10.1021/acsomega.8b00113

123.Khorasani, M.Y., Langari, H., Sany, S.B.T., Rezayi, M., Sahebkar, A., 2019. The role of curcumin and its derivatives in sensory applications. Mater. Sci. Eng. C Mater. Biol. Appl. 103, 109792. https://doi.org/10.1016/j.msec.2019.109792

124.Khurana, A., Allawadhi, P., Khurana, I., Allwadhi, S., Weiskirchen, R., Banothu, A.K., Chhabra, D., Joshi, K., Bharani, K.K., 2021. Role of nanotechnology behind the success of mRNA vaccines for COVID-19. Nano Today 38, 101142.

125.Khutoryanskiy, V.V., 2011. Advances in Mucoadhesion and Mucoadhesive Polymers: Advances in Mucoadhesion and Mucoadhesive Polymers. Macromol. Biosci. 11, 748–764. https://doi.org/10.1002/mabi.201000388

126.Kinloch, A.J., 1980. The science of adhesion. J. Mater. Sci. 15, 2141–2166. https://doi.org/10.1007/BF00552302

127.Konduru, N.V., Molina, R.M., Swami, A., Damiani, F., Pyrgiotakis, G., Lin, P., Andreozzi, P., Donaghey, T.C., Demokritou, P., Krol, S., 2017. Protein corona: implications for nanoparticle interactions with pulmonary cells. Part. Fibre Toxicol. 14, 1–12.

128.Kopac, T., 2021. Protein corona, understanding the nanoparticle-protein interactions and future perspectives: A critical review. Int. J. Biol. Macromol. 169, 290–301. https://doi.org/10.1016/j.ijbiomac.2020.12.108

129.Korsmeyer, R.W., Gurny, R., Doelker, E., Buri, P., Peppas, N.A., 1983. Mechanisms of solute release from porous hydrophilic polymers. Int. J. Pharm. 15, 25–35. https://doi.org/10.1016/0378-5173(83)90064-9

130.Kumar, V.V., Chandrasekar, D., Ramakrishna, S., Kishan, V., Rao, Y.M., Diwan, P.V., 2007. Development and evaluation of nitrendipine loaded solid lipid nanoparticles: influence of wax and glyceride lipids on plasma pharmacokinetics. Int. J. Pharm. 335, 167–175. https://doi.org/10.1016/j.ijpharm.2006.11.004

131.Kundu, S., Nithiyanantham, U., 2013. In situ formation of curcumin stabilized shape-selective Ag nanostructures in aqueous solution and their pronounced SERS activity. RSC Adv. 3, 25278–25290.

132.Kurien, B.T., Matsumoto, H., Scofield, R.H., 2017. Nutraceutical Value of Pure Curcumin. Pharmacogn. Mag. 13, S161–S163. https://doi.org/10.4103/0973-1296.203988

133.Kushwaha, A.K., Vuddanda, P.R., Karunanidhi, P., Singh, S.K., Singh, S., 2013. Development and Evaluation of Solid Lipid Nanoparticles of Raloxifene Hydrochloride for Enhanced Bioavailability. BioMed Res. Int. 2013, 584549. https://doi.org/10.1155/2013/584549

134.Lacerda, S.H.D.P., Park, J.J., Meuse, C., Pristinski, D., Becker, M.L., Karim, A., Douglas, J.F., 2010. Interaction of gold nanoparticles with common human blood proteins. ACS Nano 4, 365–379.

135.Lai, S.K., Wang, Y.-Y., Hanes, J., 2009. Mucus-penetrating nanoparticles for drug and gene delivery to mucosal tissues. Adv. Drug Deliv. Rev. 61, 158–171. https://doi.org/10.1016/j.addr.2008.11.002

136.Lamson, N.G., Berger, A., Fein, K.C., Whitehead, K.A., 2019. Anionic nanoparticles enable the oral delivery of proteins by enhancing intestinal permeability. Nat. Biomed. Eng. 4, 84–96. https://doi.org/10.1038/s41551-019-0465-5

137.Lavertu, M., Xia, Z., Serreqi, A.N., Berrada, M., Rodrigues, A., Wang, D., Buschmann, M.D., Gupta, A., 2003. A validated 1H NMR method for the determination of the degree of deacetylation of chitosan. J. Pharm. Biomed. Anal. 32, 1149–1158.

138.Lea, T., 2015. Caco-2 cell line. Impact Food Bioact. Health Vitro Ex Vivo Models 103–111.

139.Leal, J., Smyth, H.D.C., Ghosh, D., 2017. Physicochemical properties of mucus and their impact on transmucosal drug delivery. Int. J. Pharm. 532, 555–572. https://doi.org/10.1016/j.ijpharm.2017.09.018

140.Lee, W.-H., Loo, C.-Y., Bebawy, M., Luk, F., Mason, R.S., Rohanizadeh, R., 2013. Curcumin and its Derivatives: Their Application in Neuropharmacology and Neuroscience in the 21st Century. Curr. Neuropharmacol. 11, 338–378. https://doi.org/10.2174/1570159X11311040002

141.Lee, Y.K., Lee, W.S., Hwang, J.T., Kwon, D.Y., Surh, Y.J., Park, O.J., 2009. Curcumin exerts antidifferentiation effect through AMPKα-PPAR-γ in 3T3-L1 adipocytes and antiproliferatory effect through AMPKα-COX-2 in cancer cells. J. Agric. Food Chem. 57, 305–310.

142.Lehr, C.-M., Poelma, F.G.J., Junginger, H.E., Tukker, J.J., 1991. An estimate of turnover time of intestinal mucus gel layer in the rat in situ loop. Int. J. Pharm. 70, 235–240. https://doi.org/10.1016/0378-5173(91)90287-X

143.Lengyel, M., Kállai-Szabó, N., Antal, V., Laki, A.J., Antal, I., 2019. Microparticles, Microspheres, and Microcapsules for Advanced Drug Delivery. Sci. Pharm. 87, 20. https://doi.org/10.3390/scipharm87030020

144.Li, Jianghua, Cai, C., Li, Jiarui, Li, Jun, Li, Jia, Sun, T., Wang, L., Wu, H., Yu, G., 2018. Chitosan-Based Nanomaterials for Drug Delivery. Mol. J. Synth. Chem. Nat. Prod. Chem. 23, 2661. https://doi.org/10.3390/molecules23102661

145.Li, L., Mathias, N.R., Heran, C.L., Moench, P., Wall, D.A., Smith, R.L., 2006. Carbopol-mediated paracellular transport enhancement in Calu-3 cell layers. J. Pharm. Sci. 95, 326–335. https://doi.org/10.1002/jps.20541

146.Liang, X., Gao, M., Xie, H., Xu, Q., Wu, Y., Hu, J., Lu, A., Zhang, L., 2019. Controllable Wrinkling Patterns on Chitosan Microspheres Generated from Self-Assembling Metal Nanoparticles. ACS Appl. Mater. Interfaces 11, 22824–22833. https://doi.org/10.1021/acsami.9b02127

147.Lieleg, O., Vladescu, I., Ribbeck, K., 2010. Characterization of Particle Translocation through Mucin Hydrogels. Biophys. J. 98, 1782–1789. https://doi.org/10.1016/j.bpj.2010.01.012

148.Lin, C.-H., Chen, C.-H., Lin, Z.-C., Fang, J.-Y., 2017. Recent advances in oral delivery of drugs and bioactive natural products using solid lipid nanoparticles as the carriers. J. Food Drug Anal. 25, 219–234.

149.Lin, S., Lin, X., Lou, X.-T., Yang, F., Lin, D.-Y., Lu, Z.-W., 2015. Rapid and sensitive SERS method for determination of Rhodamine B in chili powder with paper-based substrates. Anal. Methods 7, 5289–5294.

150.Lin, Y.-H., Mi, F.-L., Chen, C.-T., Chang, W.-C., Peng, S.-F., Liang, H.-F., Sung, H.-W., 2007. Preparation and Characterization of Nanoparticles Shelled with Chitosan for Oral Insulin Delivery. Biomacromolecules 8, 146–152. https://doi.org/10.1021/bm0607776

151.Lindmark, T., Kimura, Y., Artursson, P., 1998. Absorption enhancement through intracellular regulation of tight junction permeability by medium chain fatty acids in Caco-2 cells. J. Pharmacol. Exp. Ther. 284, 362–369.

152.Liu, C., Jiang, X., Gan, Y., Yu, M., 2021. Engineering nanoparticles to overcome the mucus barrier for drug delivery: Design, evaluation and state-of-the-art. Med. Drug Discov. 12, 100110. https://doi.org/10.1016/j.medidd.2021.100110

153.Liu, D., Liu, C., Zou, W., Zhang, N., 2010. Enhanced gastrointestinal absorption of N 3-O-toluyl-fluorouracil by cationic solid lipid nanoparticles. J. Nanoparticle Res. 12, 975–984.

154.Liu, D., Wei, Y., Yao, P., Jiang, L., 2006. Determination of the degree of acetylation of chitosan by UV spectrophotometry using dual standards. Carbohydr. Res. 341, 782–785. https://doi.org/10.1016/j.carres.2006.01.008

155.Liu, M., Zhang, J., Shan, W., Huang, Y., 2015. Developments of mucus penetrating nanoparticles. Asian J. Pharm. Sci. 10, 275–282. https://doi.org/10.1016/j.ajps.2014.12.007

156.Loo, C.-Y., Rohanizadeh, R., Young, P.M., Traini, D., Cavaliere, R., Whitchurch, C.B., Lee, W.-H., 2016. Combination of silver nanoparticles and curcumin nanoparticles for enhanced anti-biofilm activities. J. Agric. Food Chem. 64, 2513–2522.

157.Luo, C.-F., Yuan, M., Chen, M.-S., Liu, S.-M., Zhu, L., Huang, B.-Y., Liu, X.-W., Xiong, W., 2011. Pharmacokinetics, tissue distribution and relative bioavailability of puerarin solid lipid nanoparticles following oral administration. Int. J. Pharm. 410, 138–144. https://doi.org/10.1016/j.ijpharm.2011.02.064

158.Luo, Y., Teng, Z., Li, Y., Wang, Q., 2015. Solid lipid nanoparticles for oral drug delivery: Chitosan coating improves stability, controlled delivery, mucoadhesion and cellular uptake. Carbohydr. Polym. 122, 221–229. https://doi.org/10.1016/j.carbpol.2014.12.084

159.Lustriane, C., Dwivany, F., Suendo, V., Reza, M., 2018. Effect of chitosan and chitosan-nanoparticles on post harvest quality of banana fruits. J. Plant Biotechnol. 45, 36–44. https://doi.org/10.5010/JPB.2018.45.1.036

160.Lyu, Y., Yu, M., Liu, Q., Zhang, Q., Liu, Z., Tian, Y., Li, D., Changdao, M., 2020. Synthesis of silver nanoparticles using oxidized amylose and combination with curcumin for enhanced antibacterial activity. Carbohydr. Polym. 230, 115573. https://doi.org/10.1016/j.carbpol.2019.115573

161.M. Ways, T.M., Lau, W.M., Khutoryanskiy, V.V., 2018. Chitosan and Its Derivatives for Application in Mucoadhesive Drug Delivery Systems. Polymers 10, 267. https://doi.org/10.3390/polym10030267

162.Madara, J.L., 1987. Intestinal absorptive cell tight junctions are linked to cytoskeleton. Am. J. Physiol.-Cell Physiol. 253, C171–C175. https://doi.org/10.1152/ajpcell.1987.253.1.C171

163.Madara, J.L., Barenberg, D., Carlson, S., 1986. Effects of cytochalasin D on occluding junctions of intestinal absorptive cells: further evidence that the cytoskeleton may influence paracellular permeability and junctional charge selectivity. J. Cell Biol. 102, 2125–2136. https://doi.org/10.1083/jcb.102.6.2125

164.Madara, J.L., Moore, R., Carlson, S., 1987. Alteration of intestinal tight junction structure and permeability by cytoskeletal contraction. Am. J. Physiol.-Cell Physiol. 253, C854–C861. https://doi.org/10.1152/ajpcell.1987.253.6.C854

165.Makadia, H.K., Siegel, S.J., 2011. Poly lactic-co-glycolic acid (PLGA) as biodegradable controlled drug delivery carrier. Polymers 3, 1377–1397.

166.Makeen, H.A., Mohan, S., Al-Kasim, M.A., Attafi, I.M., Ahmed, R.A., Syed, N.K., Sultan, M.H., Al-Bratty, M., Alhazmi, H.A., Safhi, M.M., Ali, R., Intakhab Alam, M., 2020. Gefitinib loaded nanostructured lipid carriers: characterization, evaluation and anti-human colon cancer activity in vitro. Drug Deliv. 27, 622–631. https://doi.org/10.1080/10717544.2020.1754526

167.Mandracchia, D., Tripodo, G., 2020. Micro and Nano-drug Delivery Systems. https://doi.org/10.1039/9781839162664-00001

168.Manju, S., Sreenivasan, K., 2011. Conjugation of curcumin onto hyaluronic acid enhances its aqueous solubility and stability. J. Colloid Interface Sci. 359, 318–325.

169.Martirosyan, A., Schneider, Y.-J., 2014. Engineered nanomaterials in food: implications for food safety and consumer health. Int. J. Environ. Res. Public. Health 11, 5720–5750.

170.Masaoka, Y., Tanaka, Y., Kataoka, M., Sakuma, S., Yamashita, S., 2006. Site of drug absorption after oral administration: assessment of membrane permeability and luminal concentration of drugs in each segment of gastrointestinal tract. Eur. J. Pharm. Sci. 29, 240–250.

171.Medeiros Borsagli, F.G.L., Carvalho, I.C., Mansur, H.S., 2018. Amino acid-grafted and N-acylated chitosan thiomers: Construction of 3D bio-scaffolds for

potential cartilage repair applications. Int. J. Biol. Macromol. 114, 270–282. https://doi.org/10.1016/j.ijbiomac.2018.03.133

172.Medina-Reyes, E.I., Rodríguez-Ibarra, C., Déciga-Alcaraz, A., Díaz-Urbina, D., Chirino, Y.I., Pedraza-Chaverri, J., 2020. Food additives containing nanoparticles induce gastrotoxicity, hepatotoxicity and alterations in animal behavior: The unknown role of oxidative stress. Food Chem. Toxicol. 146, 111814. https://doi.org/10.1016/j.fct.2020.111814

173.Mehnert, W., Mäder, K., 2001. Solid lipid nanoparticles: Production, characterization and applications. Adv. Drug Deliv. Rev., Lipid Assemblies for Drug Delivery 47, 165–196. https://doi.org/10.1016/S0169-409X(01)00105-3

174.Meo, S.A., Bukhari, I.A., Akram, J., Meo, A.S., Klonoff, D.C., 2021. COVID-19 vaccines: comparison of biological, pharmacological characteristics and adverse effects of Pfizer/BioNTech and Moderna Vaccines. Eur. Rev. Med. Pharmacol. Sci. 25, 1663–1669. https://doi.org/10.26355/eurrev_202102_24877

175.Meza, I., Sabanero, M., Stefani, E., Cereijido, M., 1982. Occluding Junctions in MDCK Cells: Modulation of Transepithelial Permeability by the Cytoskeleton. J. Cell. Biochem. 18, 407–421. https://doi.org/10.1002/jcb.1982.240180403

176.Midekessa, G., Godakumara, K., Ord, J., Viil, J., Lättekivi, F., Dissanayake, K., Kopanchuk, S., Rinken, A., Andronowska, A., Bhattacharjee, S., Rinken, T., Fazeli, A., 2020. Zeta Potential of Extracellular Vesicles: Toward Understanding the Attributes that Determine Colloidal Stability. ACS Omega 5, 16701–16710. https://doi.org/10.1021/acsomega.0c01582

177.Mittal, A., Singh, A., Zhang, B., Visessanguan, W., Benjakul, S., 2022. Chitooligosaccharide Conjugates Prepared Using Several Phenolic Compounds via Ascorbic Acid/H2O2 Free Radical Grafting: Characteristics, Antioxidant, Antidiabetic, and Antimicrobial Activities. Foods 11, 920. https://doi.org/10.3390/foods11070920

178.Mohan, P.K., Sreelakshmi, G., Muraleedharan, C.V., Joseph, R., 2012. Water soluble complexes of curcumin with cyclodextrins: Characterization by FT-Raman spectroscopy. Vib. Spectrosc. 62, 77–84.

179.Mooradian, A., 1969. Photoluminescence of metals. Phys. Rev. Lett. 22, 185.

180.Moreno, J.A.S., Mendes, A.C., Stephansen, K., Engwer, C., Goycoolea, F.M., Boisen, A., Nielsen, L.H., Chronakis, I.S., 2018. Development of electrosprayed mucoadhesive chitosan microparticles. Carbohydr. Polym. 190, 240–247. https://doi.org/10.1016/j.carbpol.2018.02.062

181.Moussout, H., Ahlafi, H., Aazza, M., Bourakhouadar, M., 2016. Kinetics and mechanism of the thermal degradation of biopolymers chitin and chitosan using thermogravimetric analysis. Polym. Degrad. Stab. 130, 1–9. https://doi.org/10.1016/j.polymdegradstab.2016.05.016

182.Mu, H., Høy, C.-E., 2000. Effects of different medium-chain fatty acids on intestinal absorption of structured triacylglycerols. Lipids 35, 83–89. https://doi.org/10.1007/s11745-000-0498-x

183.Mubeen, B., Ansar, A.N., Rasool, R., Ullah, I., Imam, S.S., Alshehri, S., Ghoneim, M.M., Alzarea, S.I., Nadeem, M.S., Kazmi, I., 2021. Nanotechnology as a Novel Approach in Combating Microbes Providing an Alternative to Antibiotics. Antibiot. Basel Switz. 10, 1473. https://doi.org/10.3390/antibiotics10121473

184.Mudie, D.M., Amidon, G.L., Amidon, G.E., 2010. Physiological Parameters for Oral Delivery and in Vitro Testing [WWW Document]. ACS Publ. https://doi.org/10.1021/mp100149j

185.Mura, P., Maestrelli, F., D'Ambrosio, M., Luceri, C., Cirri, M., 2021. Evaluation and Comparison of Solid Lipid Nanoparticles (SLNs) and Nanostructured Lipid Carriers (NLCs) as Vectors to Develop Hydrochlorothiazide Effective and Safe Pediatric Oral Liquid Formulations. Pharmaceutics 13, 437. https://doi.org/10.3390/pharmaceutics13040437

186.Naseri, N., Valizadeh, H., Zakeri-Milani, P., 2015. Solid Lipid Nanoparticles and Nanostructured Lipid Carriers: Structure, Preparation and Application. Adv. Pharm. Bull. 5, 305–313. https://doi.org/10.15171/apb.2015.043

187.Nasrollahi, F., Sana, B., Paramelle, D., Ahadian, S., Khademhosseini, A., Lim, S., 2020. Incorporation of Graphene Quantum Dots, Iron, and Doxorubicin in/on Ferritin Nanocages for Bimodal Imaging and Drug Delivery. Adv. Ther. 3, 1900183. https://doi.org/10.1002/adtp.201900183

188.Nasrollahi, F., Varshosaz, J., Khodadadi, A.A., Lim, S., Jahanian-Najafabadi, A., 2016. Targeted Delivery of Docetaxel by Use of Transferrin/Poly(allylamine hydrochloride)-functionalized Graphene Oxide Nanocarrier. ACS Appl. Mater. Interfaces 8, 13282–13293. https://doi.org/10.1021/acsami.6b02790

189.Nelson, K.M., Dahlin, J.L., Bisson, J., Graham, J., Pauli, G.F., Walters, M.A., 2017. The Essential Medicinal Chemistry of Curcumin. J. Med. Chem. 60, 1620–1637. https://doi.org/10.1021/acs.jmedchem.6b00975

190.Nimiya, Y., Wang, W., Du, Z., Sukamtoh, E., Zhu, J., Decker, E., Zhang, G., 2016. Redox modulation of curcumin stability: Redox active antioxidants increase chemical stability of curcumin. Mol. Nutr. Food Res. 60, 487–494.

191.Noble, G.T., Stefanick, J.F., Ashley, J.D., Kiziltepe, T., Bilgicer, B., 2014. Ligand-targeted liposome design: challenges and fundamental considerations. Trends Biotechnol. 32, 32–45. https://doi.org/10.1016/j.tibtech.2013.09.007

192.Nolting, D., Aziz, E.F., Ottosson, N., Faubel, M., Hertel, I.V., Winter, B., 2007. pH-Induced Protonation of Lysine in Aqueous Solution Causes Chemical Shifts in X-ray Photoelectron Spectroscopy. J. Am. Chem. Soc. 129, 14068–14073. https://doi.org/10.1021/ja072971l

193.Novais, P., Silva, P.M.A., Amorim, I., Bousbaa, H., 2021. Second-Generation Antimitotics in Cancer Clinical Trials. Pharmaceutics 13, 1011. https://doi.org/10.3390/pharmaceutics13071011

194.Oh, J.-W., Chun, S.C., Chandrasekaran, M., 2019. Preparation and In Vitro Characterization of Chitosan Nanoparticles and Their Broad-Spectrum Antifungal Action Compared to Antibacterial Activities against Phytopathogens of Tomato. Agronomy 9, 21. https://doi.org/10.3390/agronomy9010021

195.Onugwu, A.L., Attama, A.A., Nnamani, P.O., Onugwu, S.O., Onuigbo, E.B., Khutoryanskiy, V.V., 2022. Development and optimization of solid lipid nanoparticles coated with chitosan and poly(2-ethyl-2-oxazoline) for ocular drug delivery of ciprofloxacin. J. Drug Deliv. Sci. Technol. 74, 103527. https://doi.org/10.1016/j.jddst.2022.103527

196.Orteca, G., Pisaneschi, F., Rubagotti, S., Liu, T.W., Biagiotti, G., Piwnica-Worms, D., Iori, M., Capponi, P.C., Ferrari, E., Asti, M., 2019. Development of a

Potential Gallium-68-Labelled Radiotracer Based on DOTA-Curcumin for Colon-Rectal Carcinoma: From Synthesis to In Vivo Studies. Mol. Basel Switz. 24, 644. https://doi.org/10.3390/molecules24030644

197. Othman, N., Masarudin, M.J., Kuen, C.Y., Dasuan, N.A., Abdullah, L.C., Md. Jamil, S.N.A., 2018. Synthesis and Optimization of Chitosan Nanoparticles Loaded with l-Ascorbic Acid and Thymoquinone. Nanomaterials 8, 920. https://doi.org/10.3390/nano8110920

198. Pardeike, J., Hommoss, A., Müller, R.H., 2009. Lipid nanoparticles (SLN, NLC) in cosmetic and pharmaceutical dermal products. Int. J. Pharm. 366, 170–184.

199. Pardi, N., Hogan, M.J., Porter, F.W., Weissman, D., 2018. mRNA vaccines — a new era in vaccinology. Nat. Rev. Drug Discov. 17, 261–279. https://doi.org/10.1038/nrd.2017.243

200. Parize, A.L., Stulzer, H.K., Laranjeira, M.C.M., Brighente, I.M. da C., Souza, T.C.R. de, 2012. Evaluation of chitosan microparticles containing curcumin and crosslinked with sodium tripolyphosphate produced by spray drying. Quím. Nova 35, 1127–1132. https://doi.org/10.1590/S0100-40422012000600011

201. Park, C.G., Huh, B.K., Kim, S.-N., Lee, S.H., Hong, H.R., Choy, Y.B., 2017. Nanostructured mucoadhesive microparticles to enhance oral drug bioavailability. J. Ind. Eng. Chem. 54, 262–269. https://doi.org/10.1016/j.jiec.2017.06.001

202. Park, Hyeong-Ho, Zhang, X., Choi, Y.-J., Park, Hyung-Ho, Hill, R.H., 2011. Synthesis of Ag nanostructures by photochemical reduction using citrate-capped Pt seeds. J. Nanomater. 2011.

203. Parvez, S., Yadagiri, G., Gedda, M.R., Singh, A., Singh, O.P., Verma, A., Sundar, S., Mudavath, S.L., 2020. Modified solid lipid nanoparticles encapsulated with Amphotericin B and Paromomycin: an effective oral combination against experimental murine visceral leishmaniasis. Sci. Rep. 10, 12243. https://doi.org/10.1038/s41598-020-69276-5

204. Pasaribu, S.P., Kaban, J., Ginting, M., Sinaga, K.R., 2018. Synthesis and evaluation antibacterial activity of phosphate buffer solution (pH 7.4)-Soluble

acylated chitosan derivative, in: AIP Conference Proceedings. AIP Publishing LLC, p. 020025.

205. Pate, K., Safier, P., 2016. 12 - Chemical metrology methods for CMP quality, in: Babu, S. (Ed.), Advances in Chemical Mechanical Planarization (CMP). Woodhead Publishing, pp. 299–325. https://doi.org/10.1016/B978-0-08-100165-3.00012-7

206. Patel, P., Raval, M., Sheth, N., 2020. Silibinin Loaded Solid Lipid Nanoparticles: Effect of Different Lipids and Surfactants on Physicochemical Properties of Nanoparticle. Int. J. Pharm. Investig. 10, 332–338. https://doi.org/10.5530/ijpi.2020.3.59

207. Patil, S., Sandberg, A., Heckert, E., Self, W., Seal, S., 2007. Protein adsorption and cellular uptake of cerium oxide nanoparticles as a function of zeta potential. Biomaterials 28, 4600–4607. https://doi.org/10.1016/j.biomaterials.2007.07.029

208. Patra, Ch.N., Priya, R., Swain, S., Kumar Jena, G., Panigrahi, K.C., Ghose, D., 2017. Pharmaceutical significance of Eudragit: A review. Future J. Pharm. Sci. 3, 33–45. https://doi.org/10.1016/j.fjps.2017.02.001

209. Peppas, N.A., Buri, P.A., 1985. Surface, interfacial and molecular aspects of polymer bioadhesion on soft tissues. J. Controlled Release 2, 257–275.

210. Peres, Luana Becker, Peres, Laize Becker, de Araújo, P.H.H., Sayer, C., 2016. Solid lipid nanoparticles for encapsulation of hydrophilic drugs by an organic solvent free double emulsion technique. Colloids Surf. B Biointerfaces 140, 317–323.

211. Permanadewi, I., Kumoro, A.C., Wardhani, D.H., Aryanti, N., 2019. Modelling of controlled drug release in gastrointestinal tract simulation. J. Phys. Conf. Ser. 1295, 012063. https://doi.org/10.1088/1742-6596/1295/1/012063

212. Petrochenko, P.E., Pavurala, N., Wu, Y., Yee Wong, S., Parhiz, H., Chen, K., Patil, S.M., Qu, H., Buoniconti, P., Muhammad, A., Choi, S., Kozak, D., Ashraf, M., Cruz, C.N., Zheng, J., Xu, X., 2018. Analytical considerations for measuring the globule size distribution of cyclosporine ophthalmic emulsions. Int. J. Pharm. 550, 229–239. https://doi.org/10.1016/j.ijpharm.2018.08.030

213.Pinto, J.F., 2010. Site-specific drug delivery systems within the gastro-intestinal tract: from the mouth to the colon. Int. J. Pharm. 395, 44–52.

214.Ponchel, G., Touchard, F., Wouessidjewe, D., Duchêne, D., Peppas, N.A., 1987. Bioadhesive analysis of controlled-release systems. III. Bioadhesive and release behavior of metronidazole-containing poly(acrylic acid)-hydroxypropyl methylcellulose systems. Int. J. Pharm. 38, 65–70. https://doi.org/10.1016/0378-5173(87)90098-6

215.Prabhu, S., Ortega, M., Ma, C., 2005. Novel lipid-based formulations enhancing the in vitro dissolution and permeability characteristics of a poorly water-soluble model drug, piroxicam. Int. J. Pharm. 301, 209–216.

216.Prasad, S., Aggarwal, B.B., 2011. Turmeric, the golden spice, in: Herbal Medicine: Biomolecular and Clinical Aspects. 2nd Edition. CRC Press/Taylor & Francis.

217.Prasad, S., DuBourdieu, D., Srivastava, A., Kumar, P., Lall, R., 2021. Metal–Curcumin Complexes in Therapeutics: An Approach to Enhance Pharmacological Effects of Curcumin. Int. J. Mol. Sci. 22, 7094. https://doi.org/10.3390/ijms22137094

218.Prasad, S., Lall, R., 2022. Zinc-curcumin based complexes in health and diseases: An approach in chemopreventive and therapeutic improvement. J. Trace Elem. Med. Biol. 73, 127023. https://doi.org/10.1016/j.jtemb.2022.127023

219.Prasad, V., De Jesús, K., Mailankody, S., 2017. The high price of anticancer drugs: origins, implications, barriers, solutions. Nat. Rev. Clin. Oncol. 14, 381–390. https://doi.org/10.1038/nrclinonc.2017.31

220.Prasadani, W.C., Senanayake, C.M., Jayathilaka, N., Ekanayake, S., Seneviratne, K.N., 2017. Effect of three edible oils on the intestinal absorption of caffeic acid: An in vivo and in vitro study. PLoS ONE 12. https://doi.org/10.1371/journal.pone.0179292

221.Priyadarsini, K.I., 2014. The chemistry of curcumin: from extraction to therapeutic agent. Molecules 19, 20091–20112.

222.Pucci, D., Crispini, A., Mendiguchía, B.S., Pirillo, S., Ghedini, M., Morelli, S., De Bartolo, L., 2013. Improving the bioactivity of Zn (II)-curcumin based complexes. Dalton Trans. 42, 9679–9687.

223.Queiroz, M.F., Teodosio Melo, K.R., Sabry, D.A., Sassaki, G.L., Rocha, H.A.O., 2014. Does the Use of Chitosan Contribute to Oxalate Kidney Stone Formation? Mar. Drugs 13, 141–158. https://doi.org/10.3390/md13010141

224.Quintela-Fandino, M., González-Martín, A., Colomer, R., 2010. Targeting cytoskeleton reorganisation as antimetastatic treatment. Clin. Transl. Oncol. 12, 662–669. https://doi.org/10.1007/s12094-010-0575-8

225.Raja, M.M., Lim, P.Q., Wong, Y.S., Xiong, G.M., Zhang, Y., Venkatraman, S., Huang, Y., 2019. Polymeric nanomaterials: methods of preparation and characterization, in: Nanocarriers for Drug Delivery. Elsevier, pp. 557–653.

226.Ranaldi, G., Marigliano, I., Vespignani, I., Perozzi, G., Sambuy, Y., 2002. The effect of chitosan and other polycations on tight junction permeability in the human intestinal Caco-2 cell line. J. Nutr. Biochem. 13, 157–167.

227.Ravishankar, K., Shelly, K.M., Desingh, R.P., Subramaniyam, R., Narayanan, A., Dhamodharan, R., 2018. Green, Solid-State Synthesis of Maleated Chitosan and Ionotropic Gelation with Chitosan. ACS Sustain. Chem. Eng. 6, 15191–15200. https://doi.org/10.1021/acssuschemeng.8b03648

228.Rehman, M., Ihsan, A., Madni, A., Bajwa, S.Z., Shi, D., Webster, T.J., Khan, W.S., 2017. Solid lipid nanoparticles for thermoresponsive targeting: evidence from spectrophotometry, electrochemical, and cytotoxicity studies. Int. J. Nanomedicine 12, 8325–8336. https://doi.org/10.2147/IJN.S147506

229.Rehman, M., Madni, A., Ihsan, A., Khan, W.S., Khan, M.I., Mahmood, M.A., Ashfaq, M., Bajwa, S.Z., Shakir, I., 2015. Solid and liquid lipid-based binary solid lipid nanoparticles of diacerein: in vitro evaluation of sustained release, simultaneous loading of gold nanoparticles, and potential thermoresponsive behavior. Int. J. Nanomedicine 10, 2805–2814. https://doi.org/10.2147/IJN.S67147

230.Reinus, J.F., Simon, D., 2014. Gastrointestinal anatomy and physiology: the essentials. John Wiley & Sons.

231.Rekha, M.R., Sharma, C.P., 2011. Glutamine-chitosan microparticles as oral insulin delivery matrix: In vitro characterization. J. Appl. Polym. Sci. 122, 2374–2382. https://doi.org/10.1002/app.34315

232.Rivolta, I., Panariti, A., Lettiero, B., Sesana, S., Gasco, P., Gasco, M.R., Masserini, M., Miserocchi, G., 2011. Cellular uptake of coumarin-6 as a model drug loaded in solid lipid nanoparticles. J. Physiol. Pharmacol. 62, 45.

233.Rubagotti, S., Croci, S., Ferrari, E., Orteca, G., Iori, M., Capponi, P.C., Versari, A., Asti, M., 2017. Uptake of Ga-curcumin derivatives in different cancer cell lines: Toward the development of new potential 68Ga-labelled curcuminoids-based radiotracers for tumour imaging. J. Inorg. Biochem. 173, 113–119. https://doi.org/10.1016/j.jinorgbio.2017.05.002

234.Sadeghi, A.M.M., Dorkoosh, F.A., Avadi, M.R., Weinhold, M., Bayat, A., Delie, F., Gurny, R., Larijani, B., Rafiee-Tehrani, M., Junginger, H.E., 2008. Permeation enhancer effect of chitosan and chitosan derivatives: Comparison of formulations as soluble polymers and nanoparticulate systems on insulin absorption in Caco-2 cells. Eur. J. Pharm. Biopharm. 70, 270–278. https://doi.org/10.1016/j.ejpb.2008.03.004

235.Sandek, A., Anker, S., Haehling, S., 2009. The Gut and Intestinal Bacteria in Chronic Heart Failure. Curr. Drug Metab. 10, 22–28. https://doi.org/10.2174/138920009787048374

236.Sandhya, S., Talukdar, J., Bhaishya, D., 2016. Chemical and biological properties of lauric acid: A review. Int J Adv Res 4, 1123–1128.

237.Sanjula, B., Shah, F.M., Javed, A., Alka, A., 2009. Effect of poloxamer 188 on lymphatic uptake of carvedilol-loaded solid lipid nanoparticles for bioavailability enhancement. J. Drug Target. 17, 249–256. https://doi.org/10.1080/10611860902718672

238.Sant, S., Tao, S.L., Fisher, O.Z., Xu, Q., Peppas, N.A., Khademhosseini, A., 2012. Microfabrication technologies for oral drug delivery. Adv. Drug Deliv. Rev., Advances in Oral Drug Delivery: Improved Biovailability of Poorly Absorbed Drugs by Tissue and Cellular Optimization 64, 496–507. https://doi.org/10.1016/j.addr.2011.11.013

239.Santoso, J., Adiputra, K.C., Soerdirga, L.C., Tarman, K., 2020. Effect of acetic acid hydrolysis on the characteristics of water soluble chitosan, in: IOP Conference Series: Earth and Environmental Science. IOP Publishing, p. 012021.

240.Sapsford, K.E., Tyner, K.M., Dair, B.J., Deschamps, J.R., Medintz, I.L., 2011. Analyzing Nanomaterial Bioconjugates: A Review of Current and Emerging Purification and Characterization Techniques. Anal. Chem. 83, 4453–4488. https://doi.org/10.1021/ac200853a

241.Sareen, R., Jain, N., Dhar, K.L., 2016. Curcumin–Zn (II) complex for enhanced solubility and stability: an approach for improved delivery and pharmacodynamic effects. Pharm. Dev. Technol. 21, 630–635.

242.Sarı, A., Karaipekli, A., Alkan, C., 2009. Preparation, characterization and thermal properties of lauric acid/expanded perlite as novel form-stable composite phase change material. Chem. Eng. J. 155, 899–904. https://doi.org/10.1016/j.cej.2009.09.005

243.Sarkar, T., Butcher, R.J., Banerjee, S., Mukherjee, S., Hussain, A., 2016. Visible light-induced cytotoxicity of a dinuclear iron(III) complex of curcumin with low-micromolar IC50 value in cancer cells. Inorganica Chim. Acta 439, 8–17. https://doi.org/10.1016/j.ica.2015.09.026

244.Sashidhar, R.B., Capoor, A.K., Ramana, D., 1994. Quantitation of ϵ-amino group using amino acids as reference standards by trinitrobenzene sulfonic acid. J. Immunol. Methods 167, 121–127. https://doi.org/10.1016/0022-1759(94)90081-7

245.Schattling, P., Taipaleenmäki, E., Zhang, Y., Städler, B., 2017. A Polymer Chemistry Point of View on Mucoadhesion and Mucopenetration. Macromol. Biosci. 17. https://doi.org/10.1002/mabi.201700060

246.Schipper, N.G., Olsson, S., Hoogstraate, J.A., deBoer, A.G., Vårum, K.M., Artursson, P., 1997. Chitosans as absorption enhancers for poorly absorbable drugs 2: mechanism of absorption enhancement. Pharm. Res. 14, 923–929. https://doi.org/10.1023/a:1012160102740

247.Schneider, C., Gordon, O.N., Edwards, R.L., Luis, P.B., 2015. Degradation of Curcumin: From Mechanism to Biological Implications. J. Agric. Food Chem. 63, 7606–7614. https://doi.org/10.1021/acs.jafc.5b00244

248.Schwarz, C., Mehnert, W., Lucks, J.S., Müller, R.H., 1994. Solid lipid nanoparticles (SLN) for controlled drug delivery. I. Production, characterization and sterilization. J. Controlled Release 30, 83–96.

249.Severino, P., Pinho, S.C., Souto, E.B., Santana, M.H.A., 2011. Polymorphism, crystallinity and hydrophilic–lipophilic balance of stearic acid and stearic acid–capric/caprylic triglyceride matrices for production of stable nanoparticles. Colloids Surf. B Biointerfaces 86, 125–130. https://doi.org/10.1016/j.colsurfb.2011.03.029

250.Shah, N.D., Limketkai, B.N., 2017. The Use of Medium-Chain Triglycerides in Gastrointestinal Disorders. Pract. Gastroenterol. 7.

251.Shah, R.M., Malherbe, F., Eldridge, D., Palombo, E.A., Harding, I.H., 2014. Physicochemical characterization of solid lipid nanoparticles (SLNs) prepared by a novel microemulsion technique. J. Colloid Interface Sci. 428, 286–294. https://doi.org/10.1016/j.jcis.2014.04.057

252.Shaikh, R., Raj Singh, T.R., Garland, M.J., Woolfson, A.D., Donnelly, R.F., 2011. Mucoadhesive drug delivery systems. J. Pharm. Bioallied Sci. 3, 89–100. https://doi.org/10.4103/0975-7406.76478

253.Shameli, K., Ahmad, M.B., Zamanian, A., Sangpour, P., Shabanzadeh, P., Abdollahi, Y., Zargar, M., 2012. Green biosynthesis of silver nanoparticles using Curcuma longa tuber powder. Int. J. Nanomedicine 7, 5603.

254.Sharma, A., 2018. FTIR study of RhodamineB in some solvents. AIP Conf. Proc. 1953, 140035. https://doi.org/10.1063/1.5033210

255.Sharma, R.K., Cwiklinski, K., Aalinkeel, R., Reynolds, J.L., Sykes, D.E., Quaye, E., Oh, J., Mahajan, S.D., Schwartz, S.A., 2017. Immunomodulatory activities of curcumin-stabilized silver nanoparticles: Efficacy as an antiretroviral therapeutic. Immunol. Invest. 46, 833–846. https://doi.org/10.1080/08820139.2017.1371908

256.Shawkey, A.M., Rabeh, M.A., Abdulall, A.K., Abdellatif, A.O., 2013. Green nanotechnology: Anticancer Activity of Silver Nanoparticles using Citrullus colocynthis aqueous extracts 13.

257.Shen, C.-R., Liu, C.-L., Lee, H.-P., Chen, J.-K., 2013. The Identification and Characterization of Chitotriosidase Activity in Pancreatin from Porcine Pancreas. Molecules 18, 2978–2987. https://doi.org/10.3390/molecules18032978

258.Shen, L., Turner, J.R., 2005. Actin Depolymerization Disrupts Tight Junctions via Caveolae-mediated Endocytosis□V. Mol. Biol. Cell 16, 18.

259.Shogren, R., Gerken, T.A., Jentoft, N., 2002. Role of glycosylation on the conformation and chain dimensions of O-linked glycoproteins: light-scattering studies of ovine submaxillary mucin [WWW Document]. ACS Publ. https://doi.org/10.1021/bi00439a029

260.Shu, M., He, F., Li, Z., Zhu, X., Ma, Y., Zhou, Z., Yang, Z., Gao, F., Zeng, M., 2020. Biosynthesis and antibacterial activity of silver nanoparticles using yeast extract as reducing and capping agents. Nanoscale Res. Lett. 15, 14.

261.Silva, A.C., Lopes, C.M., Fonseca, J., Soares, M.E., Santos, D., Souto, E.B., Ferreira, D., 2012. Risperidone release from solid lipid nanoparticles (SLN): validated HPLC method and modelling kinetic profile. Curr. Pharm. Anal. 8, 307–316.

262.Silva, E.L., Carneiro, G., De Araújo, L.A., Trindade, M. de J.V., Yoshida, M.I., Oréfice, R.L., Farias, L. de M., De Carvalho, M.A.R., Dos Santos, S.G., Goulart, G.A.C., Alves, R.J., Ferreira, L.A.M., 2015. Solid Lipid Nanoparticles Loaded with Retinoic Acid and Lauric Acid as an Alternative for Topical Treatment of Acne Vulgaris. J. Nanosci. Nanotechnol. 15, 792–799. https://doi.org/10.1166/jnn.2015.9184

263.Sindhu, K., Rajaram, A., J. Sreeram, K., Rajaram, R., 2014. Curcumin conjugated gold nanoparticle synthesis and its biocompatibility. RSC Adv. 4, 1808–1818. https://doi.org/10.1039/C3RA45345F

264.Singh, D.K., Jagannathan, R., Khandelwal, P., Abraham, P.M., Poddar, P., 2013. In situ synthesis and surface functionalization of gold nanoparticles with

curcumin and their antioxidant properties: an experimental and density functional theory investigation. Nanoscale 5, 1882–1893.

265.Sirviö, J.A., Kantola, A.M., Komulainen, S., Filonenko, S., 2021. Aqueous Modification of Chitosan with Itaconic Acid to Produce Strong Oxygen Barrier Film. Biomacromolecules 22, 2119–2128. https://doi.org/10.1021/acs.biomac.1c00216

266.Sleeman, J.P., 2000. The lymph node as a bridgehead in the metastatic dissemination of tumors. Recent Results Cancer Res. Fortschritte Krebsforsch. Progres Dans Rech. Sur Cancer 157, 55–81. https://doi.org/10.1007/978-3-642-57151-0_6

267.Slifer, Z.M., Blikslager, A.T., 2020. The Integral Role of Tight Junction Proteins in the Repair of Injured Intestinal Epithelium. Int. J. Mol. Sci. 21, 972. https://doi.org/10.3390/ijms21030972

268.Smart, J., 2005. The basics and underlying mechanisms of mucoadhesion. Adv. Drug Deliv. Rev. 57, 1556–1568. https://doi.org/10.1016/j.addr.2005.07.001

269.Smith, J., Wood, E., Dornish, M., 2004. Effect of chitosan on epithelial cell tight junctions. Pharm. Res. 21, 43–49. https://doi.org/10.1023/b:pham.0000012150.60180.e3

270.Smith, J.M., Dornish, M., Wood, E.J., 2005. Involvement of protein kinase C in chitosan glutamate-mediated tight junction disruption. Biomaterials 26, 3269–3276. https://doi.org/10.1016/j.biomaterials.2004.06.020

271.Sonaje, K., Chuang, E.-Y., Lin, K.-J., Yen, T.-C., Su, F.-Y., Tseng, M.T., Sung, H.-W., 2012. Opening of Epithelial Tight Junctions and Enhancement of Paracellular Permeation by Chitosan: Microscopic, Ultrastructural, and Computed-Tomographic Observations. Mol. Pharm. 9, 1271–1279. https://doi.org/10.1021/mp200572t

272.Song, Z., Wu, Y., Wang, H., Han, H., 2019. Synergistic antibacterial effects of curcumin modified silver nanoparticles through ROS-mediated pathways. Mater. Sci. Eng. C 99, 255–263. https://doi.org/10.1016/j.msec.2018.12.053

273.Sonia, T.A., Rekha, M.R., Sharma, C.P., 2011. Bioadhesive hydrophobic chitosan microparticles for oral delivery of insulin: In vitro characterization and

in vivo uptake studies. J. Appl. Polym. Sci. 119, 2902–2910. https://doi.org/10.1002/app.32979

274.Srinivasan, B., Kolli, A.R., Esch, M.B., Abaci, H.E., Shuler, M.L., Hickman, J.J., 2015. TEER measurement techniques for in vitro barrier model systems. J. Lab. Autom. 20, 107–126. https://doi.org/10.1177/2211068214561025

275.Srivatsan, K.V., Duraipandy, N., Begum, S., Lakra, R., Ramamurthy, U., Korrapati, P.S., Kiran, M.S., 2015. Effect of curcumin caged silver nanoparticle on collagen stabilization for biomedical applications. Int. J. Biol. Macromol. 75, 306–315.

276.Stanić, Z., 2017. Curcumin, a Compound from Natural Sources, a True Scientific Challenge – A Review. Plant Foods Hum. Nutr. 72, 1–12. https://doi.org/10.1007/s11130-016-0590-1

277.Su, F.-Y., Lin, K.-J., Sonaje, K., Wey, S.-P., Yen, T.-C., Ho, Y.-C., Panda, N., Chuang, E.-Y., Maiti, B., Sung, H.-W., 2012. Protease inhibition and absorption enhancement by functional nanoparticles for effective oral insulin delivery. Biomaterials 33, 2801–2811. https://doi.org/10.1016/j.biomaterials.2011.12.038

278.Subudhi, M.B., Jain, Ankit, Jain, Ashish, Hurkat, P., Shilpi, S., Gulbake, A., Jain, S.K., 2015. Eudragit S100 Coated Citrus Pectin Nanoparticles for Colon Targeting of 5-Fluorouracil. Mater. Basel Switz. 8, 832–849. https://doi.org/10.3390/ma8030832

279.Suciati, T., Rachmawati, P., Soraya, E., Mahardhika, A.B., Hartarti, R., Anggadiredja, K., 2018. A novel acemannan-chitosan modified lipid nanoparticles as intracellular delivery vehicles of antibiotic. J. Appl. Pharm. Sci. 8, 001–011.

280.Sugano, K., Takata, N., Machida, M., Saitoh, K., Terada, K., 2002. Prediction of passive intestinal absorption using bio-mimetic artificial membrane permeation assay and the paracellular pathway model. Int. J. Pharm. 241, 241–251. https://doi.org/10.1016/s0378-5173(02)00240-5

281.Sugiyama, Y., Kawakishi, S., Osawa, T., 1996. Involvement of the β-diketone moiety in the antioxidative mechanism of tetrahydrocurcumin. Biochem. Pharmacol. 52, 519–525.

282.Sung, Y.K., Kim, S.W., 2020. Recent advances in polymeric drug delivery systems. Biomater. Res. 24, 12. https://doi.org/10.1186/s40824-020-00190-7

283.Suzuki, T., 2013. Regulation of intestinal epithelial permeability by tight junctions. Cell. Mol. Life Sci. CMLS 70, 631–659. https://doi.org/10.1007/s00018-012-1070-x

284.Swider, E., Koshkina, O., Tel, J., Cruz, L.J., de Vries, I.J.M., Srinivas, M., 2018. Customizing poly(lactic-co-glycolic acid) particles for biomedical applications. Acta Biomater. 73, 38–51. https://doi.org/10.1016/j.actbio.2018.04.006

285.Szilágyi, B.Á., Mammadova, A., Gyarmati, B., Szilágyi, A., 2020. Mucoadhesive interactions between synthetic polyaspartamides and porcine gastric mucin on the colloid size scale. Colloids Surf. B Biointerfaces 194, 111219. https://doi.org/10.1016/j.colsurfb.2020.111219

286.Takeuchi, H., Thongborisute, J., Matsui, Y., Sugihara, H., Yamamoto, H., Kawashima, Y., 2005. Novel mucoadhesion tests for polymers and polymer-coated particles to design optimal mucoadhesive drug delivery systems. Adv. Drug Deliv. Rev. 57, 1583–1594. https://doi.org/10.1016/j.addr.2005.07.008

287.Talari, A.C.S., Movasaghi, Z., Rehman, S., Rehman, I. ur, 2015. Raman Spectroscopy of Biological Tissues. Appl. Spectrosc. Rev. 50, 46–111. https://doi.org/10.1080/05704928.2014.923902

288.Tawfik, E., Ahamed, M., Almalik, A., Alfaqeeh, M., Alshamsan, A., 2017. Prolonged exposure of colon cancer cells to 5-fluorouracil nanoparticles improves its anticancer activity. Saudi Pharm. J. 25, 206–213. https://doi.org/10.1016/j.jsps.2016.05.010

289.Tenchov, R., Bird, R., Curtze, A.E., Zhou, Q., 2021. Lipid Nanoparticles─From Liposomes to mRNA Vaccine Delivery, a Landscape of Research Diversity and Advancement. ACS Nano 15, 16982–17015. https://doi.org/10.1021/acsnano.1c04996

290.Thant, A.A., Wu, Y., Lee, J., Mishra, D.K., Garcia, H., Koeffler, H.P., Vadgama, J.V., 2008. Role of Caspases in 5-FU and Selenium Induced Growth Inhibition of Colorectal Cancer Cells. Anticancer Res. 28, 3579–3592.

291.Thirawong, N., Nunthanid, J., Puttipipatkhachorn, S., Sriamornsak, P., 2007. Mucoadhesive properties of various pectins on gastrointestinal mucosa: An in vitro evaluation using texture analyzer. Eur. J. Pharm. Biopharm. 67, 132–140. https://doi.org/10.1016/j.ejpb.2007.01.010

292.Tiwari, G., Tiwari, R., Sriwastawa, B., Bhati, L., Pandey, S., Pandey, P., Bannerjee, S.K., 2012. Drug delivery systems: An updated review. Int. J. Pharm. Investig. 2, 2–11. https://doi.org/10.4103/2230-973X.96920

293.Tønnesen, H.H., Karlsen, J., 1985. Studies on curcumin and curcuminoids. VI. Kinetics of curcumin degradation in aqueous solution. Z. Lebensm. Unters. Forsch. 180, 402–404. https://doi.org/10.1007/BF01027775

294.Tranchant, T., Besson, P., Hoinard, C., Delarue, J., Antoine, J.M., Couet, C., Goré, J., 1997. Mechanisms and kinetics of alpha-linolenic acid uptake in Caco-2 clone TC7. Biochim. Biophys. Acta 1345, 151–161. https://doi.org/10.1016/s0005-2760(96)00171-3

295.Turner, J.R., 2009. Intestinal mucosal barrier function in health and disease. Nat. Rev. Immunol. 9, 799–809. https://doi.org/10.1038/nri2653

296.ul-Islam, S., Butola, B.S., 2018. The Impact and Prospects of Green Chemistry for Textile Technology. Woodhead Publishing.

297.Valentini, A., Conforti, F., Crispini, A., De Martino, A., Condello, R., Stellitano, C., Rotilio, G., Ghedini, M., Federici, G., Bernardini, S., 2009. Synthesis, oxidant properties, and antitumoral effects of a heteroleptic palladium (II) complex of curcumin on human prostate cancer cells. J. Med. Chem. 52, 484–491.

298.van Breemen, R.B., Li, Y., 2005. Caco-2 cell permeability assays to measure drug absorption. Expert Opin. Drug Metab. Toxicol. 1, 175–185. https://doi.org/10.1517/17425255.1.2.175

299.Vanichvattanadecha, C., Supaphol, P., Rujiravanit, R., 2008. Preparation and Physico-Chemical Characteristics of N-Maleoyl Chitosan Films. Macromol. Symp. 264, 121–126. https://doi.org/10.1002/masy.200850419

300.Vinner, G.K., Vladisavljević, G.T., Clokie, M.R.J., Malik, D.J., 2017. Microencapsulation of Clostridium difficile specific bacteriophages using

microfluidic glass capillary devices for colon delivery using pH triggered release. PLOS ONE 12, e0186239. https://doi.org/10.1371/journal.pone.0186239

301. Vitulo, M., Gnodi, E., Meneveri, R., Barisani, D., 2022. Interactions between Nanoparticles and Intestine. Int. J. Mol. Sci. 23, 4339. https://doi.org/10.3390/ijms23084339

302. Wallace, C.J., Medina, S.H., ElSayed, M.E.H., 2014. Effect of rhamnolipids on permeability across Caco-2 cell monolayers. Pharm. Res. 31, 887–894. https://doi.org/10.1007/s11095-013-1210-5

303. Wan, S., Kelly, P.M., Mahon, E., Stöckmann, H., Rudd, P.M., Caruso, F., Dawson, K.A., Yan, Y., Monopoli, M.P., 2015. The "Sweet" Side of the Protein Corona: Effects of Glycosylation on Nanoparticle–Cell Interactions. ACS Nano 9, 2157–2166. https://doi.org/10.1021/nn506060q

304. Wang, J., Kong, M., Zhou, Z., Yan, D., Yu, X., Cheng, X., Feng, C., Liu, Y., Chen, X., 2017. Mechanism of surface charge triggered intestinal epithelial tight junction opening upon chitosan nanoparticles for insulin oral delivery. Carbohydr. Polym. 157, 596–602. https://doi.org/10.1016/j.carbpol.2016.10.021

305. Wang, W., Meng, Q., Li, Q., Liu, J., Zhou, M., Jin, Z., Zhao, K., 2020. Chitosan Derivatives and Their Application in Biomedicine. Int. J. Mol. Sci. 21, 487. https://doi.org/10.3390/ijms21020487

306. Wang, Y.-J., Pan, M.-H., Cheng, A.-L., Lin, L.-I., Ho, Y.-S., Hsieh, C.-Y., Lin, J.-K., 1997. Stability of curcumin in buffer solutions and characterization of its degradation products. J. Pharm. Biomed. Anal. 15, 1867–1876. https://doi.org/10.1016/S0731-7085(96)02024-9

307. Wanninger, S., Lorenz, V., Subhan, A., T. Edelmann, F., 2015. Metal complexes of curcumin – synthetic strategies, structures and medicinal applications. Chem. Soc. Rev. 44, 4986–5002. https://doi.org/10.1039/C5CS00088B

308. Wayne, R., 2019. Chapter 7 - Fluorescence Microscopy, in: Wayne, R. (Ed.), Light and Video Microscopy (Third Edition). Academic Press, pp. 151–170. https://doi.org/10.1016/B978-0-12-816501-0.00007-X

309. Wei, X.-Q., Hao, L.-Y., Shao, X.-R., Zhang, Q., Jia, X.-Q., Zhang, Z.-R., Lin, Y.-F., Peng, Q., 2015. Insight into the Interaction of Graphene Oxide with Serum

Proteins and the Impact of the Degree of Reduction and Concentration. ACS Appl. Mater. Interfaces 7, 13367–13374. https://doi.org/10.1021/acsami.5b01874

310. Wilhelm, C., Billotey, C., Roger, J., Pons, J.N., Bacri, J.-C., Gazeau, F., 2003. Intracellular uptake of anionic superparamagnetic nanoparticles as a function of their surface coating. Biomaterials 24, 1001–1011. https://doi.org/10.1016/S0142-9612(02)00440-4

311. Woodley, J., 2001. Bioadhesion: new possibilities for drug administration? Clin. Pharmacokinet. 40, 77–84.

312. Xi, Y., Xu, P., 2021. Global colorectal cancer burden in 2020 and projections to 2040. Transl. Oncol. 14, 101174. https://doi.org/10.1016/j.tranon.2021.101174

313. Xiao, Y., Zhou, X., 2008. Synthesis and properties of a novel crosslinked chitosan resin modified by l-lysine. React. Funct. Polym. 68, 1281–1289. https://doi.org/10.1016/j.reactfunctpolym.2008.06.015

314. Yang, J., Zhang, Q., Liu, T., 2018. Autophagy facilitates anticancer effect of 5-fluorouracil in HCT-116 cells. J. Cancer Res. Ther. 14, 1141. https://doi.org/10.4103/0973-1482.204898

315. Yang, X.X., Li, C.M., Huang, C.Z., 2016. Curcumin modified silver nanoparticles for highly efficient inhibition of respiratory syncytial virus infection. Nanoscale 8, 3040–3048.

316. Yuan, H., Miao, J., Du, Y.-Z., You, J., Hu, F.-Q., Zeng, S., 2008. Cellular uptake of solid lipid nanoparticles and cytotoxicity of encapsulated paclitaxel in A549 cancer cells. Int. J. Pharm. 348, 137–145. https://doi.org/10.1016/j.ijpharm.2007.07.012

317. Yuan, Y., Chesnutt, B.M., Haggard, W.O., Bumgardner, J.D., 2011. Deacetylation of chitosan: Material characterization and in vitro evaluation via albumin adsorption and pre-osteoblastic cell cultures. Materials 4, 1399–1416.

318. Zebib, B., Mouloungui, Z., Noirot, V., 2010. Stabilization of curcumin by complexation with divalent cations in glycerol/water system. Bioinorg. Chem. Appl. 2010.

319.Zhang, L., Wang, S., Zhang, M., Sun, J., 2013. Nanocarriers for oral drug delivery. J. Drug Target. 21, 515–527. https://doi.org/10.3109/1061186X.2013.789033

320.Zhang, T., Zhu, G., Lu, B., Qian, Z., Peng, Q., 2021. Protein corona formed in the gastrointestinal tract and its impacts on oral delivery of nanoparticles. Med. Res. Rev. 41, 1835–1850. https://doi.org/10.1002/med.21767

321.Zhang, T.-X., Zhu, G.-Y., Lu, B.-Y., Zhang, C.-L., Peng, Q., 2017. Concentration-dependent protein adsorption at the nano–bio interfaces of polymeric nanoparticles and serum proteins. Nanomed. 12, 2757–2769. https://doi.org/10.2217/nnm-2017-0238

322.Zhao, D., Yu, S., Sun, B., Gao, S., Guo, S., Zhao, K., 2018. Biomedical Applications of Chitosan and Its Derivative Nanoparticles. Polymers 10. https://doi.org/10.3390/polym10040462

323.Zhao, R., Xiang, J., Wang, B., Chen, L., Tan, S., 2022. Recent Advances in the Development of Noble Metal NPs for Cancer Therapy. Bioinorg. Chem. Appl. 2022, e2444516. https://doi.org/10.1155/2022/2444516

324.Zhao, T., Qiu, D., 2011. One-Pot Synthesis of Highly Folded Microparticles by Suspension Polymerization. Langmuir 27, 12771–12774. https://doi.org/10.1021/la2028912

325.Zhao, X., Zhou, L., Li, Q., Zou, Q., Du, C., 2018. Biomimetic mineralization of carboxymethyl chitosan nanofibers with improved osteogenic activity in vitro and in vivo. Carbohydr. Polym. 195, 225–234. https://doi.org/10.1016/j.carbpol.2018.04.090

326.Zhou, Y., Liang, K., Zhao, S., Zhang, C., Li, J., Yang, H., Liu, X., Yin, X., Chen, D., Xu, W., Xiao, P., 2018. Photopolymerized maleilated chitosan/methacrylated silk fibroin micro/nanocomposite hydrogels as potential scaffolds for cartilage tissue engineering. Int. J. Biol. Macromol. 108, 383–390. https://doi.org/10.1016/j.ijbiomac.2017.12.032

327.Zhu, J., Sanidad, K.Z., Sukamtoh, E., Zhang, G., 2017. Potential roles of chemical degradation in the biological activities of curcumin. Food Funct. 8, 907–914. https://doi.org/10.1039/C6FO01770C

328.Zhu, X., Fan, H., Li, D., Xiao, Y., Zhang, X., 2007. Protein adsorption and zeta potentials of a biphasic calcium phosphate ceramic under various conditions. J. Biomed. Mater. Res. B Appl. Biomater. 82B, 65–73. https://doi.org/10.1002/jbm.b.30706

329.Zvezdova, D., 2010. Synthesis and characterization of chitosan from marine sources in Black Sea 5.

ANNEXURES

LIST OF PUBLICATIONS

1. **Dhanya, C.S.**, Paul, W., Victor, S.P., Joseph, R., **2021**. On improving the physiological stability of curcuminoids: Curcumininoid-silver nanoparticle complex as a better and efficient therapeutic agent. *Nano-Structures & Nano-Objects*, 25, 100661. https://doi.org/10.1016/j.nanoso.2020.100661. Available online -5 January 2021. (Current cite score – 11.9).

2. **Dhanya, C.S.**, Paul, W., Rekha, M.R., Joseph, R., **2023**. Solid lipid nanoparticles of lauric acid: A prospective drug carrier for oral drug delivery. *Journal of Molecular Liquids*, 380, 121738. https://doi.org/10.1016/j.molliq.2023.121738. Available online – 15 June 2023. (Impact factor – 6.0).

APPENDICES

A1. SDS-PAGE REAGENTS

Acrylamide/bisacrylamide

Acrylamide-87.6 g

N, N-Methylene Bisacrylamide-2.4 g

Distilled water-300 mL

Filter and store in dark bottles at 4 ºC

Sodium dodecyl sulphate (SDS) (10%)

SDS (10%) stock solution was prepared in distilled water and stored at room temperature.

Ammonium per sulphate (APS)

APS (10%) was freshly prepared in distilled water.

Tris buffers

1.5 M tris-HCl buffer (pH-8.8) for resolving gel and 0.5 M tris-HCl buffer (pH-6.8) for stacking gel were used.

SDS -PAGE running buffer (10x)

Prepared by dissolving 30.3 g of Tris base, 144.1 g of glycine, and 10 g SDS in 1000 mL of distilled water. To prepare 1x buffer 100 mL of the 10x stock solution was diluted with 900 mL of distilled water

SDS-PAGE sample buffer: The composition of the buffer used was 0.5 mM Tris-HCl (pH-6.8), 10 % SDS, 1% bromophenol blue, and 25% glycerol. Add β-mercaptoethanol immediately before use.

Gel preparation: The glass plates were cleaned with ethanol and assembled the gel casting mold. Resolving gel (12 %) was prepared as per Table A1 and poured into the gap between the glass plates. To maintain an even and horizontal resolving gel surface, overlayed the surface with water. After completion of polymerization (30 min), the overlay was poured off and then 5 % stacking gel was poured. The stacking gel was prepared according to Table A1. The comb was inserted gently into the stacking gel solution and the gel was allowed to polymerize (20-30 minutes). Remove the combs and rinse the wells with distilled water.

Table A1. Composition of resolving and stacking gel

Components	12 % Resolving gel (10 mL)	5 % Stacking gel (3 mL)
Water	3.3	2.1
30 % Acrylamide mix	4.0	0.5
1.5 M Tris (pH 8.8) for resolving gel or 0.5 M Tris (pH 6.8) for stacking gel	2.5	0.38
10 % SDS	0.1	0.03
10 % APS	0.1	0.03
TEMED	0.004	0.003

TEMED must be the last ingredient added

A2. COOMASSIE BRILLIANT BLUE STAINING OF SDS-PAGE GEL

Methanol: acetic acid solution: 100 mL of 40 % methanol: 100 mL of 20% glacial acetic acid.

Coomassie brilliant blue stain: 0.2 g of coomassie brilliant blue dissolved in 200 mL of methanol: acetic acid solution and filtered to remove particulate matter.

Destaining solution (500 mL): Methanol (250 mL), Acetic acid (50 mL), and water (200 mL).

The gel was removed carefully from the glass plates and immersed in Coomassie brilliant blue stain and stained the gel overnight by giving gentle rocking. The gel was destained by adding a destaining solution with gentle shaking for 4 hours. The destaining solution was changed 3- 4 times.